Developing broad-spectrum pan-sarbecovirus countermeasures

Ji Min Lee

A dissertation

submitted in partial fulfillment of the

requirements for the degree of

Doctor of Philosophy

University of Washington

2026

Reading Committee:

David Veesler, Chair

Neil King

Deborah Fuller

Program Authorized to Offer Degree:

Biochemistry

University of Washington

Abstract

Developing broad-spectrum pan-sarbecovirus countermeasures

Ji Min Lee

Chair of the Supervisory Committee:

David Veesler

Department of Biochemistry

Two sarbecoviruses, severe acute respiratory syndrome coronavirus (SARS-CoV) in 2003 and severe acute respiratory syndrome coronavirus 2 (SARS-CoV-2) in 2019, have crossed species barriers and spilled over to humans. The latter of the two resulted in a pandemic exerting an unprecedented toll on global healthcare capacity, claiming millions of lives while simultaneously inflicting collateral damage to the world economy. Pandemic experience has deepened our understanding of sarbecoviruses and shaped our frameworks for developing therapeutics and vaccines against them. Sarbecovirus spike glycoprotein is the key molecular machinery for viral entry and fusion into the host cell, making it the principal target when developing countermeasures against sarbecoviruses. The primary goal of therapeutics and vaccines is to directly neutralize the virus and/or to confer protection by eliciting immune responses. In the following

chapters of this dissertation, I detail our efforts to develop pan-sarbecovirus countermeasures with a broad spectrum. First, I will describe a *de novo* designed miniprotein against the SARS-CoV-2 receptor binding domain that retained its inhibitory functions across multiple SARS-CoV-2 variants. Then, I will delineate the potential of receptor tropism and zoonotic spillover of a clade 3 sarbecovirus and what countermeasures might be applicable, propelling us to prepare better for a pandemic should there be another one from sarbecoviruses. In the final sections of the dissertation, I will focus on the development and assessment of broad-spectrum pan-sarbecovirus vaccines focusing on the highly conserved prefusion-stabilized fusion machinery of sarbecoviruses. Our focus on prefusion-stabilized sarbecovirus fusion machinery vaccines provides a roadmap for the development of next-generation pan-sarbecovirus vaccines. Our work, collectively, highlights the importance of sarbecovirus countermeasures and provides a foundation for developing broadly applicable therapeutics and vaccines.

Table of Contents

List of Figures

List of Tables

ACKNOWLEDGEMENTS

Completing this dissertation has been a journey as demanding as it has been rewarding, and it would not have been possible without the collective support of my academic supervisors, colleagues, collaborators, friends, and family. I am deeply grateful for the wonderful journey we shared together and wish to express my sincere gratitude to everyone who contributed to this process.

First, thank you to my academic mentors and my thesis committee for providing valuable insights on the project along the way. Most importantly, I want to express my deepest gratitude to my advisor, David. Over the past four years, your mentorship, support, and the resources you provided have been instrumental to my growth. You helped me realize my own strength and shaped me into the scientist I only dreamed of becoming when I first stepped off the airplane from Korea to Seattle in 2021, determined to take on the challenges of PhD life.

Next, to all members of the Veesler Lab: thank you for being an incredible community. From Day 1 of my rotation, I have been inspired by your willingness to step in and support one another’s projects and by your rigorous insight. Your passion for science has always inspired me and kept me motivated. I am also grateful for the countless memories we made together—both inside the lab as colleagues and outside as friends—which offered so much joy and camaraderie throughout this journey.

Finally, I would like to thank my collaborators and the UW community. This research was made possible through the combined support of our fantastic collaborators at the University of Washington, the UW Institute for Protein Design (IPD), Fred Hutch, the University of North Carolina, the University of Utah, Washington University in St. Louis, and Vir. I also want to extend a big thanks to everyone I have interacted with at UW, including the BPSD-Biochem 2021-2022 cohort. I am so happy to have met you all, and I truly appreciate the experiences we shared.

Lastly, my deepest thanks go to my family and my partner for your patience and for always supporting my decisions. Spending time with you all is what I enjoy most in life, and being so far away—navigating such significant time differences—has been tough for us all. I miss you more than words can describe. It is only because of your unconditional support and unwavering belief in me that I was able to keep moving forward and finally achieve what I set out to do—what WE set out to do. I am so fortunate to have all of you in my life.

CHAPTER 1. INTRODUCTION

1.1 Sarbecoviruses and their spike glycoproteins

Coronaviruses are enveloped, positive-strand RNA viruses that display surface glycoproteins that infect a wide range of species including humans (V'kovski et al., 2021). Coronavirus constitutes the Orthocoronavirinae subfamily which is divided into four genera: *alphacoronavirus*, *betacoronavirus*, *deltacoronavirus*, and *gammacoronavirus (V'kovski et al., 2021)*. Betacoronavirus is further divided into subgenuses embecovirus, merbecovirus, sarbecovirus, nobecovirus, and hibecovirus. Throughout the subsequent chapters in this dissertation, I will focus on sarbecoviruses.

Sarbecoviruses have been reported to infect several animal species such as bats and occasionally jump species over to humans with SARS-CoV (severe acute respiratory syndrome coronavirus, referred to as SARS-CoV-1 from here after) and SARS-CoV-2 (severe acute respiratory syndrome coronavirus 2) from the subgenus causing a global outbreak in 2002 and a pandemic in 2019 implementing significant threat on global health and economy (Boni et al., 2020; B. Liu et al., 2023). Each spillover event resulted in over 500 and 7 million deaths worldwide, respectively, urging the development of countermeasures against them (*CDC SARS Response Timeline*, 2023, *COVID-19 Cases*, n.d.). Furthermore, more sarbecovirus samples are being discovered and isolated to this date with many of its host and animal reservoirs remaining yet to be identified (Boni et al., 2020; Crook et al., 2021; Evans et al., 2023; Seifert et al., 2022; Wells et al., 2021). Many of these newly discovered sarbecoviruses have the potential to infect humans after undergoing a few or no mutations in their genome, which highlights the risk of potential zoonotic spillover (Lee et al., 2023; Seifert et al., 2022; Starr, Zepeda, et al., 2022; Wells et al., 2021).

Sarbecovirus genome consists of several non-structural proteins (nsps) that are involved in viral RNA synthesis and other various functions, and four structural proteins (S: spike protein, E: envelope protein, M: membrane protein, and N: nucleocapsid protein) that are critical for viral assembly (V'kovski et al., 2021). The spike (S) glycoprotein is a large homotrimer glycoprotein that coats the surface of the virus, thereby giving the virus its name Coronavirus, and is responsible for host cell recognition, initiating viral entry into host cells (Pennington, 2004; Tortorici & Veesler, 2019). The spike glycoprotein has two key structural subunits, S_1 and S_2. The S_1 subunit that sits at the top of the spike interacts with host cell receptors and carbohydrates, and includes the N-terminal domain (NTD, also known as domain A) and receptor binding domain (RBD, also known as domain B). S_1 subunit is the most diverse region of the spike across sarbecoviruses, resulting in a wide range of receptor tropism among sarbecoviruses. The S_2 subunit, which is also known as the fusion machinery, is anchored to the viral membrane and is responsible for triggering the fusion of the viral membrane and the host cell membrane upon cleavage by a cellular protease at the S_2' site (Belouzard et al., 2009; Bosch et al., 2003; Kirchdoerfer et al., 2016). Spike glycoprotein is a class 1 fusion glycoprotein, which is a type of fusion machinery that is well represented by envelope protein (Env) gp41 of HIV-1 and hemagglutinin (HA) of influenza virus. S_2 subunit has key features of class 1 fusion protein such as two heptad repeat (HR) regions called HR1 and HR2 that will come together in space to form a six-helix bundle structure at the end of the fusion process (Harrison, 2008; Shi et al., 2023). Due to the transient nature of the fusion process, fusion intermediate structures of the spike glycoprotein are not well described. In a recent study, a group of researchers reported an early fusion intermediate (EFIC) conformation of SARS-CoV-2 spike where HR1 ejected towards the host cell membrane before protease cleavage at S_2' site (Xing et al., 2025). Upon activation by cellular proteases cleaving S_2 subunit upstream (S_2' site) of the fusion peptide, S_1 subunits are shedded and S_2 subunit undergoes dramatic conformational change from prefusion state to postfusion state, inserting hydrophobic fusion peptide into the host cell membrane, and bringing the two membranes together completing the fusion process (Bosch et al., 2003; Heald-Sargent & Gallagher, 2012; Millet & Whittaker, 2015; A. C. Walls et al., 2017). Some coronaviruses like SARS-CoV-2 spike glycoprotein harbor an additional cleavage site between the S_1 and the S_2 subunits by furin-like proteases (S_1/S_2 site) that is cleaved during biogenesis of the virus (Y. Wu & Zhao, 2021; W. Zhu et al., 2023). Despite the different characteristics of the spike glycoprotein within sarbecovirus, it is often the most targeted and most effective viral protein when developing countermeasures against the viruses since the spike glycoprotein in sarbecoviruses are involved in host cell engagement and fusion.

1.2 Immune responses against viruses

Viral infections induce a complex defense mechanism in humans, which is a sophisticated combination of a more rapid innate immunity and a relatively slower but more specific adaptive immunity. Once a virus infects humans, the immune system starts responding at the infection site and nearby lymph nodes or spleen (Rich et al., n.d.). At the infection site, innate immunity is the first response against a virus with antigen-presenting cells (APCs) and lymphocytes drawn to the tissue by chemokines and cytokines. This is the first line of defense, which will slow down the viral infection to allow time for the more specific adaptive immune response to begin.

Adaptive immune responses can be divided into two major types: humoral immunity, driven by antibodies produced by B cells, and cellular immunity, driven by T cells. At the site of infection, dendritic cells (DCs), in general, will bring viral antigens to lymph nodes or spleen, where they will encounter B-cells in the B-cell follicles (Rich et al., n.d.). Antigens on viruses interact with B-cell receptors (BCRs) that are expressed on the surface of B cells (Janeway et al., 2001). B cells recognize the exposed surface of an antigen. Downstream signaling produced by sufficient binding will activate transcription factors to trigger B cell activation where some will become short-lived plasma cells while others interact with helper T cells (CD4+ T cells) (Rich et al., n.d.). These B cells will initiate germinal center (GC) reactions where somatic hypermutation happens. B cells that have undergone successful affinity maturation, meaning their BCRs have been selected to have high-affinity against the presented antigen, will either partly become long-lived plasma cells that produce antibodies or partly become memory B cells to provide long-term memory. T cell responses also happen within lymphoid tissues. T cells recognize antigens through processed peptides presented by major histocompatibility complexes (MHCs). MHC class I presents viral peptides from inside the cell, and MHC class II presents peptides from endocytosed extracellular antigens. CD8+ T cells recognize virus-derived peptides presented on MHC class I and will kill infected cells. CD4+ T cells recognize virus-derived peptides presented on MHC class II and primarily function as helper cells for CD8+ T cell and B cell responses.

Immunoglobulins (Ig) or antibodies are Y-shaped proteins produced by plasma cells. Antibodies are composed of fragment antigen binding (Fab) regions, where it recognize and bind to a specific antigen, and fragment crystallizable (Fc) region. Two classes of antibodies to consider in immune responses against a virus are neutralizing antibodies (nAb) and non-neutralizing antibodies. Neutralizing antibodies disrupt the viral lifecycle mostly by binding to the viral glycoprotein that mediates entry and fusion, thus blocking such processes. Also, they can bind to viral glycoproteins that are expressed on the surface of infected cells and prevent progeny viruses from budding out, which stops the spread of infection from one cell to another. Non-neutralizing antibodies also play a critical role in *in vivo* protection against viruses, mainly through their Fc region, which interacts with Fc gamma receptors (FcγRs) on effector cells to facilitate effector functions. Fc-mediated effector functions include antibody-dependent cell-mediated cytotoxicity (ADCC), where antibodies are bound to viral protein expressed on the surface of infected cells and interact with FcγRIIIA to induce release of cytotoxic granules from effector cells such as natural killer (NK) cells (van Erp et al., 2019). These cytotoxic granules contain perforins and granzymes that kill infected cells (van Erp et al., 2019). Antibody-dependent cellular phagocytosis (ADCP) is another example of Fc-mediated effector function where phagocytic cells take up and traffick the virus-antibody complex or antibody-coated infected cells to lysosomes for degradation (van Erp et al., 2019). Complement-dependent cytotoxicity (CDC) results from C1q molecule binding to the Fc domain of antibodies that are bound to infected cells expressing viral proteins, which leads to downstream cascade reactions that result in the formation of membrane attack complexes (MACs), which create holes in membrane, followed by subsequent cell lysis (van Erp et al., 2019).

1.3 Therapeutic miniproteins against viral pathogens

Viral inhibitors are drugs that disrupt steps in the general viral lifecycle, including interfering with viral entry to the host cell, viral protein production and assembly, and viral egress. De novo designed miniproteins using computational protein design has emerged to be cutting-edge tools in various fields, such as designing agonists/antagonists or designing viral inhibitors. Several miniproteins have been designed and are currently being designed against multiple viral pathogens, including HB36.6 targeting influenza haemagglutinin (Chevalier et al., 2017; Fleishman et al., 2011; Koday et al., 2016), and cb3 targeting the RBD of MERS-CoV (Ragotte et al., 2025). These miniproteins hold potential advantages over conventional monoclonal antibody therapeutics. First, miniproteins, due to its small size, typically ranging around 5 kDa, allows direct intranasal administration, nebulization, or dry powder aerosol, which can be beneficial for treating infection with respiratory viruses. Moreover, with a successful design engineering, miniproteins can be hyper-stable, maximizing the delivery efficacy and eliminating the need for cold chain supply. Miniproteins can also be rapidly produced from the design step to the manufacturing step, aided with the recent development of computational tools. Miniproteins often exhibit picomolar affinity, resulting in exceptionally high potency. Overall, miniproteins could hold promising potential as therapeutics with their high stability and maximal efficacy coming from high potency and high local density of inhibitory domains.

1.4 Fusion machinery vaccines against viral pathogens

Vaccines are biological products that are used to elicit an immune response against a pathogen-induced disease in a safe manner. The main goal of vaccines is to train the adaptive immune system to recognize pathogens readily upon encounter and confer protection against the pathogen. Vaccines are therefore composed of antigens that are either directly from the pathogen or recombinantly produced *in vitro*. There are many platforms of vaccines that have been developed, ranging from the more traditional live attenuated vaccines to subunit vaccines, virus-like particle (VLP) vaccines, and mRNA vaccines (Pollard & Bijker, 2021). Vaccinated individuals also develop immune memory via memory cells that, upon reencountering the same or related pathogen, will rapidly start producing antibodies. Vaccines can confer protection not just in vaccinated individuals but also in unvaccinated individuals through herd immunity if enough population in a community has been vaccinated (Pollard & Bijker, 2021). Finding the right vaccine candidate, along with an appropriate adjuvant if needed, and optimizing vaccination doses and schemes are key factors to consider when developing a new vaccine candidate.

The fusion machinery of a virus is a crucial component of viral proteins that mediates the fusion of the viral membrane and the host cell membrane. Due to its significant functional role, it is therefore often the highest conserved part of viral proteins across different virus variants, making it an ideal target for broad-spectrum vaccine development. However, fusion machinery of a virus is frequently metastable, meaning it readily changes conformation from a highly unstable prefusion state to an energetically favorable postfusion state, which is often less effective as a vaccine target. Fusion machinery that has been successfully engineered to be stabilized in prefusion conformation will be an optimal immunogen and will elicit antibodies against the fusion machinery, thereby locking the virus fusion protein in prefusion state and abrogating the subsequent fusion process.

Respiratory syncytial virus (RSV) fusion protein (F) is one successful example of developing prefusion stabilized fusion machinery vaccines. Researchers discovered potent RSV-neutralizing antibodies that did not bind to the postfusion state but recognized the apex of the prefusion F, unraveling a critically susceptible site on the virus (Magro et al., 2012; McLellan, Chen, Leung, et al., 2013). RSV fusion protein was engineered to be locked in a prefusion state by incorporating disulfide bonds and cavity-filling mutations (McLellan, Chen, Joyce, et al., 2013). Prefusion-stabilized RSV F protein generated potent neutralizing antibodies leading to FDA approval of Pfizer Abrysvo and GSK Arexvy vaccines in 2023 (McLellan, Chen, Joyce, et al., 2013).

Hemagglutinin (HA) facilitates influenza virus binding and entry into host cells, followed by membrane fusion of the virus and the host cell, making it the main target for influenza vaccine development. The stem of HA is highly conserved across different flu strains compared to the constantly-changing head domain and is the main target of broadly neutralizing antibodies (Corti et al., 2011; Ekiert et al., 2009, 2011; Sui et al., 2009; Throsby et al., 2008). However, HA is metastable in prefusion conformation, especially in the absence of the HA head, and undergoes extensive conformational rearrangements when exposed to low pH, which requires extensive protein engineering to develop an HA stem-derived immunogen (Skehel et al., 1982; Skehel & Waterfield, 1975; Wilson et al., 1981). Consequently, there have been intensive efforts in developing a universal flu vaccine that focuses on presenting the stem of the HA in a stabilized prefusion conformation (Impagliazzo et al., 2015; Krammer et al., 2013; Yassine et al., 2015).

Similarly, the fusion protein Env of human immunodeficiency virus (HIV) has been a popular target for vaccine design (Houser et al., 2022; Olia et al., 2023; Pancera et al., 2014). The hurdle here is that Env is heavily glycosylated, resulting in epitopes shielded by glycans. Env, also being highly unstable, makes it a difficult target for vaccine design despite its high sequence identity between different HIV strains.

1.5 Severe acute respiratory syndrome coronavirus 2 pandemic and countermeasures

Severe acute respiratory syndrome coronavirus 2, more well known as SARS-CoV-2, emerged late 2019 in Hubei Province, China. Thereafter, it has spread worldwide rapidly, causing the COVID-19 pandemic, resulting in over 700 million positive cases and over 7 million deaths reported as of December 2025 (*COVID-19 Cases*, n.d.). SARS-CoV-2 is highly transmissible and primarily spreads through droplets and aerosols from infected individuals, making contact with mucous membranes in the respiratory tract of another. Once infected with SARS-CoV-2, individuals can have symptoms varying from mild cold-like symptoms to severe respiratory disorders and subsequent organ failures (Argenziano et al., 2020; Chu et al., 2005; Connors & Levy, 2020; Giamarellos-Bourboulis et al., 2020; C. Huang et al., 2020; Lin et al., 2020; L. Mao et al., 2020).

SARS-CoV-2 interacts with host cell receptor angiotensin-converting enzyme 2 (ACE2) via spike protein RBD to enter the host cell followed by the host cell transmembrane serine protease 2 (TMPRSS2) cleaving the S_2' site (upstream of fusion peptide) to mediate fusion of the viral membrane and the host cell membrane (Hoffmann, Kleine-Weber, & Pöhlmann, 2020; Hoffmann, Kleine-Weber, Schroeder, et al., 2020; Ou et al., 2020; P. Zhou et al., 2020). Due to its significant role in the host cell interaction process, the spike protein has been the primary target of countermeasures against SARS-CoV-2. All therapeutic monoclonal antibodies that have been licensed for COVID-19 treatment target the spike protein, primarily the RBD of the spike protein, to neutralize the virus by blocking the virus's interaction with the host cell receptor (Corti et al., 2021).

Accordingly, the vaccine developed to tackle SARS-CoV-2 intends to elicit neutralizing antibodies against the spike glycoprotein. Thus, all approved vaccines for COVID-19 composed of the spike protein or subunits of the spike protein either by encoding the gene or delivering the spike glycoprotein as a component of the vaccine (Chi et al., 2022). The two mRNA-LNP vaccines, mRNA-1273 from Moderna and BNT162b from Pfizer/BioNTech, encode membrane anchored prefusion-stabilized spike (S2P) (Jackson et al., 2020; Vogel et al., 2021). Our previous work with collaborators resulted in the development of the protein subunit vaccine SKYCovione that utilizes self-assembling nanoparticles that display RBD on its surface (A. C. Walls, Fiala, et al., 2020). Another example of a protein subunit vaccine is NVX-CoV2373 from Novavax, which contains S2P formulated into nanoparticles (Keech et al., 2020). Ad26.COV2.S from Janssen/Johnson & Johnson and AZ1222 from Oxford/AstraZeneca are examples of non-replicating viral vector vaccines that deliver DNA encoding S2P and wild-type spike, respectively (Bos et al., 2020; Folegatti et al., 2020). Other types of vaccines include inactivated viruses such as CoronaVac from Sinovac (*Efficacy Safety COVID-19 Inactivated Vaccine Healthcare Professionals Brazil: PROFISCOV Study*, n.d.).

Despite all aforementioned efforts, the constant evolution of SARS-CoV-2, especially the immune pressure on the RBD, has resulted in the emergence of variants that carry mutations that evade therapeutic monoclonal antibodies and polyclonal antibodies elicited by vaccines, resulting in the need for frequent updates on the vaccines. Considering the potential zoonotic spillover events of other sarbecoviruses as well, the necessity of developing broadly applicable sarbecovirus therapeutics and vaccines is crucial. This is why many researchers, including ourselves, whose work will be described in this dissertation focuses on developing vaccine candidates concentrating on the fusion machinery of SARS-CoV-2 (Halfmann et al., 2022; Ng et al., 2022). In our works, we target the whole ectodomain or full length of SARS-CoV-2 S_2, whereas some others concentrate on smaller domains such as fusion peptide or HR1 and HR2 (Ma et al., 2020; Maeda et al., 2021; Pang et al., 2022).

In this dissertation, I describe our efforts to develop various countermeasures that are broadly applicable to not just SARS-CoV-2 variants, but sarbecoviruses, focusing on SARS-CoV-1 (clade 1a), SARS-CoV-2 (clade 1b), and PRD-0038 (clade 3) as our representative model system.

CHAPTER 2. The computationally designed TRI2-2 miniprotein inhibitor protects against multiple SARS-CoV-2 Omicron variants

In this chapter, I describe how previously studied *de novo* designed miniprotein TRI2-2 still retains its function against multiple SARS-CoV-2 Omicron variants that are highly immune-evasive. This study was initiated in early 2022, only a few months after the first identification of the SARS-CoV-2 Omicron variant, and it covers representative Omicron variants from then to up until mid 2024. In the subsequent sections, I detail how TRI2-2 confers protection against these Omicron variants *in vivo*. This chapter highlights the robustness of *de novo* miniprotein and its potential role as an effective sarbecovirus therapeutics.

Adapted from: Lee, J., Case, J. B., Park, Y.-J., Ravichandran, R., Asarnow, D., Tortorici, M. A., Brown, J. T., Sanapala, S., Carter, L., Baker, D., Diamond, M. S., & Veesler, D. (2026). The computationally designed TRI2-2 miniprotein inhibitor protects against multiple SARS-CoV-2 Omicron variants. *Communications Biology*. https://doi.org/10.1038/s42003-025-09499-2

2.1 Chapter Introduction

The severe acute respiratory syndrome coronavirus 2 (SARS-CoV-2) spike (S) glycoprotein interacts with its host receptor ACE2 and initiates viral entry into cells (Hoffmann, Kleine-Weber, Schroeder, et al., 2020; Letko et al., 2020; A. C. Walls, Park, et al., 2020; P. Zhou et al., 2020). The emergence of SARS-CoV-2 Omicron variants at the end of 2021 and afterwards have reduced the efficacy of vaccines and monoclonal antibodies, increased the number of reinfections or breakthrough infections, and led to successive waves of global infection (Bowen, Addetia, et al., 2022; Cameroni et al., 2022; Y. Cao et al., 2023; Tegally et al., 2022; Viana et al., 2022; A. C. Walls et al., 2022).

We previously described a computationally-designed, homotrimeric miniprotein inhibitor, designated TRI2-2, that binds with high avidity to SARS-CoV-2 S as a result of simultaneously engaging all three receptor-binding domains (RBDs) within an S trimer (L. Cao et al., 2020; Hunt et al., 2022). We showed that intranasal administration of TRI2-2 after viral exposure protected mice from challenge with the SARS-CoV-2 Beta and Delta variants (Hunt et al., 2022). Here, we show that TRI2-2 retains *in vitro* neutralization and *in vivo* protective activity against virtually all Omicron variants that have emerged for 5 years of the COVID-19 pandemic, highlighting its robustness as a possible next-generation therapeutic.

2.2 Cross-reactivity and neutralizing activity of TRI2-2 minibinder against SARS-CoV-2 Omicron variants

To investigate the ability of TRI2-2 to recognize SARS-CoV-2 Omicron variants associated with recent infection waves, we assessed binding to a panel of biotinylated RBDs immobilized on biolayer interferometry (BLI) biosensors. TRI2-2 bound to the Wuhan-Hu-1 and Delta RBDs with single digit picomolar avidities and to the BA.1, BA.2, BA.2.12.1, BA.2.75.2, BA.5, BQ.1.1, XBB.1.5, BA.2.86, and JN.1 variant RBDs with nanomolar avidities. However, no binding to the KP.3 RBD was detected (**Figure 2.1a**

and Figure 2.2). These data establish that TRI2-2 binds avidly (i.e. with slow off-rates) to most Omicron variants evaluated despite accumulation of RBD mutations in the receptor-binding motif (ACE2-binding site), which overlaps with the TRI2-2-binding site. We subsequently tested the ability of TRI2-2 to inhibit vesicular stomatitis virus (VSV) particles pseudotyped with the Wuhan-Hu-1 D614G, Delta, BA.1, BA.2, BA.2.12.1, BA.2.75.2, BA.5, BQ.1.1, XBB.1.5, BA.2.86, JN.1, or KP.3 S using HEK293T target cells stably expressing human ACE2 (Crawford et al., 2020). TRI2-2 potently neutralized all pseudoviruses tested, in a concentration-dependent manner, with half-maximal inhibition concentrations ranging between ~0.5 and ~5 nM except for JN.1, for which its potency was reduced to ~300 nM and KP.3 that was not inhibited in our assay, concurring with its lack of binding to this variant RBD (**Figure 2.1b and Figure 2.3**). Comparatively, the AHB2 minibinder, which is the monomer from which TRI2-2 derives (through genetic fusion to a trimerization motif), inhibited Wuhan-Hu-1 D614G S- and Delta S VSV pseudoviruses but failed to block any of the Omicron variants evaluated (**Figure 2.1b and Figure 2.3**). These findings demonstrate that harnessing the binding avidity resulting from trivalent engagement of S trimers endows TRI2-2 with broadly neutralizing activity.

We subsequently assessed the ability of TRI2-2 to inhibit syncytia formation between cells using a split green fluorescent protein (GFP) system with Vero E6/TMPRSS2 target cells (Vero E6 cells stably expressing TMPRSS2 and GFP β strand 11) and BHK-21 effector cells (stably expressing GFP β strands 1 to 10) transiently transfected with Wuhan-Hu-1 D614G, BQ.1.1, XBB.1.5 or BA.2.86 S (Bowen, Addetia, et al., 2022; Kodaka et al., 2015). Consistent with the broadly neutralizing activity observed, addition of TRI2-2 decreased S-mediated syncytia formation with all variants tested (**Figure 2.1c and Figure 2.4**) (Bussani et al., 2020).

2.3 Molecular basis of TRI2-2 minibinder and SARS-CoV-2 BA.2.86 spike interaction

To determine the molecular basis of the exceptional resilience to antigenic changes that have emerged in the S glycoprotein of SARS-CoV-2 variants, we determined a cryoEM structure of the BA.2.86 S trimer bound to TRI2-2 at 2.4 Å resolution (**Figure 2.1d and Figure 2.5**). Local refinement of the region comprising the RBD and TRI2-2 yielded a reconstruction at 3.2 Å resolution with improved local resolution, revealing key interacting residues that are mutated or conserved in the SARS-CoV-2 Wuhan-Hu-1 RBD and BA.2.86 RBD (**Figure 2.1e**). The BA.2.86 S $K417N_{\text{SARS-CoV-2}}$ (**Figure 2.1e-i**) and $Q498R_{\text{SARS-CoV-2}}$ (**Figure 2.1e-ii**) mutations abolish hydrogen bonds formed with $N36_{\text{TRI2-2}}$ and $E3_{\text{TRI2-2}}$, respectively, possibly contributing to the reduced binding avidity observed for Omicron variants relative to SARS-CoV-2 Wuhan-Hu-1 and Delta. The Q498R and N501Y mutations are sterically incompatible with the positioning of the TRI2-2 I47 side chain observed in the Wuhan-Hu-1 complex structure and leads to reorganization of the minibinder region comprising the C-terminal part of the second helix and loop connecting to the third helix (**Figure 2.1e-ii**, highlighted with black arrows). Our structure also suggests that the JN.1 $L455S_{\text{SARS-CoV-2}}$ residue substitution would reduce van der Waals packing at the interface with the minibinder (**Figure 2.1e-iii**), thereby decreasing TRI2-2 binding avidity and consequently neutralizing activity (**Figure 2.1a-b**). However, hydrogen bonds formed between H18$_{\text{TRI2-2}}$ and D420$_{\text{SARS-CoV-2}}$ (**Figure 2.1e-i**), H22$_{\text{TRI2-2}}$ and Y421$_{\text{SARS-CoV-2}}$ (**Figure 2.1e-i**), E30$_{\text{TRI2-2}}$ and N487$_{\text{SARS-CoV-2}}$ (**Figure 2.1e-iii**), T40$_{\text{TRI2-2}}$/E41$_{\text{TRI2-2}}$ and Q493$_{\text{SARS-CoV-2}}$ (**Figure 2.1e-iii**), are conserved in the Wuhan-Hu-1 and BA.2.86 RBD complex structures. We note that although BA.1 and BA.2 harbored the Q493R substitution (Bowen, Addetia, et al., 2022; Cameroni et al., 2022), TRI2-2 retained potent neutralizing activity against these variants (**Figure 2.1b,f**). However, the KP.3 Q493E$_{\text{SARS-CoV-2}}$ mutation (**Figure 2.1e-iii**) would introduce charge repulsion with the nearby E41$_{\text{TRI2-2}}$ residue (**Figure 2.1e-iii**), which likely explains the loss of binding and of neutralizing activity of this variant. Contacts in several regions are remodeled by residue changes between Wuhan-Hu-1 and BA.2.86, as revealed by our structural data. The BA.2.86 S Y505H substitution leads to formation of a salt bridge triad with TRI2-2 residues E4 and D11, whereas D11 is salt bridged and hydrogen bonded to K403 and N405 (which are mutated from R403 and D405 in Wuhan-Hu-1 S), respectively (**Figure 2.1e-iv**). Moreover, the BA.2.86 S N460K$_{\text{SARS-CoV-2}}$ mutation replaces the hydrogen bond formed with H22$_{\text{TRI2-2}}$ by a cation-pi interaction with the same residue (**Figure 2.1e-i**). Overall, TRI2-2 buries a comparable surface at the interface with the Wuhan-Hu-1 and the BA.2.86 RBDs despite the aforementioned residue mutations. These data explain the retained TRI2-2 binding and neutralization of virtually all SARS-CoV-2 variants tested despite variations within the targeted epitope that are accommodated.

2.4 TRI2-2 minibinder therapeutically protects mice against SARS-CoV-2 BQ.1.1, XBB.1.5, and BA.2.86

To study the protective efficacy of TRI2-2 *in vivo* against immune evasive SARS-CoV-2 Omicron variants, we intranasally inoculated highly susceptible K18-hACE2 mice (Winkler et al., 2020) with 10^4 FFU of BQ.1.1, XBB.1.5, or BA.2.86. One day later, we intranasally administered a single 10 mg/kg dose of TRI2-2 or an influenza virus control minibinder (L. Cao et al., 2022). For all variants evaluated, post-exposure TRI2-2 treatment protected against weight loss throughout the duration of the experiments and reduced viral titers in the lungs and nasal turbinates six days post-challenge as compared to the control minibinder (**Figure 2.6 and Figure 2.7**). These results indicate that intranasal administration of TRI2-2 confers protection against SARS-CoV-2 challenge in a stringent model of disease with three key SARS-CoV-2 Omicron variants.

2.5 Chapter Discussion

Intramuscular vaccination results in lower neutralizing antibody titers within the human upper respiratory tract compared to natural infection (Park, Pinto, et al., 2022; Tang et al., 2022; Yisimayi et al., 2024). These findings, coupled with waning natural immunity and viral antigenic changes, likely contribute to susceptibility to SARS-CoV-2 breakthrough infections. This results in the continued transmission of SARS-CoV-2 globally, and motivates the development of next-generation countermeasures that may be administered intranasally or orally. Preclinical assessment of intranasally administered influenza and sarbecovirus vaccine candidates demonstrated the induction of lung-resident protective mucosal humoral and cellular immunity at the site of viral entry (Hassan et al., 2021; Langel et al., 2022; T. Mao et al., 2022; Oh et al., 2021; Ying et al., 2024) and lipopeptide fusion inhibitors prevented SARS-CoV-2 direct-contact transmission in ferrets (de Vries et al., 2021). Furthermore, post-exposure prophylaxis nasal spray administration of the SA58 monoclonal antibody in humans was shown to markedly reduce the risk of contracting COVID-19 (R. Song et al., 2023).

The computationally-designed TRI2-2 minibinder mediates broadly neutralizing activity and *in viv*o protection of mice in both the upper and lower airways against the highly immune evasive SARS-CoV-2 BQ.1.1, XBB.1.5, and BA.2.86 variants. These data show that TRI2-2 can accommodate residue substitutions within its epitope and provide a molecular framework to explain the remarkable neutralization breadth of SARS-CoV-2 variants that have emerged since the pandemic more than five years ago, with the exception of KP.3 due to the Q493E residue mutation. TRI2-2 is therefore endowed with exceptionally broad neutralizing activity, outperforming all monoclonal antibodies developed against SARS-CoV-2 except VIR-7229 (Rosen et al., 2024) and SA55 (Y. Cao, Jian, et al., 2022). Moreover, TRI2-2 has exceptional biophysical stability, enabling cost-effective, large-scale production, setting it apart from monoclonal antibodies that are expensive to manufacture and more challenging to scale.

Recent advances in computational protein design have markedly accelerated the workflow enabling design and optimization of minibinders (Dauparas et al., 2022; Pacesa et al., 2025; Watson et al., 2023; Zambaldi et al., 2024). Additionally, our cryo-EM structure of the BA.2.86 RBD bound to TRI2-2 will guide the future design of TRI2-2 derivative minibinders to accommodate new mutations that abrogate the binding between TRI2-2 and the SARS-CoV-2 KP.3 variant. The low manufacturing cost and the rapid design workflow along with its antiviral efficacy when delivered to the upper respiratory tract are attractive properties of minibinders that could change the drug development paradigm against rapidly evolving respiratory viruses of public health concern.

2.6 Methods

Cells

Cell lines used in this study were DH10B competent cells (Thermo Fisher Scientific), HEK293T (ATCC, CRL-11268), Vero E6-TMPRSS2-GFP$_{11}$ and BHK-21-GFP$_{1\text{-}10}$ (Bowen, Addetia, et al., 2022) and HEK293T cells with stable human ACE2 expression (kindly provided by Jesse Bloom) (Crawford et al., 2020). Cells were cultured in 10% FBS (Fisher Scientific-Cytiva), 1% penicillin-streptomycin (Thermo Fisher Scientific) DMEM at 37℃, 5% CO_2. BHK-21-GFP$_{1\text{-}10}$ and Vero E6-TMPRSS2-GFP$_{11}$ cells were generated in-house and were cultured supplemented with 2 µg/mL of Puromycin for BHK and 8 µg/mL of Puromycin and 4 µg/mL of Blasticidin for Vero cells in 10% FBS (Fisher Scientific-Cytiva), 1% penicillin-streptomycin (Thermo Fisher Scientific) DMEM at 37℃, 5% CO_2. Expi293F (Thermo Fisher Scientific) were cultured at 37°C and 8% CO_2. None of the cell lines were authenticated or tested for mycoplasma contamination.

Vero-TMPRSS2 (R. E. Chen et al., 2021) cells were cultured at 37°C in Dulbecco's modified Eagle medium (DMEM) supplemented with 10% fetal bovine serum (FBS), 10 mM HEPES pH 7.3, 1 mM sodium pyruvate, 1x non-essential-essential amino acids, and 100 U/mL of penicillin-streptomycin. Vero-TMPRSS2 cells were supplemented with 5 µg/mL of blasticidin. Vero-hACE2-TMPRSS2 cells were supplemented with 10 µg/mL of puromycin. All cells routinely tested negative for mycoplasma using a PCR-based assay.

Production of recombinant SARS-CoV-2 S RBDs

The SARS-CoV-2 RBDs were expressed in Expi293 cells (Thermo) at 37°C and 8% CO_2. Cells were transfected with the corresponding plasmids using Expifectamine (Thermo) following the manufacturer's protocol. Four days post-transfection, supernatants were clarified by centrifugation at 3000 g for 30 min, supplemented with 25 mM phosphate pH 8.0, and 300 mM NaCl and then passed through a 0.22 µm sterile filter. Supernatants were then bound to 1 mL Histrap excel columns (Cytiva) previously equilibrated in 25 mM phosphate pH 8.0, 300 mM NaCl. Nickel columns were washed with 25 mM phosphate pH 8.0, 300 mM NaCl, and 10 mM imidazole prior to elution with 25 mM phosphate pH 8.0, 300 mM NaCl and 300 mM imidazole. After buffer exchanging into 20 mM phosphate pH 8.0 and 100 mM NaCl using a centrifugal filter device with a MWCO of 10 kDa, the purified RBDs were biotinylated using the BirA biotin-protein ligase reaction kit (Avidity). The biotinylated RBD’s were bound, washed, and eluted again on the same affinity column. Purified biotinylated RBD’s were then concentrated and eluted on a Superdex200 increase 10/300 size-exclusion column (Cytiva) equilibrated in 20 mM phosphate pH 8.0 and 100 mM NaCl. Fractions containing monomeric and monodisperse RBDs were flash frozen and stored at -80°C until use.

Production of recombinant TRI2-2 and influenza virus minibinders

The TRI2-2 and influenza virus minibinders were cloned into pET29b between the NdeI and XhoI restriction sites by Genscript. The TRI2-2 minibinder was cloned with a C-terminal polyhistidine tag and the influenza minibinder was cloned with an N-terminal polyhistidine tag (MHHHHHHGSDDDSHKKKLEDELESLIKKARNPEARKMVEWLARKAKKAADLGNKISVEFLLRLARQFAEASAR) (L. Cao et al., 2022). Minibinders were expressed in Lemo21(DE3) cells (NEB) in TB II Media (MP Bio) at 37°C with IPTG induction. After cell harvest, pellets were resuspended in Gibco dPBS and lysed by microfluidization at 18,000 psi. Whole cell lysates were clarified by centrifugation at 18000 g for 30 minutes and supernatants were then bound to a 5 mL Histrap Nickel Sepharose FF column (Cytiva) previously equilibrated in Gibco dPBS supplemented with 30mM Imidazole. Nickel columns were washed with Gibco dPBS (ThermoFisher) supplemented with 30mM imidazole prior to elution with Gibco dPBS supplemented with 500mM Imidazole. Using a centrifugal filter device with a MWCO of 3 kDa, the IMAC fractions containing minibinders of interest were concentrated and then further purified by size-exclusion chromatography using an Superdex S75 Increase 10/300 GL column (Cytiva) equilibrated in Gibco dPBS as running buffer. Fractions containing TRI2-2 or Influenza minibinders were concentrated (as needed), filtered with a 0.2 μm filter, and then tested for endotoxin (LAL Charles River) prior to being flash frozen and stored at -80°C until use.

Binding analysis using biolayer interferometry (BLI)

BLI binding assays were performed on an Octet Red (Sartorius) instrument operated at 30℃ with shaking (1000 rpm). Streptavidin biosensors were hydrated in a 10x kinetics buffer (Sartorius) for 10 min prior to the experiment. Biosensors were incubated in a 10x kinetics buffer for 60s followed by the loading of biotinylated RBDs to the tip, all to a final level of 1 nm. Loaded biosensors were equilibrated in a 10x kinetics buffer for 120 s. For affinity binding assays to determine K_D values, RBD-loaded tips were dipped into a concentration series of TRI2-2 (3-fold serial dilution from 25 nM to 0.9 nM) for 300 s followed by 300 s of dissociation in a 10x kinetics buffer. Global fits were used to calculate K_D values using a 1:1 binding fit model. Data were plotted using GraphPad Prism. Assays were replicated with two biological replicates (recombinant RBD proteins generated on different days) and representative graphs and values are shown in **Figure 2.2** and **Table 2.1**, respectively.

Production of VSV pseudoviruses

SARS-CoV-2 spike VSV pseudoviruses were produced using HEK293T cells seeded on BioCoat Cell Culture Dish: poly-D-Lysine 100 mm (Corning). The following day, cells were transfected with spike constructs using Lipofectamine 2000 (Thermo Fisher Scientific) in Opti-MEM transfection medium. After 5 h of incubation at 37 °C with 5% CO_2, cells were supplemented with DMEM containing 10% of FBS. On the next day, cells were washed with three times with DMEM and infected with VSV (G*ΔG-luciferase) for 2 h, followed by five washes with DMEM medium before addition of anti-VSV G antibody (I1-mouse hybridoma supernatant diluted 1:40, ATCC

CRL-2700) and medium. After 18-24 h of incubation at 37 °C with 5% CO_2, pseudoviruses were collected and cell debris removed by centrifugation at 3,000 x g for 10 min. Pseudoviruses were further filtered using a 0.45 µm syringe filter and concentrated 10x prior to storage at -80°C.

Neutralization assays

For SARS-CoV-2 S VSV neutralization with TRI2-2 and AHB2, HEK293T cells with stable human ACE2 expression in DMEM supplemented with 10% FBS and 1% PenStrep were seeded at 40,000 cells/well into 96-well plates [3610] (Corning) coated with poly-lysine [P4707] (Sigma) and incubated overnight at 37°C. The following day, a half-area 96-well plate (Greiner) was prepared with 3-fold serial dilutions of TRI2-2 and AHB2 with a starting concentration of 1 µM. An equal volume of DMEM with diluted pseudoviruses was added to each well. All pseudoviruses were diluted between 1:3 - 1:27 to reach a target entry of ~10^6 RLU. The mixture was incubated at room temperature for 45-60 min. Media was removed from the cells, and 40 µL from each well of the half-area 96-well plate containing minibinder and pseudovirus were transferred to the 96-well plate seeded with cells and incubated at 37°C for 1 h. After 1 h, an additional 40 µL of DMEM supplemented with 20% FBS and 2% PenStrep was added to the cells. After 18-20 h, 40 µL of One-Glo-EX substrate (Promega) was added to each well and incubated on a plate shaker in the dark for 5 min before reading the relative luciferase units using a BioTek Neo2 plate reader. Relative luciferase units were plotted and normalized in Prism (GraphPad): 0% entry being cells lacking pseudovirus and 100% entry being cells containing virus but lacking minibinder. Prism (GraphPad) nonlinear regression with "[Inhibitor] versus normalized response with a variable slope" was used to determine IC_{50} values from curve fits with 3 technical repeats. 3 biological replicates were carried out for each sample-pseudovirus pair.

Fusion assays

Cell to cell fusion assay using a split-GFP system was conducted as previously described. BHK-21-$GFP_{1\text{-}10}$ cells were split into 6-well plates at a density of 250,000 cells per well. The following day, the growth medium was removed from the 6-well plates and cells were washed with DMEM followed by addition of the growth medium. Then, the cells were transfected with 4 µg of S protein DNA using Lipofectamine 2000 transfection kit. Vero E6-TMPRSS2-GFP_{11} cells were plated into 96-well, glass bottom, black-walled plates (CellVis) at a density of 36,000 cells per well. Twenty-four hours after transfection, BHK-21-$GFP_{1\text{-}10}$ cells expressing the S protein were washed three times using FluoroBrite DMEM (Thermo Fisher) and detached using an enzyme-free cell dissociation buffer (Gibco). 9,000 BHK-21-$GFP_{1\text{-}10}$ cells were added to each well with or without TRI2-2 with the 1:4 serial dilution starting from the initial concentration of 70 nM, and the mixture was incubated at 37°C and 5% CO_2 for 2 h before being transferred on top of the Vero E6-TMPRSS2-GFP_{11} that was washed three times with FluoroBrite DMEM. The mixture was incubated at 37°C and 5% CO_2 in a Cytation 7 plate Imager (BioTek) and both bright-field and GFP images were collected every 30 min for 18 h. Fusogenicity was assessed by measuring the area showing GFP fluorescence for each image using Gen5 Image Prime v3.11 software. Raw grayscale 16-bit images were pseudocolored in ImageJ using Green Hot Look Up Table.

Production of recombinant SARS-CoV-2 S BA.2.86

The SARS-CoV-2 BA.2.86 hexapro S ectodomain construct includes its native signal peptide, hexapro mutations (F817P, A892P, A899, A942P, K986P, V987P), and a C-terminal foldon, avi tag, and a 8x histidine tag. SARS-CoV-2 BA.86 hexapro S ectodomain was expressed in Expi293 cells (Thermo) at 37°C and 8% CO_2. Cells were transfected using Expifectamine293 (Thermo) following the manufacturer's protocol. Four days post-transfection, Expi293 cell supernatant was clarified by centrifugation at 4,121g for 30 min, supplemented with 25 mM phosphate pH 8.0, 300 mM NaCl. Supernatant was then bound to His-Trap Excel column (Cytiva) previously equilibrated in 25 mM phosphate pH 8.0, 300 mM NaCl. Nickel columns were washed with 20-40mL of 25 mM phosphate pH 8.0, 300 mM NaCl, and 40 mM Imidazole. S protein was eluted using 25 mM phosphate pH 8.0, 300 mM NaCl, and 300 mM imidazole prior to being buffer exchanged to 50 mM Tris-HCl pH 8.0, 150 mM NaCl using a centrifugal filter device with a MWCO of 100 kDa. Protein was then flash frozen and stored at -80°C.

Cryo-EM sample preparation and data collection

The SARS-CoV-2 BA.2.86 S complex with TRI2-2 at a molar ratio of 1:8 just before the grid preparation. The cryo-EM dataset was collected over two different sessions which were combined to be processed together. 3 µL of SARS-CoV-2 BA.2.86 S (Acro Biosystems, SPN-C524y) complex with TRI2-2 at 0.6mg/mL was added to a glow discharged (30s at 15 mA) UltraAuFoil R1.2/1.3:Au300 grid (Russo & Passmore, 2014) prior to plunge freezing using a vitrobot MarkIV (ThermoFisher Scientific) with a blot force of -1, wait time of 10s, and 6 sec blot time at 100 % humidity and 22°C. 3.5 µL of SARS-CoV-2 BA.2.86 S produced following the aforementioned protein production complex with TRI2-2 at 0.2mg/mL was added to a glow discharged (10s at 15mA) Quantifoil 2nm C Au300 grid prior to plunge freezing using a vitrobot MarkIV (ThermoFisher Scientific) with a blot force of -1, 4 sec blot time, and 10s wait time at 100 % humidity and 22°C. Data were acquired using an FEI Titan Krios transmission electron microscope operated at 300 kV and equipped with a Gatan K3 direct detector and Gatan Quantum GIF energy filter, operated in zero-loss mode with a slit width of 20 eV. Automated data collection was carried out using serialEM (Mastronarde, 2005) at a nominal magnification of 105,000x with a pixel size of 0.829 Å. The dose rate was adjusted to $53e^{-}/Å^{2}$, and each movie was acquired in counting mode fractionated in 79 frames of 50ms for UltraAuFoil and 99 frames of 40ms for Quantifoil dataset, respectively. A total of 20,217 and 15,703 micrographs were collected for each datasets, respectively. Stage was tilted 0, 30, and 45 degrees for collection with the UltraAuFoil grid.

Cryo-EM data processing, model building and refinement

Particles were extracted with a box size of 320 pixels with a pixel size of 1.658 Å using WARP. Two rounds of reference-free 2D classification were performed using CryoSPARC (Punjani et al., 2017) to select well-defined particle images from each dataset. Particles belonging to classes with the best resolved spike protein density were selected. To improve particle picking further, we trained the Topaz (Bepler et al., 2019) picker on Warp-picked particle sets belonging to the selected classes after 2D classification. The particles picked using Topaz were extracted and subjected to 2D classification using cryoSPARC. The two different particle sets picked from Warp and Topaz were merged and duplicate particle picks were removed using a minimum distance cutoff of 90 Å. Initial model generation was done using ab-initio reconstruction in cryoSPARC and used as references for a heterogenous 3D refinement in cryoSPARC. After two rounds of ab-initio reconstructions and heterogeneous refinements to remove junk particles, 3D refinement was carried out using non-uniform refinement in cryoSPARC (Punjani et al., 2020) and the particles were transferred from cryoSPARC to Relion using pyem (Asarnow et al., 2019) (https://github.com/asarnow/pyem) to be subjected to the Bayesian polishing procedure implemented in Relion (Zivanov et al., 2019) during which particles were re-extracted with a box size of 512 pixels and a pixel size of 1.0 Å. After ab-initio reconstructions and heterogeneous refinements to select best class, subsequent 3D refinement used non-uniform refinement along with per-particle defocus refinement in cryoSPARC to yield the final reconstruction at 2.4 Å resolution comprising 811,069 particles. To further improve the density at the RBD:TRI2-2 interface, 3D classification and local refinement was performed using Relion and cryoSPARC with a soft mask comprising the RBD and TRI2-2 yielding a reconstruction at 3.2 Å resolution enabling model building. Reported resolutions are based on the 0.143 gold-standard Fourier shell correlation (FSC) criterion and Fourier shell correlation curves were corrected for the effects of soft masking by high-resolution noise substitution (S. Chen et al., 2013; Rosenthal & Henderson, 2003). To further improve the N terminus domain (NTD) density, particles belonging to the best selected classes were subjected to another round of heterogeneous refinement, followed by non-uniform refinement with per-particle defocus. Particles were then symmetry expanded following the C3 axis and local refinement was performed using cryoSPARC with a soft mask comprising the NTD domain yielding a reconstruction at 2.8 Å resolution enabling model building. UCSF Chimera, UCSF ChimeraX, ModelAngelo (Jamali et al., 2024), and Coot were used to fit and rebuild atomic models into the cryoEM maps utilizing sharpened and unsharpened maps. The models were refined and relaxed using Rosetta (Frenz et al., 2019; R. Y.-R. Wang et al., 2016) and Phenix (Liebschner et al., 2019), and validated using Phenix, Molprobity (V. B. Chen et al., 2010) and Privateer (Agirre et al., 2015).

Virus

The BQ.1.1 (hCoV-19/USA/CA-Stanford-106_S04/2022; EPI_ISL_15196219) and XBB.1.5 hCoV-19/USA/MD-HP40900-PIDYSWHNUB/2022; EPI_ISL_16026423 strains were obtained from nasopharyngeal isolates and provided as generous gifts by Mehul Suthar (Emory University) and Andrew Pekosz (Johns Hopkins), respectively. All virus stocks were generated in Vero-TMPRSS2 cells and subjected to next-generation sequencing as described previously (R. E. Chen et al., 2021) to confirm the presence and stability of expected substitutions. All virus experiments were performed in an approved biosafety level 3 (BSL-3) facility.

Mouse experiments

Animal studies were carried out in accordance with the recommendations in the Guide for the Care and Use of Laboratory Animals of the National Institutes of Health.

The protocols were approved by the Institutional Animal Care and Use Committee at the Washington University School of Medicine (assurance number A3381-01). Virus inoculations were performed under anesthesia that was induced and maintained with ketamine hydrochloride and xylazine, and all efforts were made to minimize animal suffering. We have complied with all relevant ethical regulations for animal use.

Heterozygous K18-hACE2 C57BL/6J mice (strain: 2B6.Cg-Tg(K18-ACE2)2Prlmn/J) were obtained from The Jackson Laboratory. All animals were housed in groups and fed standard chow diets. For all mouse experiments, 8-week-old female K18-hACE2 mice were administered 10^4 FFU of the respective SARS-CoV-2 strains by intranasal administration. One day later, animals were administered a single 10 mg/kg dose of influenza-specific control or TRI2-2 minibinder intranasally. All animals were monitored for body weight loss until being humanely euthanized at the indicated time post-infection. *In vivo* studies were not blinded, and mice were randomly assigned to treatment groups. No sample-size calculations were performed to power each study. Instead, sample sizes were determined based on prior *in vivo* virus challenge experiments.

Measurement of viral RNA levels

Tissues were weighed and homogenized with zirconia beads in a MagNA Lyser instrument (Roche Life Science) in 1 mL of DMEM medium supplemented with 2% heat-inactivated FBS. Tissue homogenates were clarified by centrifugation at 10,000 rpm for 5 min and stored at −80°C. RNA was extracted using the MagMax mirVana Total RNA isolation kit (Thermo Fisher Scientific) on the Kingfisher Flex extraction robot

(Thermo Fisher Scientific). RNA was reverse transcribed and amplified using the TaqMan RNA-to-CT 1-Step Kit (Thermo Fisher Scientific). Reverse transcription was carried out at 48°C for 15 min followed by 2 min at 95°C. Amplification was accomplished over 50 cycles as follows: 95°C for 15 s and 60°C for 1 min. Copies of SARS-CoV-2 N gene RNA in samples were determined using a previously published assay (Case et al., 2020). Briefly, a TaqMan assay was designed to target a highly conserved region of the N gene (Forward primer: ATGCTGCAATCGTGCTACAA; Reverse primer: GACTGCCGCCTCTGCTC; Probe: /56-FAM/TCAAGGAAC/ZEN/AACATTGCCAA/3IABkFQ/). This region was included in an RNA standard to allow for copy number determination down to 10 copies per reaction. The reaction mixture contained final concentrations of primers and probes of 500 and 100 nM, respectively.

Viral plaque assay

Vero-TMPRSS2-hACE2 cells were seeded at a density of 1 × 10^5 cells per well in 24-well tissue culture plates. The following day, medium was removed and replaced with 200 µL of material to be titrated diluted serially in DMEM supplemented with 2% FBS. After 1 h, 1 mL of methylcellulose overlay was added. Plates were incubated for 72 h, then fixed with 4% paraformaldehyde (final concentration) in phosphate-buffered saline (PBS) for 20 min. Plates were stained with 0.05% (wt/vol) crystal violet in 20% methanol and washed twice with distilled, deionized water.

Statistics and reproducibility

All statistical tests were performed as described in the indicated figure legends using Prism 9.4.1 or 10.1.1. When comparing against control value in fusion assay, one sample t test was performed to determine statistical significance. When comparing two groups in viral challenge studies, a Mann-Whitney test was performed to determine statistical significance. The number of independent experiments performed is indicated in the relevant figure legends.

Data availability

The sharpened and unsharpened cryoEM reconstructions and atomic models of SARS-CoV-2 BA.2.86 S in complex with TRI2-2 minibinder, SARS-CoV-2 BA.2.86 RBD in complex with TRI2-2 minibinder, and SARS-CoV-2 BA.2.86 NTD have been deposited in the Electron Microscopy Data Bank and the Protein Data Bank with accession codes EMD-45972 and PDB 9CWR (SARS-CoV-2 BA.2.86 S in complex with TRI2-2 minibinder), EMD-45969 and PDB 9CWP (SARS-CoV-2 BA.2.86 RBD in complex with TRI2-2 minibinder), and EMD-45971 and PDB 9CWQ (SARS-CoV-2 BA.2.86 NTD).

2.7 Figures & Tables

Figure 2.1. TRI2-2 cross-reacts with and potently neutralizes SARS-CoV-2 Omicron variants.

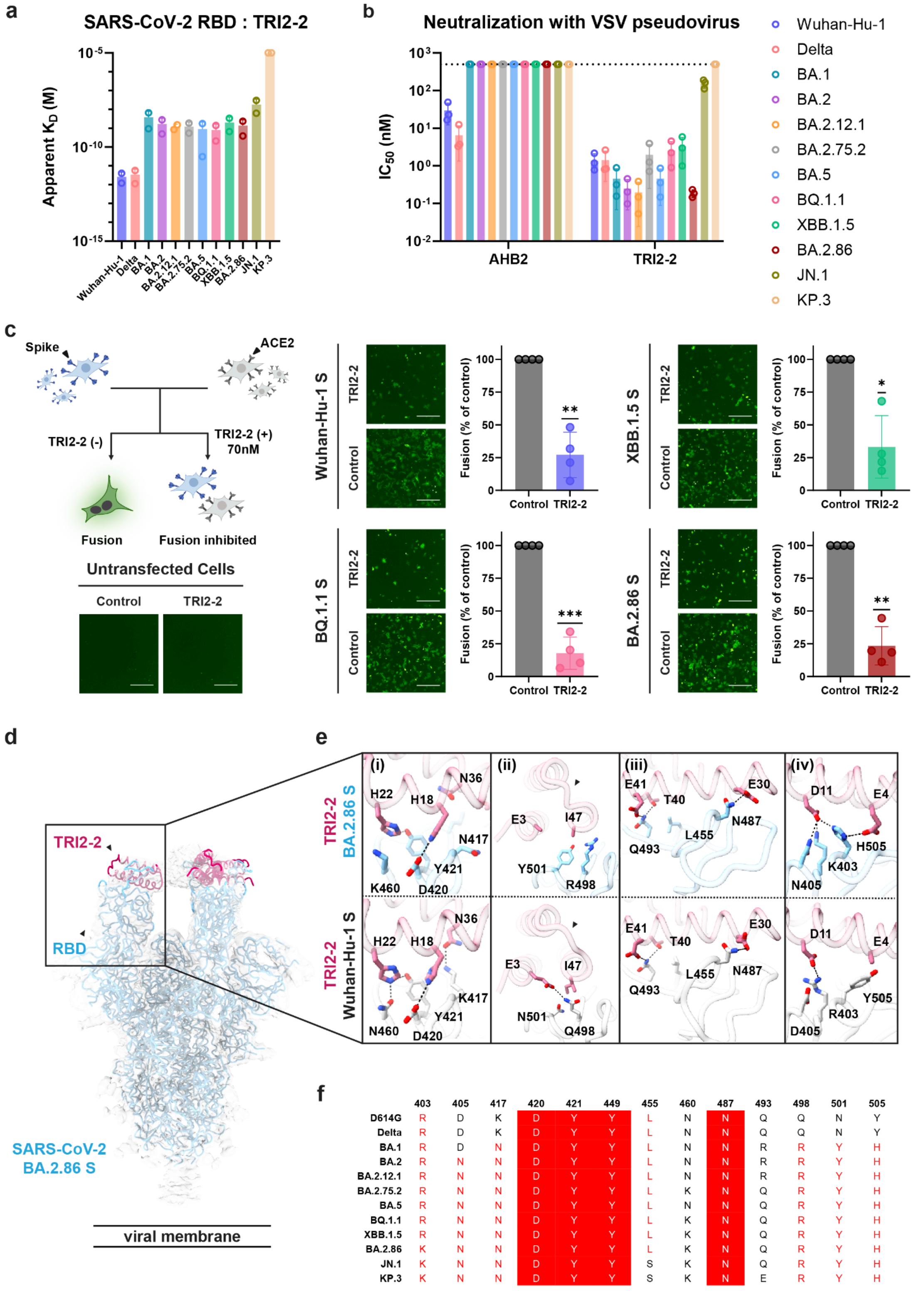

	403	405	417	420	421	449	455	460	487	493	498	501	505
D614G	R	D	K	D	Y	Y	L	N	N	Q	Q	N	Y
Delta	R	D	K	D	Y	Y	L	N	N	Q	Q	N	Y
BA.1	R	D	N	D	Y	Y	L	N	N	R	R	Y	H
BA.2	R	N	N	D	Y	Y	L	N	N	R	R	Y	H
BA.2.12.1	R	N	N	D	Y	Y	L	N	N	R	R	Y	H
BA.2.75.2	R	N	N	D	Y	Y	L	K	N	Q	R	Y	H
BA.5	R	N	N	D	Y	Y	L	N	N	Q	R	Y	H
BQ.1.1	R	N	N	D	Y	Y	L	K	N	Q	R	Y	H
XBB.1.5	R	N	N	D	Y	Y	L	K	N	Q	R	Y	H
BA.2.86	K	N	N	D	Y	Y	L	K	N	Q	R	Y	H
JN.1	K	N	N	D	Y	Y	S	K	N	Q	R	Y	H
KP.3	K	N	N	D	Y	Y	S	K	N	E	R	Y	H

(a) Binding of TRI2-2 to variant RBDs immobilized at the surface of BLI biosensors. Means of two biological replicates (each replicate is shown as a circle) are shown as bar graphs with lines representing SD. **(b)** Neutralization of SARS-CoV-2 S VSV pseudoviruses harboring the Wuhan-Hu-1 D614G, Delta, BA.1, BA.2, BA.2.12.1, BA.2.75.2, BA.5, BQ.1.1, XBB.1.5, BA.2.86, or JN.1 S. Means of three biological replicates (each replicate is shown as a circle) rendered as bar graphs with SD. **(c)** Cell-cell fusion assay between BHK21 cells expressing SARS-CoV-2 D614G, BQ.1.1, XBB.1.5, or BA.2.86 S glycoprotein and VeroE6-TMPRSS2 cells in the absence of TRI2-2 (control) or in the presence of 70nM TRI2-2. Each dot represents replicate from four different biological replicates. SDs shown as lines. One sample t tests between control and TRI2-2 treatment; ns, not significant; $*p < 0.05$, $**p < 0.01$, $***p < 0.001$, $****p < 0.0001$, $p=0.0035$ (Wuhan-Hu-1), $p=0.0009$ (BQ1.1), $p=0.0113$ (XBB.1.5), $p=0.0018$ (BA.2.86). The schematic of the cell-cell fusion assay was created in BioRender. Tortorici, A. (2026) https://BioRender.com/xjsmgd6. Scale bar: 1mm. **(d-e)** CryoEM structure of TRI2-2 bound to the BA.2.86 S glycoprotein trimer (electron potential map shown as a semi-transparent gray surface) **(d)** and close-up views of the binding interface between TRI2-2 and BA.2.86 RBD compared to that obtained in complex with the Wuhan-Hu-1 RBD (PDB 7UHB) **(e)** Black arrows highlight the conformationally reorganized loop in (**e-ii**). **(f)** Amino acid sequences of the key residues at the binding interface. Coloring scheme follows ESPript 3 (Robert & Gouet, 2014).

Figure 2.2. Kinetic analysis of TRI2-2 binding to SARS-CoV-2 variant RBDs using biolayer interferometry.

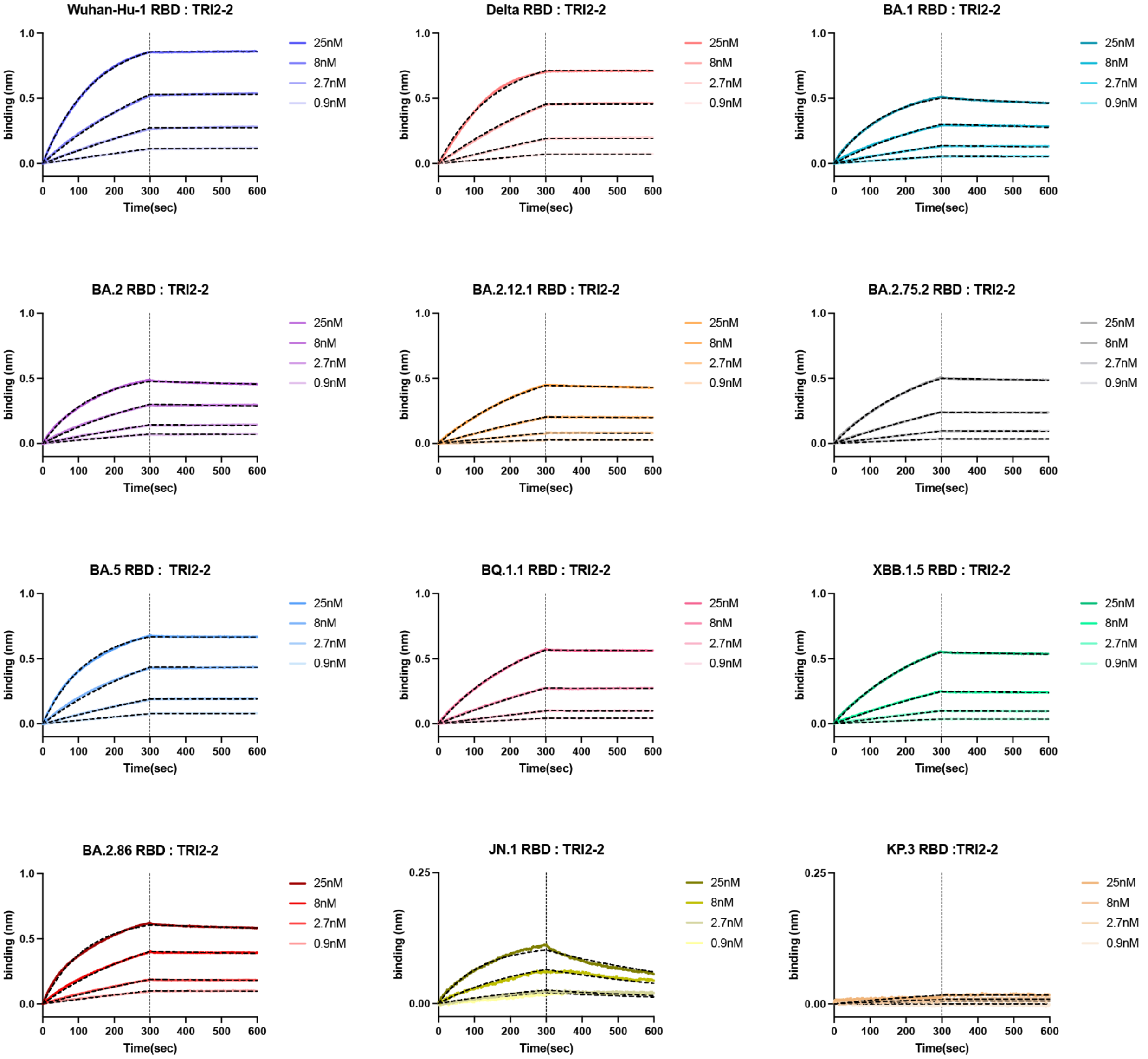

Biotinylated RBDs were immobilized on streptavidin biosensors to a final level of 1 nm shift each. The TRI2-2 concentrations used are provided in the color keys. Dashed black lines represent curve fits obtained using global fitting and a 1:1 binding model in the ForteBio BLI software. Representative graphs are shown from two biological replicates.

Figure 2.3. Dose-response curves for neutralization of SARS-CoV-2 S variant VSV pseudoviruses by the TRI2-2 and AHB2 miniprotein inhibitors.

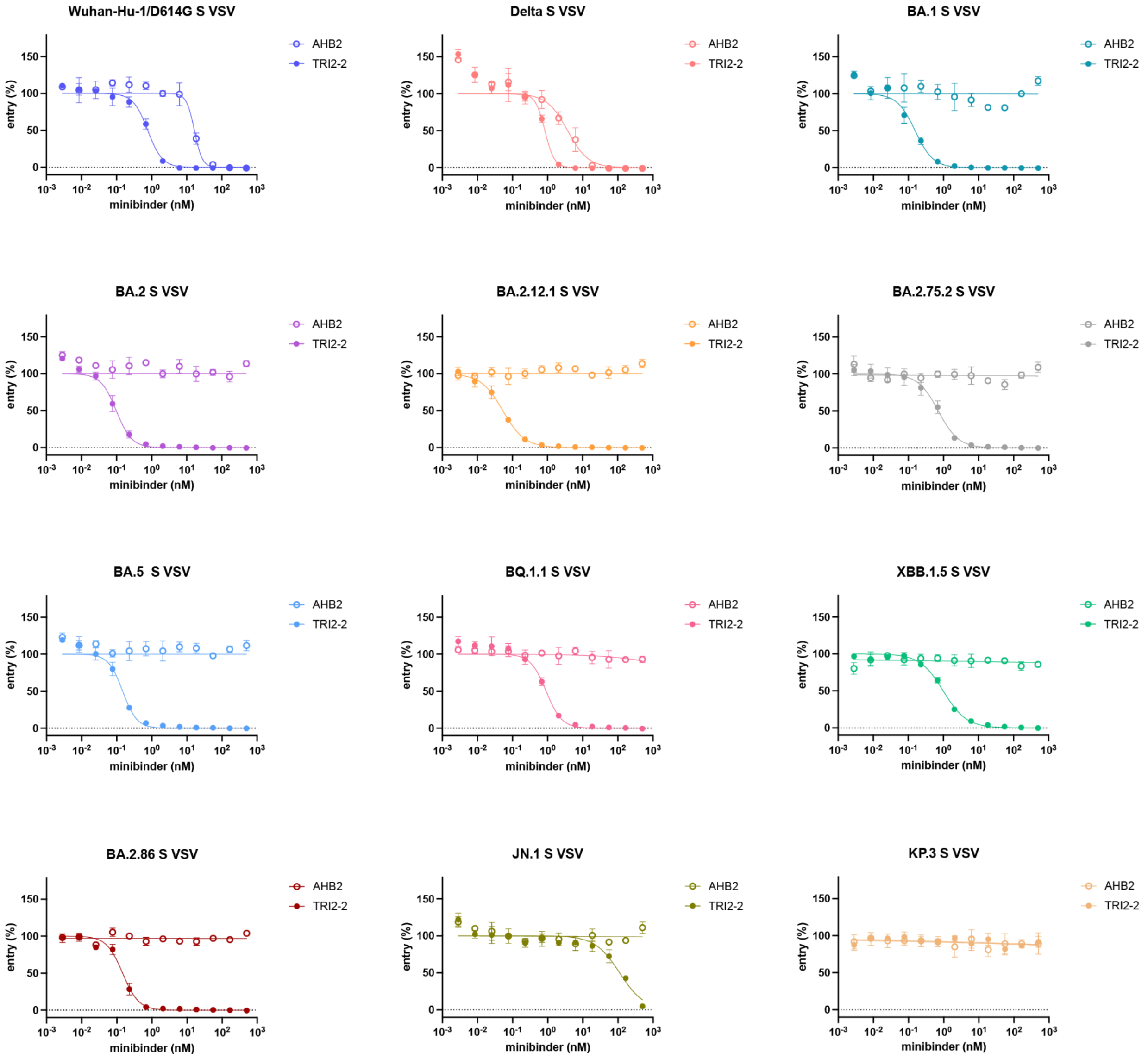

Each dot represents the mean of three technical replicates. SD shown as lines. Representative graphs are shown from three biological replicates.

Figure 2.4. Dose-response curves for TRI2-2-mediated fusion inhibition of SARS-CoV-2 S variants.

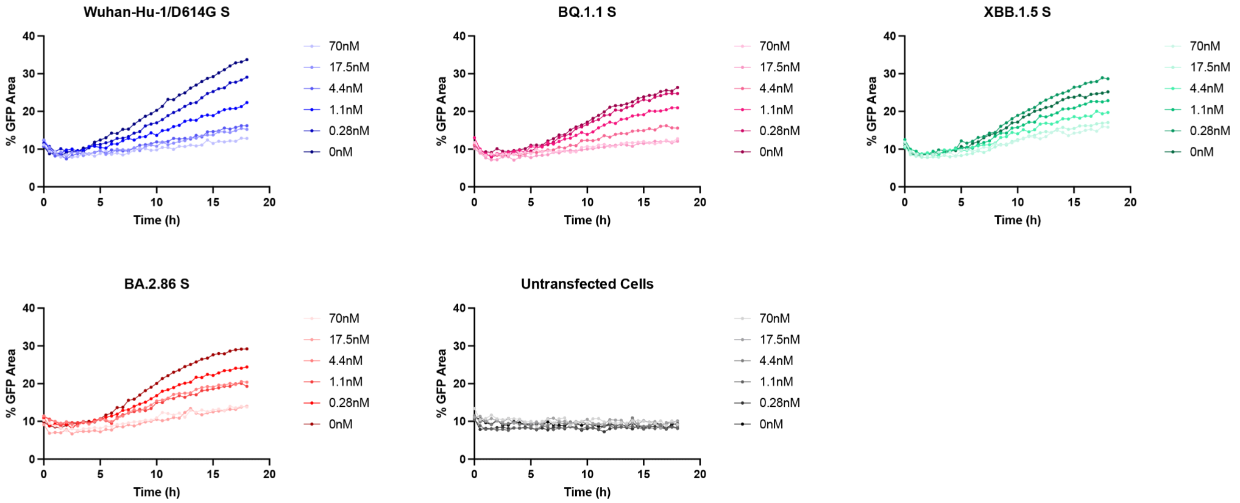

Representative graphs are shown from four biological replicates.

Figure 2.5. CryoEM data collection and refinement of TRI2-2 bound to the BA.2.86 S glycoprotein trimer.

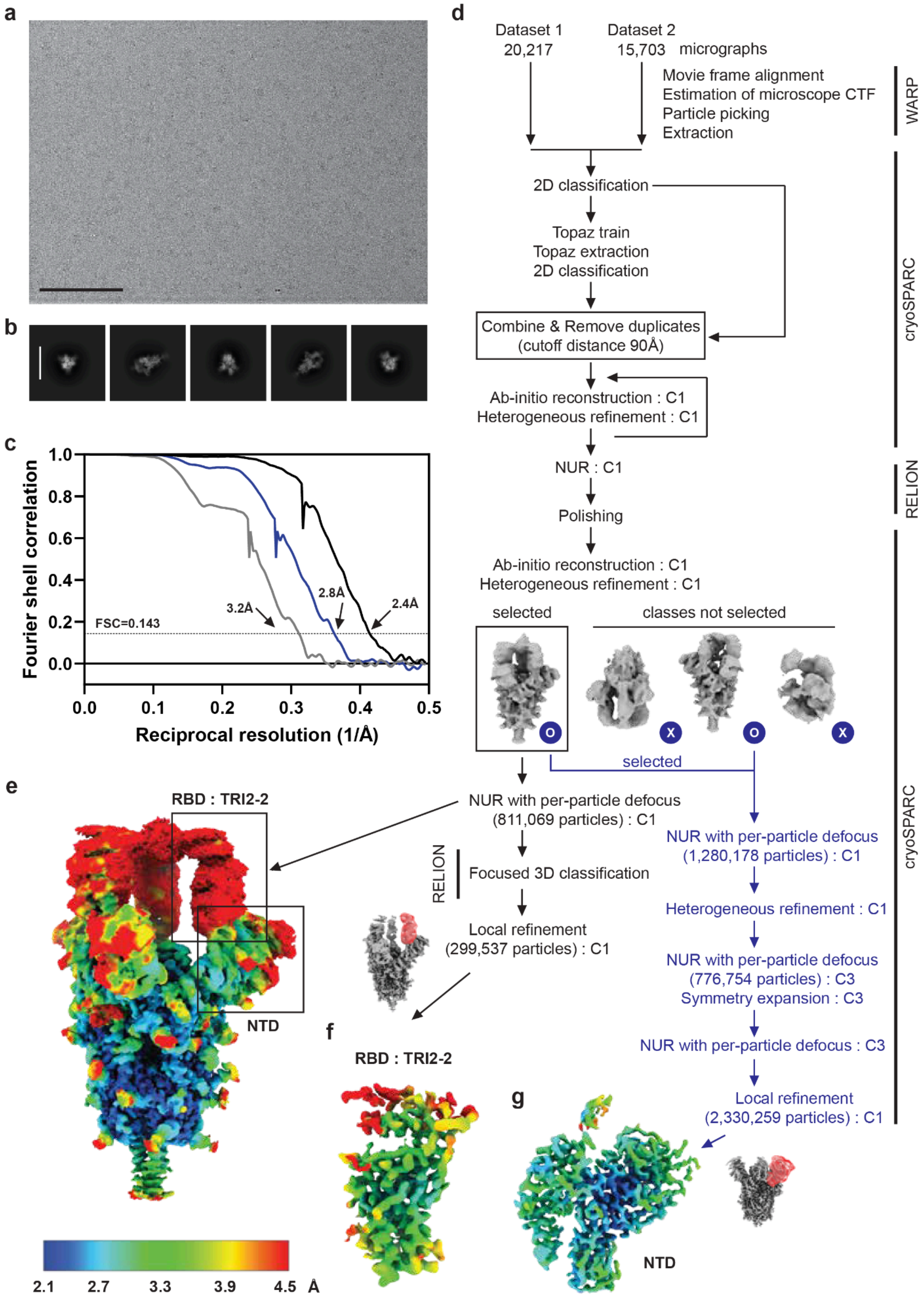

(a-b) Representative electron micrograph (**a**) and 2D class averages (**b**) of SARS-CoV-2 BA.2.86 S in complex with TRI2-2. The scale bar represents 100nm (**a**) and 210Å (**b**). **(c)** Gold-standard Fourier shell correlation curves for the cryoEM reconstructions. The 0.143 cutoff is indicated with a gray dashed line. Black, gray, and blue curves correspond to the global, RBD, and NTD reconstructions, respectively. **(d)** Data processing flowchart. NUR: non-uniform refinement. Masks used for local refinement are shown in red. **(e-g)** CryoEM map of SARS-CoV-2 BA.2.86 S in complex with TRI2-2 (**e**), locally refined map of the BA.2.86 RBD in complex with TRI2-2 (**f**), and locally refined map of the BA.2.86 NTD (**g**) colored by local resolution as determined using cryoSPARC.

Figure 2.6. Post-exposure TRI2-2 administration protects mice challenged with the SARS-CoV-2 BQ.1.1, XBB.1.5, and BA.2.86 variants.

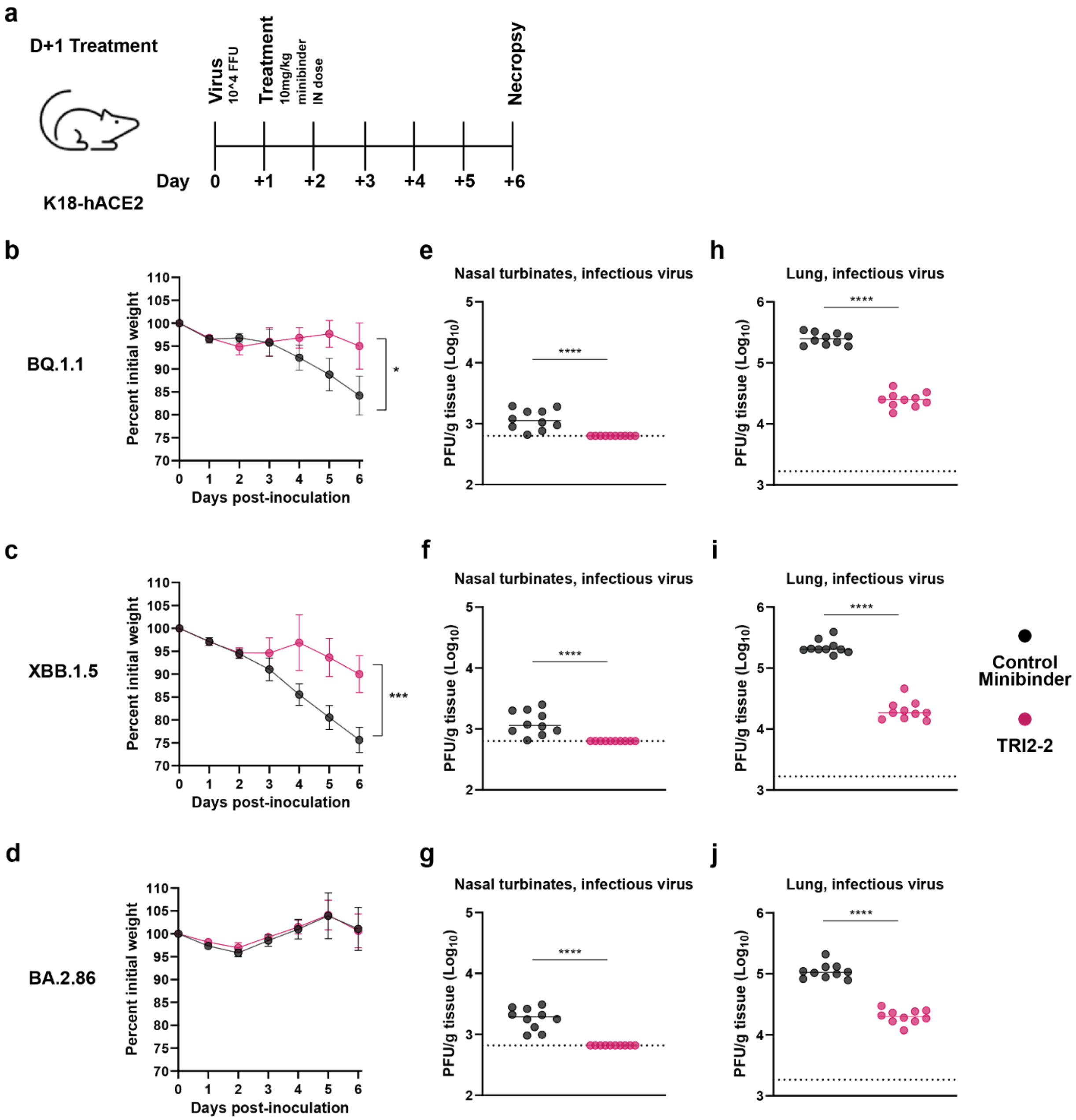

(a) Schematic of study design. **(b-d)** Weight loss for mice challenged with BQ.1.1 (**b**), XBB.1.5 (**c**), or BA.2.86 (**d**) (dots represent mean and lines represent SD.; n=10 mice per group per challenge virus; differences in area under the curves assessed by Student's t-test with Welch's correction for each virus; *P < 0.01; ***P<0.001). **(e-g)** Nasal turbinate infectious viral titers for mice challenged with BQ.1.1 (**e**), XBB.1.5 (**f**), or BA.2.86 (**g**). **(h-j)** Lung infectious viral titers for mice challenged with BQ.1.1 (**h**), XBB.1.5 (**i**), or BA.2.86 (**j**) (solid lines indicate median values; dotted lines indicate limit of detection of assay, n=10 mice per group per challenge virus, two experiments; Two-tailed Mann-Whitney test between control and TRI2-2 treatment; ****p<0.0001 (e-j).

Figure 2.7. Quantification of viral RNA loads.

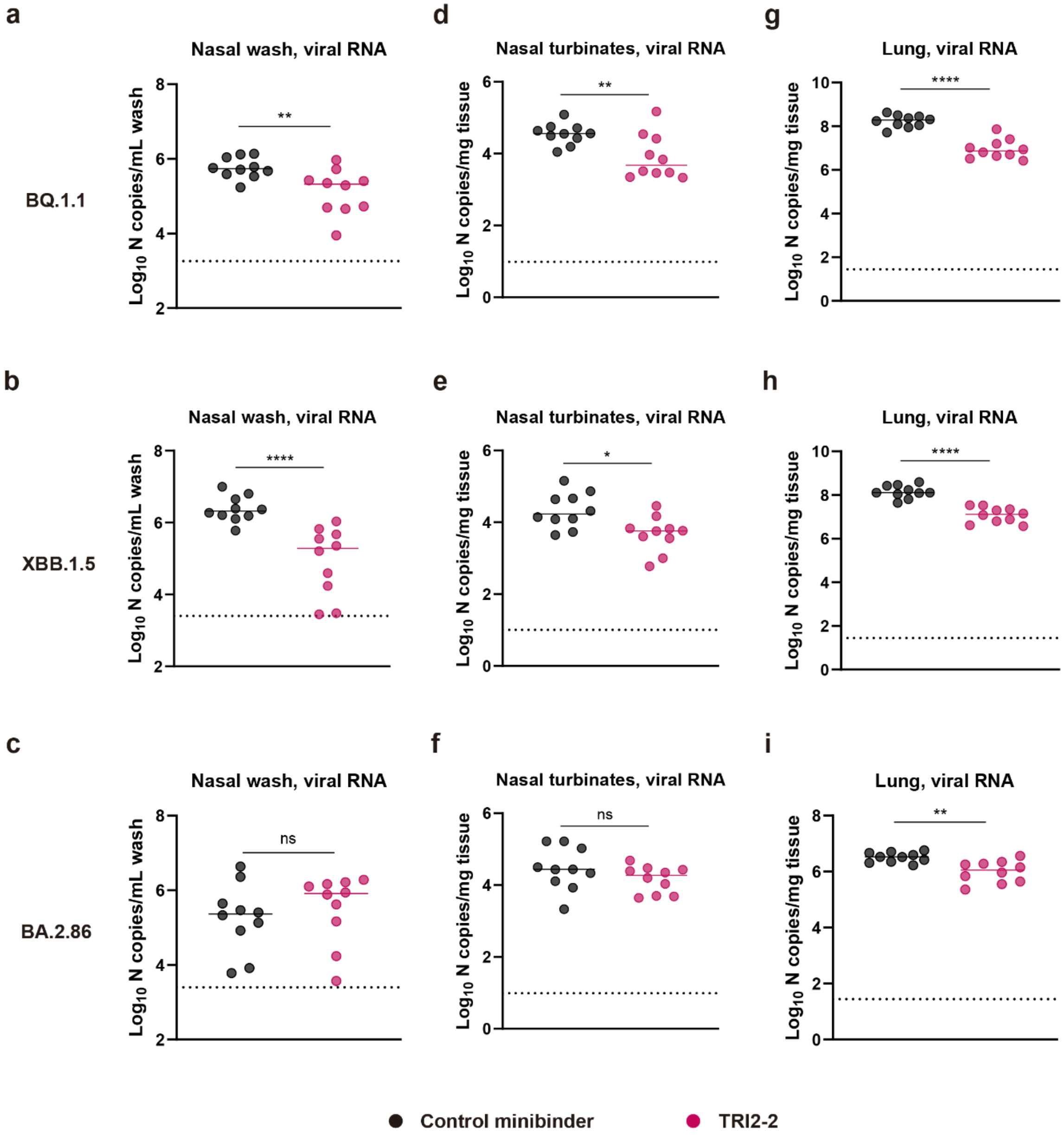

(a-c) Genomic viral RNA levels in nasal washes for mice challenged with BQ.1.1 (**a**), XBB.1.5 (**b**), or BA.2.86 (**c**). **(d-f)** Genomic viral RNA levels in nasal turbinates for mice challenged with BQ.1.1 (**d**), XBB.1.5 (**e**), or BA.2.86 (**f**). **(g-i)** Genomic viral RNA levels in lungs for mice challenged with BQ.1.1 (**g**), or XBB.1.5 (**h**), or BA.2.86 (**i**) (solid lines indicate median values; dotted lines indicate limit of detection of assay, n=10 mice per group per virus challenge, two experiments; Two-tailed Mann-Whitney test between control and TRI2-2 treatment; ns, not significant; $*p< 0.05$, $**p<0.01$, $***p< 0.001$,

****$p < 0.0001$, $p=0.0089$ (a), $p<0.0001$ (b), $p=0.4359$ (c), $p=0.0089$ (d), $p=0.0185$ (e), $p=0.2176$ (f), $p<0.0001$ (g), $p<0.0001$ (h), $p=0.0015$ (i).

Table 2.1. Representative TRI2-2 binding kinetics and avidities (apparent affinities denoted KD,app) to SARS-CoV-2 variant RBDs obtained by biolayer interferometry.

	KD,app (M)	KD,app error	kon (1/Ms)	kon error	koff (1/s)	koff error
D614G	1.21E-12	N/A	2.86E+05	2.42E+02	3.46E-07	N/A
Delta	1.14E-12	N/A	2.59E+05	4.17E+02	2.95E-07	N/A
BA.1	9.28E-10	6.07E-12	2.84E+05	5.09E+02	2.64E-04	1.66E-06
BA.2	4.93E-10	5.82E-12	2.97E+05	5.47E+02	1.47E-04	1.71E-06
BA.2.12.1	8.51E-10	8.90E-12	1.37E+05	2.93E+02	1.17E-04	1.20E-06
BA.2.75.2	5.42E-10	6.40E-12	1.65E+05	2.67E+02	8.93E-05	1.05E-06
BA.5	3.06E-11	4.60E-12	3.25E+05	4.97E+02	9.92E-06	1.49E-06
BQ.1.1	2.10E-10	5.49E-12	1.60E+05	2.23E+02	3.36E-05	8.78E-07
XBB.1.5	6.58E-10	7.02E-12	1.60E+05	2.78E+02	1.05E-04	1.11E-06
BA.2.86	3.88E-10	5.79E-12	3.39E+05	6.69E+02	1.31E-04	1.95E-06
JN.1	6.19E-09	6.11E-11	2.82E+05	2.42E+03	1.75E-03	8.53E-06
KP.3	N/A	N/A	N/A	N/A	N/A	N/A

Values shown here are calculated from the curve fit from **Figure 2.2**.

Table 2.2. CryoEM data collection and refinement statistics.

	SARS-CoV-2 S BA.2.86 in complex with TRI2-2 minibinder	**SARS-CoV-2 BA.2.86 RBD in complex with TRI2-2 minibinder**	**SARS-CoV-2 BA.2.86 NTD**
Data collection and processing	EMD-45972 PDB 9CWR	EMD-45969 PDB 9CWP	EMD-45971 PDB 9CWQ
Magnification	**105,000**	**105,000**	**105,000**
Voltage (kV)	**300**	**300**	**300**
Electron exposure ($e^{-}/Å^2$)	**53.25**	**53.25**	**53.25**
Defocus range (μm)	**-0.8 - -1.8**	**-0.8 - -1.8**	**-0.8 - -1.8**
Pixel size (Å)	**0.829**	**0.829**	**0.829**
Symmetry imposed	**C1**	**C1**	**C1**
Final particle images (no.)	**811,069**	**299,537**	**2,330,259**
Map resolution (Å)	**2.4**	**3.2**	**2.8**
FSC threshold	**0.143**	**0.143**	**0.143**
Map sharpening B factor ($Å^2$)	**-76.2**	**-117.8**	**-91.7**
Validation			
MolProbity score	**1.04**	**0.82**	**1.64**
Clashscore	**2.21**	**0.79**	**2.33**
Poor rotamers (%)	**0.88**	**0.54**	**2.69**
Ramachandran plot			
Favored (%)	**97.80**	**97.68**	**95.73**
Allowed (%)	**2.20**	**2.32**	**4.27**
Disallowed (%)	**0.00**	**0.00**	**0.00**

CHAPTER 3. Broad receptor tropism and immunogenicity of a clade 3 sarbecovirus

Here, I discuss the potential of zoonotic sarbecovirus spillover, focusing on a clade 3 sarbecovirus called PRD-0038. In the following sections, I describe what factors in PRD-0038 spike could potentially play a role in utilizing human ACE2 receptors and their impacts on countermeasures that have already been developed against SARS-CoV-1 and SARS-CoV-2. This study hypothesizes a zoonotic sarbecovirus spilling over to the human population, possibly resulting in a pandemic, and emphasizes what countermeasures could be employed for better pandemic preparedness, such as monoclonal antibody therapeutics and vaccination schemes, should such cases arise.

Adapted from: Lee, J., Zepeda, S. K., Park, Y.-J., Taylor, A. L., Quispe, J., Stewart, C., Leaf, E. M., Treichel, C., Corti, D., King, N. P., Starr, T. N., & Veesler, D. (2023). Broad receptor tropism and immunogenicity of a clade 3 sarbecovirus. *Cell Host & Microbe*, *31*(12), 1961-1973.e11. https://doi.org/10.1016/j.chom.2023.10.018

3.1 Chapter Introduction

Two sarbecoviruses have crossed the species barrier and spilled over to humans in the past two decades. SARS-CoV-1 emerged in 2002 and spread worldwide through air travel routes, leading to an epidemic with 8,098 cases and 774 deaths (Drosten et al., 2003; Ksiazek et al., 2003). SARS-CoV-2 emerged at the end of 2019 and led to the devastating COVID-19 pandemic that claimed millions of lives worldwide (P. Zhou et al., 2020; N. Zhu et al., 2020). Both viruses enter human cells via spike (S)-mediated fusion of the viral and host membranes upon binding to the angiotensinconverting enzyme 2 (ACE2) receptor (Hoffmann, Kleine-Weber, Schroeder, et al., 2020; Letko et al., 2020; W. Li et al., 2003; A. C. Walls, Park, et al., 2020; P. Zhou et al., 2020).

Reports of additional sarbecovirus spillovers to humans (Evans et al., 2023; N. Wang et al., 2018) along with detection of numerous sarbecoviruses in bats and other wild animals (Ge et al., 2013; Hu et al., 2017; Lam et al., 2020; Temmam et al., 2022; Wacharapluesadee et al., 2021; Yang et al., 2015; P. Zhou et al., 2020) underscore the recurrent zoonotic threat to public health posed by these viruses. The S glycoprotein of some of these sarbecoviruses harbors a receptor-binding domain (RBD) that utilizes the human ACE2 receptor to enter host cells, indicating that they could possibly cross the species barrier to infect humans (Letko et al., 2020; Menachery et al., 2015, 2016; Niu et al., 2022; Temmam et al., 2022; Wrobel et al., 2021).

Phylogenetic classification of sarbecoviruses based on their RBD sequences led to the definition of at least four clades: clade 1a (e.g., SARS-CoV-1), clade 1b (e.g., SARS-CoV-2), clade 2 (e.g., RmYN02), and clade 3 (e.g., BtKY72) (Starr et al., 2021; Tortorici et al., 2021). Clade 3 sarbecoviruses have been identified in bats in Europe and Africa (Alkhovsky et al., 2022; Crook et al., 2021; Drexler et al., 2010; Tao & Tong, 2019; Tong et al., 2009; Wells et al., 2021), such as BtKY72 and PRD-0038 for which sequences were found in Kenya and Rwanda, respectively. We recently showed that the S glycoprotein of one of them (BtKY72) could utilize two *Rhinolophus affinis* (*R. affinis*) ACE2 alleles to promote entry into cells (Starr, Zepeda, et al., 2022). Furthermore, two amino acid residue substitutions in the BtKY72 RBD enabled

S-mediated entry into human ACE2-expressing cells, broadening the range of sarbecoviruses with spillover potential (Starr, Zepeda, et al., 2022). The importance of this observation was further underscored by the recent discovery of the clade 3 Khosta-2 virus (Alkhovsky et al., 2022), which independently acquired the ability to bind (Starr, Zepeda, et al., 2022) and enter cells (Seifert et al., 2022) using the human ACE2 receptor. Studying the structure and functional properties of clade 3 sarbecovirus S glycoproteins is therefore crucial to understand spillover risk and assist in pandemic preparedness.

Here, we report that the S glycoprotein of the clade 3 sarbecovirus PRD-0038, which is a member of the largely uncharacterized African bat-borne sarbecoviruses, has a broad ACE2 usage and that PRD-0038 RBD mutations further expand entry receptor tropism to additional *Rhinolophus* bat species and human ACE2. We determined structures of the PRD-0038 RBD bound to *Rhinolophus* alcyone (*R. alcyone*) ACE2 and of the PRD-0038 S trimer, explaining receptor tropism and the distinct antigenicity of clade 3 sarbecoviruses relative to SARS-CoV-2 and SARS-CoV-1. Evaluation of a panel of monoclonal antibodies enabled identification of PRD-0038 cross-neutralizing antibodies that could be deployed for outbreak response. Vaccination of mice with PRD-0038 S elicited greater titers of antibodies cross-reacting with vaccine mismatched clade 2 and clade 1a sarbecoviruses, relative to SARS-CoV-2 S immunization, indicating that addition of clade 3 antigens in vaccine formulations could enhance the resilience of antibody responses to viral evolution. Our findings highlight a molecular pathway for possible zoonotic spillover of a clade 3 sarbecovirus and the necessity of developing pan-sarbecovirus vaccines and countermeasures.

3.2 PRD-0038 S can utilize a broad spectrum of *Rhinolophus* bat ACE2 orthologs as entry receptors

To investigate the promiscuity of clade 3 sarbecovirus host receptor usage, we first assessed binding of a panel of *Rhinolophus* bat ACE2 orthologs harboring a C-terminal human Fc fusion to the immobilized PRD-0038 RBD using biolayer interferometry (BLI) (**Figures 3.1a and 3.1b**). We selected PRD-0038 as a representative member of African bat-borne sarbecoviruses due to its more ancestral phylogenetic positioning relative to the other two sarbecoviruses isolated on the same continent (Starr, Zepeda, et al., 2022) (BtKY72 and PDF-2370) and the high sequence similarity of their S glycoproteins. Our ACE2 panel comprised eight distinct *Rhinolophus sinicus* (*R. sinicus*) alleles and two distinct *R. affinis* alleles, which were defined based on polymorphisms within the region recognized by sarbecovirus RBDs (Guo et al., 2020; Starr, Zepeda, et al., 2022) as well as *R. alcyone* and *Rhinolophus landeri* (*R. landeri*) orthologs. *R. sinicus* Asian bats are probable reservoir hosts for SARS-CoV-1 (Ge et al., 2013), R. affinis bats have been shown to host closely related viruses to SARS-CoV-2 (P. Zhou et al., 2020), whereas *R. alcyone* and *R. landeri* bats are found in sub-Saharan Africa, overlapping with the regions of sampling of several clade 3 sarbecoviruses (the exact *Rhinolophus* species from which PRD-0038 and BtKY72 have been sampled is unknown) (Tao & Tong, 2019; Wells et al., 2021) (**Figure 3.1c**). We observed the strongest binding to the PRD-0038 RBD with *R. alcyone* ACE2, which exhibited the slowest dissociation kinetics in our panel (**Figure 3.1a**). The PRD-0038 RBD also interacted with both *R. affinis* ACE2s, albeit more tightly with the 9479 allele than the 787 allele, and with *R. landeri* ACE2 (**Figure 3.1a**). Finally, we detected binding to four out of the eight *R. sinicus* alleles evaluated (**Figure 3.1b**).

To further evaluate receptor tropism, we pseudotyped vesicular stomatitis virus (VSV) particles with PRD-0038 S and assessed entry into HEK293T cells transiently transfected with the corresponding set of full-length, membrane-anchored ACE2s (**Figure 3.1d**). Concurring with our binding data, *R. alcyone* enabled robust entry of PRD-0038 S VSV (**Figure 3.1d**), in line with a previous study (Roelle et al., 2022). Moreover, we also detected efficient entry into cells expressing *R. affinis* 9479 and 787 ACE2 alleles, *R. landeri* ACE2, and the four *R. sinicus* ACE2 alleles for which binding was detected by BLI (**Figure 3.1d**). Collectively, these data show that PRD-0038 S recognizes and can utilize a broad spectrum of *Rhinolophus* bat ACE2 orthologs as entry receptors, including those from bat species known to be found in geographic areas proximal to the site of PRD-0038 discovery.

3.3 Molecular basis of PRD-0038 RBD engagement of the *R. alcyone* ACE2 receptor

To reveal the structural determinants of ACE2 recognition by clade 3 sarbecoviruses, we determined a reconstruction of the PRD-0038 RBD bound to the natively dimeric *R. alcyone* ACE2 (RaACE2) ectodomain using single-particle cryoelectron microscopy (cryo-EM) (**Figures 3.1e and 3.2; Table 3.2**). Symmetry expansion and local refinement yielded a structure at 3.2 A° resolution of the ACE2 peptidase domain bound to the RBD revealing the molecular interactions mediating complex formation. An average surface of ~750 $A^{\circ 2}$ is buried at the ACE2/RBD interface as compared with ~840A$^{\circ 2}$ for the complexes of human ACE2 (hACE2) bound to the SARS-CoV-2 RBD (Lan et al., 2020) or to the SARS-CoV-1 RBD (F. Li et al., 2005). The relative orientation of the binding partners is similar for these three structures, likely due to the conservation of several key ACE2-interacting residues including L444$_{\text{PRD-0038}}$/L455$_{\text{SARS-CoV-2}}$ and F445$_{\text{PRD-0038}}$/F456$_{\text{SARS-CoV-2}}$, L475$_{\text{PRD-0038}}$/L472$_{\text{SARS-CoV-1}}$, Y478$_{\text{PRD-0038}}$/Y489$_{\text{SARS-CoV-2}}$/Y475$_{\text{SARS-CoV-1}}$, G485$_{\text{PRD-0038}}$/G496$_{\text{SARS-CoV-2}}$/G482$_{\text{SARS-CoV-1}}$, G491$_{\text{PRD-0038}}$/G502$_{\text{SARS-CoV-2}}$/G488$_{\text{SARS-CoV-1}}$, and Y494$_{\text{PRD-0038}}$/Y505$_{\text{SARS-CoV-2}}$/Y491$_{\text{SARS-CoV-1}}$ (**Figures 3.1f-3.1i**). However, the salt bridge formed between K417$_{\text{SARS-CoV-2}}$ and D30$_{\text{hACE2}}$ is absent due to substitution to V408$_{\text{PRD-0038}}$ and V404$_{\text{SARS-CoV-1}}$ (**Figures 3.1f, 3.1g, and 3.1j**). Furthermore, the electrostatic interactions involving residues D38$_{\text{hACE2}}$ and Q42$_{\text{hACE2}}$ with Y449$_{\text{SARS-CoV-2}}$ and Q498$_{\text{SARS-CoV-2}}$ or Y436$_{\text{SARS-CoV-1}}$ and Y484$_{\text{SARS-CoV-1}}$ are lost due to truncation and remodeling of the PRD-0038 433-440 loop along with substitution of Q498$_{\text{SARS-CoV-2}}$ to T487$_{\text{PRD-0038}}$ (**Figures 3.1f-3.1h, 3.1k, and 3.3**). The interface between T500/N501$_{\text{SARS-CoV-2}}$ (or Y501 in currently circulating variants) and Y41$_{\text{hACE2}}$ is replaced by tenuous contacts between the topologically equivalent residues T489/V490$_{\text{PRD-0038}}$ and H41$_{\text{RaACE2}}$ (**Figures 3.1f, 3.1g, and 3.1k**). Q493$_{\text{SARS-CoV-2}}$ optimally interacts with K31$_{\text{hACE2}}$/E35$_{\text{hACE2}}$, whereas the topologically equivalent residue K482$_{\text{PRD-0038}}$ is better adapted to N31$_{\text{RaACE2}}$/E35$_{\text{RaACE2}}$ due to swapping of the position of a positively charged amino acid side chain across the interface (**Figures 3.1f, 3.1g, and 3.1l**). These findings concur with (1) the enhanced entry of the closely related BtKY72 RBD-harboring pseudovirus into cells expressing a human ACE2 K31D mutant relative to wild-type ACE2 (Roelle et al., 2022); (2) the isolation of a mouse-adapted SARS-CoV-2 isolate harboring the Q493K substitution (Leist et al., 2020) that promotes favorable interactions with mouse ACE2, the latter ortholog also possessing residues N31/E35 (Cameroni et al., 2022; McCallum et al., 2022); and (3) the emergence of $R493_{SARS\text{-}CoV\text{-}2}$ in Omicron BA.1 and BA.2 (Cameroni et al., 2022; McCallum et al., 2022), which was subsequently reverted to the more favorable $Q493_{SARS\text{-}CoV\text{-}2}$ in subsequent variants, likely due to relieving electrostatic repulsion with $K31_{hACE2}$ (Starr, Greaney, Stewart, et al., 2022). Overall, most of the PRD-0038 RBD binding interface with *R. alcyone* ACE2 is remodeled as compared with human ACE2 bound to SARS-CoV-2 or SARS-CoV-1, thereby explaining the shift in receptor species tropism.

3.4 PRD-0038 RBD mutations enable human ACE2 utilization and expand receptor tropism to additional geographically relevant bat species

To investigate how viral evolution could alter the PRD-0038 receptor species tropism for pandemic preparedness, we evaluated the impact of RBD mutations on utilization of several ACE2 orthologs. Using BLI, we observed that human ACE2-Fc did not bind to the wild-type PRD-0038 RBD (**Figure 3.4a**). However, we found that two amino acid residue substitutions promoted binding of human ACE2-Fc to the immobilized PRD-0038 K482Y/T487W RBD mutant (**Figure 3.4a**, SARS-CoV-2 numbering 493Y/498W) (Starr, Zepeda, et al., 2022), in line with their ability to enable BtKY72 S-mediated utilization of human ACE2 (Starr, Zepeda, et al., 2022). Moreover, we found that human ACE2-Fc interacted with the T487W RBD, albeit weakly (**Figure 3.4a**). We validated these findings using deep mutational scanning (DMS) of the yeast-displayed PRD-0038 RBD showing that T487W is the only single amino acid mutation enabling detection of human ACE2-Fc binding (**Figures 3.4b and 3.5**). The geographically relevant *R. alcyone* and *R. landeri* ACE2 orthologs exhibited enhanced binding to the PRD-0038 T487W RBD relative to the wild-type RBD, with 1:1 binding affinity improvements corresponding to 2- and greater than 1 order of magnitude, respectively (**Figures 3.4c and 3.4d; Table 3.3**). These data concur with our DMS measurements showing that T487W mutation had the most marked positive effect on *R. landeri* ACE2 binding (**Figures 3.4b and 3.5**). Furthermore, the PRD-0038 T487W RBD mutation enhanced binding to the *R. affinis* 787 allele as well as to the *R. sinicus* alleles recognized by the wildtype PRD-0038 RBD and enabled detectable binding to the *R. sinicus* WJ1 allele (**Figures 3.6a and 3.6b**). By contrast, the K482Y mutation was deleterious for binding to *R. alcyone*, *R. landeri*, *R. affinis*, and *R. sinicus* ACE2 orthologs (**Figures 3.4e, 3.4f, 3.5, 3.6c, and 3.6d**). We observed that wild-type PRD-0038 S and all three mutants (K482Y, T487W, and K482Y/T487W) promoted entry of VSV pseudotypes in HEK293T cells transiently transfected with *R. alcyone* ACE2 or with *R. landeri* ACE2 except for PRD-0038 K482Y S VSV that did not enter *R. landeri* ACE2-expressing cells (**Figures 3.4g, 3.4h, and 3.6e**), suggesting that binding avidity could overcome to some extent the observed differences in affinity. To broaden our understanding of PRD-0038 tropism, we also examined cell entry promoted by transient transfection of ACE2 alleles from *Rhinolophus ferrumequinum* (*R. ferrumequinum*) bats, which are found in northern Africa, southern Europe, and southeast Asia. We observed that *R. ferrumequinum* ACE2 allele XM_033107295.1 promoted entry of wild-type and T487W PRD-0038 S VSV, whereas *R. ferrumequinum* ACE2 allele FJ598617.1 enabled entry of T487W and even more so of K482Y/T487W PRD-0038 S VSV (**Figures 3.4i and 3.4j**). Finally, we observed entry of PRD-0038 T487W S and even more so of

PRD-0038 K482Y/T487W S VSV pseudoviruses in HEK293T cells stably expressing human ACE2 (**Figure 3.4k**). These findings indicate that a single RBD residue mutation is sufficient for broadening the *Rhinolophus* bat ACE2 tropism and for enabling PRD-0038 S-mediated entry into cells overexpressing the human ACE2 receptor, highlighting the possible future zoonotic risk of this virus and related clade 3 sarbecoviruses.

3.5 Architecture of the PRD-0038 S trimer

To unveil the three-dimensional (3D) organization of the clade 3 sarbecovirus infection machinery, we determined the structure of prefusion PRD-0038 S using single-particle cryo-EM. After 3D classification and refinement, we obtained a 2.8 A° resolution reconstruction (**Figures 3.7a, 3.7b, 3.7c, and 3.8; Table 3.2**) of the trimer with the three RBDs in the closed conformation applying C3 symmetry, as we did not detect particle images corresponding to S trimers with open RBD conformations (**Figure 3.8**). We used local refinement to improve the resolution of the N-terminal domain (NTD) within the S trimer yielding a map at 2.9 A° resolution (**Figure 3.8**). The final model contains residues 18-1,125 with chain breaks between residues 667-673 and 812-830.

The overall architecture of the PRD-0038 S trimer is similar to that of SARS-CoV-1 and SARS-CoV-2, and a PRD-0038 S protomer can be superimposed with root-mean-square deviation values of 4.9 and 7.2 A° to SARS-CoV-1 S and SARS-CoV-2 S with which it shares 75% and 72% amino acid sequence identity, respectively (**Figure 3.9**). Glycosylation at RBD residue N360, which is present in most sarbecoviruses except SARS-CoV-2 (position N370), has been reported to favor the closed S conformation (Harbison et al., 2022; Zhang et al., 2022), which could possibly explain the sole observation of closed PRD-0038 S trimers in our cryo-EM dataset. However, glycosylation at this site is also present in SARS-CoV-1, which spontaneously adopts open RBD conformations (Kirchdoerfer et al., 2018; A. C. Walls et al., 2019; Yuan et al., 2017). The closed PRD-0038 S RBD conformation is most similar to the linoleic acid (LA)-bound form of SARS-CoV-2 S previously described (Toelzer et al., 2020) (**Figures 3.7d and 3.9**). Indeed, the conformation of the RBD helix containing residues 354-359 (equivalent to SARS-CoV-2 residues 364-369) closely resembles that of the linoleic acid-bound SARS-CoV-2 S (F**igure 3.7d**) or that of F371-harboring SARS-CoV-2 Omicron variants (Addetia et al., 2023b; Y. Cao, Yisimayi, et al., 2022; Park, Pinto, et al., 2022; Stalls et al., 2022). This conformation, however, is distinct from that observed in the structure of the isolated PRD-0038 RBD bound to *R. alcyone* ACE2 described above (**Figure 3.7e**). No linoleic acid density is resolved in our cryo-EM map, although the RBD pocket that accommodates this ligand is conserved in the PRD-0038 S structure, including residues R399 and Q400 (equivalent to SARS-CoV-2 R408 and Q409 forming electrostatic interactions with the linoleic acid carboxylate). Instead, we found that the Y355 side chain (equivalent to SARS-CoV-2 Y365) partially obstructs the hydrophobic pocket, which would have otherwise been occupied by the linoleic acid hydrocarbon tail (**Figure 3.7f**). The PRD-0038 S Y355 side chain rotamer resembles that of apo SARS-CoV-2 S (PDB: 6VXX (A. C. Walls, Park, et al., 2020)) and apo SARS-CoV-1 S (PDB: 5X58 (Yuan et al., 2017)), suggesting that this rotameric configuration is accessible to SARS-CoV-2 Y365 and likely changes to allow linoleic acid binding (Toelzer et al., 2020).

3.6 Antigenicity of the PRD-0038 S trimer

To define the antigenic landscape of clade 3 sarbecoviruses, we probed binding of a panel of monoclonal antibodies with broadly neutralizing activity against sarbecoviruses (Park, De Marco, et al., 2022; Park, Pinto, et al., 2022; Piccoli et al., 2020; Starr et al., 2021; Tortorici et al., 2021) and α- and β- coronaviruses (Low et al., 2022; Pinto et al., 2021; Sauer et al., 2021; Silva et al., 2023) to prefusion-stabilized PRD-0038 S harboring the HexaPro mutations (Hsieh et al., 2020) using an enzyme-linked immunosorbent assay (ELISA) (**Figure 3.7g**). We found that S2X259 (Tortorici et al., 2021) and S2X35 (Piccoli et al., 2020) (antigenic site II) as well as S2H97 (Starr et al., 2021) (antigenic site V) cross-reacted with PRD-0038 S, whereas S309 (Pinto et al., 2020) (antigenic site IV) bound very weakly (**Figure 3.7g**). The markedly dampened S309 binding likely results from the E340SARS-CoV-2/Q330PRD-0038 escape substitution previously identified by DMS of the yeast-displayed SARS-CoV-2 Wuhan-Hu-1 RBD21 (**Figure 3.10**). The S2X324 (Park, Pinto, et al., 2022) antibody (antigenic site Ib), which neutralizes a broad panel of SARS-CoV-2 variants and resembles LY-COV1404 (Westendorf et al., 2022), recognizes the SARS-CoV-2 437-448 loop, which is truncated and remodeled in the PRD-0038 RBD, explaining the lack of binding observed (**Figure 3.10**). The S2K146 (Park, De Marco, et al., 2022) antibody (antigenic site Ia), which contacts an epitope sharing several residues with the ACE2-binding site, bound very weakly to wild-type PRD-0038 S, whereas S2M11 (Tortorici et al., 2020) (antigenic site Ia) did not bind at all, as a result of extensive RBM (receptor-binding motif) mutations (**Figure 3.10**).

Nevertheless, we previously showed that S2K146 weakly neutralized VSV pseudotyped with BtKY72 S (clade 3) harboring the K482Y/T487W mutations (SARS-CoV-2 numbering 493Y/498W) (Park, De Marco, et al., 2022), underscoring the possible usefulness of this antibody if such mutations arose in related clade 3 sarbecoviruses.

The stem helix-targeting S2P6 (Pinto et al., 2021) antibody and the RAY53 (Silva et al., 2023) antibody (recognizing the fusion machinery apex) cross-reacted as efficiently with PRD-0038 S as they did with SARS-CoV-2 S, whereas the fusion peptide-directed 76E1 (Sun et al., 2022) antibody did not, possibly as a result of the F823$_{\text{SARS-CoV-2}}$Y806$_{\text{PRD-0038}}$ epitope mutation (which is shared with other clade 3 sarbecoviruses) along with the presence of the F800P$_{\text{PRD-0038}}$ HexaPro stabilizing mutation (Low et al., 2022) (**Figures 3.7g and 3.10**).

Consistent with the ELISA data, we found that PRD-0038 K482Y/T487W S VSV pseudovirus was neutralized in a concentration-dependent manner by S2X259, S2X35, and more weakly by 76E1, and the activity of the latter antibody is likely explained by the absence of the F800P$_{\text{PRD-0038}}$ HexaPro stabilizing mutation in our pseudovirus construct (**Figures 3.7g and 3.7h**). Collectively, these data show that monoclonal antibodies targeting RBD antigenic sites or fusion machinery epitopes that are conserved across sarbecoviruses or α- and β- coronaviruses, respectively, retain neutralizing activity against PRD-0038 and are possible candidates for pandemic preparedness.

3.7 Immunogenicity of the PRD-0038 S trimer

To better understand the immunogenicity of clade 3 sarbecoviruses and the impact of their possible inclusion in next-generation vaccine candidates, we immunized groups of six mice with three 1 mg doses of either PRD-0038 S or SARS-CoV-2 S (**Figure 3.11a**), both stabilized in the prefusion conformation using the HexaPro mutations (Hsieh et al., 2020). Serum-neutralizing activity, expressed as half-maximum inhibition dilution (ID_{50}), was analyzed 2 weeks post dose 3 using VSV particles pseudotyped with clade 1a (SARS-CoV-1), clade 1b (SARS-CoV-2/G614, BA.2, BA.5, RaTG13) or clade 3 (PRD-0038 and Khosta-1) S glycoproteins. SARS-CoV-2 S-immunized mice had the strongest serum-neutralizing activity against SARS-CoV-2/G614 VSV S (ID_{50}=8,730, vaccine-matched), which was reduced against BA.2 S VSV (ID_{50}=247) and even more so against BA.5 S VSV (ID_{50}=71) (**Figures 3.11b and 3.12**). RaTG13 S VSV (vaccine-mismatched), however, was neutralized with almost comparable potency (ID_{50}=7,752) to that against SARS-CoV-2/G614 S VSV (ID_{50}=8,730), whereas no neutralization of PRD-0038 S VSV and Khosta-1 S VSV clade 3 sarbecoviruses (vaccine-mismatched) was detected except for a subset of animals with very weak neutralization (mouse 1-1, 1-3, 1-5) (**Figures 3.11b and 3.12**). PRD-0038 S-immunized mice had the strongest serum neutralizing activity against PRD-0038 S VSV (ID_{50}=3,634, vaccine-matched) and Khosta-1 S VSV (ID_{50}=863, vaccine-mismatched), whereas we could not detect any neutralization of clade 1a and 1b pseudoviruses tested besides RaTG13 inhibition (ID_{50}=928) (**Figures 3.11b and 3.12**). Although none of the sera could block SARS-CoV-1 S-mediated entry into target cells in standard experimental conditions, we observed very weak SARS-CoV-1 S VSV neutralization with greater dilution of the pseudovirus stock when using PRD-0038 S- but not SARS-CoV-2 S-elicited sera (**Figure 3.13**). These results suggest that this clade 3 S trimer immunogen induced slightly more broadly neutralizing antibody responses than SARS-CoV-2 S against a clade 1a pseudovirus.

Serum binding titers positively correlate with neutralization potency (Piccoli et al., 2020; Robbiani et al., 2020), and the RBD is the main target of neutralizing antibodies against vaccine/infection-matched and mismatched viruses (Bowen, Park, et al., 2022; Greaney et al., 2021; Piccoli et al., 2020; Stamatatos et al., 2021). We analyzed binding of selected vaccine-elicited sera to a panel of yeast-displayed RBDs spanning the known sarbecovirus phylogenetic diversity using two mice immunized with PRD-0038 S and four mice immunized with SARS-CoV-2 S. We selected two mice with greatest (mouse 1-3, 1-5) and two mice with the weakest (mouse 1-4, 1-6) serum-neutralizing activity against our panel of pseudoviruses from the group immunized with SARS-CoV-2 HexaPro S as well as two mice with the greatest SARS-CoV-1 cross-neutralization (mouse 2-3, 2-6) from the group immunized with PRD-0038 HexaPro S (**Figures 3.12 and 3.13**). In line with the serum neutralization data, inclusion of an antigen in the vaccine formulation was associated with strong cross-reactivity with vaccine-matched and related antigens within the same clade among the sera analyzed (**Figures 3.11c and 3.14**). Furthermore, PRD-0038 S immunization elicited greater titers of antibodies cross-reacting with clade 2 and clade 1a RBDs, as well as the RsYN04 RBD that branches independently of the four previously known clades (H. Zhou et al., 2021), likely explaining the weak but detectable SARS-CoV-1 neutralization (**Figures 3.11b, 3.11c, and 3.13**). These data indicate that inclusion of a clade 3 antigen in a vaccine formulation could not only elicit clade 3 serum-neutralizing activity but also enhance cross-reactive (and weakly neutralizing) antibody responses against vaccine-mismatched antigens from distinct clades, which could participate in protection through direct neutralization and Fc-mediated effector functions (Adams et al., 2023; Addetia et al., 2023b; Mackin et al., 2023; Schäfer et al., 2021; Winkler et al., 2021).

To understand the molecular basis for variation in breadth of serum cross-reactivity across mice and vaccine regimen, we mapped the dominant epitope specificities in these six sera using yeast-displayed DMS libraries in the vaccine-matched SARS-CoV-2 Wuhan-Hu-1 and PRD-0038 RBDs as well as in the vaccine-mismatched SARS-CoV-2 Omicron BA.2 and SARS-CoV-1 Urbani RBDs (**Figures 3.11d and 3.15**). SARS-CoV-2 S-elicited polyclonal serum antibodies predominantly targeted the SARS-CoV-2 Wuhan-Hu-1 RBD region comprising residues 484-490, consistent with the strong antigenic pressure on this position that drove early variant evolution at residue E484 during the COVID-19 pandemic (Freitas et al., 2021; Fujino et al., 2021; Tegally et al., 2021). These residues are highly variable among sarbecoviruses, consistent with the weaker cross-reactive breadth seen in these sera. By contrast, PRD-0038 S-elicited polyclonal serum antibodies showed no dominant targeting of specific PRD-0038 RBD antigenic sites, which could indicate a more balanced binding antibody response that would be less susceptible to single amino acid mutations. Epitope mapping to vaccine-mismatched RBDs revealed that PRD-0038 and SARS-CoV-2 S-elicited sera contained antibodies targeting antigenic sites II, IV, and V (Piccoli et al., 2020; Starr et al., 2021), which are typically recognized by subdominant broadly-reactive and neutralizing antibodies (Jette et al., 2021; Martinez et al., 2022;

Pinto et al., 2020; Starr et al., 2021; Tortorici et al., 2021) (**Figure 3.15**). However, DMS using vaccine-mismatched RBD strains also revealed the presence of antibodies in SARS-CoV-2 S-elicited sera that target suboptimal sites for sarbecovirus breadth. For example, we observed strong antibody responses to the N370 glycan hole (resulting from mutations of this glycosylation sequon in our DMS experiments) for two of the four SARS-CoV-2-immunized mice analyzed. Antibody responses targeting this site are elicited as a result of the absence of this oligosaccharide in the SARS-CoV-2 RBD immunogen but its presence in all other sarbecovirus RBDs. Restoration of the N370 glycan in SARS-CoV-2 vaccines could therefore possibly limit these off-target responses by reducing the elicitation of antibodies to this strain-specific epitope. In conclusion, the DMS data indicate that PRD-0038 S-elicited serum antibodies analyzed here target a broader spectrum of antigenic sites present on vaccine-matched and mismatched RBDs than SARS-CoV-2 S-elicited antibodies, providing a molecular basis for enhanced cross-reactivity (**Figures 3.11d and 3.15**).

3.8 Chapter Discussion

Coronavirus S glycoproteins are evolutionary hotspots and can acquire amino acid substitutions, insertions, deletions, or even recombine distinct domains (*SARS-CoV-2 Evolution, Post-Omicron*, 2023). These mutational changes can alter host receptor tropism (Xiong et al., 2022), binding affinity (Bowen, Addetia, et al., 2022; Starr et al., 2020; Starr, Greaney, Stewart, et al., 2022), entry route (Addetia et al., 2023b; Meng et al., 2022; Willett et al., 2022), and immune evasion (Bowen, Addetia, et al., 2022; Cameroni et al., 2022; McCallum, Bassi, et al., 2021; McCallum, De Marco, et al., 2021; McCallum et al., 2022; Starr, Greaney, Hannon, et al., 2022). Most mutations occur within the RBD, which engage the host receptor and account for most of the neutralizing activity against vaccine/infection-matched and mismatched sarbecoviruses (Bowen, Park, et al., 2022; Greaney et al., 2021; Piccoli et al., 2020; Stamatatos et al., 2021).

Spillover is a complex process involving multiple factors such as receptor recognition, proteolytic S activation, immune antagonism, and contact opportunity. To examine potential spillover pathways of clade 3 sarbecoviruses, we evaluated binding of PRD-0038 RBD mutants to a panel of *Rhinolophus* bat ACE2 orthologs. Although human ACE2 cannot serve as entry receptor for wild-type PRD-0038 S (or the closely related BtKY72 S (Starr, Zepeda, et al., 2022)), introduction of a single amino acid RBD mutation (T487W) enabled binding and S-mediated entry into cells expressing human ACE2. Moreover, this point mutation broadened host receptor tropism by enabling utilization of the geographically relevant *R. landeri* and *R. ferrumequinum* ACE2 receptors without compromising binding to *R. alcyone*, *R. sinicus*, and *R. affinis* ACE2 alleles. Although the T487W RBD mutation requires 3 nucleotide substitutions, these findings point to a possible spillover pathway in which a single amino acid change expands host receptor tropism markedly. Indeed, acquisition of *R. landeri*, *R. ferrumequinum* (allele FJ598617.1), and human ACE2 tropism would allow PRD-0038 (and likely BtKY72 and related clade 3 viruses) to expand the geographic range of host reservoirs that can be infected and, in turn, the likelihood of zoonotic transmission. Broadly neutralizing antibodies with activity against sarbecoviruses (RBD-directed) and beyond (fusion machinery directed) inhibited PRD-0038 S-mediated entry into cells and could be stockpiled as possible countermeasures for pandemic preparedness.

We observed that three immunizations with a clade 1b or with a clade 3 sarbecovirus S trimer predominantly elicited vaccinematched serum-neutralizing antibody responses. We note that our neutralization data of clade 1b pseudoviruses underscore the distinction between antigenic and genetic distance: although RaTG13 harbors a greater number of RBD mutations than Omicron BA.2 or BA.5, neutralizing activity was higher against RaTG13 than against these SARS-CoV-2 variants, which accumulated mutations to erode neutralizing antibody titers (Y. Cao et al., 2023; C. W. Tan et al., 2022). Compared with SARS-CoV-2 S, we found that PRD-0038 S-elicited polyclonal serum antibodies were more broadly reactive with vaccine-mismatched antigens, including clades 1a and 2 RBDs, which likely account for the weak but detectable crossneutralization of SARS-CoV-1 with sera from mice immunized with PRD-0038 S but not with SARS-CoV-2 S. However, we also note that sera from three SARS-CoV-2 S-immunized mice had weak but detectable neutralization against clade 3 sarbecoviruses, whereas none of the PRD-0038 S-elicited sera could neutralize the SARS-CoV-2 S pseudoviruses tested. As non- or weakly neutralizing monoclonal and polyclonal antibodies have been shown to participate in protection against SARS-CoV-2 challenge in small animal models through Fc-mediated effector functions (Adams et al., 2023; Addetia et al., 2023b; Mackin et al., 2023; Schäfer et al., 2021; Winkler et al., 2021), our findings motivate the inclusion of clade 3 and other divergent RBDs in updated multi-antigen sarbecovirus vaccine formulations (Cohen et al., 2021, 2022; Martinez et al., 2021; A. C. Walls et al., 2021). This would allow the elicitation of potent clade 3 neutralizing antibodies and cross-clade binding (and possibly neutralizing) antibodies with maximal breadth to achieve optimal protection against continuously evolving SARS-CoV-2 variants and sarbecoviruses found in wildlife.

The analysis of cross-reactivity of vaccine-elicited serum antibodies is based on a small number of animals. Furthermore, there is currently no known animal challenge model for clade 3 sarbecoviruses, and we were therefore not able to evaluate the contribution of the broadly reactive antibody responses elicited upon PRD-0038 S vaccination to in vivo protection.

3.9 Methods

Cell lines

Cell lines used in this study were obtained from DH10B competent cells (Thermo Fisher Scientific), HEK293T (ATCC, CRL-11268) and Expi293F (Thermo Fisher Scientific, A14527) except for the HEK293T cells with stable human ACE2 expression which was kindly provided by Jesse Bloom (Crawford et al., 2020). Cells were cultured in 10% FBS (Fisher Scientific-Cytiva), 1% penicillin-streptomycin (Thermo Fisher Scientific) DMEM at 37℃, 5% CO_2. AWY101 S.cerevisiae strain was used for yeast surface-display experiments. None of the cell lines were authenticated or tested for mycoplasma contamination.

In vivo animal studies

Female BALB/c mice were purchased from Envigo (order code 047) at 7 weeks of age and were maintained in a specific pathogen free facility within the Department of

Comparative Medicine at the University of Washington, Seattle, accredited by the Association for Assessment and Accreditation of Laboratory Animal Care (AAALAC). Animal experiments were conducted in accordance with the University of Washington's Institutional Animal Care and Use Committee.

Production of recombinant PRD-0038 RBDs

The PRD-0038 S glycoprotein sequence was obtained from Genbank (MT726045). Both wildtype and mutant PRD-0038 RBDs (residues 318-520) were synthesized by GenScript with an N-terminal mu-phosphatase signal peptide and C-terminal 8x His tag, a short linker (GGSS) followed by an Avi tag in a pCMVR plasmid and sub-cloned with E. coli DH10B Competent cells. Expi293F cells were grown at 37°C with 8% CO_2 and DNA transfections were conducted with the ExpiFectamine 293 Transfection Kit (Thermo Fisher Scientific). Cell culture supernatants were harvested three days post transfection. RBDs were purified using nickel based affinity chromatography using HisTrap High Performance column (Cytiva). Proteins were first washed with 10 column volumes of a buffer containing 25mM sodium phosphate (pH8.0) and 300 mM NaCl, before elution with 8 column volumes of a buffer containing 25 mM sodium phosphate (pH8.0), 300 mM NaCl, 500mM imidazole. Eluted proteins were buffer exchanged into 1x PBS (137mM NaCl, 2.7mM KCl, 10mM Na2HPO4, 1.8mM KH2PO4, pH 8.0) using Amicon Ultra-15 Centrifugal Filter Unit (10 kDa) (Millipore). Overnight biotinylation reactions were performed using the BirA Biotin-Protein Ligase Kit (Avidity) at 4°C in 1x BiomixA, BiomixB. Biotinylated proteins were once again affinity purified using the HisTrap column as previously described to get rid of BirA. Once purified, buffer exchanged into PBS, and concentrated, proteins were flash-frozen and stored at -80°C until use.

Production of recombinant ACE2 ectodomains

Genbank accession numbers for all ACE2s can be found in **Table 3.1**. Recombinant ACE2 ectodomain constructs were synthesized by GenScript. ACE2-His ectodomain constructs comprise of residues 19-615 with an N-terminal mu-phosphatase signal peptide and C-terminal 8x His tag, a short GGSS linker, and an Avi tag. ACE2-Fc ectodomain (Starr et al., 2020) constructs comprise residues 19-615 with an N-terminal mu-phosphatase signal peptide and C-terminal fusion to a sequence encoding a thrombin cleavage site, a short linker (GGGG) and a human Fc fragment and were cloned in a pCMV plasmid. The native *R. alcyone* ACE2 ectodomain dimer comprises residues 1-740 and a C-terminal 8x His tag, a GGSS linker and an Avi tag and was cloned in a pCMVR plasmid. All ACE2 orthologue ectodomains were produced in Expi293F cells at 37°C supplemented and 8% CO_2. Transfections were performed with the ExpiFectamine 293 Transfection Kit (Thermo Fisher Scientific). Cell culture supernatants were harvested four days after transfection and proteins were purified using HiTrap Protein A HP (Cytiva) or HisTrapHigh Performance column (Cytiva). ACE2-Fc proteins were first washed with 10 column volumes of 20mMsodium phosphate (pH8.0) then eluted with 0.1Mcitric acid (pH 3.0) directly into tubes containing 1M Tris-HCl (pH 9.0). Purified proteins were buffer exchanged into PBS (pH 8.0), concentrated using Spin-X UF 20 mL Centrifugal Concentrator, 100,000MWCOMembrane (PES) (Corning), and flash-frozen. ACE2-His proteins were washed with 10 column volumes of a buffer containing 25 mM sodium phosphate (pH 8.0), 300 mM NaCl, then eluted with 8 column volumes of a buffer containing 25 mM sodium phosphate (pH 8.0), 300 mM NaCl and 500 mM imidazole. Eluted proteins were buffer exchanged into 1xPBS (pH8.0) using Amicon Ultra-15 Centrifugal Filter Unit (10 kDa) (Millipore) and flash-frozen.

Production of recombinant PRD-0038 PentaPro S, HexaPro S, and SARS-CoV-2 HexaPro S

The PRD-0038 S glycoprotein sequence was obtained from Genbank (MT726045). Recombinant PRD-0038 S glycoprotein ectodomain (residues 16-1194) constructs with pre-fusion stabilizing mutations (PentaPro: F800P, S882P, S925P, K969P, V970P or HexaPro: F800P, A875P, S882P, S925P, K969P, V970P) were synthesized by GenScript with an N-terminal mu-phosphatase signal peptide and C-terminal short linker (SG), TEV protease site (RENLYFQ), a short linker (GGGGSG), Foldon, 8x His tag, a short linker (GGSS) followed by an Avi tag in a pCMVR plasmid. The SARS-CoV-2 S glycoprotein ectodomain construct comprises residues 1-1208 with the native signal peptide, the HexaPro prefusion stabilizing mutations55 (F817P, A892P, A899P, A942P, K986P, V987P), abrogation of the furin cleavage site (residues 682-685, GSAS) and a C-terminal short linker (GSG), followed by a foldon, HRV 3C site (LEVLFQGP), a short linker (GSG), an avi tag, a short linker (GSG), an 8x his tag in a pcDNA3.1(-) plasmid. Expi293F cells were grown at 37℃ with 8% CO_2 and DNA transfections were conducted with the ExpiFectamine 293 Transfection Kit (Thermo Fisher Scientific). Cell culture supernatants were harvested four days post-transfection and proteins were purified using HisTrap High Performance column (Cytiva). Proteins were first washed with 10-15 column volumes of a buffer containing 25 mM sodium phosphate, 300 mM NaCl, 20 mM imidazole, pH 8.0, followed by elution with 10-15 column volumes using 300 mM imidazole, pH 8.0. Eluted proteins were concentrated and buffer exchanged into 1x PBS or 1x TBS (20mMTris, 150mM NaCl, pH 8.0) using Amicon Ultra-15 Centrifugal Filter Unit (100 kDa) (Millipore). Purified proteins were snap frozen and stored at -80℃. Purified proteins were checked for endotoxin level using Charles River Limulus Amebocyte Lysate (LAL) cartridges (Charles River, PTS201F). Endotoxinfree SARS-CoV-2 HexaPro S and PRD-0038 HexaPro S were flash-frozen and stored at -80℃ until the day of immunization.

Production of PRD-0038 wild-type RBD- Natively Dimerized R. alcyone Complex

For complex formation, wild-type PRD-0038 RBD was mixed with natively dimerized *R. alcyone* ACE2 His at a 4:1 molar ratio, then incubated at room temperature for 5-10 min. Gel filtration was performed to remove excess RBD on a Superose 6 10/300 GL column (Cytiva) equilibrated in 50mM Tris-HCl, 150mM NaCl. Complex formation was confirmed by SDS-PAGE, and the PRD-0038 RBD- *R. alcyone* ACE2 complex was snap frozen and stored at -80℃ until day of grid preparation.

Binding analysis using biolayer interferometry (BLI)

BLI binding assays were performed on an Octet Red (Sartorius) instrument operated at 30℃ with shaking (1000 rpm). For biotinylated RBD and ACE2-Fc or ACE2-His binding assays, streptavidin biosensors were hydrated in water for 10 min prior to the experiment. Biosensors were incubated in 10x kinetics buffer (Sartorius) for 60 s followed by the loading of biotinylated RBDs to the tip, all to a final level of 1 nm. Loaded biosensors were equilibrated in 10x kinetics buffer for 120 s which served as our baseline. For avidity binding assays, association with 1 mMACE2-Fc (dimeric form) was performed for 300 s followed by 300 s of dissociation in 10x kinetics buffer. For affinity binding assays to determine KD values, RBD-loaded tips were dipped into a concentration series of ACE2-His (2 fold serial dilution from 100 nM to 6.25 nM for *R. alcyone* ACE2-His, 3 fold serial dilution from 660 nM to 8 nM for *R. landeri* ACE2-His) for 600 s followed by 600 s of dissociation in 10x kinetics buffer. Global fits were used to calculate KD values using a 1:1 binding fit model. Data were plotted using GraphPad Prism. Assays were replicated with three biological replicates (recombinant RBD proteins generated on different days) and representative graphs are shown.

Production of VSV pseudoviruses

Wildtype and mutant PRD-0038 S constructs consisting of residues 1-1235 and containing a 21 residue C-terminal deletion (del21) followed by a 3x FLAG tag were synthesized by GenScript and placed into an HDM plasmid. VSV pseudoviruses were produced using HEK293T cells seeded on BioCoat Cell Culture Dish : poly-D-Lysine 100 mm (Corning). Cells were transfected with PRD-0038 S-Flag constructs using Lipofectamine 2000 (Thermo Fisher Scientific) in Opti-MEM transfection medium. After 5h of incubation at 37 °C with 5% CO_2, cells were supplemented with DMEM containing 10% of FBS. On the next day, cells were infected with VSV (G*DG-luciferase) (Kaname et al., 2010) for 2h, followed by five time wash with DMEM medium before addition of anti-VSV G antibody (I1-mouse hybridoma supernatant diluted 1:40, ATCC CRL-2700) and medium. After 18-24 h of incubation at 37 ℃ with 5% CO_2, pseudoviruses were collected and cell debris removed by centrifugation at 3,000xg for 10 min. Pseudoviruses were further filtered using a 0.45 mm syringe filter and concentrated 25-50x prior to storage at -80℃. Mock VSV pseudoviruses were prepared as above but without S transfection.

Cell entry assays comparing wildtype and mutant PRD-0038 S VSV pseudoviruses

HEK293T cells were transfected with full length *Rhinolophus* ACE2 orthologs using Lipofectamine 2000 (Thermo Fisher Scientific) in Opti-MEM five hours prior to plating into 96-well plates [3610] (Corning) coated with poly-lysine [P4707] (Sigma) and incubated 18-24 h before infection with VSV pseudoviruses. For human ACE2 entry assays, HEK293T cells with stable hACE2 expression were plated into poly-lysine-coated 96-well plates and incubated for 18-24h before infection with VSV pseudoviruses. The amount of pseudovirus used for infection was adjusted using Western Blot based on S incorporation across different mutants to use a constant input of S. Detection of VSV backbone was performed with 1:1,000 Anti-VSV-M [23H12] Antibody (Kerafast). Detection of 3x-FLAG tagged S was performed with 1:400 monoclonal ANTI-FLAG M2 antibody [F3165] produced in mouse (Sigma). 1:50,000 Alexa Fluor 680 AffiniPure Goat Anti-Mouse IgG [115-625-174] (Jackson ImmunoResearch) was used as the secondary antibody. A representative Western Blot is shown in **Figure 3.6e**. Genbank accession numbers for all ACE2s can be found in **Table 3.1**. After 1h of infection, an additional 40 mL of DMEM supplemented with 20%

FBS and 2% PenStrep was added to the cells. After 18-20 h, 40 mL of One-Glo-EX substrate (Promega) was added to each well and incubated on a plate shaker in the dark for 5 min before reading the relative luciferase units using a BioTek Neo2 plate reader. Fold change of relative luciferase units over mock VSV were plotted in Prism (GraphPad) with mock being cells that were not transfected with an S-encoding plasmid. 3 biological replicates, each of which with 3 technical replicates were carried out.

Cell entry assay for PRD-0038 S VSV with distinct Rhinolophus ACE2s

For wildtype PRD-0038 S VSV entry into HEK293T cells transfected with *R. affinis*, *R. sinicus*, *R. landeri*, and *R. alcyone* alleles fulllength ACE2 alleles (**Figure 3.1d**), HEK293T cells (ATCC) were cultured in 10% FBS, 1% penicillin-streptomycin DMEM at 37℃ in a humidified 5% CO_2 incubator. Cells were plated 18-24 hours prior to transfection into 96-well plates [3610] (Corning) coated with poly-lysine [P4707] (Sigma). All transfections were performed using full-length *Rhinolophus* ACE2 placed into a HDM plasmid (synthesized by GenScript). Transfection of ACE2 alleles into HEK293T cells was performed using 0.2 mg DNA and 0.15 mL Lipofectamine 2000 (Thermo Fisher Scientific) per well in Opti-MEM. After a 5 h incubation at 37℃ in a humidified 8% CO_2 incubator, DMEM was added to obtain a final concentration of 10% FBS and 1% penicillin-streptomycin. Cells were incubated at 37 C in a humidified 8% CO_2 incubator for 36-48 h prior to infection. For each infection test, 2-3 technical replicates were performed, and the assays were repeated on a second day, for a total of 4-6 technical replicates. Three biological replicates (pseudovirus generated on different days) were used for cell entry and each point shown represents the mean fold change for each biological replicate. Results were plotted using Graphpad Prism (**Figure 3.1d**). Genbank accession numbers for all ACE2s can be found in **Table 3.1**.

Cryo-EM sample preparation and data collection

Cryo-EM grids of PRD-0038 PentaPro S were prepared using two separate methods and data were combined during data processing. The first dataset was collected from the grids prepared using a reverse grid-blotting method. 3 mL of sample was added to the carbon side of a glow discharged C-flat R2/2 copper grid and 1mL was added to the back side before addition of 1 mL of CHEMS lipid dissolved in chloroform on the front side. The sample was allowed to sit on the grid for 1 minute and then manually blotted from the back side using a strip of Whatman #1 filter paper and plunged into liquid ethane. The second dataset was collected from a lacey carbon grid with a thin home-made continuous carbon layer. 3 mL of 0.15 mg/mL PRD-0038 Pentapro S was loaded onto the glow discharged (6s at 20mA) grid followed by plunge freezing using a vitrobot MarkIV (ThermoFisher Scientific). The grid was blotted with a blot force of -1, 3 second blot time, and 10 second wait time before the plunge freeze at 100% humidity and 25°C. For the PRD-0038 RBD-ACE2 complex, grids were prepared by applying 3 mL of 4 mg/ml PRD-0038 RBD bound to the *R. alcyone* ACE2 dimer with 7 mM CHAPSO (Anatrace) were applied and blotted twice as previously described (Snijder et al., 2017), onto freshly glow discharged R 2/2 UltrAuFoil grids prior to plunge freezing using a vitrobot MarkIV (ThermoFisher Scientific) with a blot force of 0 and 5 sec blot time at 100 % humidity and 22°C. Data were acquired using an FEI Titan Krios transmission electron microscope operated at 300 kV and equipped with a Gatan K3 direct detector and Gatan Quantum GIF energy filter, operated in zero-loss mode with a slit width of 20 eV. Automated data collection was carried out using Leginon (Suloway et al., 2005) at a nominal magnification of 105,000x with a pixel size of 0.843 A°. The dose rate was adjusted to 15 counts/pixel/s, and each movie was acquired in counting mode fractionated in 75 frames of 40 ms. A total of 2,482 and 11,743 micrographs were collected for the PRD-0038 S and PRD-0038 RBD-ACE2 datasets, respectively.

Cryo-EM data processing, model building and refinement

Motion correction, contrast-transfer function (CTF) parameter estimation, automatic particle picking, and extraction were performed using Warp (Tegunov & Cramer, 2019) for each data set. For the PRD-0038 S structure, particle images were extracted with a box size of 260 pixels with a pixel size of 1.686 A°. After two rounds of 2D classification using cryoSPARC (Punjani et al., 2017), well-defined particles were selected and particles from each dataset were combined and binned to a box size of 130 pixels with a pixel size of 3.372 A° for subsequent 3D classification using Relion (Scheres, 2012b; Zivanov et al., 2018) with 50 iterations (angular sampling 7.5 for 25 iterations and 1.8 with local search for 25 iterations). 103,347 particles were selected and re-extracted with a box size of 260 and pixel size of 1.686 A° for cryoSPARC non-uniform refinement (Punjani et al., 2020) with C3 symmetry and further subjected to Bayesian polishing (Zivanov et al., 2019) in Relion. Finally, another round of non-uniform refinement with C3 symmetry and optimized per-particle defocus was carried out to the polished particles. To improve the density of the NTD, we used symmetry expansion and local refinement using cryoSPARC. For the PRD-0038 RBD - *R. alcyone* ACE2 structure, two rounds of reference-free 2D classification were performed using cryoSPARC to select well-defined particle images. These selected particles were subjected to two rounds of 3D classification with 50 iterations each (angular sampling 7.5for 25 iterations and 1.8with local search for 25 iterations) using Relion with an initial model generated with ab-initio reconstruction in cryoSPARC. 3D refinements were carried out using non-uniform refinement along with per-particle defocus refinement in CryoSPARC. To improve the density of the RBD-ACE2 dimer, the particles were subjected to cryoSPARC heterogeneous refinement. Particles belonging to classes with the best resolved RBD-ACE2 density were selected and subjected to the Bayesian polishing procedure implemented in Relion before performing another round of non-uniform refinement in cryoSPARC followed by per-particle defocus refinement and again non-uniform refinement. To further improve the density of the RBD-ACE2 domains, the particles were symmetry expanded and subjected to focus 3D classification without refining angles and shifts using a soft mask encompassing the RBD and monomer ACE2 using a tau value of 40 in Relion. Particles belonging to classes with the best resolved RBD-ACE2 density were selected and then subjected to local refinement using CryoSPARC. Local resolution estimation, filtering, and sharpening were carried out using CryoSPARC. Reported resolutions are based on the gold-standard Fourier shell correlation (FSC) of 0.143 criterion and Fourier shell correlation curves were corrected for the effects of soft masking by high-resolution noise substitution (S. Chen et al., 2013; Rosenthal & Henderson, 2003). UCSF Chimera (Pettersen et al., 2004), UCSF ChimeraX (Goddard et al., 2018), and Coot (Emsley et al., 2010) were used to fit atomic models into the cryoEM maps. S and RBD-ACE2 models were refined and relaxed using Rosetta (Frenz et al., 2019; R. Y.-R. Wang et al., 2016) using sharpened and unsharpened maps and validated using Phenix (Liebschner et al., 2019), Molprobity (V. B. Chen et al., 2010) and Privateer (Agirre et al., 2015). Analysis of interface residues was assisted by PISA (Krissinel & Henrick, 2007).

Monoclonal antibody ELISAs

For PRD-0038 HexaPro S and SARS-CoV-2 HexaPro S ELISAs, 30 ml of the proteins at 3 mg/mL were plated onto 384-well Nunc Maxisorp plate (ThermoFisher, 464718) in 1x TBS and incubated 1h at 37℃ followed by slap drying and blocking with 80 mL of Casein for 1 h at 37℃. After incubation, plates were slap dried and 1:4 serial dilutions of the corresponding mAbs starting from 0.1 mg/ml were made in 30 ml TBST, added to the plate and incubated at 37℃ for 1 h. Plates were washed 4x in TBST and 30 ml of 1:5,000 Goat anti-Human IgG Fc Secondary Antibody, HRP (Thermo Fisher, A18817) or Goat anti-Syrian Hamster IgG (H+L) Secondary Antibody, HRP (Thermo Fisher, PA1-28823) were added to each well and incubated at 37℃. After 1 h, plates were washed 4x in TBST and 30 ml of TMB (SeraCare) was added to every well for 2 min at room temperature. Reactions were quenched with the addition of 30 ml of 1N HCl. Plates were immediately read at 450 nm on a BioTek Neo2 plate reader and data plotted and fit in Prism 9 (GraphPad) using nonlinear regression sigmoidal, 4PL, X is the concentration to determine EC_{50} values from curve fits.

Deep mutational scanning for mutational effects on ACE2 binding

The complete deep mutational scanning pipeline can be found at: https://github.com/tstarrlab/SARSr-CoV-RBD_DMS/blob/main/results/summary/summary.md. Deep mutational scanning libraries for sarbecovirus strains including PRD-0038 and SARS-CoV-1 Urbani were constructed as previously described (Starr, Greaney, Hannon, et al., 2022). Briefly, site-saturation mutagenesis libraries spanning all RBD positions were produced by Twist Bioscience (or NNS mutagenesis for positions that failed Twist mutagenesis), tagged with an N16 barcode, and cloned into a yeast display vector backbone via Gibson Assembly. Libraries were electroporated into E. coli and plated at a target bottleneck of 40,000 unique barcodes per library to overrepresent the 4,000 possible amino acid mutations. Colonies were scraped from each transformation plate, library plasmid purified, and transformed into the AWY101 S. cerevisiae strain (Wentz & Shusta, 2007) for yeast surface display experiments. Library plasmids were sequenced using a PacBio Sequel IIe to generate long sequence reads spanning the N16 barcodes and RBD coding sequence. Raw CCS reads are available on the NCBI Sequence Read Archive, BioProject PRJNA962117, BioSample SAMN34384156. Reads were processed using alignparse (version 0.2.4) (Crawford & Bloom, 2019) to generate a table linking each N16 barcode to its unique RBD mutant, available at: https://github.com/tstarrlab/SARSr-CoV-RBD_DMS/blob/main/results/variants/codon_variant_table_PRD0038.csv and https://github.com/tstarrlab/SARSr-CoV-RBD_DMS/blob/main/results/variants/codon_variant_table_SARS1.csv. The RBD expression level and ACE2-binding avidity of each RBD mutant was determined via high-throughput FACS-seq assays as previously described (Starr, Greaney, Hannon, et al., 2022). ACE2-binding titrations were performed by incubating induced yeast-display libraries with a concentration series of dimeric ACE2 ligands from 10^{-6} to 10^{-13} M at 1-log intervals, plus a 0 M ACE2 sample, with samples equilibrated overnight at room temperature with mixing. Yeast were washed with PBS-BSA (0.2 mg/L), labeled with 1:100 FITC-conjugated chicken anti-Myc (Immunology Consultants CMYC-45F) to detect yeast-displayed RBD and 1:200 PE-conjugated streptavidin (Thermo Fisher S866) or goat anti-human-IgG (Jackson ImmunoResearch 109-115-098) to detect binding of biotinylated (human, Acro Biosystems H82E6) or Fc-tagged (*R. alcyone*, *R. landeri*) ACE2. For each titration sample, RBD+ yeast were fractionated into four bins of PE fluorescence (ACE2 binding), grown overnight, plasmid isolated, N16 barcode amplified, and barcodes counted via high-throughput sequencing on an Illumina NextSeq. RBD expression was measured by sorting cells into four bins on the basis of Myc-FITC labeling, followed by outgrowth, plasmid isolation, N16 barcode amplification, and sequencing. Sequencing reads are available on the NCBI Sequence Read Archive, BioProject PRJNA962117, BioSample SAMN34384823. Demultiplexed Illumina barcode reads were aligned to library barcodes using dms_variants (version 0.8.9), yielding a table of counts of each barcode in each FACS bin which is available at https://github.com/tstarrlab/SARSr-CoV-RBD_DMS/blob/main/results/counts/variant_counts.csv.gz. Reads were downweighted by the ratio of total sequence reads from a bin to the number of

cells sorted into that bin. For each barcode, we inferred the apparent dissociation constant for avid binding (KD,app) by fitting the standard non-cooperative Hill equation to the mean FACS bin of a barcode variant as a function of ACE2 concentration. For each barcode, expression was determined via a maximum likelihood estimator of log-MFI based on the distribution of barcode counts across FACS bins and the known fluorescence boundaries of those bins. The computational pipelines for computing per-barcode binding constants and expression phenotypes are available at: https://github.com/tstarrlab/SARSr-CoV-RBD_DMS/blob/main/results/summary/compute_binding_Kd_huACE2.md and https://github.com/tstarrlab/SARSr-CoV-RBD_DMS/blob/main/results/summary/compute_expression_meanF.md. Because most mutants in the library were independently associated with more than one N16 barcode, we derived the final mutant phenotype as the average of per-barcode measurements, as computed at: https://github.com/tstarrlab/SARSr-CoV-RBD_DMS/blob/main/results/summary/collapse_barcodes_lib40_41.md. The final per-mutant deep mutational scanning phenotypes are available at: https://github.com/tstarrlab/SARSr-CoV-RBD_DMS/blob/main/results/final_variant_scores/final_variant_scores_lib40_41.csv.

Immunogenicity

Prior to each immunization, immunogens (endotoxin-free SARS-CoV-2 HexaPro S or PRD-0038 HexaPro S) were diluted to 20 mg/mL in 1x TBS (20mM Tris, 150mM NaCl, pH 8.0) and mixed with 1:1 vol/vol AddaVax (InvivoGen vac-adx-10) to reach a final dose of 1 mg of immunogen per injection. At 8 weeks of age, 6 mice per group were anesthetized and injected intramuscularly in the quadriceps with 50 mL of immunogen per leg, 100mL total at weeks 0, 3, and 6. Mice were bled via the submental route at weeks 0, 2, 5, and 8. Blood was collected in serum separator tubes (BD # 365967) and rested for 30 min at room temperature for coagulation. Serum tubes were then centrifuged for 10 min at 2,000 x g and serum was collected and stored at -80℃ until use.

Neutralization assays

For mAb neutralization against SARS-CoV-2 S VSV and PRD-0038 S K482Y/T487W VSV, HEK293T cells with stable human ACE2 expression in DMEM supplemented with 10% FBS and 1% PenStrep were seeded at 40,000 cells/well into 96-well plates [3610] (Corning) coated with poly-lysine [P4707] (Sigma) and incubated overnight at 37℃. After 16-20h of incubation, a half-area 96-well plate (Greiner) was prepared with 1:5 serial dilutions of S2X259 and S2X35 starting from 0.1 mg/ml in DMEM, and 1:3 serial dilutions of 76E1 starting from 0.5 mg/ml in DMEM, for a total of 22 mL per well. An equal volume of DMEM with diluted pseudoviruses was added to each well. All pseudoviruses were diluted between 1:3-1:27 to reach a target entry of 10^6 RLU. The mixture was incubated at room temperature for 45-60 minutes. Media was removed from the cells and 40 mL from each well of the half-area 96-well plate containing mAb and pseudovirus were transferred to the 96-well plate seeded with cells and incubated at 37℃ for 1h. After 1h, an additional 40 mL of DMEM supplemented with 20% FBS and 2% PenStrep was added to the cells. After 18-20h, 40 mL of One-Glo-EX substrate (Promega) was added to each well and incubated on a plate shaker in the dark for 5 min before reading the relative luciferase units using a BioTek

Neo2 plate reader. Relative luciferase units were plotted and normalized in Prism (GraphPad): 100% neutralization being cells lacking pseudovirus and 0% neutralizing being cells containing virus but lacking mAb. Prism (GraphPad) nonlinear regression with “[inhibitor] versus normalized response with a variable slope” was used to determine IC_{50} values from curve fits with 2 technical repeats. 3 biological replicates were carried out for each mAb. For SARS-CoV-2 D614G S VSV,88 BA.2 S VSV, BA.5 S VSV,75 RaTG13 S VSV,84 and SARS-CoV-1 S VSV (Millet & Whittaker, 2016) neutralization, HEK293T cells with stable human ACE2 expression in DMEM supplemented with 10% FBS and 1% PenStrep were seeded at 40,000 cells/well into 96-well plates [3610] (Corning) coated with poly-lysine [P4707] (Sigma) and incubated overnight at 37℃. For PRD-0038 S VSV and Khosta-1 S VSV neutralization, HEK293T cells were transfected with full length *R. alcyone* ACE2 using Lipofectamine 2000 (Thermo Fisher Scientific) in Opti-MEM five hours prior to plating into 96-well plates [3610] (Corning) coated with poly-lysine [P4707] (Sigma) and incubated overnight at 37℃. The following day, a half-area 96-well plate (Greiner) was prepared with 3-fold serial sera dilutions (starting dilutions determined for each serum and pseudovirus, 22 µL per well). An equal volume of DMEM with diluted pseudoviruses was added to each well. All pseudoviruses were diluted between 1:3-1:27 to reach a target entry of 10^6 RLU. The mixture was incubated at room temperature for 45-60 minutes. Media was removed from the cells and 40 mL from each well of the half-area 96-well plate containing sera and pseudovirus were transferred to the 96-well plate seeded with cells and incubated at 37℃ for 1h. After 1h, an additional 40 mL of DMEM supplemented with 20% FBS and 2% PenStrep was added to the cells. After 18-20h, 40 mL of

One-Glo-EX substrate (Promega) was added to each well and incubated on a plate shaker in the dark for 5 min before reading the relative luciferase units using a BioTek Neo2 plate reader. Relative luciferase units were plotted and normalized in Prism (GraphPad): 100% neutralization being cells lacking pseudovirus and 0% neutralizing being cells containing virus but lacking sera. Prism (GraphPad) nonlinear regression with "log[inhibitor] versus normalized response with a variable slope" was used to determine ID_{50} values from curve fits with 3 technical repeats. 3 biological replicates were carried out for each sample-pseudovirus pair.

Breadth- and epitope-mapping of vaccine sera via deep mutational scanning

The complete serum deep mutational scanning pipeline is described https://github.com/tstarrlab/SARSr-CoV_MAP_PRD0038-vaccine/blob/main/results/summary/summary.md. Binding of serum was evaluated against deep mutational scanning pools for PRD-0038 and SARS-CoV-1 whose construction is described above, previously published deep mutational scanning pools for SARS-CoV-2 Wuhan-Hu-1 (Starr, Greaney, Hannon, et al., 2022) and Omicron BA.2 (Starr, Greaney, Stewart, et al., 2022), and a previously published pan-sarbecovirus panel (Starr, Zepeda, et al., 2022) that was supplemented with additional newly described sarbecovirus and SARS-CoV-2 variants. Serum was first depleted of non-specific yeast-reactive antibodies as previously described (Greaney et al., 2022). Yeast-display RBD libraries were pooled, induced for yeast surface expression, and labeled with serum at 1:100, 1:1000, 1:10,000, and 1:100,000 dilutions for one hour at room temperature. Yeast were washed with PBS-BSA and labeled with secondary Myc-FITC antibody and

APC-conjugated goat anti-mouse-IgG (Jackson ImmunoResearch 115-605-008). As with ACE2-binding titrations, libraries were then partitioned into four bins of serum binding on a BD FACSAria, collecting a minimum of 6 million RBD+ cells per sample concentration across the four bins. Cells were grown post-sort, plasmid purified, N16 barcode amplified, and sequenced on an Illumina NextSeq. Raw Illumina sequencing data is available from the NCBI Sequence Read Archive, BioProject PRJNA714677, BioSample SAMN36715819. Barcode reads were mapped to library barcodes, with raw counts found at: https://github.com/tstarrlab/SARSr-CoV_MAP_PRD0038-vaccine/blob/main/results/counts/variant_counts.csv. For each library barcode, an area under the curve (AUC) metric was derived from its distribution of sequence reads across sort bins. First, the strength of serum binding to each barcode at each serum dilution was determined as the simple mean bin from cell counts

across integer-weighted bins, and subtracted by background mean bin determined from a sort from yeast libraries not incubated with sera. Any barcode with less than 3 cell counts at any sample concentration was eliminated from analysis. An AUC metric was then calculated from the relationship between mean bin and serum dilution. AUC calculation can be found at: https://github.com/tstarrlab/SARSr-CoV_MAP_PRD0038-vaccine/blob/main/results/summary/compute_AUC.md, and per-barcode AUC metrics are available at: https://github.com/tstarrlab/SARSr-CoV_MAP_PRD0038-vaccine/blob/main/results/bc_sera_binding/bc_sera_binding.csv. We then computed the per-variant AUC as the robust mean of replicate barcodes linked with the identical RBD variant, by taking the mean per-barcode AUC after trimming tails of the top and bottom 2.5% of AUC values among the replicate barcodes. Because mutations that disrupt RBD expression artifactually decrease serum binding, we applied two final filters: first, we censored the AUC measurement for any mutant with a measured impact on RBD expression of greater than one log-MFI unit (RBD expression < -1) from DMS measurements described above; and second, we derived a normalization constant from the slope of the linear model relating serum AUC and expression globally across all library variants for variants with expression >-1, and normalized our raw AUC measurements by this constant. The final variant derivation can be found at: https://github.com/tstarrlab/SARSr-CoV_MAP_PRD0038-vaccine/blob/main/results/summary/collapse_barcodes_SARSr-DMS.md, and final per-variant serum-binding values are available at: https://github.com/tstarrlab/SARSr-CoV_MAP_PRD0038-vaccine/blob/main/results/final_variant_scores/final_variant_scores_wts.csv and https://github.com/tstarrlab/SARSr-CoV_MAP_PRD0038-vaccine/blob/main/results/final_variant_scores/final_variant_scores_dms.csv.

3.10 Figures & Tables

Figure 3.1. The clade 3 PRD-0038 sarbecovirus has a broad *Rhinolophus* bat ACE2 tropism.

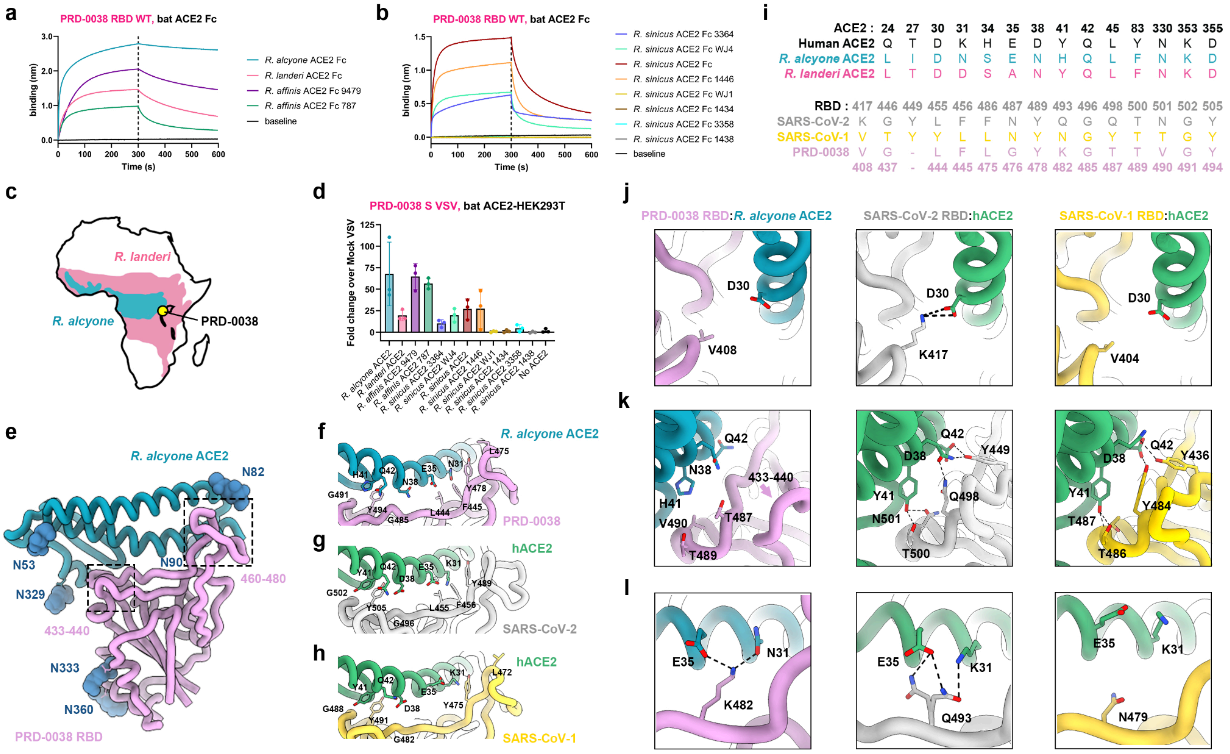

(**a and b**) BLI binding analysis of *R. affinis*, *R. alcyone* and *R. landeri* (see also **Table 3.1**) (**a**) or *R. sinicus* (**b**) ACE2-Fc alleles at a concentration of 1 µM to the biotinylated PRD-0038 RBD immobilized on streptavidin biosensors. Baselines represent non-specific binding of non-coated streptavidin biosensors to 0.25 µM ACE2 Fc. (**c**) Known geographic distribution of *R. alcyone* and *R. landeri* bats in sub-saharan Africa (https://www.iucnredlist.org/). The yellow area indicates the site of PRD-0038 sampling (Rwanda). (**d**) Entry of VSV pseudotyped with wildtype PRD-0038 S in HEK293T cells transiently transfected with the indicated *Rhinolophus* bat ACE2 orthologs. Each point represents the average of technical duplicates from each biological triplicate. Means and standard deviations shown as bars and error bars. (**e**) CryoEM structure of the PRD-0038 RBD bound to *R. alcyone* ACE2. N-linked glycans are shown as dark blue spheres and labeled with the corresponding asparagine residue number. The dotted gray boxes highlight regions with major structural deviations from SARS-CoV-2 (see also **Figure 3.3**) (**f-h**) Close-up views of the interface between the PRD-0038 RBD and *R. alcyone* ACE2 (**f**, pink and blue, respectively), the SARS-CoV-2 RBD and human ACE2 (**g**, gray and green, respectively, PDB ID 6M0J (Lan et al., 2020)) and the SARS-CoV-1 RBD and human ACE2 (**h**, gold and green, respectively, PDB ID 2AJF (F. Li et al., 2005)). Key conserved residues at the interface are rendered as sticks. (**i**) Sequence alignments of the key ACE2 and RBD residues at the binding interfaces.

Numberings used are for human ACE2 (black), SARS-CoV-2 (gray), and PRD-0038 (pink) (see also **Table 3.1**). (**j-l**) Close-up views of selected key contact residues at the interface between the PRD-0038 RBD and *R. alcyone* ACE2, the SARS-CoV-2 RBD and human ACE2 and the SARS-CoV-1 RBD and human ACE2 colored as in panel (**f**). Panel (**j**) shows that the salt bridge formed between K417$_{\text{SARS-CoV-2}}$ and D30$_{\text{hACE2}}$ is absent due to substitution to V408$_{\text{PRD-0038}}$ and V404$_{\text{SARS-CoV-1}}$. Panel (**k**) shows that the electrostatic interactions involving residues D38$_{\text{hACE2}}$ and Q42$_{\text{hACE2}}$ with Y449$_{\text{SARS-CoV-2}}$ and Q498$_{\text{SARS-CoV-2}}$ or Y436$_{\text{SARS-CoV-1}}$ and Y484$_{\text{SARS-CoV-1}}$are lost due to truncation and remodeling of the PRD-0038 433-440 loop along with substitution of Q498$_{\text{SARS-CoV-2}}$ to T487$_{\text{PRD-0038}}$ Panel (**l**) shows that Q493$_{\text{SARS-CoV-2}}$ optimally interacts with K31$_{\text{hACE2}}$/E35$_{\text{hACE2}}$ whereas the topologically equivalent residue K482$_{\text{PRD-0038}}$ is better adapted to N31$_{\text{RaACE2}}$/E35$_{\text{RaACE2}}$ due to swapping of the position of a positively charged amino acid side chain across the interface.

Figure 3.2. CryoEM data collection and refinement of the dimeric *R. alcyone* ACE2-bound PRD-0038 RBD complex (related to Figure 3.1).

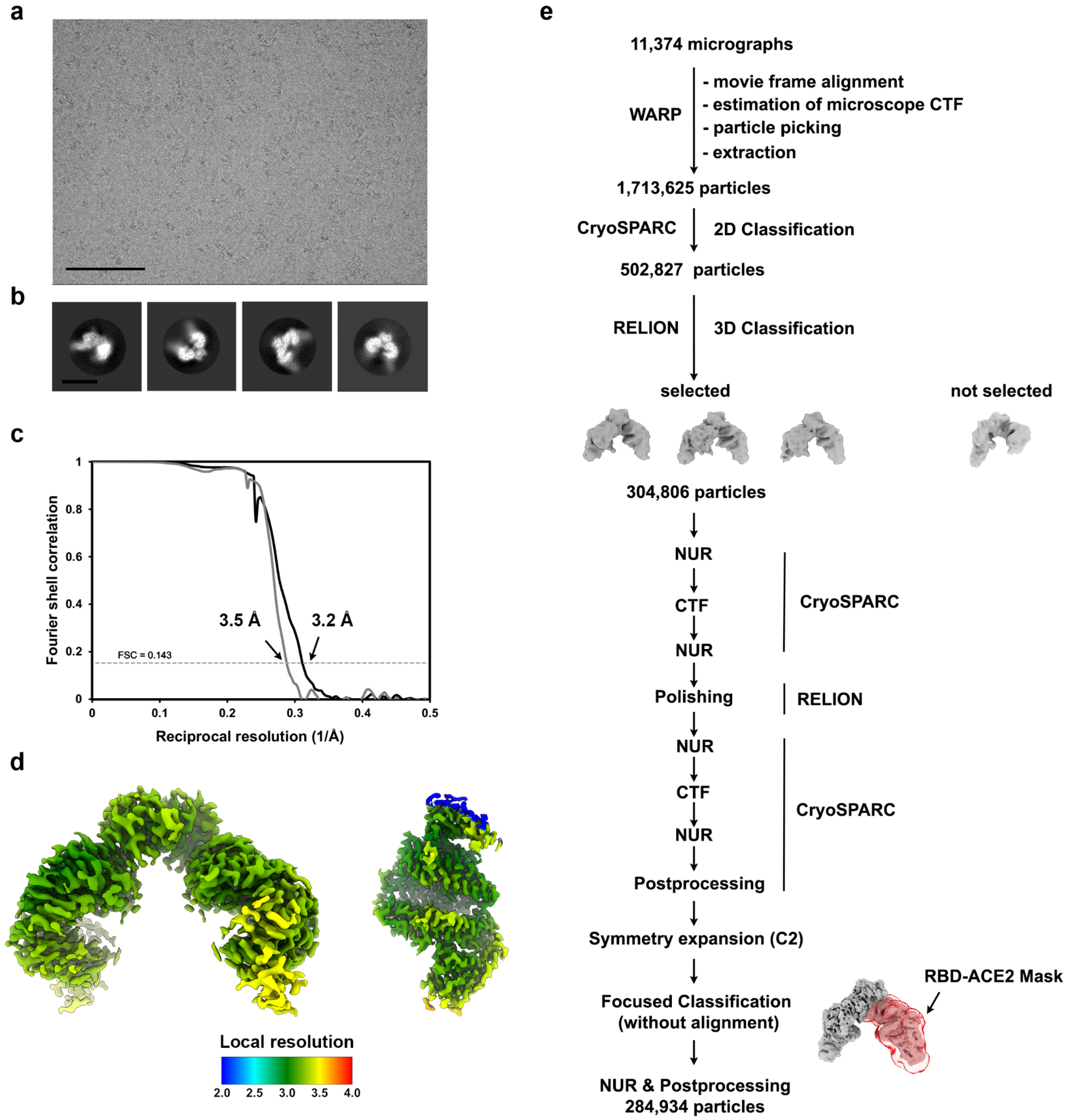

(**a and b**) Representative electron micrograph (**a**) and 2D class averages (**b**) of -the dimeric *R. alcyone* ACE2-bound PRD-0038 RBD embedded in vitreous ice. The scale bar represents 100 nm (**a**) or 100 Å (**b**). (**c**) Gold-standard Fourier shell correlation curves for the final cryoEM reconstructions of the dimeric-ACE2/RBD complex (solid gray line) and locally refined ACE2/RBD (solid black line) shown in (**d**). The 0.143 cutoff is indicated with a gray dashed line.

(**d**) Local resolution map calculated using CryoSPARC and plotted onto the sharpened cryoEM map. (**e**) Data processing flowchart. CTF: contrast transfer function; NUR: non-uniform refinement.

Figure 3.3. Structural distinctions between the PRD-0038, SARS-CoV-2 and SARS-CoV-1 RBDs near the ACE2-binding interface (RBM) (related to Figure 3.1).

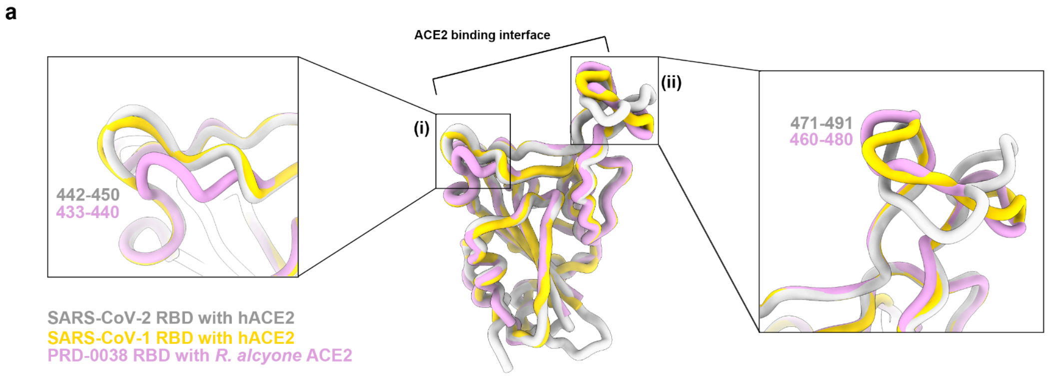

b

(i)

	442	443	444	445	446	447	448	449	450
SARS-CoV-2	D	S	K	V	G	G	N	Y	N
SARS-CoV-1	D	A	T	S	T	G	N	Y	N
PRD-0038	D	S	K	Q	G	N	N	-	-
	433	434	435	436	437	438	439		

(ii)

	471	472	473	474	475	476	477	478	479	480	481	482	483	484	485	486	487	488	489	490	491
SARS-CoV-2	E	I	Y	Q	A	G	S	T	P	C	N	G	V	E	G	F	N	C	Y	F	P
SARS-CoV-1	V	P	F	S	P	D	G	K	P	C	T	P	-	P	A	L	N	C	Y	W	P
PRD-0038	V	L	Y	N	S	A	G	G	T	C	S	S	T	S	Q	L	G	C	Y	E	P
	460	461	462	463	464	465	466	467	468	469	470	471	472	473	474	475	476	477	478	479	480

(**a**) Ribbon diagrams showing a superimposition of the *R. alcyone* ACE2-bound PRD-0038 RBD (pink) superimposed to the human ACE2-bound SARS-CoV-2 RBD (gray, PDB 6M0J (Lan et al., 2020)) and SARS-CoV-1 RBD (gold, PDB 2AJF (F. Li et al., 2005)) structures (ACE2s not shown for clarity). Insets: close-up views of two RBM regions. (**b**) Amino acid sequence alignment of the SARS-CoV-2, SARS-CoV-1, and PRD-0038 RBD regions highlighted in the insets shown in panel (**a**). - indicate deletions.

Figure 3.4. PRD-0038 RBD amino acid mutations broaden receptor tropism.

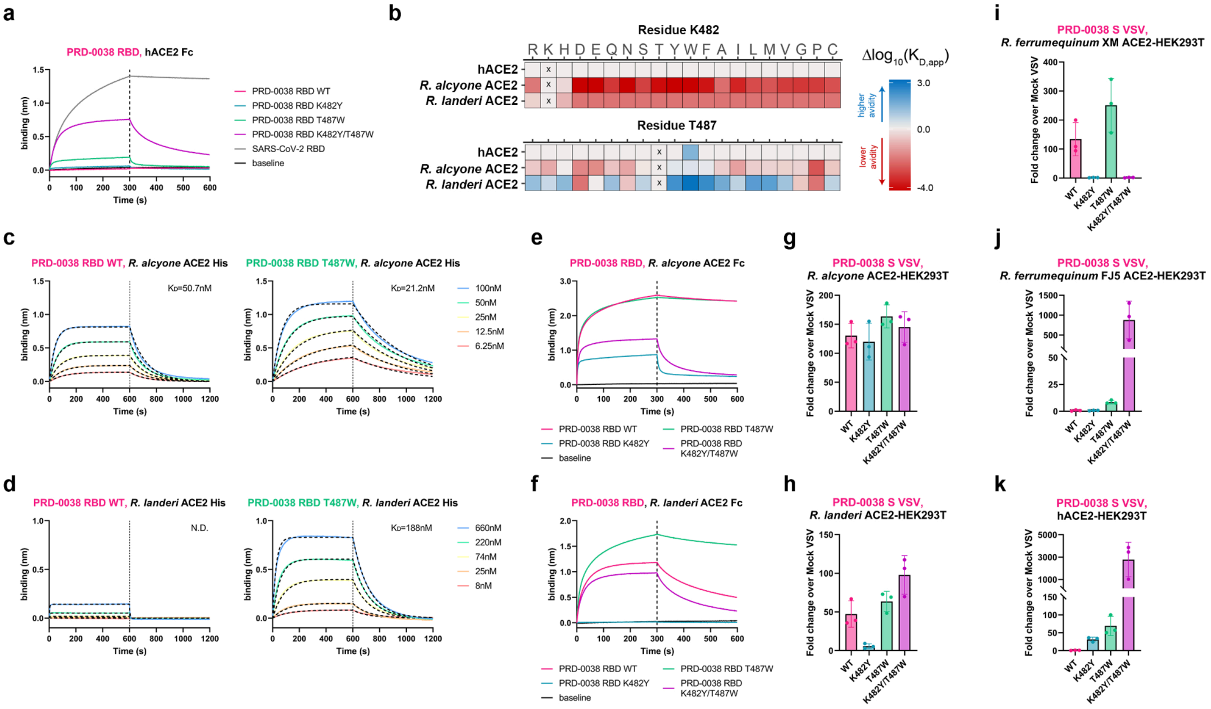

(**a**) BLI binding analysis of 1 μM dimeric hACE2-Fc to biotinylated wildtype and mutant PRD-0038 RBDs immobilized on streptavidin biosensors. (**b**) DMS heatmaps of change in binding avidity to several ACE2-Fc orthologs caused by all possible mutations of the PRD-0038 RBD residues K482 and T487. An interactive version of the DMS data can be found at https://tstarrlab.github.io/SARSr-CoV-RBD_DMS/RBD-heatmaps_delta/. (**c**) BLI binding analysis of various concentrations of monomeric *R. alcyone* ACE2 to biotinylated wildtype (left) and T487W (right) PRD-0038 RBDs immobilized on streptavidin biosensors. (**d**) BLI binding analysis of various concentrations of monomeric *R. landeri* ACE2 to biotinylated wildtype (left) and T487W (right) PRD-0038 RBDs immobilized on streptavidin biosensors. (**e**) BLI binding analysis of 1 μM dimeric *R. alcyone* ACE2-Fc to biotinylated wildtype and mutant PRD-0038 RBDs immobilized on streptavidin biosensors. (**f**) BLI binding analysis of 1 μM dimeric *R. landeri* ACE2-Fc to biotinylated wildtype and mutant PRD-0038 RBDs immobilized on streptavidin biosensors. (**g-k**) Entry of VSV pseudotyped with wildtype and mutants PRD-0038 S into HEK293T cells transiently transfected with *R. alcyone* ACE2 (**g**), *R. landeri* ACE2 (**h**), *R. ferrumequinum* XM_033107295.1 (**i**, XM), *R. ferrumequinum* FJ598617.1 (**j**, FJ5), or stably expressing human ACE2 (**k**). See methods section and **Figure 3.6e** for VSV S pseudotype normalization details.

Figure 3.5. Heatmaps of change in ACE2-binding avidity resulting from RBD mutations determined by DMS (related to Figure 3.4).

a

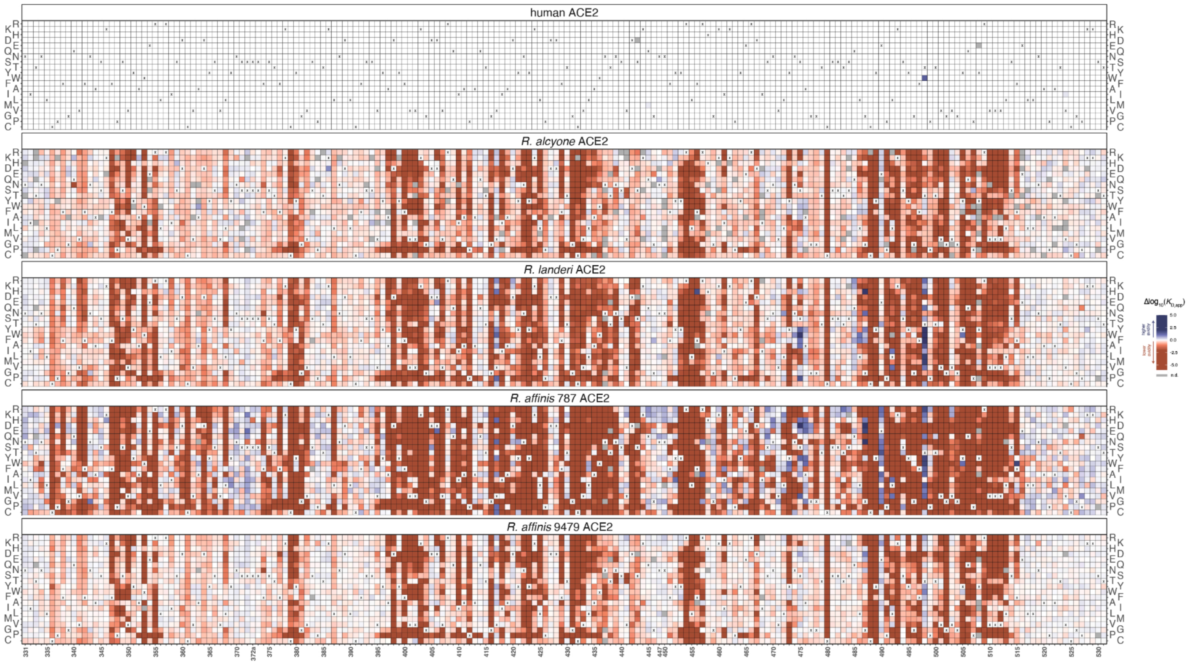

(**a**) Change in ACE2-binding avidity for hACE2, *R. alcyone* ACE2, and *R. landeri* ACE2 (delta-log$_{10}$K$_D$,apparent). Residue numbering corresponds to SARS-CoV-2.

Figure 3.6. Binding data and Western blot analysis (related to Figure 3.4).

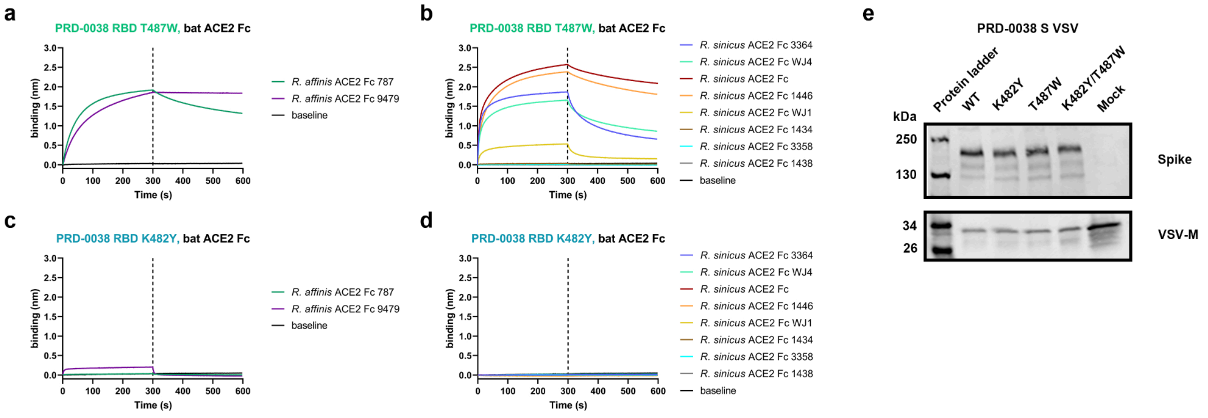

(**a and b**) BLI binding analysis of 1 µM dimeric *R. affinis* (**a**) and *R. sinicus* (**b**) ACE2-Fc alleles to the biotinylated T487W PRD-0038 RBD immobilized on streptavidin biosensors. (**c and d**) BLI binding analysis of 1 µM dimeric *R. affinis* (**c**) and *R. sinicus* (**d**) ACE2-Fc alleles to the biotinylated K482Y PRD-0038 RBD immobilized on streptavidin biosensors. (**e**) Representative Western Blot of wildtype (WT) and mutant PRD-0038 S VSV pseudoviruses normalized based on the amount of incorporated S and VSV-M. Anti-VSV-M Antibody (Kerafast) and Monoclonal ANTI-FLAG® M2 antibody produced in mouse (Sigma) were used as the primary antibody against VSV backbone and S, respectively. Alexa Fluor® 680 AffiniPure Goat Anti-Mouse IgG (Jackson ImmunoResearch) was used as the secondary antibody. iBright™ Prestained Protein Ladder (Invitrogen, LC5615) was used as protein molecular weight markers.

Figure 3.7. Architecture and antigenicity of the PRD-0038 S trimer.

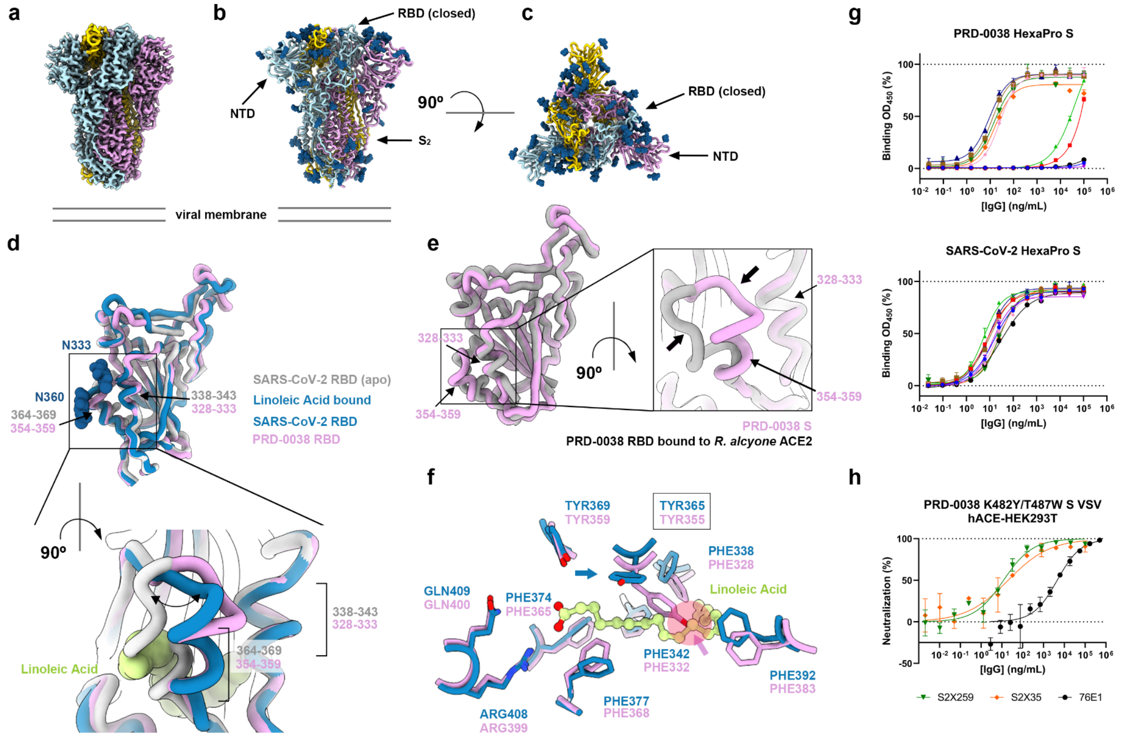

(**a**) Unsharpened cryo-EM map of the closed PRD-0038 S trimer at 2.8 Å resolution. (**b and c**) Ribbon diagram of the PRD-0038 S trimer atomic model viewed along (**b**, side) and normal (**c**, top) to the viral membrane. N-linked glycans are rendered as blue spheres. (**d**) Superimposition of the PRD-0038 S structure described here to the apo (gray, PDB 6VXX (A. C. Walls, Park, et al., 2020)) and linoleic acid-bound (blue, PDB 6ZB5 (Toelzer et al., 2020)) SARS-CoV-2 S structures with a close-up view of the linoleic acid-binding pocket. N-linked glycans at positions N333 and N360 are rendered as blue spheres. (**e**) Superimposition of the PRD-0038 RBDs from the apo S structure (pink) and from the *R. alcyone* ACE2-bound RBD structure (gray). (**f**) Conservation of the SARS-CoV-2 linoleic acid-binding residues in PRD-0038 S. The PRD-0038 S Y355 side chain rotamer (Y365 in SARS-CoV-2 numbering) would sterically hinder linoleic acid binding (semi-transparent red circle denoted with an arrow). (**g**) Evaluation of binding of a panel of monoclonal antibodies to PRD-0038 S Hexapro S and SARS-CoV-2 Hexapro S measured by ELISA. (**h**) Monoclonal antibody-mediated neutralization of PRD-0038 K482Y/T487W S pseudotyped VSV entry into HEK293T cells stably expressing human ACE2.

Figure 3.8. CryoEM data collection and refinement of PRD-0038 S (related to Figure 3.7).

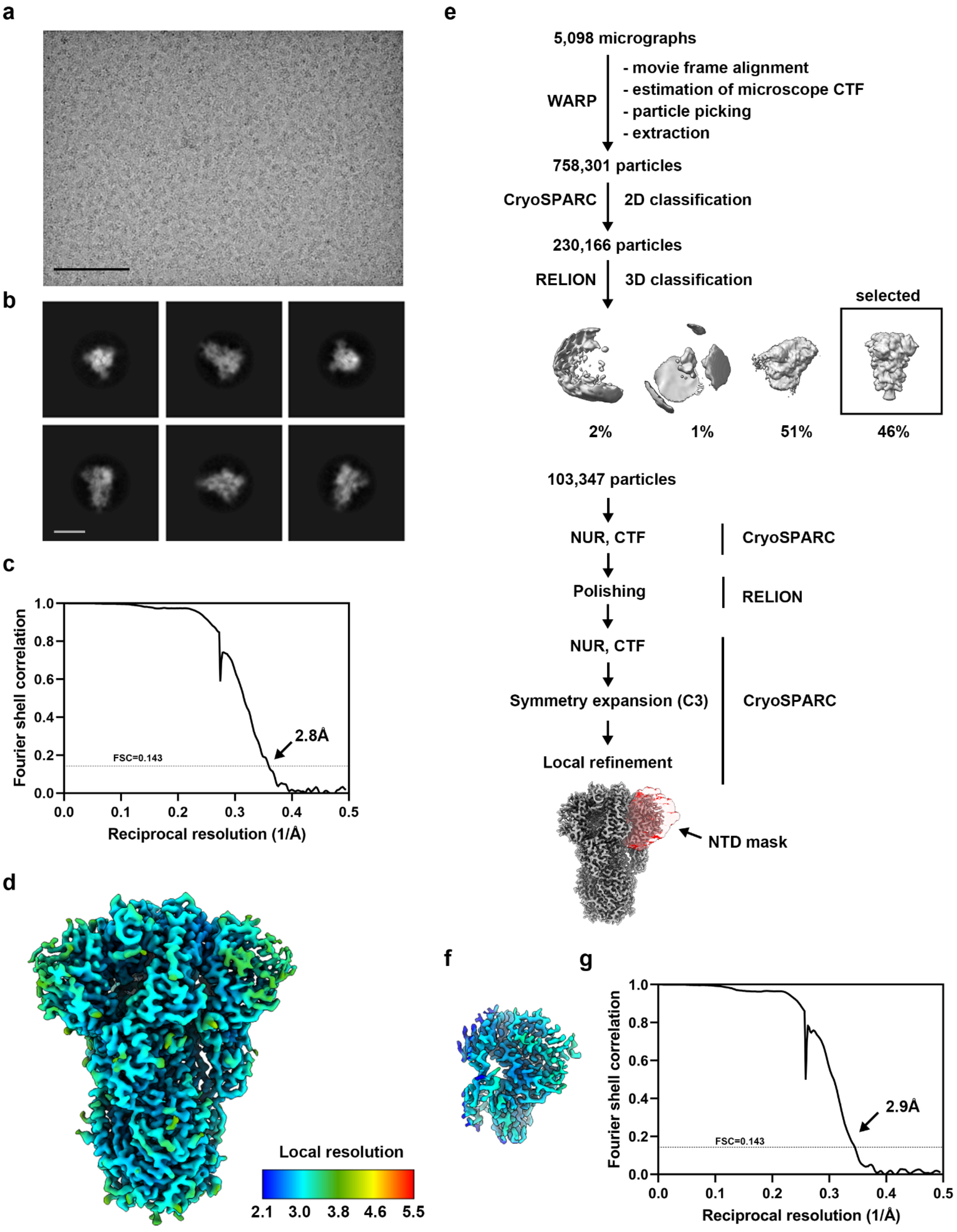

(**a and b**) Representative electron micrograph (**a**) and 2D class averages (**b**) of PRD-0038 PentaPro S embedded in vitreous ice. The scale bar represents 100 nm (**a**) or 100Å (**b**). (**c**) Gold-standard Fourier shell correlation curve for the cryoEM reconstruction. The 0.143 cutoff is indicated with a gray dashed line. (**d**) 3D reconstruction of PRD-0038 PentaPro S colored by local resolution as determined using cryoSPARC. (**e**) Data processing flowchart. CTF: contrast transfer function; NUR: non-uniform refinement. (**f**) 3D reconstruction obtained by local refinement of the PRD-0038 S NTD colored by local resolution as determined using cryoSPARC. (**g**) Gold-standard Fourier shell correlation curve. The 0.143 cutoff is indicated with a gray dashed line.

Figure 3.9. Structural resemblance of PRD-0038 S to SARS-CoV-2 and SARS-CoV-1 (related to Figure 3.7).

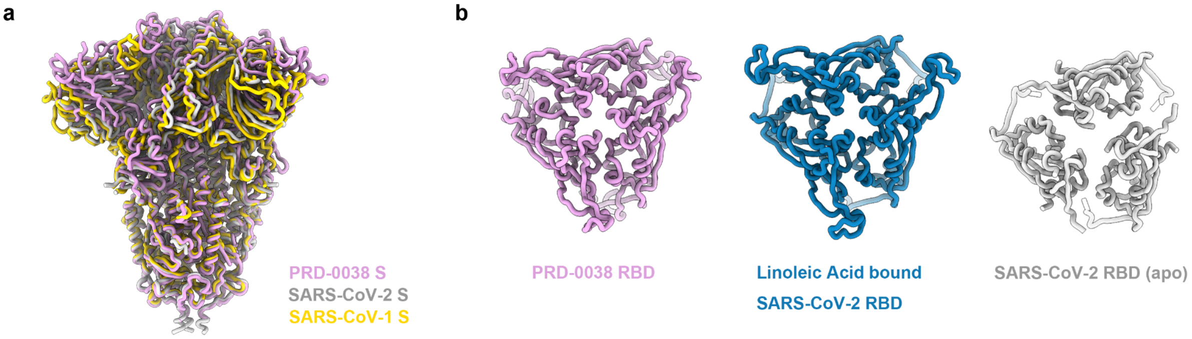

(**a**) Ribbon diagram of the PRD-0038 S trimer superimposed to SARS-CoV-2 S (PDB 6VXX (A. C. Walls, Park, et al., 2020)) and SARS-CoV-1 S (PDB 5X5B (Yuan et al., 2017)) underscoring the similarity of the three trimers which mostly differ due to differences in domain orientation. (**b**) Contact among RBDs within S trimers viewed from the apex along the 3-fold molecular axis of PRD-0038 S (pink), linoleic acid-bound SARS-CoV-2 S (blue, PDB 6ZB5 (Toelzer et al., 2020)), and apo SARS-CoV-2 S (gray, PDB 6VXX (A. C. Walls, Park, et al., 2020)).

Figure 3.10. Conservation analysis of epitopes targeted by monoclonal antibodies between PRD-0038 S and SARS-CoV-2 S (related to Figure 3.7).

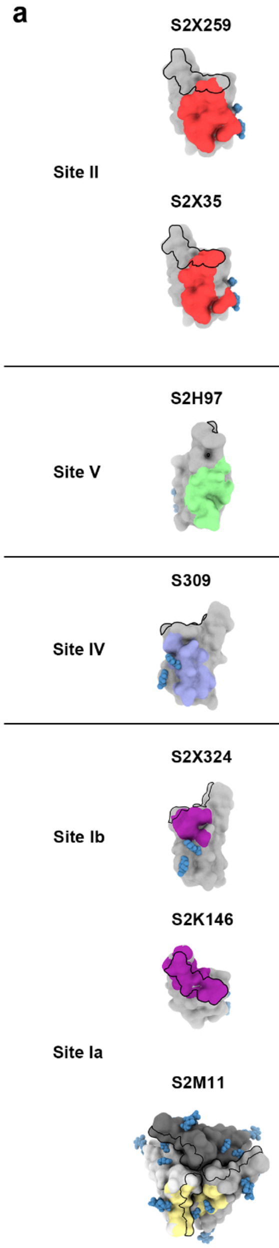

S2X259

	369	370	371	372	373		374	375	376	377	378	379	380	381	382	383	384	385	404	405	407	408
SARS-CoV-2	Y	N	S	A	S		F	S	T	F	K	C	Y	G	V	S	P	T	G	D	V	R
PRD-0038	Y	N	S	S	S	S	F	S	T	F	K	C	Y	G	V	S	P	T	G	D	V	R
	359	360	361	362	363	364	365	366	367	368	369	370	371	372	373	374	375	376	395	396	398	399

	414	437	501	502	503	504	505	506	508
SARS-CoV-2	Q	N	N	G	V	G	Y	Q	Y
PRD-0038	Q	N	V	G	V	G	Y	Q	Y
	405	428	490	491	492	493	494	495	497

S2X35

	369	370	371	372	374	375	376	377	378	379	380	381	382	383	384	385	403	404	405	407	408	496
SARS-CoV-2	Y	N	S	A	F	S	T	F	K	C	Y	G	V	S	P	T	R	G	D	V	R	G
PRD-0038	Y	N	S	S	F	S	T	F	K	C	Y	G	V	S	P	T	K	G	D	V	R	G
	359	360	361	362	365	366	367	368	369	370	371	372	373	374	375	376	394	395	396	398	399	485

	498	500	501	502	503	504	505	508
SARS-CoV-2	Q	T	N	G	V	G	Y	Y
PRD-0038	T	T	V	G	V	G	Y	Y
	487	489	490	491	492	493	494	497

S2H97

	353	355	357	393	394	396	426	427	428	429	430	459	460	462	463	464	465	466	514	515	516	518
SARS-CoV-2	W	R	R	T	N	Y	P	D	D	F	T	S	N	K	P	F	E	R	S	F	E	L
PRD-0038	W	R	R	S	S	Y	P	D	D	F	T	G	K	K	P	Y	E	R	S	F	E	L
	343	345	347	384	385	387	417	418	419	420	421	448	449	451	452	453	454	455	503	504	505	507

	519	520	521
SARS-CoV-2	H	A	P
PRD-0038	N	A	P
	508	509	510

S309

	333	334	335	337	339	340	341	343	344	345	346	354	356	357	358	359	360	361	440	441	444	509
SARS-CoV-2	T	N	L	P	G	E	V	N	A	T	R	N	K	R	I	S	N	C	N	L	K	R
PRD-0038	T	N	L	P	G	Q	V	N	A	S	K	E	L	R	I	S	D	C	S	V	K	R
	323	324	325	327	329	330	331	333	334	335	336	344	346	347	348	349	350	351	431	432	435	498

S2X324

	345	439	440	441	443	444	445	446	447	448	449	450	498	499	500	501	502	506	509
SARS-CoV-2	T	N	N	L	S	K	V	G	G	N	Y	N	Q	P	T	N	G	Q	R
PRD-0038	S	N	S	V	S	K	Q	G	N	N	-	-	T	P	T	V	G	Q	R
	335	430	431	432	434	435	436	437	438	439	-	-	487	488	489	490	491	495	498

S2K146

	403	406	409	417	421	449	452	455	456	473	475	476	477	478	484	485	486	487	488	489	490	492
SARS-CoV-2	R	E	Q	K	Y	Y	L	L	F	Y	A	G	S	T	E	G	F	N	C	Y	F	L
PRD-0038	K	D	Q	V	Y	-	Y	L	F	Y	S	A	G	G	S	Q	L	G	C	Y	E	L
	394	397	400	408	412	-	441	444	445	462	464	465	466	467	473	474	475	476	477	478	479	481

	493	494	496	498	500	501	502	505
SARS-CoV-2	Q	S	G	Q	T	N	G	Y
PRD-0038	K	S	G	T	T	V	G	Y
	482	483	485	487	489	490	491	494

S2M11

	339	342	343	345	367	368	371		372	373	374	436	440	441	444	446	447	449	452	455	456
SARS-CoV-2	G	F	N	T	V	L	S		A	S	F	W	N	L	K	G	G	Y	L	L	F
PRD-0038	G	F	N	S	V	L	S	S	S	S	F	W	S	V	K	G	N	-	Y	L	F
	329	332	333	335	357	358	361	362	363	364	365	427	431	432	435	437	438	-	441	444	445

	483	484	485	486	487	488	489	490	492	493	494	496	498
SARS-CoV-2	V	E	G	F	N	C	Y	F	L	Q	S	G	Q
PRD-0038	T	S	Q	L	G	C	Y	E	L	K	S	G	T
	472	473	474	475	476	477	478	479	481	482	483	485	487

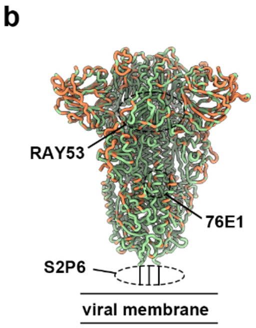

c

S2P6

	1147	1148	1149	1152	1153	1155	1156	1159
SARS-CoV-2	S	F	K	L	D	Y	F	H
PRD-0038	S	F	K	L	D	Y	F	H
	1130	1131	1132	1135	1136	1138	1139	1142

RAY53

	981	982	983	984	985	986	987	988	990	991	992	994	995	998	1001	1002	1005	1006
SARS-CoV-2	L	S	R	L	D	K	V	E	E	V	Q	D	R	T	L	Q	Q	T
PRD-0038	L	S	R	L	D	K	V	E	E	V	Q	D	R	T	L	Q	Q	T
	964	965	966	967	968	969	970	971	973	974	975	977	978	981	984	985	988	989

76E1

	813	814	815	816	818	819	820	822	823	824
SARS-CoV-2	S	K	R	S	I	E	D	L	F	N
PRD-0038	S	Y	R	S	I	E	D	L	Y	N
	796	797	798	799	801	802	803	805	806	807

(**a**) Epitope mapped onto PRD-0038 RBD structure with sequence alignment of key residues at the interface. The PRD-0038 RBD is shown in gray (three RBDs are shown with distinct shades of gray for S2M11 which recognizes a quaternary epitope) and N-linked glycans are rendered as blue spheres. SARS-CoV-2 residue numbering is shown in gray and PRD-0038 residue numbering is shown in pink. The RBM is depicted with a black outline and the monoclonal antibody epitopes are colored according to their antigenic sites (**I**, purple; **II**, red; IV, violet; V, green). (**b**) PRD-0038 S sequence conservation with SARS-CoV-2 S at key S_2 fusion machinery epitopes (indicated with dashed lines). Residues are colored according to sequence identity (orange : not conserved, green : conserved). (**c**) Sequence alignment of corresponding S_2 epitopes. SARS-CoV-2 residue numbering is shown in gray and PRD-0038 residue numbering is shown in pink.

Figure 3.11. A clade 3 sarbecovirus S trimer elicits broadly reactive antibody responses.

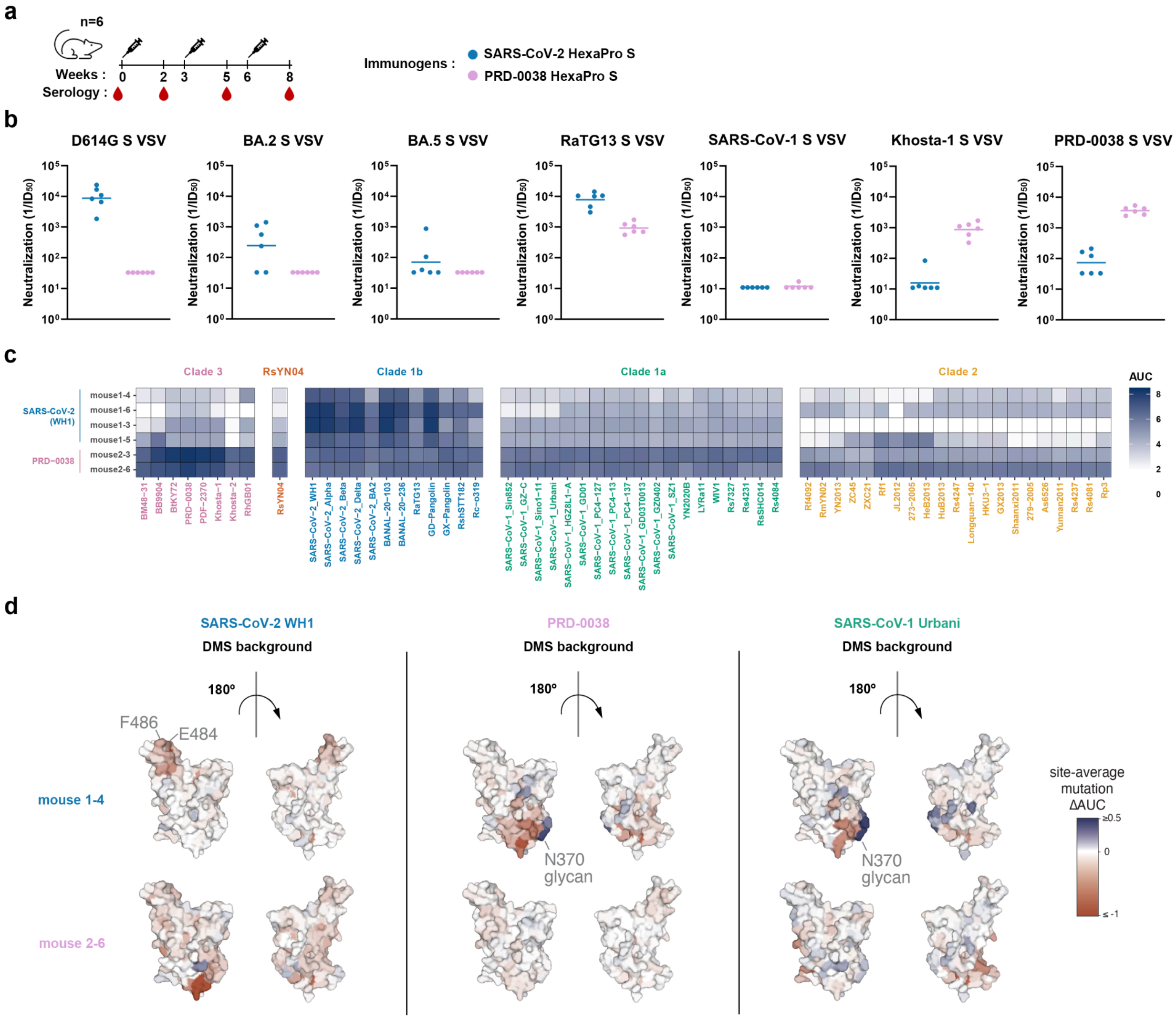

(**a**) Vaccination schedule for the mouse immunogenicity study. (**b**) Serum neutralization of VSV pseudotyped with various sarbecovirus S glycoproteins. Bar represents the geometric mean of each group. (**c**) Sarbecovirus breadth of serum binding to a pan-sarbecovirus library of yeast-displayed RBDs using a high-throughput FACS-seq assay. The strength of binding is represented as a heat map obtained by plotting the area under the curve (AUC) from titration of various serum dilutions. All the binding curves can be accessed at https://github.com/tstarrlab/SARSr-CoV_MAP_PRD0038-vaccine/blob/main/results/summary/compute_AUC.md#plot-all-curves. (**d**) Epitope targeting of serum antibodies. For two representative sera (mouse 1-4, vaccinated with SARS-CoV-2 HexaPro S and mouse 2-6, vaccinated with PRD-0038 HexaPro S), we determined the dominant antibody epitopes via DMS using vaccine-matched and mismatched RBD backgrounds.

The average effect of mutations at each site are mapped to the SARS-CoV-2 structure, where blue and red indicate positions where mutations increase or decrease serum binding, respectively. See **Figure 3.15** for all DMS profiles.

Figure 3.12. Dose-response curves of mouse serum neutralization before and after three immunizations with SARS-CoV-2 HexaPro S or PRD-0038 HexaPro S (related to Figure 3.11).

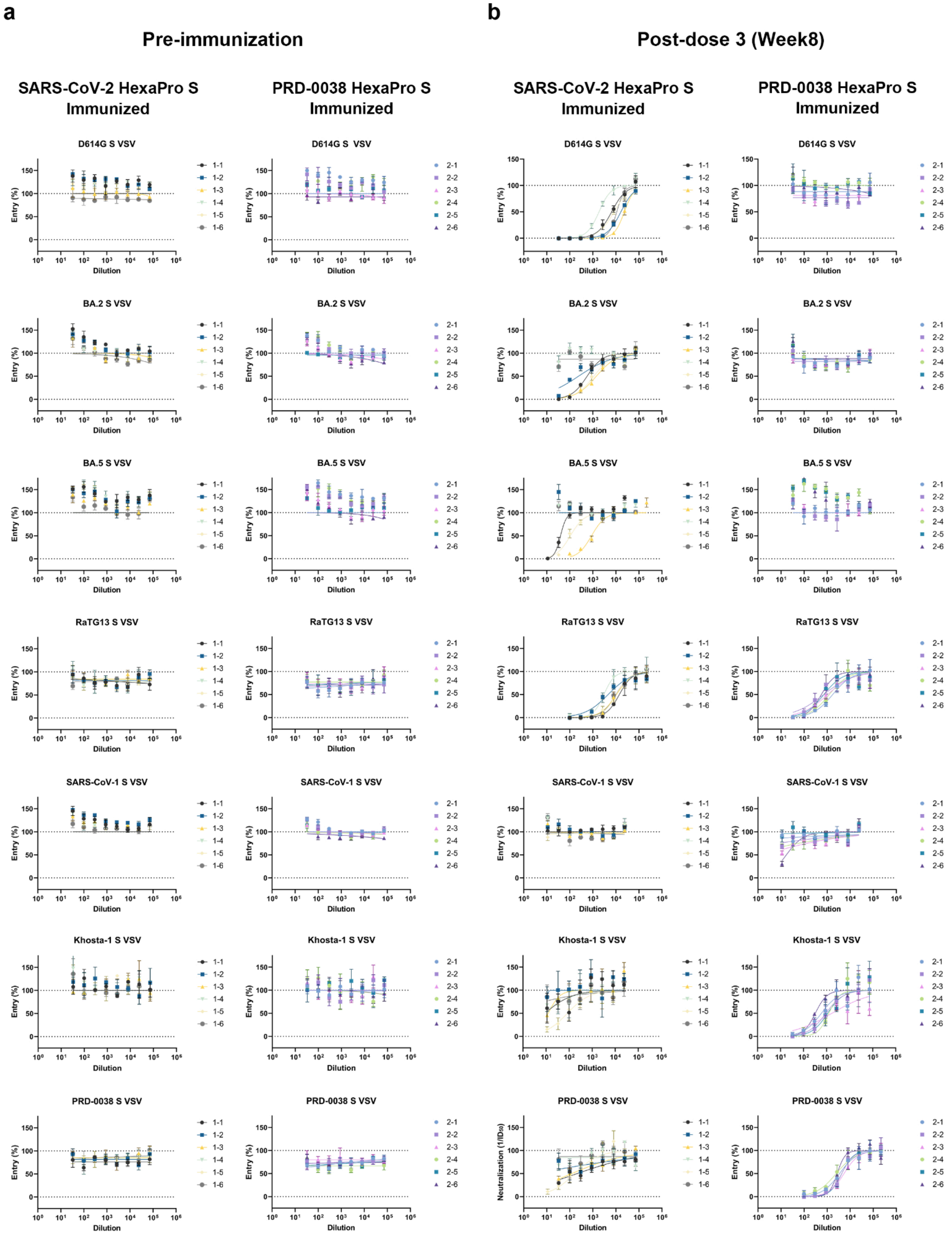

(**a and b**) Neutralization of the indicated sarbecovirus S VSV pseudotypes was assessed for each animal serum before immunization (**a**) and two weeks post dose 3 (week 8) (**b**), as indicated by the color key.

Figure 3.13. Neutralization of SARS-CoV-1 S VSV by vaccine-elicited mouse sera using a highly diluted pseudovirus input (related to Figure 3.11).

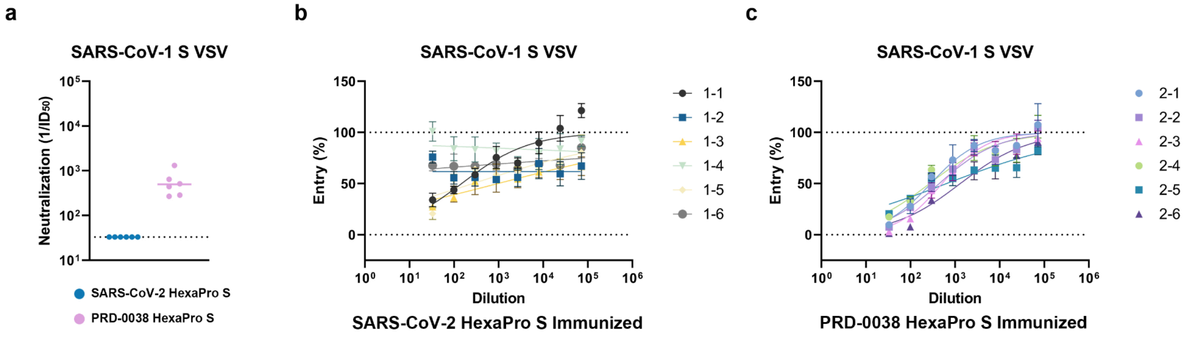

(**a**) Reciprocal ID_{50} value. Bar represents the geometric mean of each group. Limit of detection shown by a dotted line. (**b and c**) Dose-response curves for neutralization of SARS-CoV-1 S VSV by SARS-CoV-2 HexaPro S-elicited sera (**b**) and PRD-0038 HexaPro S-elicited sera (**c**).

Figure 3.14. Binding of vaccine-elicited mouse sera to yeast-displayed sarbecovirus RBDs (related to Figure 3.11).

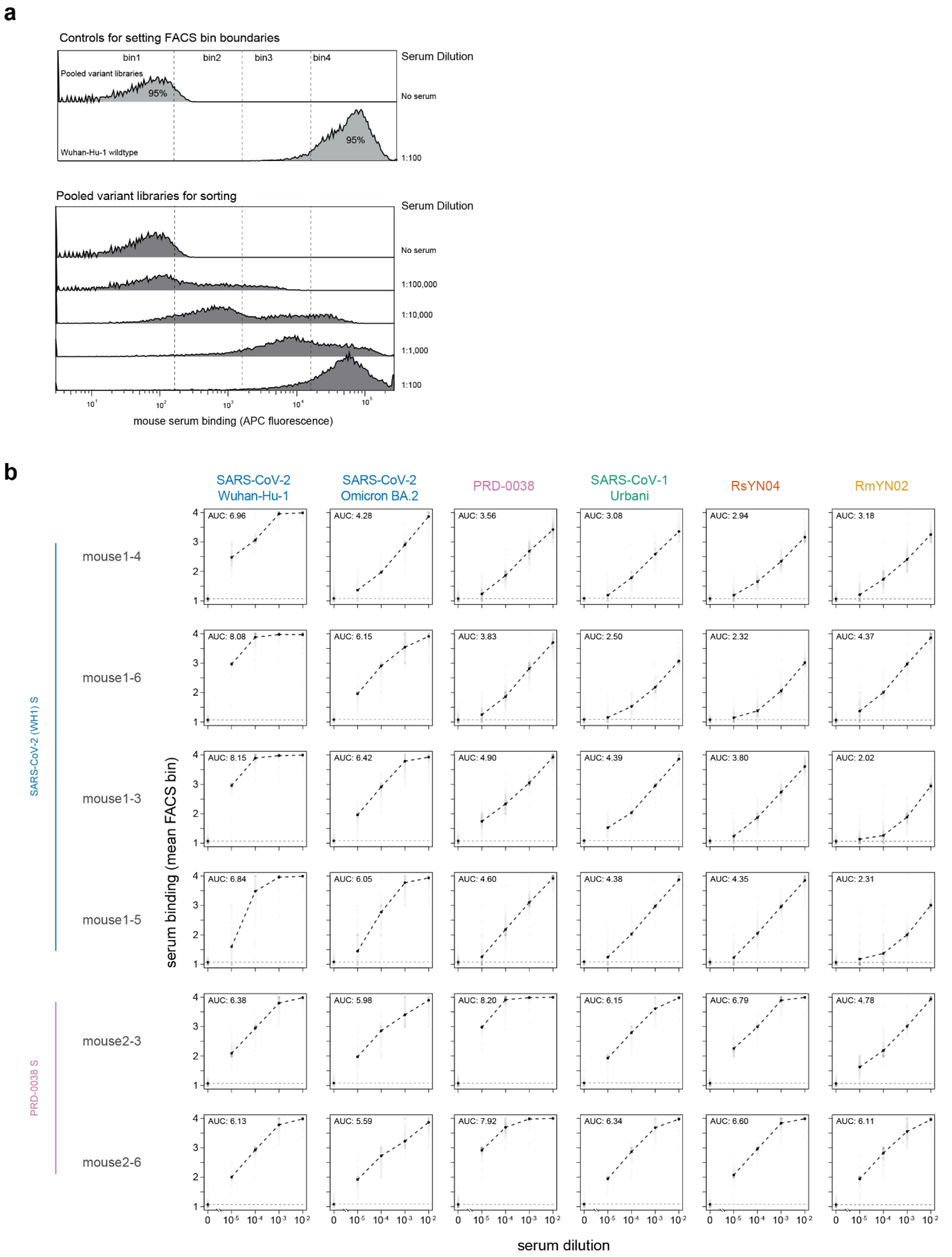

(**a**) Representative flow cytometry traces illustrating FACS binning scheme. Upstream FACS isolate single RBD+ cells via FSC/SSC and FITC(RBD)/FSC gates. Cells were then partitioned into bins based on APC fluorescence (serum binding). Bin 1 captures 95% of zero-serum cells, bin 4 captures 95% of 1:100 serum-labeled wildtype (SARS-CoV-2 Wuhan-Hu-1) control, and bins 2 and 3 split the remaining log-MFI scale evenly. Library samples labeled across a serum dilution series (mouse 1-5 serum traces shown for reference) were sorted into bins of serum-binding and deep sequenced to determine variant counts in each bin, enabling calculation of the "mean bin" into which each barcoded library genotype was sorted at each sample concentration. (**b**) Mean bin values determined from FACS-seq were plotted against serum dilution to generate an Area Under the Curve (AUC) metric (**Figure 3.11c**). Curves underlying AUC calculation for select RBD genotypes are shown. Binding curves for all variants can be accessed at https://github.com/tstarrlab/SARSr-CoV_MAP_PRD0038-vaccine/blob/main/results/summary/compute_AUC.md#plot-all-curves). For each plot, transparent gray dots show the mean bin metric for each internal-replicate library barcode linked to the given RBD, and black points show the mean serum-binding for an RBD averaged across all barcodes. AUC is calculated as the area between the dashed black line and the baseline determined from the zero-serum sample sort (dashed gray line).

Figure 3.15. DMS epitope mapping of serum antibodies (related to Figure 3.11).

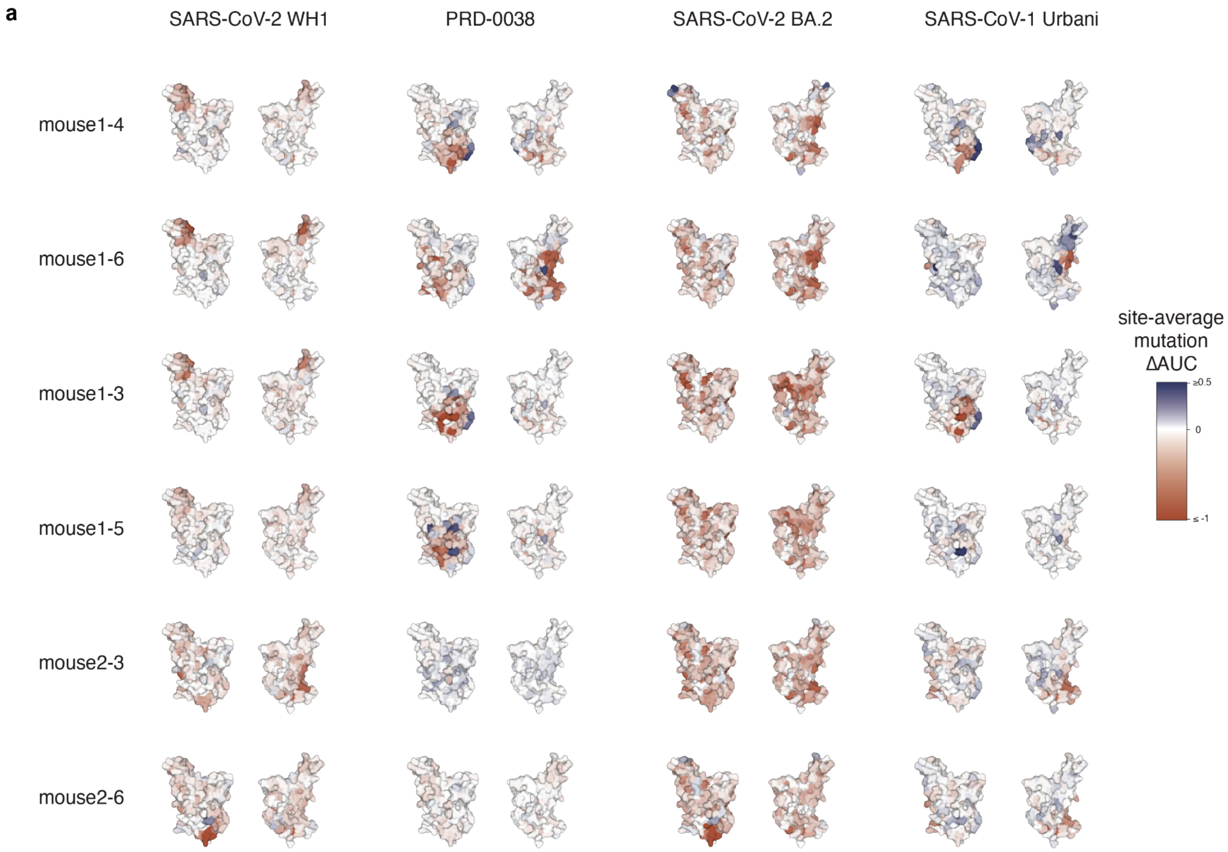

(**a**) Evaluation of epitopes targeted by serum antibodies elicited by SARS-CoV-2 HexaPro S (mouse 1-3, 1-4, 1-5, and 1-6) or PRD-0038 HexaPro S (mouse 2-3 and 2-6) vaccination using yeast-displayed DMS of vaccine-matched and mismatched RBDs (indicated above each column). The average effect of mutations at each site are mapped to the SARS-CoV-2 structure, where blue and red indicate positions where mutations increase or decrease serum binding, respectively.

Table 3.1. *Rhinolophus* ACE2 alleles and contact residues (related to Figure 3.1).

			ACE2-RBD Contact Residues													
Species	**Isolate #**	**Genbank**	**24**	**27**	**30**	**31**	**34**	**35**	**38**	**41**	**42**	**45**	**83**	**330**	**353**	**355**
R. affinis	9479	MT394208.1	R	I	D	N	H	E	D	Y	Q	L	Y	N	K	D
R. affinis	787	MT394203.1	R	I	D	N	R	E	E	Y	Q	L	Y	N	K	D
R. sinicus	3364	MT394200.1	R	I	D	E	S	E	D	Y	K	L	Y	N	K	D
R. sinicus	WJ4	MT394181.1	L	I	D	E	F	E	N	Y	Q	L	Y	N	K	D
R. sinicus	-	GQ262791.1	L	I	D	E	S	E	N	Y	Q	L	Y	N	K	D
R. sinicus	1446	MT394194.1	R	T	D	E	S	E	N	Y	Q	L	Y	N	K	D
R. sinicus	WJ1	MT394187.1	R	I	D	T	S	E	D	Y	Q	L	Y	N	K	D
R. sinicus	1434	MT394197.1	R	M	D	T	S	E	D	Y	Q	L	Y	N	K	D
R. sinicus	3358	MT394193.1	E	M	D	K	T	K	D	H	Q	L	Y	N	K	D
R. sinicus	1438	MT394184.1	E	I	D	K	T	K	D	H	Q	L	Y	N	K	D
R. alcyone	-	KR559016.1	L	I	D	N	S	E	N	H	Q	L	F	N	K	D
R. landeri	-	KR559015.1	L	T	D	D	S	A	N	Y	Q	L	F	N	K	D
R. ferrumequinum	-	XM_033107295.1	L	K	D	F	S	E	N	H	Q	L	F	N	K	D
R. ferrumequinum	-	FJ598617.1	L	T	E	K	T	E	D	Y	Q	L	Y	K	K	D
Human	-	BAB40370.1	Q	T	D	K	H	E	D	Y	Q	L	Y	N	K	D

Table 3.2. CryoEM data collection and refinement statistics (related to Figure 3.4 and 3.7).

	PRD-0038 RBD - *R. alcyone* ACE2 EMD-41786	PRD-0038 RBD - *R. alcyone* ACE2 (Local refinement) PDB 8U0T EMD-41784	PRD-0038 S PDB 8U29 EMD-41842	PRD-0038 S (NTD local refinement) EMD-41843
Data collection and processing				
Magnification	105,000	105,000	105,000	105,000
Voltage (kV)	300	300	300	300
Electron exposure (e^{-}/Å^{2})	60	60	60	60
Defocus range (µm)	0.2 - 3.0	0.2 - 3.0	0.1 - 3.0	0.1 - 3.0
Pixel size (Å)	0.843	0.843	0.843	0.843
Symmetry imposed	C2	C1	C3	C1
Final particle images (no.)	304,806	284,934	103,347	310,041
Map resolution (Å)	3.5	3.2	2.8	2.9
FSC threshold	0.143	0.143	0.143	0.143
Map sharpening *B*factor (Å^{2})	-133	-118	-82.6	-89.7
Validation				
MolProbity score		1.08	1.28	
Clashscore		1.62	1.69	
Poor rotamers (%)		0.47	1.13	
Ramachandran plot				

Favored (%)		**97.02**	**95.44**	
Allowed (%)		**2.86**	**4.38**	
Disallowed (%)		**0.12**	**0.19**	

Table 3.3. Representative K_D values determined from BLI binding analysis (related to Figure 3.4).

	K_D (M)	K_D Error	ka (1/Ms)	ka Error	kdis (1/s)	kdis Error
PRD-0038 WT RBD : monomeric *R. alcyone* ACE2	5.07E-08	1.64E-10	1.64E+05	5.10E+02	8.33E-03	7.80E-06
PRD-0038 T487W RBD : monomeric *R. alcyone* ACE2	2.12E-08	3.96E-11	1.24E+05	2.18E+02	2.62E-03	1.63E-06
PRD-0038 WT RBD : monomeric *R. landeri* ACE2	N.D.	N.D.	N.D.	N.D.	N.D.	N.D.
PRD-0038 T487W RBD : monomeric *R. landeri* ACE2	1.88E-07	4.22E-10	4.49E+04	9.64E+01	8.43E-03	5.62E-06

* N.D. - not determined due to weak binding

CHAPTER 4. A broadly generalizable stabilization strategy for sarbecovirus fusion machinery vaccines

In the following two chapters, I describe our efforts to design vaccine candidates against sarbecoviruses, including the two human coronaviruses, SARS-CoV-1 and SARS-CoV-2, and a clade 3 sarbecovirus, PRD-0038, which was described in the previous chapter. Our target for vaccine design is the highly conserved fusion machineries of sarbecoviruses. First, I detail the design strategy of the vaccine, then I report the vaccine candidate efficacy both *in vitro* and *in vivo*. This chapter outlines the design strategies that are broadly generalizable for sarbecovirus that can be utilized as a pan-sarbecovirus countermeasure and underlines the proof-of-principle works for developing sarbecovirus fusion machinery vaccines.

Adapted from: Lee, J., Stewart, C., Schäfer, A., Leaf, E. M., Park, Y.-J., Asarnow, D., Powers, J. M., Treichel, C., Sprouse, K. R., Corti, D., Baric, R., King, N. P., & Veesler, D. (2024). A broadly generalizable stabilization strategy for sarbecovirus fusion machinery vaccines. *Nature Communications*, *15*(1), 5496. https://doi.org/10.1038/s41467-024-49656-5

4.1 Chapter Introduction

Several COVID-19 vaccines have been authorized worldwide to induce antibody responses targeting the SARS-CoV-2 spike (S) glycoprotein (Corbett et al., 2020; Tian et al., 2021; Walsh et al., 2020). These vaccines enabled safe and effective protection against infection with the Wuhan-Hu-1 (Wu) isolate, which swept the globe at the beginning of the COVID-19 pandemic. However, continued viral evolution led to the emergence of SARS-CoV-2 variants with distinct antigenic properties, relative to previous isolates, eroding neutralizing antibody responses (Cameroni et al., 2022). As a result, breakthrough infections have become common (Levine-Tiefenbrun et al., 2021; Y. Liu et al., 2022; McCallum, Walls, et al., 2021; Mlcochova et al., 2021; Saito et al., 2022) although vaccinated individuals remain protected from severe disease (Addetia et al., 2023a; Y. Cao et al., 2023; Y. Cao, Wang, et al., 2022; Park, Pinto, et al., 2022; A. C. Walls et al., 2022; Yisimayi et al., 2024). Furthermore, the neutralizing activity of monoclonal antibody therapies has been compromised by these antigenic changes, resulting in the withdrawal of their regulatory authorization.

The SARS-CoV-2 S glycoprotein receptor-binding domain (RBD) is targeted by a vast diversity of antibodies and RBD-directed antibodies account for most of the plasma-neutralizing activity against infection/vaccine-matched and mismatched viruses (Bowen, Park, et al., 2022; Greaney et al., 2021; Piccoli et al., 2020). Conversely, the S N-terminal domain (NTD) is mostly targeted by variant-specific neutralizing antibodies (McCallum, Bassi, et al., 2021; McCallum, De Marco, et al., 2021; McCallum, Walls, et al., 2021). The SARS-CoV-2 S_2 subunit (fusion machinery) is much more conserved (**Figure 4.1a, Table 4.1**) than the S_1 subunit (comprising the RBD and NTD), and harbors several antigenic sites targeted by broadly reactive monoclonal antibodies, including the stem helix (Pinto et al., 2021; Sauer et al., 2021; C. Wang et al., 2021), the fusion peptide (Dacon et al., 2022; Low et al., 2022; Sun et al., 2022) and the trimer apex (Silva et al., 2023). Although some of these antibodies have neutralizing activity against a wide range of variants and distantly related coronaviruses, and protect small animals against viral challenge, their potency is limited compared to best-in-class RBD-directed antibodies (Y. Cao, Jian, et al., 2022; Park, De Marco, et al., 2022; Tortorici et al., 2020; P. Zhou et al., 2022, 2023). Furthermore, fusion machinery-directed antibodies are rare in the plasma and memory B cells of previously infected and/or vaccinated subjects and have limited contribution to neutralization mediated by polyclonal antibodies (Bowen, Park, et al., 2022; Pinto et al., 2021; P. Zhou et al., 2022). Therefore, vaccines enabling to overcome this challenge through elicitation of high titers of neutralizing antibodies targeting the conserved S_2 subunit bear the promise to limit the need for vaccine updates.

Here, we set out to design a prefusion-stabilized SARS-CoV-2 S_2 subunit vaccine enabling robust elicitation of antibodies targeting conserved fusion machinery antigenic sites to limit the impact of viral evolution on immune responses. Coronavirus S glycoproteins fold as spring-loaded trimers transitioning from the prefusion to the postfusion state, upon receptor engagement and proteolytic activation to promote membrane fusion and viral entry (A. C. Walls et al., 2016, 2017, 2019). This metastability, however, constitutes a challenge for producing the S_2 subunit (fusion machinery) in the prefusion state in the absence of the S_1 subunit. Prior work described prefusion-stabilizing mutations improving the biophysical properties of the S ectodomain trimer (Hsieh et al., 2020; Kirchdoerfer et al., 2018; Olmedillas et al., 2021; Pallesen et al., 2017; A. C. Walls, Park, et al., 2020; Wrapp et al., 2020). Furthermore, we previously designed a fusion machinery (S_2 subunit) antigen (Bowen, Park, et al., 2022) stabilized through the introduction of 4 out of 6 HexaPro mutations (A892P, A899P, A942P and V987P) (Hsieh et al., 2020), the VFLIP inter-protomer disulfide (Y707C-T883C) (Olmedillas et al., 2021), an intra-protomer disulfide (F970C-G999C) and a C-terminus foldon trimerization domain (**Figure 4.1a**). The resulting construct (designated C-44) harbored protomers with a prefusion tertiary structure but a quaternary structure in which the viral membrane distal region (apex) was splayed open compared to prefusion SARS-CoV-2 S (Bowen, Park, et al., 2022) (**Figure 4.1b**). To design a prefusion S_2 subunit trimer with native quaternary structure, we identify a set of mutations allowing high-yield recombinant production of fusion machinery trimers with native prefusion architecture and antigenicity that remained stable in various storage conditions, as revealed through structural and antigenic studies. We further show that the prefusion-stabilization strategy designed is broadly generalizable to sarbecovirus S_2 subunits and successfully ported the identified mutations to the SARS-CoV-1 and PRD-0038 fusion machinery. Immunization of mice with a designed SARS-CoV-2 fusion machinery trimer vaccine elicits broadly reactive sarbecovirus antibodies and neutralizing antibody titers of comparable magnitude against the Wu and the immune evasive XBB.1.5 variant. Vaccinated mice were protected from weight loss and disease upon challenge with SARS-CoV-2 XBB.1.5 motivating further development of this vaccine.

4.2 Design of prefusion-stabilized SARS-CoV-2 S_2 subunit vaccines

To design a prefusion S_2 subunit trimer with a native quaternary structure, we selected mutations from a deep-mutational scanning dataset of cell-surface expressed S using a library spanning residues 883 to 1034 (T. J. C. Tan et al., 2023). Mutations were ranked according to their expression/fusion score ratio, to favor prefusion-stabilizing amino acid substitutions and visually inspected to lead to a final selection of ten mutations (**Figure 4.1a, Table 4.2**). We first evaluated the effect of three individual mutations introduced in the C-44 background, namely T961F, D994E, and Q1005R, which were among the highest ranking based on their expression/fusion score ratio.We recombinantly produced each of the three constructs (designated E-31, E-32 and E-33 for the T961F, D994E and Q1005Rmutations, respectively) in human cells and characterized their monodispersity by size-exclusion chromatography (SEC). Residue 961 is part of the heptad repeat 1 (HR1) motif whereas residues 994 and 1005 are located in the central helix (CH) (A. C. Walls et al., 2016, 2017; A. C. Walls, Park, et al., 2020). All three constructs eluted mainly as monodisperse species, yielding 40-60mg of purified protein per liter of Expi293 cells (**Figure 4.1c,d**). Single-particle electron microscopy (EM) characterization of each negatively stained glycoprotein revealed that the design harboring the T961F mutation (E-31) formed prefusion closed S_2 trimers whereas the other two constructs, harboring either D994E (E-32) or Q1005R (E-33), adopted several conformations, including one with a splayed-open apex (**Figure 4.2**) similar to C-44 (Bowen, Park, et al., 2022). Furthermore, we observed a higher tendency to aggregate for E-32 and E-33 by SEC and EM (**Figures 4.1c and 4.2**). To unveil the E-31 architecture and understand the effect of the T961F mutation, we determined a cryoEM structure of this antigen at 2.7 Å resolution (**Figures 4.1e, 4.3 and Table 4.3**). Our structure shows that E-31 folds with virtually identical tertiary and quaternary structures to the S_2 subunit from the prefusion S ectodomain trimer (PDB 6VXX (A. C. Walls, Park, et al., 2020)) with which the protomers can be superimposed with r.m.s.d values of 0.7 Å. The engineered T961F substitution, which maps to the distal half of the fusion machinery apex, reinforces interactions between HR1 and the central helix of one protomer and the upstream helix of a neighboring protomer (cavity filling), likely explaining the compact, closed trimer conformation observed (**Figure 4.4a**). Although we could detect a small fraction of E-31 trimers with an open apex conformation in the cryoEM dataset, our findings demonstrate that the T961F mutation alone is sufficient to close the fusion machinery apex in a prefusion conformation (**Figures 4.1e, 4.3**).

To further improve the conformational homogeneity of our vaccine candidate, we designed two additional constructs comprising either 4 or 9 additional residue substitutions added to the E-31 trimer (**Table 4.2**). Both constructs were recombinantly produced to characterize their expression, stability, and structural properties (**Figure 4.1c, d**). The E-60 construct harbors all 9 additional mutations we selected to add to the E-31 scaffold. Although recombinant production of this protein construct led to high expression levels, its cryoEM structure at 3.5 Å resolution (**Figure 4.5, Table 4.3**) revealed that the introduction of several proline mutations in the region comprising residues 879-897 distorted an α-helix and following loop relative to its native structure (**Figure 4.4b**). Ruling out conformation distorting-mutations and a few additional mutations based on visual inspection, we designed a new construct which we named E-69 and harbors the N907E, D994Q, Q1011M and I1018Y in the E-31 background. To investigate its atomic-level organization, we determined a cryoEM structure of E-69 at 3 Å resolution and observed clear cryoEM density defining side chains of most amino acid mutations introduced and confirming folding as a prefusion closed S_2 subunit trimer, without particle images corresponding to trimers with an open apex (**Figures 4.1f and 4.6**). The overall E-69 architecture is nearly identical to that of the S_2 subunit trimer from the prefusion S ectodomain structure (PDB 6VXX (A. C. Walls, Park, et al., 2020)) (**Figure 4.1f**). Only one region noticeably deviated from prefusion S in terms of local structure downstream of the fusion peptide (residues 833-855) (**Figures 4.1f and 4.4c**). In the intact SARS-CoV-2 S trimer, this region makes contact with the S_1 subunit C and D domains of a neighboring protomer, which are absent in our design, likely allowing adoption of an altered local conformation, as is the case in all our constructs (**Figure 4.4c**). The N907E substitution places the newly introduced side chain carboxylate close to the Q913 side chain amide with which it interacts electrostatically (**Figure 4.1g**). The D994Q side chain amide forms an intraprotomer hydrogen bond with the Q755 side chain amide and an interprotomer electrostatic interaction with the R995 guanidinium, thereby strengthening interactions at the distal part of the apex (**Figure 4.1g**). The Q1011M mutation is likely stabilizing through the reinforcement of local hydrophobic packing with the nearby M731 and Y1007 residues (**Figure 4.1g**). The I1018Y mutation fills a cavity within each protomer through local interactions involving the CH, HR1, and upstream helix region (**Figure 4.1g**).

As our E-69 structure did not resolve the flexible N-terminal region, which connects the S_1 and S_2 subunits in the context of the S trimer, we designed a new construct lacking 15 residues at the N-terminus of E-69 and named it F-53 (**Figure 4.1c, d, Table 4.2**). F-53 expressed better than E-69 and retained identical antigenicity, and thus served as a template for subsequent S_2 antigen design (**Figure 4.7**).

4.3 A stable prefusion-stabilized SARS-CoV-2 fusion machinery antigen

Storage and shipping conditions are important considerations for vaccine design and manufacturing as they can impact the cost of goods, ease of distribution and in turn global access. To evaluate the stability of the prefusion-stabilized SARS-CoV-2 E-69 design, we investigated the retention of antigenicity after storage in various conditions by ELISA using a panel of monoclonal antibodies targeting the S_2 subunit (**Figure 4.8a, b**). The stem helix-targeting S2P6 antibody (Pinto et al., 2021), the fusion peptide-directed 76E1 antibody (Sun et al., 2022), and the fusion machinery apex-recognizing RAY53 (Silva et al., 2023) bound to E-69 (**Figure 4.8a-c**), as was the case with SARS-CoV-2 S. E-69 retained unaltered antigenicity for at least two weeks at room temperature and at 4°C, and could be frozen and thawed without affecting its antigenicity (**Figures 4.8c and 4.9**). To assess biophysical stability, we analyzed purified E-69 at various time points using negative staining EM. 2D class averages of E-69 showed retention of its prefusion conformation for at least two weeks both at room temperature and at 4°C and that it could be frozen and thawed without altering its structure (**Figure 4.8d-i**). Although we detected a minor population of trimers with an open apex upon storage at low temperatures (**Figure 4.8g-i**), the 2D class averages suggested that the magnitude of these structural changes might be smaller than that observed with the C-44, E-32 or E-33 designed constructs (**Figures 4.1b, 4.2c, 4.2d**). Furthermore, we did not detect any 2D class averages corresponding to open trimers in our E-69 cryoEM dataset (**Figure 4.6**). These data suggest that the E-69 design is stable, highlighting the robustness of our prefusion stabilization strategy, and endowed with optimal biophysical properties for a vaccine candidate.

4.4 A broadly generalizable prefusion-stabilization strategy for sarbecovirus fusion machinery immunogens

To assess the broad applicability of our S_2 subunit prefusion stabilization strategy, we examined the local structural environment of the residues mutated in E-69 and compared it with the corresponding regions of interest in SARS-CoV-1 S_2 (clade 1a) and PRD-0038 S_2 (clade 3) (Lee et al., 2023). The overall architecture of the SARS-CoV-1 S_2 and PRD-0038 S_2 trimers is similar to that of SARS-CoV-2 S_2 with which they can be superimposed with r.m.s.d. values of 1.1 and 1.3 Å, and share 90% and 87% amino acid sequence identity, respectively. Based on the observed conservation of the local structural environment, we hypothesized that the E-69 mutations should be portable to SARS-CoV-1 S_2 and to PRD-0038 S_2 and designed the corresponding constructs (**Figure 4.10a-i**). We additionally truncated the N-terminal region of the prefusion-stabilized SARS-CoV-1 S_2 and PRD-0038 S_2 constructs due to the enhanced expression of SARS-CoV-2 F-53 relative to E-69 (**Figure 4.1c, d**). Finally, we introduced the V940Q substitution to the PRD-0038 S_2 construct,which is the position equivalent to SARS-CoV-2 Q957 and SARS-CoV-1 Q939, to allow electrostatic interaction with R748 (similar to that observed with SARS-CoV-2 R765 and SARS-CoV-1 R747 from a neighboring protomer) (**Figure 4.10d**).

Recombinant production and purification of the designed SARS-CoV-1 and PRD-0038 S_2 subunit constructs led to even greater yields than that of SARS-CoV-2 F-53, reaching 50mg of purified SARS-CoV-1 S_2 trimer per liter of Expi293 cells (**Figure 4.10j, k**). These two trimers were stable in a variety of storage conditions and retained unaltered reactivity with fusion machinery-directed monoclonal antibodies for at least two weeks at room temperature and at 4°C and could be frozen and thawed without affecting their antigenicity (**Figures 4.10l, m, and 4.11**). Although the RAY53 and S2P6 antibodies each cross-reacted with comparable efficiency to the SARS-CoV-1 S_2 trimer and to the PRD-0038 S_2 trimer, 76E1 bound efficiently to SARS-CoV-1 S_2 but much more weakly to PRD-0038 S_2, possibly as a result of the $F823_{\text{SARS-CoV-2}}Y806_{\text{PRD-0038}}$ epitope mutation (Lee et al., 2023) (**Figure 4.10l, m**). Single particle EManalysis of negatively stained SARS-CoV-1 S_2 and PRD-0038 S_2 showed that they adopt the designed closed prefusion architecture (**Figure 4.10n, o**). Collectively, these data indicate that our S_2 prefusion stabilization strategy is broadly applicable across different sarbecovirus clades and promotes retention of native structure and antigenicity over time under various storage conditions.

4.5 A prefusion-stabilized SARS-CoV-2 fusion machinery vaccine elicits broadly reactive antibody responses

To evaluate the immunogenicity of our lead prefusion SARS-CoV-2 S_2 designed vaccine candidate, we immunized twelve BALB/c mice with four 5 μg doses of E-69 on weeks 0, 3, 10 and 17 and twelve BALB/c mice with two 1 μg doses of prefusion SARS-CoV-2 2P S on weeks 0 and 3 followed by two 5 μg doses of E-69 on weeks 10 and 17. The latter group aims to recapitulate the pre-existing immunity found in humans due to prior exposures through vaccination and/or infection. For benchmarking, we also immunized twelve BALB/c mice with four 1 μg doses of prefusion SARS-CoV-2 2P S on weeks 0, 3, 10, and 17 (**Figure 4.12a**). All immunogens were adjuvanted with Addavax using a 1:1 (v/v) ratio.

Binding antibody titers were analyzed by ELISA using sera obtained two weeks post dose 4 (week 19) against SARS-CoV-2 Wu HexaPro S, SARS-CoV-2 XBB.1.5 HexaPro S, and SARS-CoV-1 HexaPro S (**Figures 4.12b-d and 4.13**). We observed similar prefusion SARS-CoV-2 Wu S and XBB.1.5 S antibody binding titers upon immunization with E-69 (GMT: 5.2/4.9), SARS-CoV-2 2P S (GMT: 5.2/5.0) or SARS-CoV-2 2P S followed by E-69 (GMT: 5.4/5.0). However, we observed slightly higher SARS-CoV-1 S binding titers with the E-69 (GMT: 5.2) or SARS-CoV-2 2P S followed by E-69 (GMT: 5.0) vaccination regimens, as compared to SARS-CoV-2 2P S immunization (GMT: 4.5). These results suggest that E-69 vaccination elicits comparable serum antibody binding titers after four doses to the widely used prefusion 2P S trimer against SARS-CoV-2 variants but slightly higher titers against SARS-CoV-1 in these experimental conditions. ELISA analysis of vaccine-elicited serum antibodies five weeks post dose 4 (week 22) targeting SARS-CoV-2 E-69 showed that immunization with E-69 or with E-69 followed by SARS-CoV-2 2P S (GMTs: 4.9/4.8) led to slightly higher IgG binding titers than SARS-CoV-2 2P S immunization (GMT: 4.4), providing proof-of-principle for specific elicitation of fusion machinery-directed antibodies (**Figure 4.14**). Moreover, E-69 vaccination elicited a broad spectrum of IgG subclasses, including IgG1, IgG2a and IgG2b, that was comparably balanced to that induced by SARS-CoV-2 2P S vaccination (**Figure 4.14**).

We subsequently evaluated vaccine-elicited neutralizing activity using sera obtained two weeks post dose 4 (week 19) and vesicular stomatitis virus (VSV) particles pseudotyped with SARS-CoV-2 Wu/G614, XBB.1.5 S or SARS-CoV-1 S (**Figures 4.12e-g and 4.15**). SARS-CoV-2 2P S or SARS-CoV-2 2P S followed by E-69 vaccination elicited potent neutralizing antibodies against the vaccine-matched SARS-CoV-2 Wu/G614 whereas E-69 elicited modest neutralizing activity. SARS-CoV-1 S VSV neutralization was highest upon vaccination with SARS-CoV-2 2P S and comparably lower for the groups vaccinated with E-69 or SARS-CoV-2 2P S followed by E-69. Neutralization of XBB.1.5 VSV S, however, was marginally higher for mice vaccinated with E-69 or with SARS-CoV-2 2P S followed by E-69 as compared to vaccination with SARS-CoV-2 2P S.

4.6 A prefusion-stabilized SARS-CoV-2 fusion machinery vaccine protects against the SARS-CoV-2 XBB.1.5 variant

To study the in vivo protective efficacy of the designed fusion machinery SARS-CoV-2 vaccine against an immune evasive SARS-CoV-2 variant, we intranasally inoculated each animal in the three aforementioned vaccinated groups of mice with 10^5 PFU of XBB.1.5 MA10 (Leist et al., 2020) (**Figure 4.12a**).We also challenged 10 unvaccinated mice as a control group. Weight loss was followed for 4 days post infection (**Figure 4.16a**) whereas replicating viral titers in the nasal turbinates and lung as well as lung pathology were assessed at 2 and 4 days post challenge (**Figure 4.16b-d**). Although none of the immunogens evaluated protected from infection, likely due to the systemic delivery route (T. Mao et al., 2022; Oh et al., 2021; Park, Pinto, et al., 2022; Tang et al., 2022), all vaccinated mice had markedly reduced weight loss throughout the duration of the experiment, as compared to unvaccinated mice (**Figure**

4.16a, b). Furthermore, lung viral load and lung pathology were comparable for all three vaccinated groups and greatly improved compared to unvaccinated animals (**Figure 4.16c, d**). These data indicate that vaccination with our lead prefusion-stabilized SARS-CoV-2 S_2 subunit (fusion machinery) immunogen elicited protection against disease induced by the highly immune evasive SARS-CoV-2 XBB.1.5 variant in this stringent challenge model.

4.7 Chapter Discussion

The emergence of immune evasive SARS-CoV-2 variants erodes the effectiveness of COVID-19 vaccines, which led to the roll out of two updated boosters in 2022 (Chalkias et al., 2022; Scheaffer et al., 2023) and 2023 (Chalkias et al., 2023). For the foreseeable future, it is likely that COVID-19 vaccines will require yearly reformulation based on the anticipated prevalence of circulating variants, similarly to influenza virus vaccines. Next-generation vaccines that are more resilient to viral evolution and antigenic changes bear the promise of reducing the need for or the frequency of vaccine updates, which would also help with large-scale adoption by the public. The sarbecovirus S_2 subunit prefusion-stabilization strategy presented here represents a key step in this direction due to the much higher conservation of the S_2 subunit relative to the S_1 subunit among SARS-CoV-2 variants and other sarbecoviruses (Addetia et al., 2023a; McCallum et al., 2022; A. C. Walls, Park, et al., 2020). Given the limited potency of known fusion machinery-directed monoclonal antibodies (Low et al., 2022; Pinto et al., 2021; Sauer et al., 2021; Silva et al., 2023; Sun et al., 2022), relative to S_1-targeting antibodies, the plasma neutralizing activity induced by SARS-CoV-2 S_2 vaccination was weaker than that of prefusion 2P S although its breadth was much less affected by antigenic changes. In vivo evaluation of vaccine efficacy suggests that SARS-CoV-2 S_2 protected mice comparably to prefusion 2P S, based on weight loss and viral replication in the upper and lower airways, upon challenge with the immune evasive SARS-CoV-2 XBB.1.5 variant in these experimental conditions.

We note that SARS-CoV-2 S_2 subunit vaccination protected mice that did and those that did not have detectable serum neutralizing activity against SARS-CoV-2 XBB.1.5, as observed for stabilized MERS-CoV stems upon MERS-CoV challenge (Hsieh et al., 2021). Although the immunological mechanisms underlying the observed protection remain to be defined, we postulate that weakly or non-neutralizing antibodies participated in protection through Fc-mediated effector functions, as described for the S2P6 stem-helix antibody (Pinto et al., 2021) and for S-elicited fusion machinery directed polyclonal antibodies upon mismatched sarbecovirus challenge (Adams et al., 2023). Future studies will decipher the contribution of these distinct branches of the immune response to the protection observed.

The broadly generalizable prefusion-stabilization strategy described here provides a robust platform for elicitation of fusion machinery-directed antibody responses and the designed antigens will enable studies of such immune responses. Future engineering efforts may further improve the immunogenicity of this vaccine candidate through (i) multivalent display at the surface of a nanoparticle, as exemplified for the SKYcovione SARS-CoV-2 RBD vaccine (Arunachalam et al., 2021; J. Y. Song et al., 2022; A. C. Walls, Fiala, et al., 2020); (ii) mRNA-launching of a membrane-anchored

SARS-CoV-2 S_2 subunit vaccine, a vaccine platform which yielded multiple efficacious SARS-CoV-2 S 2P vaccines (Corbett et al., 2020); or (iii) a recently proposed targeted deglycosylation approach of the SARS-CoV-2 S_2 subunit to enhance neutralizing antibody titers (Cheng et al., 2023).

4.8 Methods

Cell lines

Cell lines used in this study were obtained from HEK293T (ATCC, CRL-11268), Expi293F (Thermo Fisher Scientific, A145277) and VeroE6-TMPRSS2 (JCRB1819). Cells were cultured in 10% FBS, 1% penicillin-streptomycin, 2% Geneticin (applicable for Vero cells, only) DMEM at 37°C, 5% CO_2. None of the cell lines were authenticated or tested for mycoplasma contamination.

Production of recombinant S_2 antigen proteins

Each S_2 construct was produced in Expi293F cells (ThermoFisher Scientific) and cultured at 37°C in a humidified 8% CO_2 incubator with constant rotation at 130 RPM using Expi293 Expression Medium (ThermoFisher Scientific). DNA transfections were conducted using the ExpiFectamine 293 Transfection Kit (ThermoFisher Scientific) protocols and materials and cultivated for five days before harvest. Cell culture supernatants were clarified by centrifugation and proteins were harvested using HisTrap™ High Performance Ni Sepharose columns (Cytiva). Proteins were washed using 10-15 CVs of buffer containing 25mM Tris, 150mM NaCl, 20mM Imidazole pH 8.0 followed by elution with 10-15 CVs of buffer containing 25mM Tris, 150mM NaCl, 300mM Imidazole pH8.0. Eluates were buffer exchanged and concentrated into 20mM Tris, 150mM NaCl, pH 8.0 using Amicon Ultra-15 Centrifugal Filter Unit (10 kDa) (Millipore). Gel filtration was performed to remove unfolded or aggregated protein thus samples were each run through a Superose-6 Increase 10/300 GL column (Cytiva)) equilibrated in 20mM Tris, 150mM NaCl, pH8.0. Main peaks were collected and protein was snap-frozen and stored at -80°C with some set aside for stability tests. Purified proteins for immunogenicity study were tested for endotoxin levels using Limulus Amebocyte Lysate (LAL) cartridges (Charles River PTS201F).

Production of recombinant SARS-CoV-2 2P S, HexaPro S and SARS-CoV-1 HexaPro S

The SARS-CoV-2 2P S glycoprotein ectodomain construct was previously described (A. C. Walls, Park, et al., 2020) and comprised an abrogated S_1/S_2 cleavage site (R682S, R683G and R685G) (Tortorici et al., 2019; A. Walls et al., 2017; A. C. Walls et al., 2016, 2019), two consecutive proline stabilizing mutations (K986P and V987P, so called 2P (Kirchdoerfer et al., 2018; Pallesen et al., 2017)) and a C-terminal foldon trimerization domain (Miroshnikov et al., 1998). The SARS-CoV-2 HexaPro S glycoprotein ectodomain construct comprises residues 1-1208 with the native signal peptide, the HexaPro prefusion stabilizing mutations (F817P, A892P, A899P, A942P, K986P, V987P), abrogation of the S_1/S_2 cleavage site (R682G, R683S and R685S), a C-terminal short linker (GSG) followed by a foldon, HRV 3 C site (LEVLFQGP), a short linker (GSG), an avi tag, a short linker (GSG), an 8x his tag in a pcDNA3.1(-) plasmid (Hsieh et al., 2020). The SARS-CoV-1 HexaPro S glycoprotein ectodomain construct comprises residues 1-1190 (UniProt P59594-1) with the native signal peptide, the

HexaPro prefusion stabilizing mutations (F799P, A874P, A881P, S924P, K968P, V969P) followed by a C-terminal short linker (GSG) followed by a foldon, HRV 3 C site (LEVLFQGP), an avi tag, a short linker (GSG), an 8x his tag in a CMVR plasmid. Expi293F cells were grown at 37°C with 8% CO_2 and DNA transfections were conducted with the ExpiFectamine 293 Transfection Kit (Thermo Fisher Scientific). Cell culture supernatants were harvested four days post-transfection and proteins were purified using HisTrap™ High Performance column (Cytiva). Proteins were first washed with 10-15 column volumes of a buffer containing 25mM sodium phosphate, 300mM NaCl, 20mM imidazole, pH8.0, followed by elution with 10-15 column volumes using 300mM imidazole, pH 8.0. Eluted proteins were concentrated and buffer exchanged into 1x TBS (20mM Tris, 150mM NaCl, pH 8.0) using Amicon Ultra-15 Centrifugal Filter Unit (100 kDa) (Millipore). Purified proteins were snap-frozen and stored at -80°C. SARS-CoV-2 2P S proteins for immunogenicity study were tested for ensuring low endotoxin levels using Limulus Amebocyte Lysate (LAL) cartridges (Charles River PTS201F).

Monoclonal antibody ELISAs

For monoclonal antibody ELISAs, 30 μl of the proteins at 3 μg/mL were plated onto 384-well Nunc Maxisorp plate (ThermoFisher, 464718) in 1x TBS and incubated 1 h at 37°C followed by slap drying and blocking with 80 μL of Casein for 1 h at 37°C. After incubation, plates were slapdried and 1:4 serial dilutions of the corresponding mAbs starting from 0.1mg/ml were made in 30 μl TBST, added to the plate and incubated at 37°C for 1 h. Plates were washed 4x in TBST and 30 μl of 1:5000 Goat anti-Human IgG Fc Secondary Antibody, HRP (Thermo Fisher, A18817) were added to each well and incubated at 37°C. After 1 h, plates were washed 4x in TBST and 30 µl of TMB (SeraCare) was added to every well for 2min at room temperature. Reactions were quenched with the addition of 30 µl of 1 N HCl. Plates were immediately read at 450 nm on a BioTek Neo2 plate reader and data was plotted and fit in Prism 9 (GraphPad) using nonlinear regression sigmoidal, 4PL, X is the concentration to determine EC_{50} values from curve fits.

Production of VSV pseudoviruses

SARS-CoV-2 D614G S, XBB.1.5 S, and SARS-CoV-1 S VSV pseudoviruses were produced using HEK293T cells seeded on BioCoat Cell Culture Dish: poly-D-Lysine 100mm (Corning). Cells were transfected with respective S constructs using Lipofectamine 2000 (Life Technologies) in Opti-MEMtransfection medium. After 5 h of incubation at 37°C with 5% CO_2, cells were supplemented with DMEM containing 10% of FBS. On the next day, cells were infected with VSV (G*ΔG-luciferase) for 2 h, followed by five time washwithDMEMmediumbefore addition of anti-VSV G antibody (I1-mouse hybridoma supernatant diluted 1:40, ATCC CRL-2700) and medium. After 18-24h of incubation at 37°C with 5% CO_2, pseudoviruses were collected and cell debris was removed by centrifugation at 3000 x g for 10min. Pseudoviruses were further filtered using a 0.45 µm syringe filter and concentrated 10x prior to storage at -80°C.

Serological ELISAs

For serological ELISAs, 30 µL of assorted proteins (SARS-CoV-2 HexaPro S, SARS-CoV-2 XBB.1.5 HexaPro S (AcroBiosystems, SPN-C524i) and SARS-CoV-1 HexaPro S) at 3 µg/mL were placed into 384-well Nunc Maxisorp plates (ThermoFisher, 464718) in 1x TBS and incubated for 1 h at 37°C followed by slap drying and blocking with 80 µL of Casein for 1 h at 37°C. Afterward, plates were once again slap-dried and a 1:4 serial dilution of our immunized mouse sera was performed starting from 1:20 dilution in 30 µL of TBST and incubated at 37°C for 1 h. Plates were then washed 4x in TBST and 30 µL of 1:5000 Goat antimouse IgG (H + L) Secondary Antibody HRP (ThermoFisher 62-6520) were added to each well and incubated at 37°C for 1 h. Plates were then washed 4x in TBST and 30 µL of TMB (SeraCare) was added to each well and allowed to sit for 2min at room temperature. TMB reactions were quenched with 30 µL of 1 N HCl and immediately read at 450 nm on a BioTek Neo2 plate reader and data plotted and fit in Prism 10 (Graphpad) using nonlinear regression sigmoidal, 4PL, X is the concentration to determine ED_{50} values from curve fits. Two biological replicates each comprising two technical replicates, were carried out. Due to the shortage of sera, we were unable to conduct biological replicates for mice 2-3, 2-4, and 3-12. For IgG subclass serological ELISAs, 30 µL of SARS-CoV-2HexaPro S or E-69 at 3µg/mL were placed into 384-well Nunc Maxisorp plates (ThermoFisher, 464718) in 1x TBS and incubated overnight at RT followed by slap drying and blocking with 80 µL of Casein for 1 h at 37°C. Afterward, plates were once again slap-dried and a 1:4 serial dilution of our immunized mouse sera was performed starting from 1:80 dilution in 30 µL of TBST and incubated at 37°C for 1 h. Plates were then washed 4x in TBST and 30 µL of 1:5000 Goat anti-mouse IgG(H+L) Secondary Antibody HRP (ThermoFisher 62-6520), Peroxidase AffiniPure™ Goat Anti-Mouse IgG Fcγ subclass 1 specific (Jackson Immuno Research, 115-035-205), Peroxidase AffiniPure™ Goat Anti-Mouse IgG Fcγ subclass 2a specific (Jackson Immuno Research, 115-035-206), and Peroxidase AffiniPure™ Goat Anti-Mouse IgG Fcγ subclass 2b specific (Jackson Immuno Research, 115-035-207) were added to each well and incubated at 37°C for 1 h. Plates were then washed 4x in TBST and 30 μL of TMB (SeraCare) was added to each well and allowed to sit for 1min at room temperature. TMB reactions were quenched with 30 μL of 1N HCl and immediately read at 450 nm on a BioTek Neo2 plate reader and data plotted and fit in Prism 10 (Graphpad) using nonlinear regression sigmoidal, 4PL, X is the concentration to determine ED_{50} values from curve fits. Two biological replicates each comprising two technical replicates have been carried out.

Negative stain electron microscopy preparation, data collection, and data processing

Carbon copper formvar grids (Ted Pella 01754-F) were glow discharged using a Gloqube Plus (Quorum) at 20mA for 30 s promptly followed by the addition of 3 μL of a S_2 pre-fusion constructs diluted to a concentration of 0.01mg/mL. After 1 min the protein was aspirated using filter paper and 3 μL of 2% uranyl formate was applied and quickly removed for washing. Another 3 μL of uranyl formate was added to the grid and left to stain for 30 s before drying with filter paper and left to further air dry before imaging. Automated data collection was carried out using Leginon at a nominal magnification of 67,000 with a pixel size of 1.6 Å. Each micrograph was acquired for 500-900ms. Negative stain data was processed using CryoSPARC. Automatic particle picking and extraction were performed using CryoSPARC for each data set. Particle images were extracted with a box size of 256 pixels with a pixel size of 1.6 Å and binned to 128 pixels for subsequent 2D classifications.

Cryo-EM sample preparation and data collection

The E-31 cryo-EM dataset was collected over three different sessions which were combined to be processed together. 3 µL of sample was added to a glow discharged (120 s at 20mA) UltraAuFoil R2/2:Au200 grid prior to plunge freezing using a vitrobot MarkIV (ThermoFisher Scientific) with a blot force of 0 and 6.5 sec blot time at 100% humidity and 22°C. For E-60, 3 µL of sample was added to a glow discharged (120 s at 20mA) UltraAuFoil R2/2:Au200 grid prior to plunge freezing using a vitrobot MarkIV (ThermoFisher Scientific) with a blot force of 0, 5.5 sec blot time, and 10 s wait time at 100% humidity and 22°C. For E-69, 3 µL of sample was added to a glow discharged (120 s at 20mA) UltraAuFoil R2/2:Au200 grid prior to plunge freezing using a vitrobot MarkIV (ThermoFisher Scientific) with a blot force of 0, 6 sec blot time, and 10 s wait time at 100% humidity and 22°C. Data were acquired using an FEI Titan Krios transmission electron microscope operated at 300 kV and equipped with a Gatan K3 direct detector and Gatan Quantum GIF energy filter, operated in zero-loss mode with a slit width of 20 eV. Automated data collection was carried out using Leginon (Suloway et al., 2005) at a nominal magnification of 105,000x with a pixel size of 0.843 Å. The dose rate was adjusted to 15 counts/pixel/s, and each movie was acquired in counting mode fractionated in 75 frames of 40 ms. A total of 25,829 and 6807 micrographs were collected for E-31 and E-60 datasets, respectively. The stage was tilted 0, 30, and 45 degrees for E-31 and 20 degrees for the E-60 collection. A total of 5946 micrographs were collected for E-69 at 0 and 30 degrees tilted stage.

Cryo-EM data processing, model building and refinement

For the E-31 structure, motion correction and contrast-transfer function (CTF) parameter estimation were performed using Warp (Tegunov & Cramer, 2019) and cryoSPARC, respectively. Automatic particle picking was performed using TOPAZ (Bepler et al., 2019) and particle images were extracted with a box size of 208 pixels with a pixel size of 1.686 Å. After 2D classification and hetero-refinement using cryoSPARC (Punjani et al., 2017), 1,688,203 particles were selected for cryoSPARC non-uniform refinement (Punjani et al., 2020) with C3 symmetry. Particles were further subjected to another round of 2D classification (to remove particles with splayed open conformation) followed by Bayesian polishing (Zivanov et al., 2019) in Relion. Finally, another round of cryoSPARC nonuniform refinement with C3 symmetry and per-particle defocus refinement was carried out using the polished particles. For the E-60 structure, motion correction, CTF estimation, automatic particle picking, and extraction were performed using Warp (Tegunov & Cramer, 2019). Particle images were extracted with a box size of 208 pixels and a pixel size of 1.686 Å. After 2D classification and hetero-refinement in cryoSPARC, 240,989 particles were selected. These particles were subjected to two rounds of 3D classification with 50 iterations each (angular sampling 7.5° for 25 iterations and 1.8° with local search for 25 iterations) using Relion (Scheres, 2012a, 2012b; Zivanov et al., 2018). 3D refinements were carried out using non-uniform refinement along with per-particle defocus refinement in cryoSPARC followed by

Bayesian polishing (Zivanov et al., 2019) in Relion. Finally, another round of cryoSPARC non-uniform refinement with C3 symmetry and per-particle defocus refinement was carried out using the polished particles. For the E-69 structure, motion correction, CTF estimation, automatic particle picking (blob picking), and extraction were performed using cryoSPARC LIVE and cryoSPARC. Particle images were extracted with a box size of 208 pixels and a pixel size of 1.686 Å. After 2D classification and hetero-refinement in cryoSPARC, 319,035 particles were selected and subjected to reference motion correction and beam tilt correction followed by a final non-uniform refinement with C3 symmetry using cryoSPARC. Local resolution estimation, filtering, and sharpening were carried out using cryoSPARC. Reported resolutions are based on the gold standard Fourier shell correlation (FSC) of 0.143 criterion and Fourier shell correlation curves were corrected for the effects of soft masking by high-resolution noise substitution (S. Chen et al., 2013; Rosenthal & Henderson, 2003). UCSF Chimera (Pettersen et al., 2004), UCSF ChimeraX (Goddard et al., 2018), and Coot (Emsley et al., 2010) were used to fit and rebuild atomic models into the cryoEM maps utilizing sharpened and unsharpened maps. Model building of the rearranged region C-terminal of the fusion peptide (residues 816-861) was assisted by AlphaFold2 (Jumper et al., 2021; Mirdita et al., 2022). The models were refined and relaxed using Rosetta (Frenz et al., 2019; R. Y.-R. Wang et al., 2016) and validated using Phenix (Liebschner et al., 2019), Molprobity (V. B. Chen et al., 2010) and Privateer (Agirre et al., 2015).

Immunogenicity

Female BALB/c mice were purchased from Envigo (order code 047) at 7weeks of age and were maintained in a specific pathogen-free facility within the Department of Comparative Medicine at the University of Washington, Seattle, accredited by the Association for Assessment and Accreditation of Laboratory Animal Care (AAALAC). Animal experiments were conducted in accordance with the University of Washington's Institutional Animal Care and Use Committee. Prior to each immunization, immunogens (low endotoxin immunogen) were diluted to 20 µg/mL (2P S) or 100 µg/mL (S_2) in 1x PBS (1.5mM Potassium Phosphate monobasic, 155mM NaCl, 2.7mM Sodium Phosphate diabasic, pH7.4) (ThermoFisher) and mixed with 1:1 vol/vol AddaVax (InvivoGen vac-adx-10) to reach a final dose of 1 µg (2P S) or 5 µg (S_2) of immunogen per injection. At 8 weeks of age, 12 mice per group were injected subcutaneously in the inguinal region with 100 µL of immunogen at weeks 0, 3, 10, and 17. Group 1 received four doses of 1 µg 2P S. Group 2 received four doses of 5 µg S_2. Group 3 received two doses of 1 µg 2P S and boosted with two doses of 5 µg S_2. Mice were bled via the submental route at weeks 0, 2, 5, 12, and 19. Blood was collected in serum separator tubes (BD # 365967) and rested for 30 min at room temperature for coagulation. Serum tubes were then centrifuged for 10 min at 2000 x g and serum was collected and stored at -80°C until use. Mouse 2-10 were euthanized before immunization 4 resulting in n=11 for group2 for the reported sera ELISA, IgG isotype ELISA, and neutralization assay.

Neutralization assays

For SARS-CoV-2 D614G S VSV, XBB.1.5 S VSV, and SARS-CoV-1 S VSV neutralization, VeroE6-TMPRSS2 cells in DMEM supplemented with 10% FBS, 1%

PenStrep, and 2% Geneticin were seeded at 40,000 cells/well into 96-well plates [3610] (Corning) and incubated overnight at 37°C. The following day, a half-area 96-well plate (Greiner) was prepared with 3-fold serial sera dilutions (starting dilutions determined for each serum and pseudovirus, 22 µL per well). An equal volume of DMEM with diluted pseudoviruses was added to each well. All pseudoviruses were diluted between 1:90-1:200 to reach a target entry of ~10^6 RLU. The mixture was incubated at room temperature for 45-60 min. Media was removed from the cells, and the cells were washed once with DMEM prior to the transfer of sera-pseudovirus mixture. 40 µL from each well of the half-area 96-well plate containing sera and pseudovirus were transferred to the 96-well plate seeded with cells and incubated at 37°C for 1 h. After 1 h, an additional 40 µL of DMEMsupplementedwith 20% FBS and 2% PenStrep was added to the cells. After 18-20 h, 40 µL of One-Glo-EX substrate (Promega) was added to each well and incubated on a plate shaker in the dark for 5min before reading the relative luciferase units using a BioTek Neo2 plate reader. Relative luciferase units (RLUs) were plotted and normalized in Prism (GraphPad): 100% neutralization being cells in the absence of pseudovirus and 0%neutralization being pseudovirus entry into cells without sera. Prism (GraphPad) nonlinear regression with “log[inhibitor] versus normalized response with a variable slope” was used to fit the curve. Percent neutralization was calculated by taking the interpolated percentage of entry value at a fixed dilution factor of 1/33 (v/v ratio dilution of initial sera, log(dilution factor) of 1.519) using the fit curve. 100% and 0% neutralization were defined as 0% entry and 100% entry, respectively. Calculated values from three biological replicates per sample-pseudovirus pair were used to obtain the mean percent neutralization per animal.

Mouse challenges and virus plaque assays

7weeks post-boost,mice (Envigo, stock# 047) were exported from the Comparative Medicine Facility at the University of Washington, Seattle, WA to an AAALAC accredited Animal Biosafety Level 3 (ABSL3) Laboratory at the University of North Carolina, Chapel Hill, where mice were acclimated for 7 days. For infection,mice were anesthetized with a mixture of ketamine/xylazine and challenged intranasally with 1×10^5 plaque-forming units (pfu) of a recombinant mouse-adapted coronavirus SARS-CoV-2 XBB.1.5 MA strain for the evaluation of vaccine efficacy (Powers et al., 2024) (IACUC protocol 21-272). Infected mice were monitored for daily body weight. On day 4 post-infection mice were necropsied, the degree of lung congestion was scored, and lung (caudal lobe) and nasal turbinate tissues were harvested to determine viral loads by plaque assay. For plaque assays, the appropriate tissues were homogenized in PBS and tissue debris was pelleted at 13,000 x g for 5 min. The clarified homogenates were serial-diluted and added to a confluent monolayer of Vero E6 cells (ATCC CCL-81), followed by an agarose overlay. Plaques were visualized with an overlay of Neutral Red dye on day 3 post infection.

4.9 Figures & Tables

Figure 4.1. Design of prefusion-stabilized SARS-CoV-2 fusion machinery (S_2 subunit) vaccines.

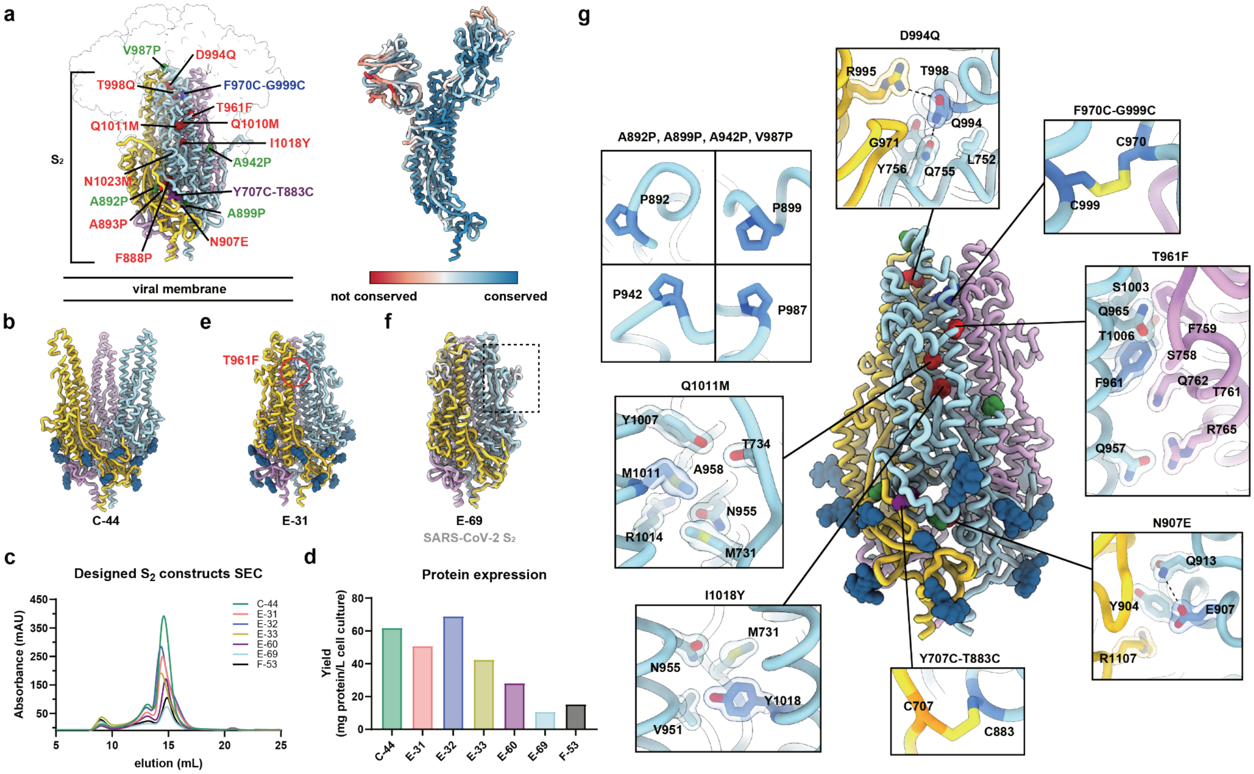

(**a**) (Left) Ribbon diagram of prefusion SARS-CoV-2 S highlighting all positions that were mutated to attempt to stabilize the metastable fusion machinery (S_2 subunit) in the prefusion conformation.Mutations are shown in blue (intra-protomer disulfide bond), purple (VFLIP inter-protomer disulfide bond (Olmedillas et al., 2021)), green (subset of proline mutations selected from HexaPro (Hsieh et al., 2020)), and red (ten mutations selected based on expression/fusion score of a deep-mutational scan (T. J. C. Tan et al., 2023)). The S_1 subunit is shown as a transparent surface and glycans are omitted for clarity (PDB 6VXX). (Right) SARS-CoV-2 S (PDB 6VXX) colored by sequence conservation across multiple sarbecoviruses. (**b**) Ribbon diagram of the C-44 cryoEM structure previously determined with splayed open apex (Bowen, Park, et al., 2022) (PDB 8DYA). (**c**) Size-exclusion chromatograms (SEC) of the designed S_2 constructs. (**d**) Purification yields of the designed S_2 constructs after size-exclusion chromatography. (**e**) Ribbon diagram of the E-31 cryoEM structure. The position of the T961F mutation is circled red in one protomer. (**f**) Superimposition of the S_2 subunits from the E-69 cryoEM structure and prefusion SARS-CoV-2 S (A. C. Walls, Park, et al., 2020) (gray, PDB 6XR8, residues 705-1146). The box denotes a region of local structural deviation downstream of the fusion peptide (residues 833-855). Glycans are omitted for clarity. (**g**) Ribbon diagram of the E-69 cryoEM structure. Insets: zoomed-in views of the mutations introduced with mutated residues rendered with darker blue/orange shades with semi-transparent surface representation of select side chains. Selected polar interactions are shown as dashed lines. The three protomers of each trimer are colored blue, pink and gold throughout the figure.

Figure 4.2. Characterization of designed SARS-CoV-2 S_2 prefusion immunogens with single mutations.

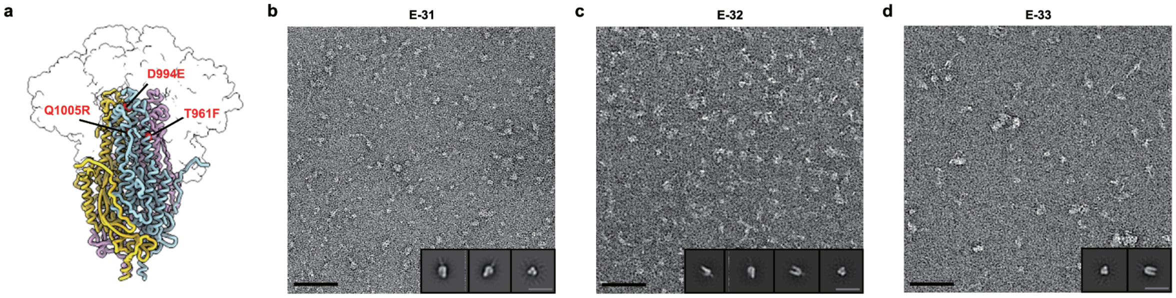

(**a**) Ribbon diagram of prefusion SARS-CoV-2 S (PDB 6VXX) highlighting all three positions shown in red (T961F, D994E, Q1005R) that were individually mutated to attempt to stabilize the metastable fusion machinery in the prefusion conformation. The S_1 subunit is shown as a semi-transparent surface and glycans are omitted for clarity. (**b-d**) EM analysis of negatively stained E-31 (T961F) (**b**), E-32 (D994E) (**c**), and E-33 (Q1005R) (**d**). Insets: 2D class averages showing compact and splayed open prefusion S_2 trimers. The scale bar represents 50 nm (black) or 200 Å (insets, gray).

Figure 4.3. CryoEM data collection and refinement of SARS-CoV-2 S_2 E-31.

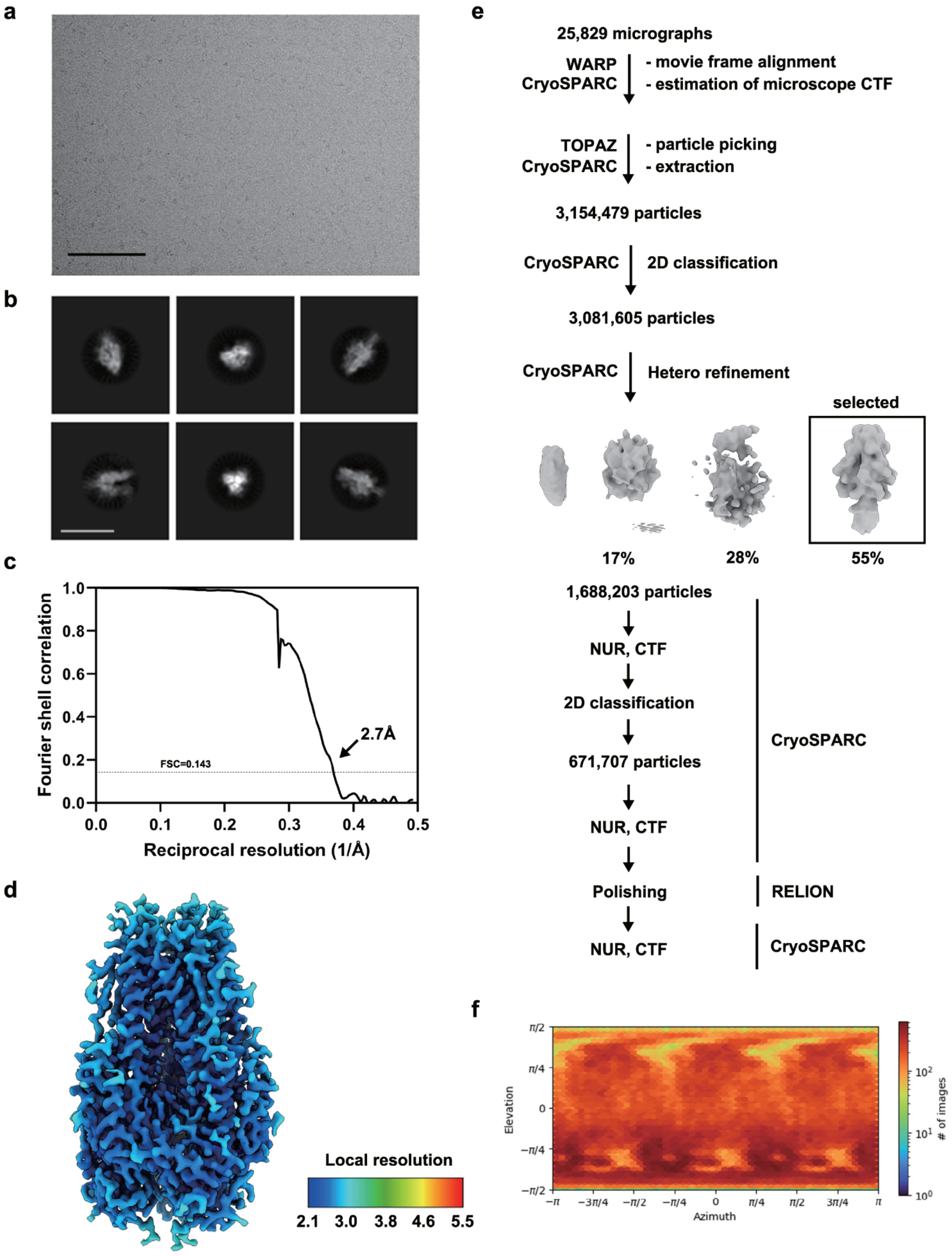

(**a-b**) Representative electron micrograph (**a**) and 2D class averages (**b**) of SARS-CoV-2 S_2 E-31 embedded in vitreous ice. The scale bar represents 100 nm (**a**) or 160Å (**b**). (**c**) Gold-standard Fourier shell correlation curve for the cryoEM reconstruction. The 0.143 cutoff is indicated with a gray dashed line. (**d**) SARS-CoV-2 S_2 E-31 cryoEM map colored by local resolution as determined using cryoSPARC. (**e**), Data processing flowchart. NUR, CTF: non-uniform refinement with per-particle defocus refinement. (**f**) Angular distribution of E-31 particle images in the final map.

Figure 4.4. Structural details of prefusion-stabilized S_2 subunit designs.

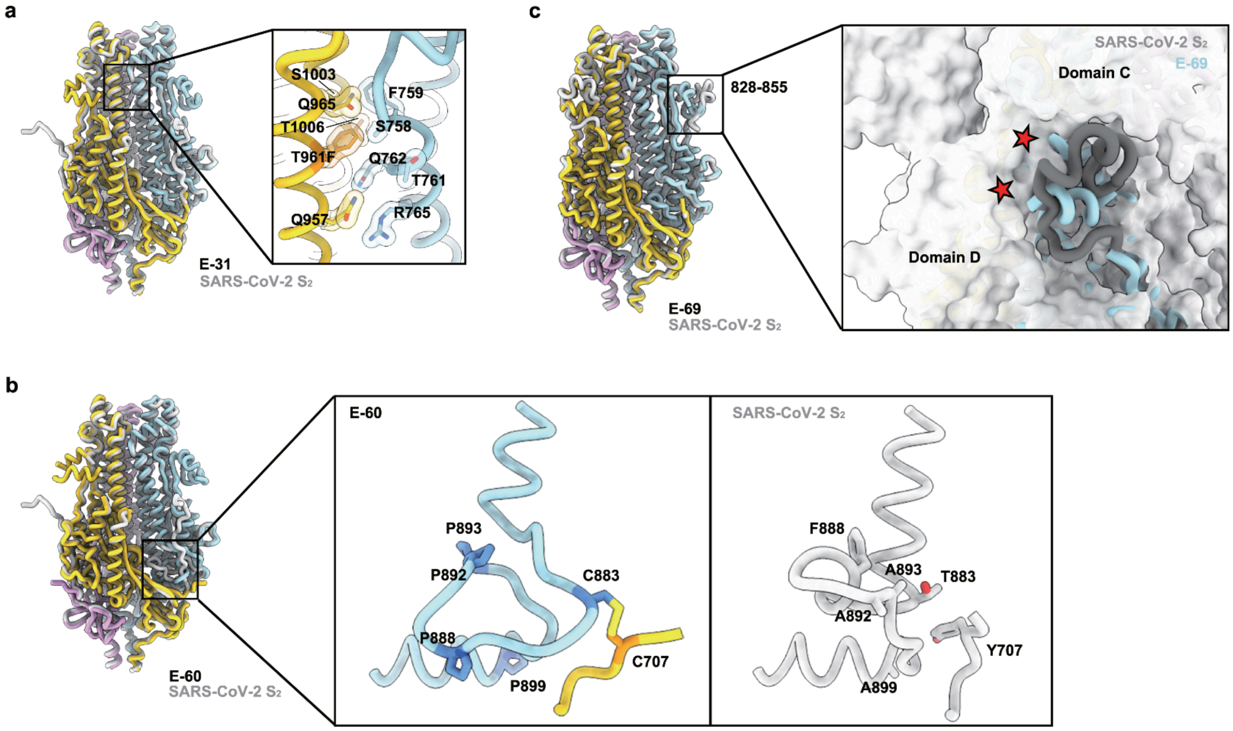

(**a**) E-31 superimposed to the SARS-CoV-2 S_2 subunit from the S ectodomain trimer (PDB 6VXX, gray). Inset: zoomed-in view of the T961F mutation and proximal residues with selected side chains shown as semi-transparent surfaces. (**b**) E-60 superimposed to the SARS-CoV-2 S_2 subunit from the S ectodomain trimer (PDB 6VXX, gray). Inset: zoomed-in view of residues 875-906 of E-60 (left) and SARS-CoV-2 S (right) to highlight local structural distortions. Mutated residues are shown in blue and orange. (**c**) E-69 superimposed to the SARS-CoV-2 S_2 subunit from the S ectodomain trimer (PDB 6XR8, residues 705-1146). Steric clashes are indicated with red stars.

Figure 4.5. CryoEM data collection and refinement of SARS-CoV-2 S$_2$ E-60.

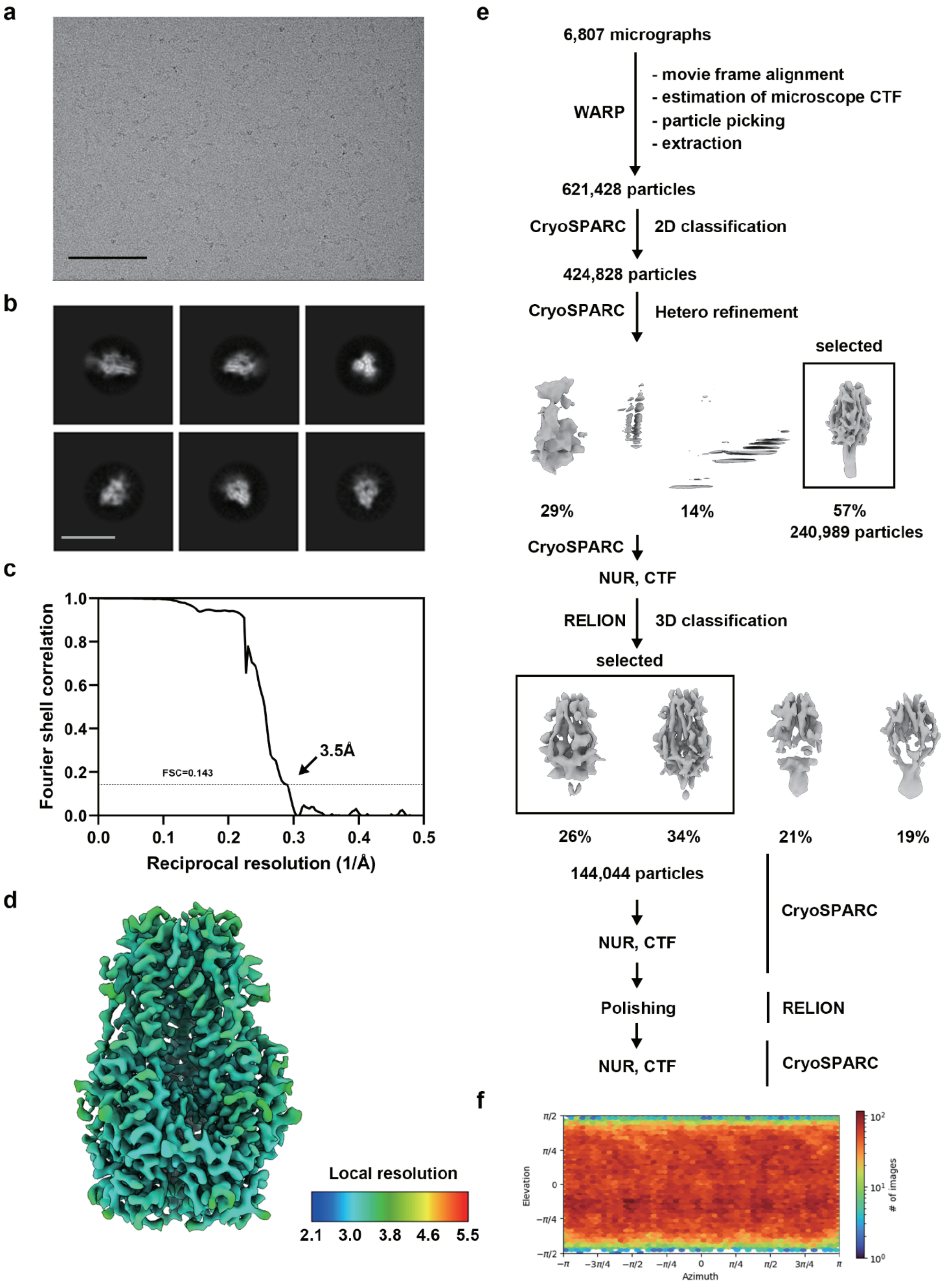

(**a-b**) Representative electron micrograph (**a**) and 2D class averages (**b**) of SARS-CoV-2 S_2 E-60 embedded in vitreous ice. The scale bar represents 100 nm (**a**) or 160Å (**b**). (**c**) Gold-standard Fourier shell correlation curve for the cryoEM reconstruction. The 0.143 cutoff is indicated with a gray dashed line. (**d**) SARS-CoV-2 S_2 E-60 cryoEM map colored by local resolution as determined using cryoSPARC. (**e**) Data processing flowchart. NUR, CTF: non-uniform refinement with per-particle defocus refinement. (**f**) Angular distribution of E-60 particle images in the final map.

Figure 4.6. CryoEM data collection and refinement of SARS-CoV-2 S_2 E-69.

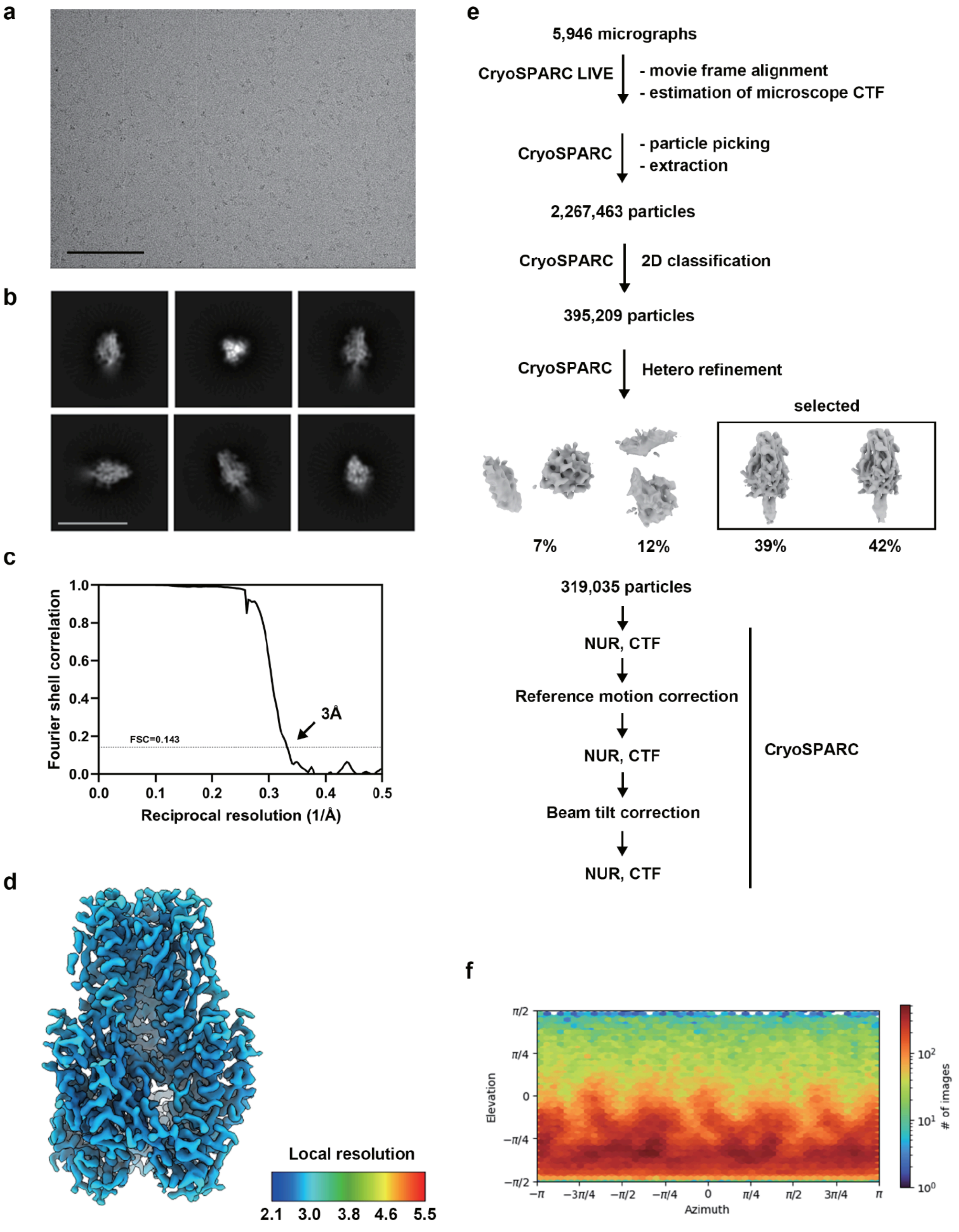

(**a-b**) Representative electron micrograph (**a**) and 2D class averages (**b**) of SARS-CoV-2 S_2 E-69 embedded in vitreous ice. The scale bar represents 100 nm (**a**) or 200Å (**b**). (**c**) Gold-standard Fourier shell correlation curve for the cryoEM reconstruction. The 0.143 cutoff is indicated with a gray dashed line. (**d**) SARS-CoV-2 S_2 E-69 colored by local resolution as determined using cryoSPARC. (**e**) Data processing flowchart. NUR, CTF: non-uniform refinement with per-particle defocus refinement. (**f**) Angular distribution of E-69 particle images in the final map.

Figure 4.7. Characterization of SARS-CoV-2 S_2 prefusion design F-53.

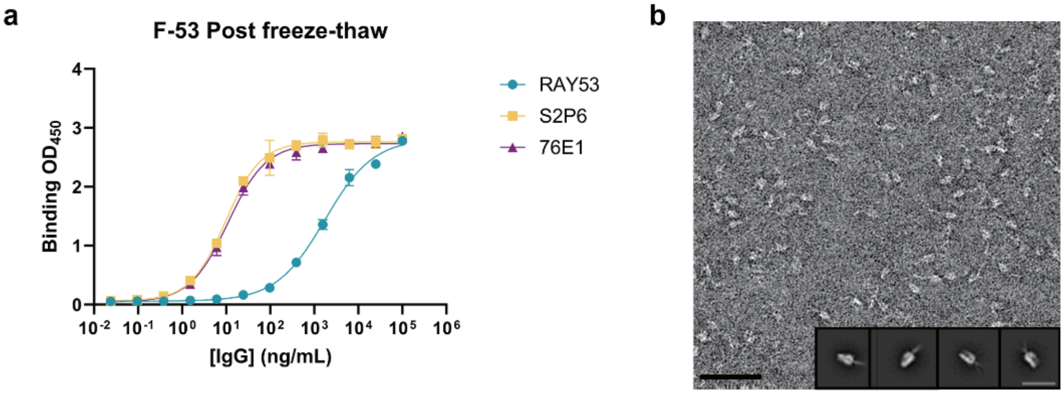

(**a**) Evaluation of binding of a panel of monoclonal antibodies to SARS-CoV-2 S_2 F-53 by ELISA. Each data point represents the mean of three technical replicates and SD are shown with bars. (**b**) EM analysis of negatively stained purified F-53. Insets: 2D class averages. The scale bar represents 50 nm (black) or 200 Å (insets, gray).

Figure 4.8. A stable prefusion-stabilized SARS-CoV-2 fusionmachinery (S_2 subunit) vaccine candidate.

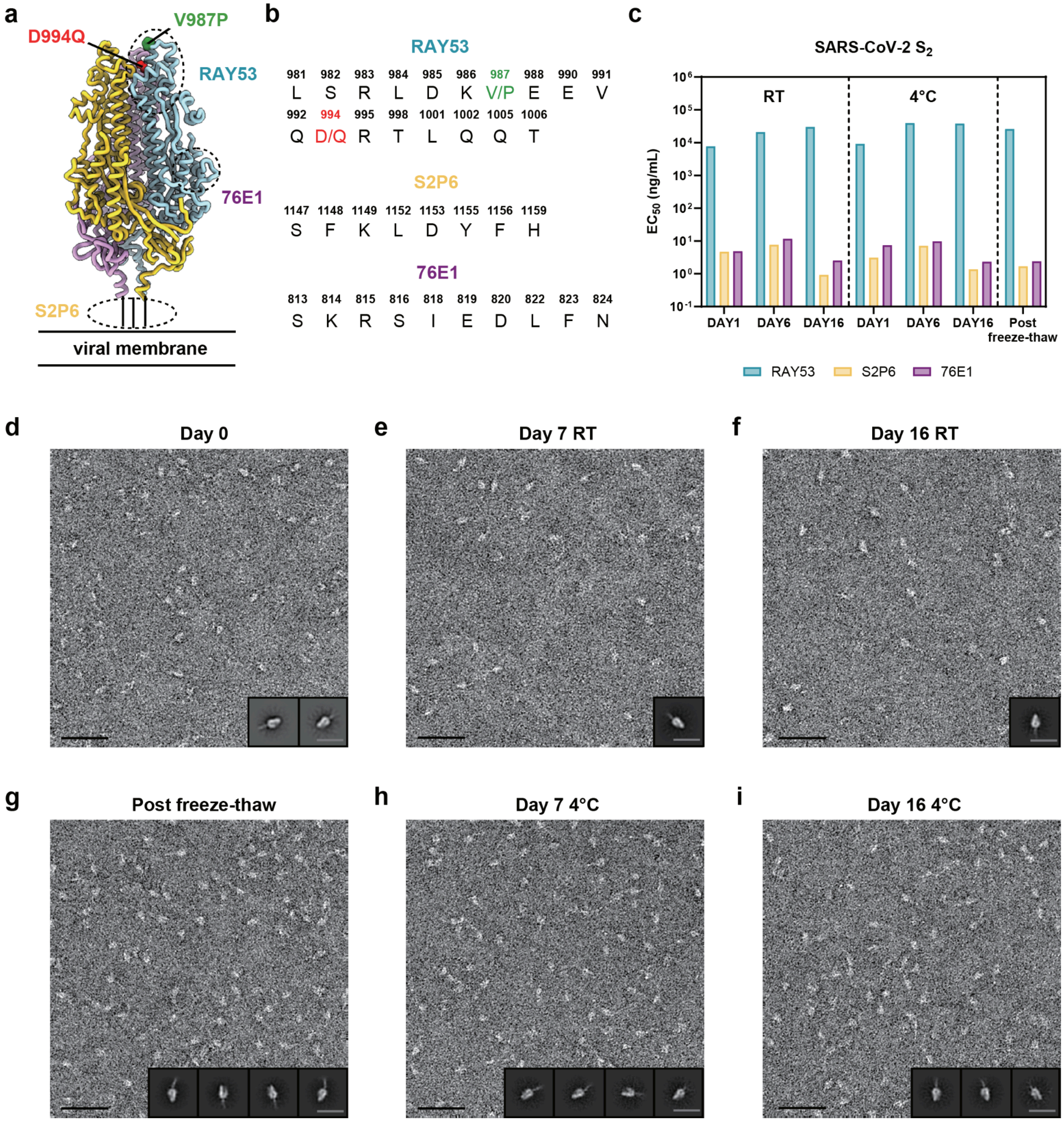

(**a**) Ribbon diagram of the E-69 prefusion-stabilized SARS-CoV-2 fusion machinery antigen highlighting the regions containing the epitopes recognized by S_2 subunit-targeting monoclonal antibodies using dashed lines. (**b**) Amino acid sequences of the RAY53, S2P6 and 76E1 epitopes. The V987P and D994Q E-69 mutations are respectively shown in green and red in panels **a-b** as they are located within the RAY53 epitope that has been previously reported (Silva et al., 2023). (**c**) Evaluation of retention of antigenicity for the E-69 antigen in various storage conditions using binding of the

S2P6, 76E1 and RAY53 monoclonal antibodies analyzed by ELISA. (**d-i**) Evaluation of retention of the native prefusion conformation for the E-69 antigen in various storage conditions analyzed by EM of negatively stained samples. Insets: 2D class averages. The scale bars represent 50 nm (micrograph) and 200 Å (2D class averages). nsEM data was collected once per storage conditions. Representative micrographs from 42, 85, 49, 42, 22, and 24 micrographs are shown respectively. Particles picked from individual sets of micrographs were used to generate 2D class averages.

Figure 4.9. Retention of antigenicity of SARS-CoV-2 S_2 E-69.

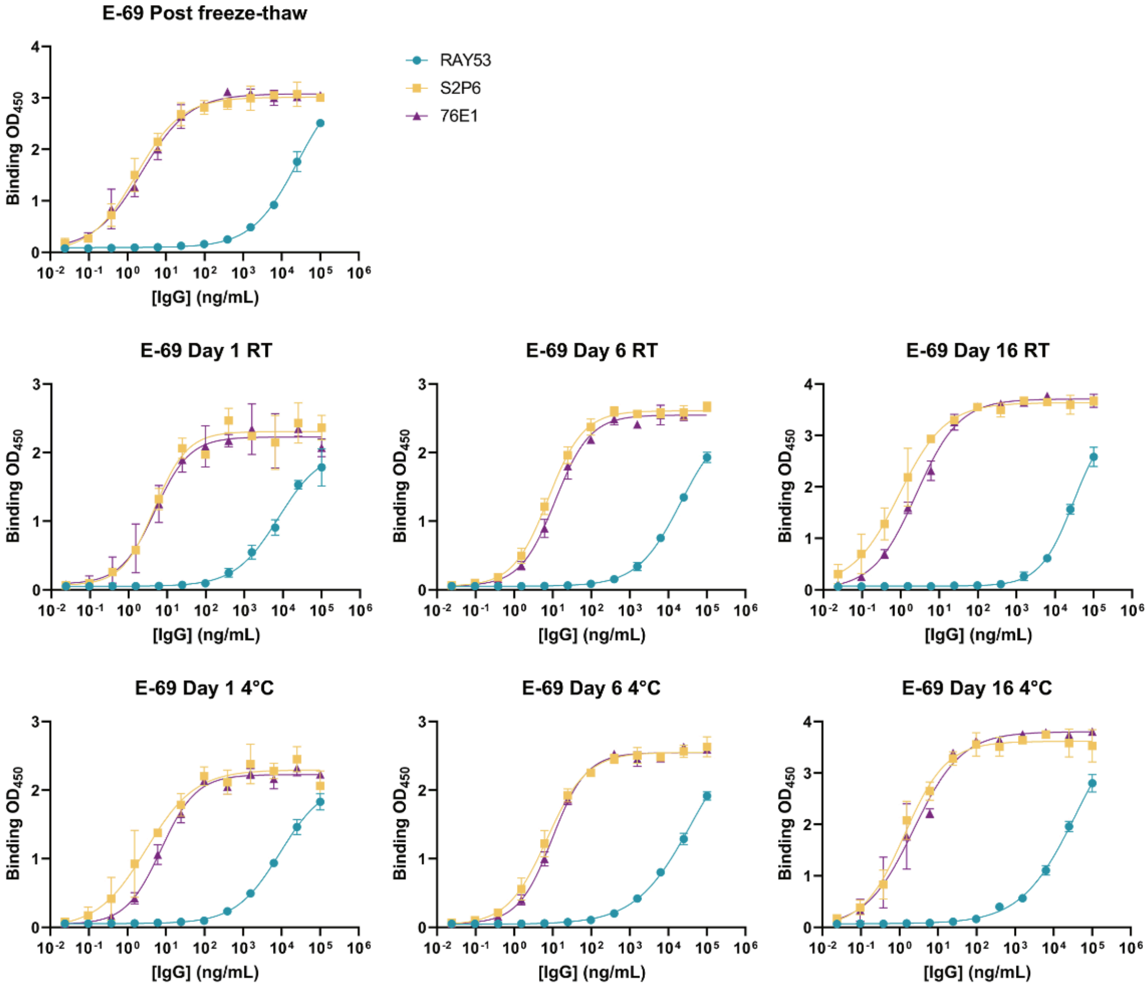

Dose-response curves for evaluation of binding of a panel of monoclonal antibodies to SARS-CoV-2 S_2 E-69 under various storage conditions measured by ELISA. Each data point represents the mean of three technical replicates and SD are shown with bars.

Figure 4.10. A broadly generalizable prefusion-stabilization strategy for sarbecovirus fusion machinery (S_2 subunit) antigens.

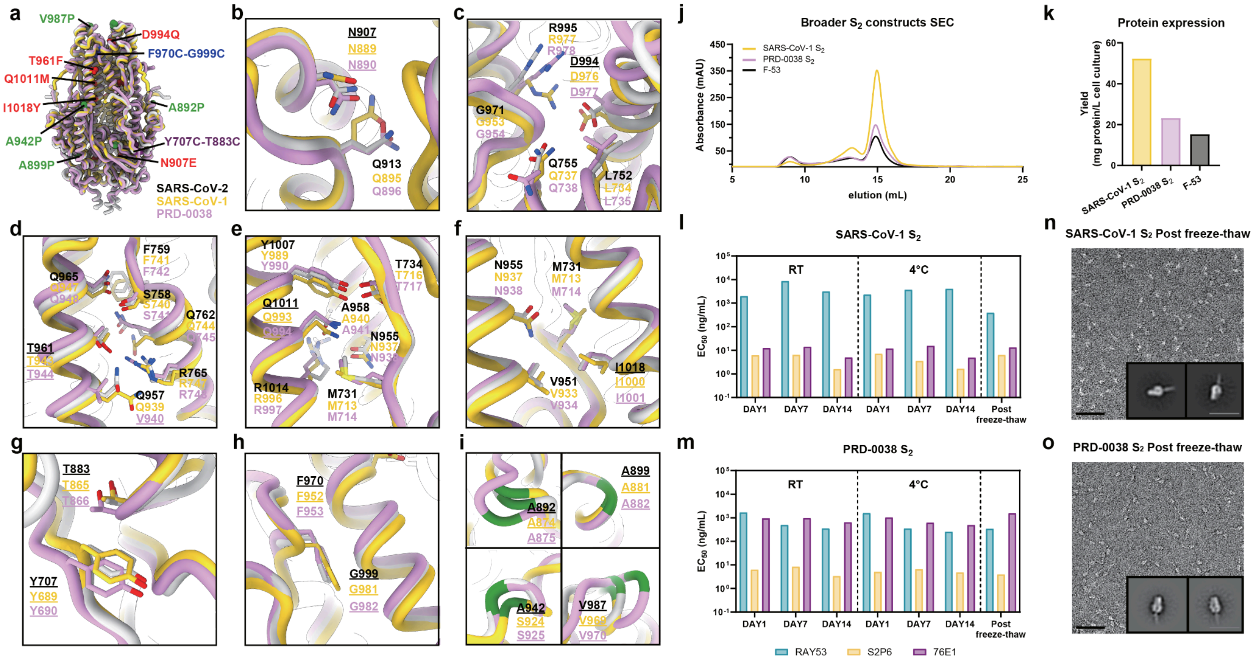

(**a**) Ribbon diagrams of superimposed S_2 subunits of the prefusion SARS-CoV-2 S (PDB 6VXX (A. C. Walls, Park, et al., 2020)), SARS-CoV-1 S (PDB 5X58 (Yuan et al., 2017)) and PRD-0038 S (PDB 8U29 (Lee et al., 2023)) structures. Prefusion-stabilizing mutations are shown in blue (intra-protomer disulfide bond), purple (VFLIP inter-protomer disulfide bond (Olmedillas et al., 2021)), green (subset of proline mutations selected from HexaPro (Hsieh et al., 2020)), and red (mutations ported from E-69). (**b-i**) Zoomed-in views of superimposed S_2 subunits of the prefusion SARS-CoV-2, SARS-CoV-1 and PRD-0038 S structures highlighting the local structural conservation of residues mutated in SARS-CoV-2 the E-69/F-53 constructs (underlined). SARS-CoV-2, SARS-CoV-1, and PRD-0038 S are respectively shown in light gray, gold, and pink in panels (**a–i**). (**j**) Size-exclusion chromatograms (SEC) of the designed SARS-CoV-1 and PRD-0038 S_2 constructs, as compared to SARS-CoV-2 F-53. (**k**) Purification yields of the designed SARS-CoV-1 and PRD-0038 S_2 constructs. The yield for the best SARS-CoV-2 S_2 construct (F-53) is included for comparison. (**l,m**) Evaluation of retention of antigenicity for the SARSCoV-1 (**l**) and PRD-0038 (**m**) S_2 antigens in various storage conditions using binding of the S2P6, 76E1 and RAY53 monoclonal antibodies analyzed by ELISA. (**n,o**) Evaluation of retention of the native prefusion conformation of the negatively stained SARS-CoV-1 (**n**) and PRD-0038 (**o**) S_2 trimers after freeze/thawing. Insets: 2D class averages showing compact prefusion S_2 trimers. The scale bar represents 50 nm (micrographs) and 200 Å (2D class averages). nsEM data was collected once per storage conditions. Representative micrographs from 82 and 98 micrographs are shown respectively. Particles picked from individual sets of micrographs were used to generate 2D class averages.

Figure 4.11. Retention of antigenicity of SARS-CoV-1 and PRD-0038 prefusion S_2 designed constructs.

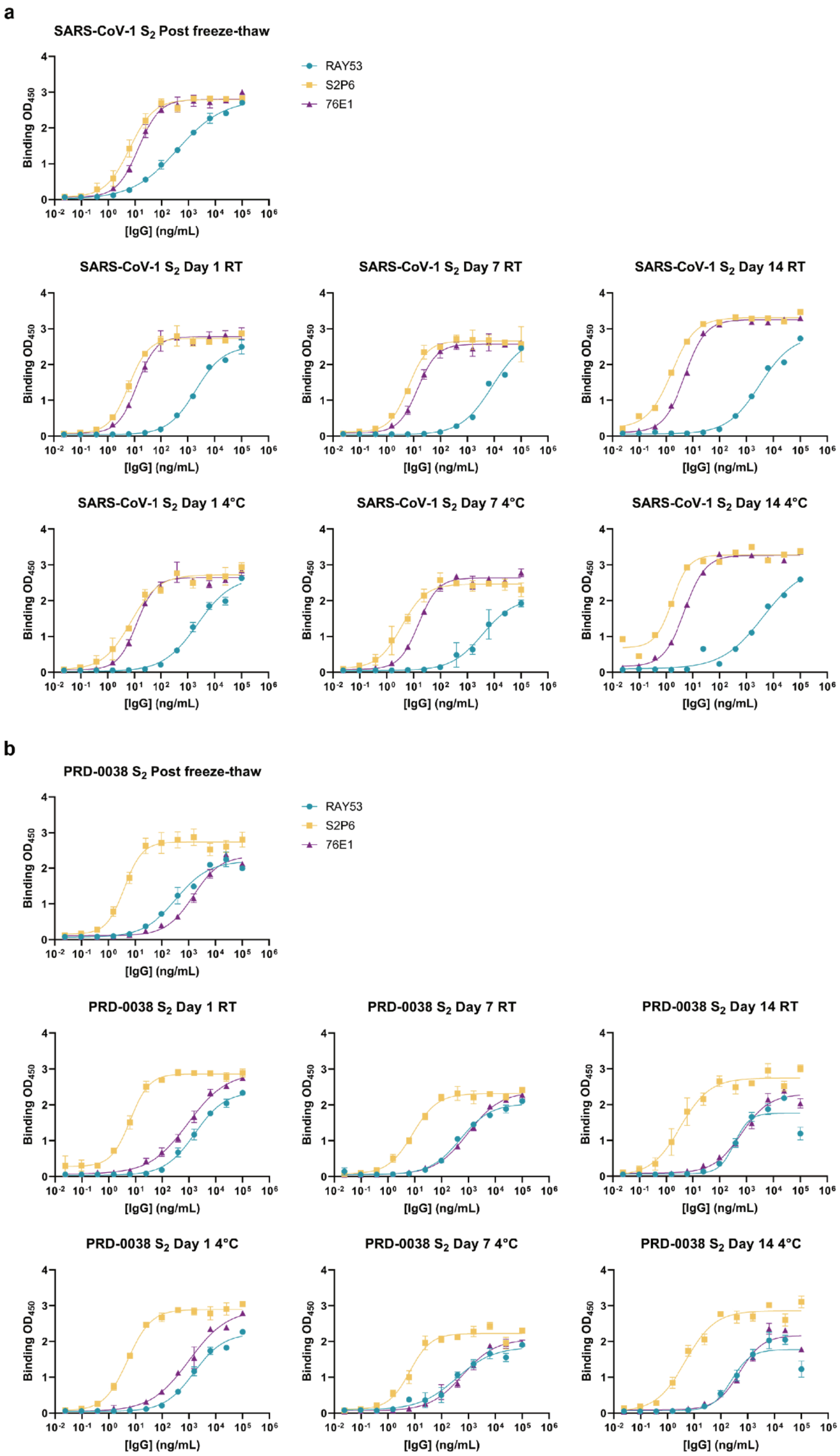

(**a-b**) Evaluation of binding of a panel of monoclonal antibodies to SARS-CoV-1 S_2 (**a**) and PRD-0038 S_2 (**b**) under various storage conditions measured by ELISA. Each data point for SARS-CoV-1 represents the mean of two technical replicates and SD are shown with bars (except for SARS-CoV-1 Day14 RT and 4˚C which comprise a single technical replicate and Post-freeze thaw which comprises three technical replicates). Each data point for PRD-0038 represents the mean of three technical replicates and SD are shown with bars (PRD-0038 Post freeze-thaw which comprises two technical replicates).

Figure 4.12. A prefusion-stabilized SARS-CoV-2 fusion machinery (S_2 subunit) vaccine elicits broadly reactive antibody responses.

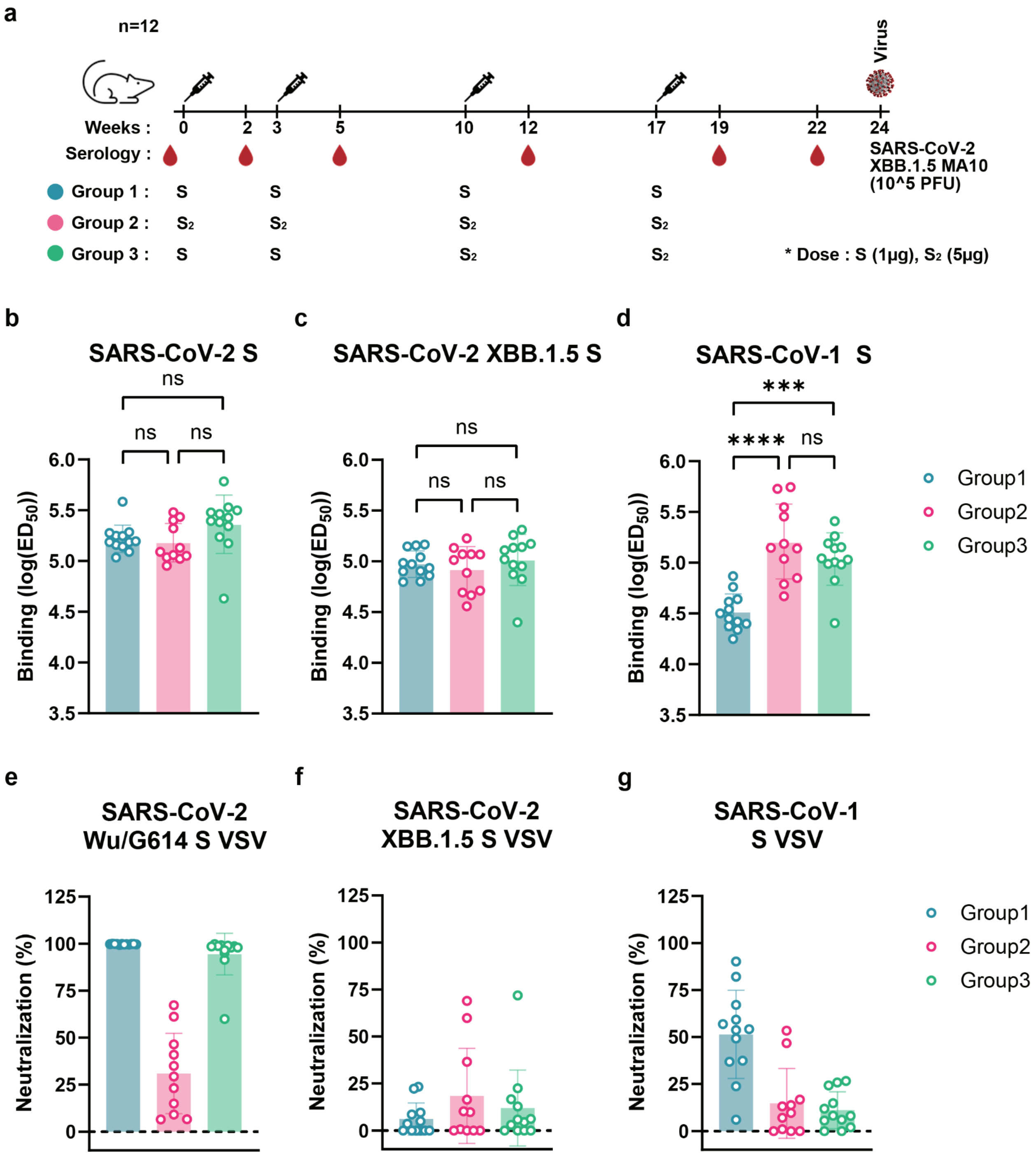

(**a**) Vaccination schedule and study design. (**b-d**) Analysis of antibody binding titers against SARS-CoV-2 Hexapro S (**b**), XBB.1.5 Hexapro S (**c**), and SARS-CoV-1 Hexapro S (**d**) analyzed by ELISAs using sera obtained two weeks post dose 4. Geometric mean and geometric standard deviation (SD) are shown as bars. Each data point represents the mean of two biological replicates each comprising two technical replicates. Comparisons between multiple groups for (**b–d**) were made by ordinary one-way analysis of variance (ANOVA) followed by Tukey's multiple comparisons test. ns: P>0.05, *: P<=0.05, **: P<=0.01, ***: P<=0.001, ****: P<=0.0001. P=2.645e-006 and P=0.0001505 for the comparisons made between groups 1&2 and groups 1&3, respectively. (**e-g**) Analysis of neutralizing antibody titers expressed as percentage of neutralization using a 1/33 dilution of sera obtained two weeks post dose 4 against SARS-CoV-2 Wu/G614 (**e**), XBB.1.5 (**f**), and SARS-CoV-1 (**g**) S VSV pseudoviruses. Each data point represents the mean values from three biological replicates. Means and SDs for each group are shown as bars (n=12 for groups 1&3 and n=11 for group2). Representative dose-response curves are shown in **Figure 4.15**.

Figure 4.13. Analysis of vaccine-elicited serum antibody binding titers against various S trimers by ELISA.

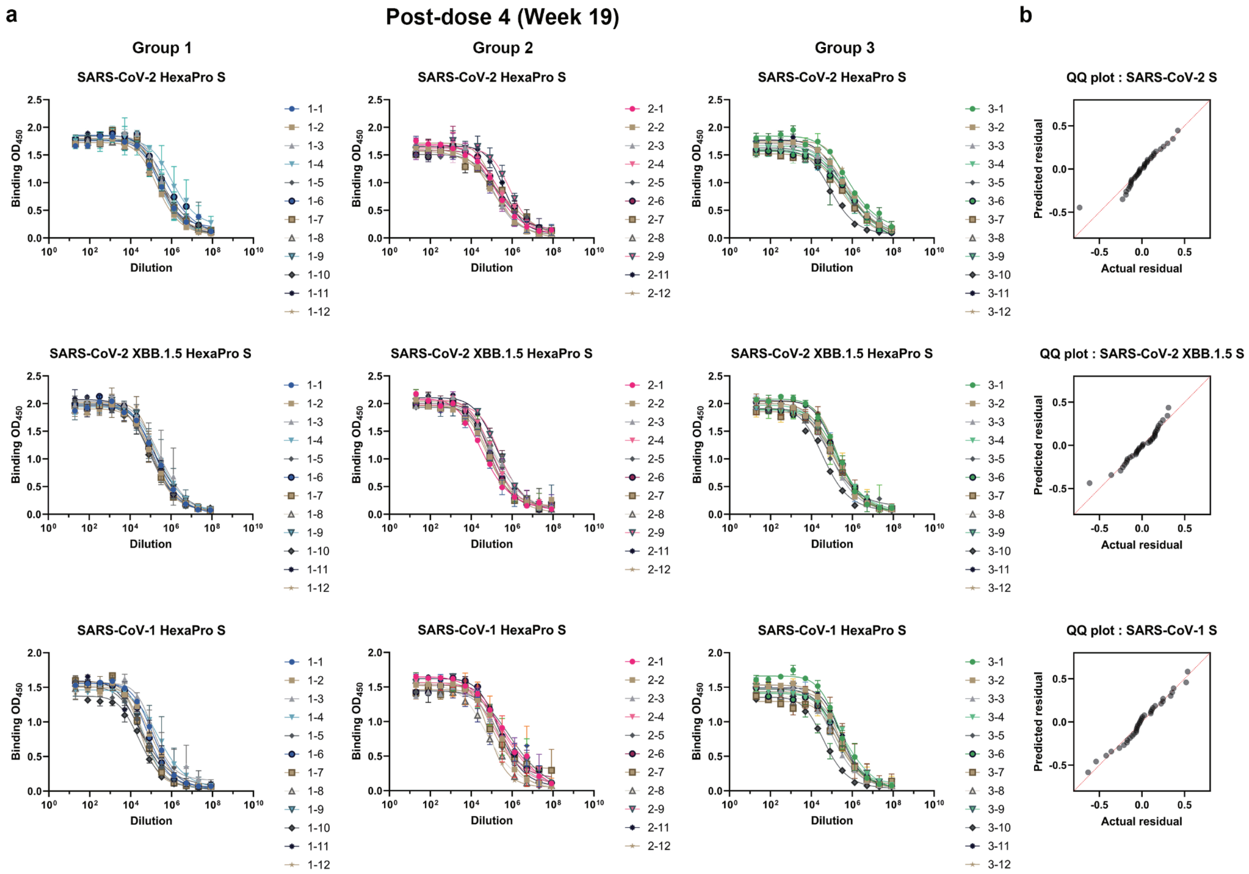

(**a**) Dose-response curves of serum antibody binding to SARS-CoV-2 Hexapro S, XBB.1.5 Hexapro S, and SARS-CoV-1 Hexapro S using sera obtained 2 weeks post dose 4. Each data point represents the mean of two technical replicates and SD are shown with bars. One representative out of two biological replicates is shown (n=12 for groups 1 &3, n=11 for group 2). (**b**) QQ plots of residuals for the mean of log(ED_{50}) values from two biological replicates of ELISA.

Figure 4.14. Analysis of vaccine-elicited serum binding titers for different IgG subclasses against SARS-CoV-2 E-69.

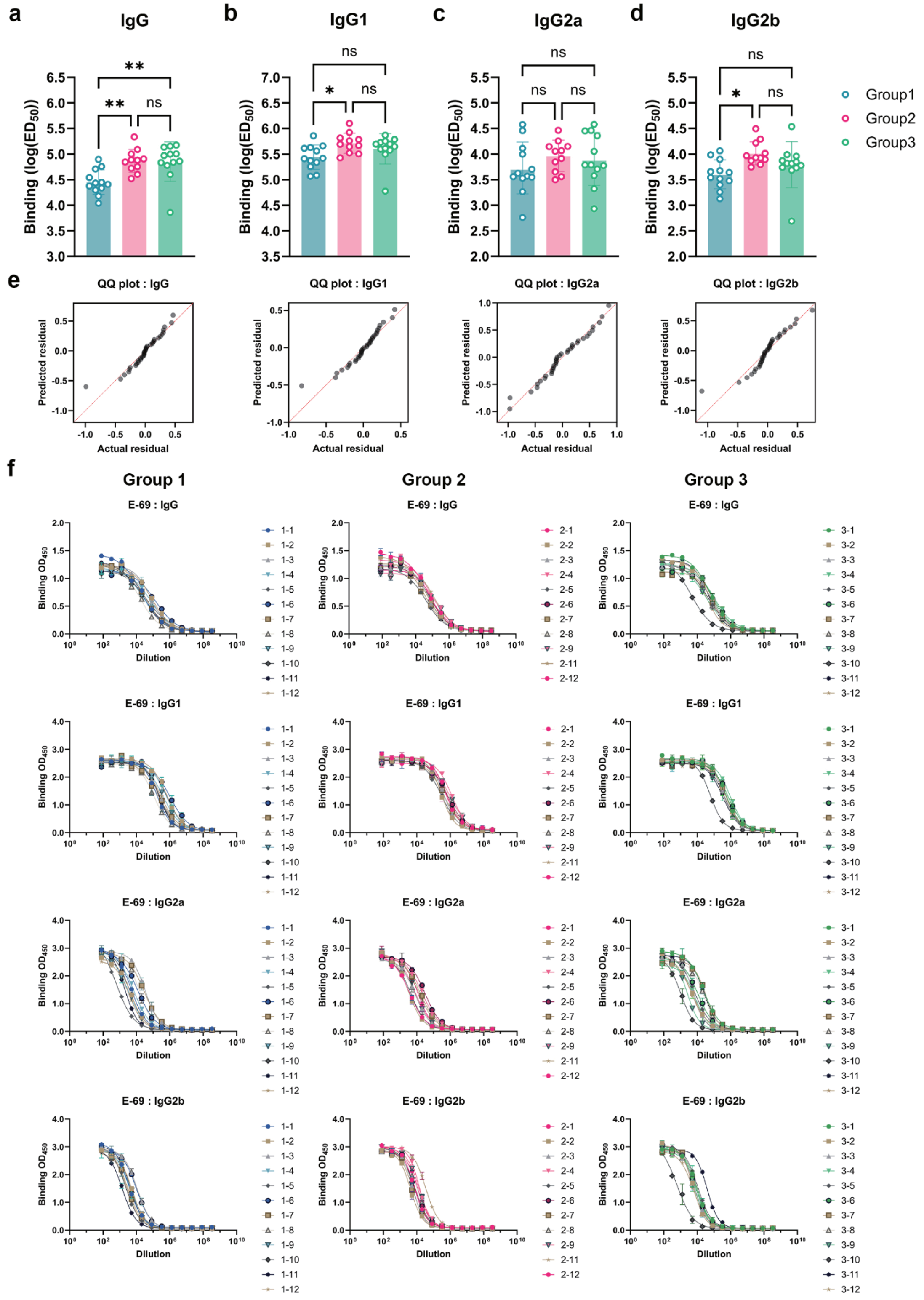

(**a-d**) Analysis of IgG (**a**), IgG1 (**b**), IgG2a (**c**), and IgG2b (**d**) binding titers against E-69 analyzed by ELISAs using sera obtained five weeks post dose 4. Geometric means are shown as bars with SD. Each data point represents the mean of two biological replicates each comprising two technical replicates. (n=12 for groups 1 &3, n=11 for group 2). (**e**) QQ plots of residuals for the mean of log(ED_{50}) values from two biological replicates of ELISA. (**f**) Dose-response curves of serum antibody binding to E-69. Each data point represents the mean of two technical replicates and SD are shown with bars. One representative out of two biological replicates is shown. (n=12 for groups 1 &3, n=11 for group 2). Comparisons between multiple groups for (**a-d**) were made by ordinary one-way analysis of variance (ANOVA) followed by Tukey's multiple comparisons test. ns : P>0.05, * : P<=0.05, ** : P <=0.01, *** : P<=0.001, **** : P<=0.0001. (**a**) P=0.0036 and P=0.0044 for the comparisons made between groups 1&2 and groups 1&3, respectively. (**b**) P=0.0277 for the comparison made between groups 1&2. (**d**) P=0.0114 for the comparison made between groups1&2.

Figure 4.15. Analysis of vaccine-elicited serum neutralizing antibody titers.

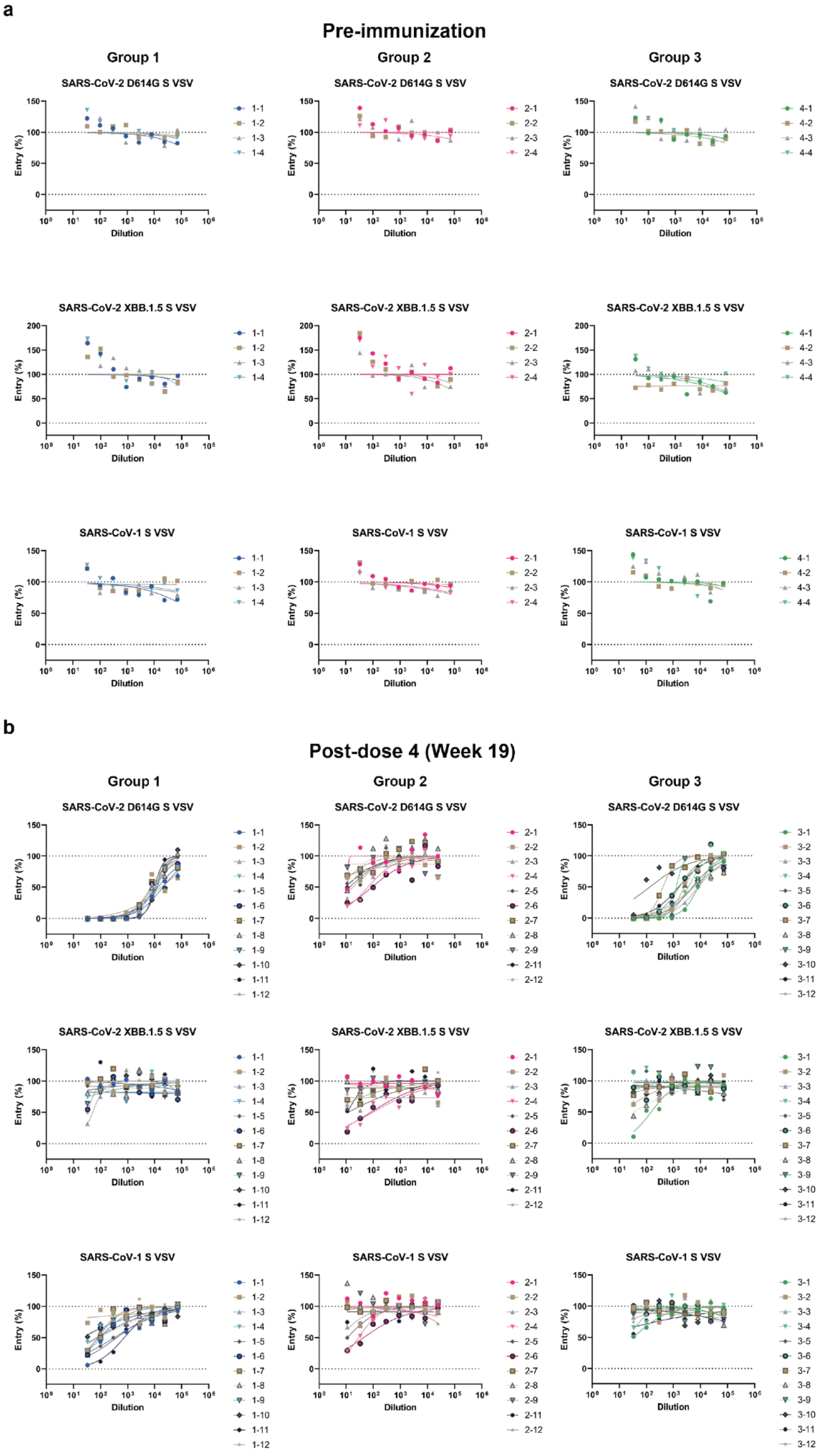

(**a-b**) Dose-response curves of serum neutralizing antibody titers against the SARS-CoV-2 Wu/G614, XBB.1.5 and SARS-CoV-1 S VSV pseudotypes using sera obtained prior to immunization (**a**) and two weeks post dose 4 (**b**). The color key indicates mouse IDs. Representative curves from one out of three biological replicates are shown.

Figure 4.16. A prefusion-stabilized SARS-CoV-2 fusion machinery (S_2 subunit) vaccine protects mice against SARS-CoV-2 XBB.1.5-induced disease.

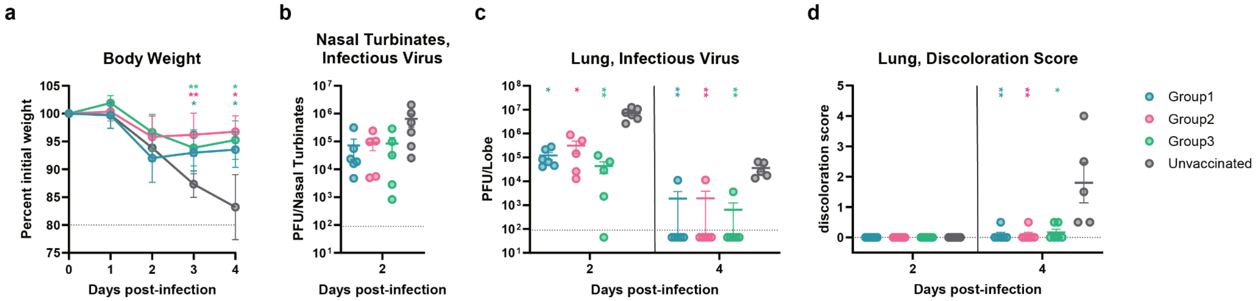

(**a**) Weight loss followed 4 days post viral challenge with SARS-CoV-2 XBB.1.5MA10. Control group corresponds to unvaccinated mice. Mean values and SD are shown (n=12 for days 0-2 for groups1 & unvaccinated and n=11 for days 0-2 for groups 2&3, and n=6 for days 3-4 for all groups except n=5 for the unvaccinated group). Comparison of percent weight loss with the control group and each of the vaccinated groups was done using two-way analysis of variance (ANOVA) followed by Sidak's multiple comparison test. ns: P>0.05, *: P<=0.05, **: P<=0.01, ***: P<=0.001, ****:P<=0.0001. For day 3, P=0.0411, P=0.0038, and P=0.0093 for the comparisons made between the unvaccinated and groups 1&2&3, respectively. For day 4, P=0.0379, P=0.0120, and P=0.0188 for the comparisons made between the unvaccinated and groups 1&2&3, respectively. (**b,c**) Quantification of replicating viral titers in the nasal turbinates (**b**) and lungs (**c**) of challenged animals at 2 and 4 days post infection, respectively. Mean values and standard error of measurement (SEM) are shown ((dpi2);n=6 for groups1 & unvaccinated and n=5 for groups 2&3, (dpi4);n=6 for groups 1&2&3 and n=5 for the unvaccinated group). For the infectious virus titer in the lung 2 days post-infection, P=0.0262, P=0.0471, and P=0.0012 for the comparisons made between the unvaccinated and groups 1&2&3, respectively. For 4 days post-infection, P=0.0030, P=0.0035, and P=0.025 for the comparisons made between the unvaccinated and groups 1&2&3, respectively. (**d**) Lung discoloration score at 2 and 4 days post infection. Mean values and SEM are shown ((dpi2);n=6 for groups1 & unvaccinated and n=5 for groups 2&3, (dpi4);n=6 for groups 1&2&3 and n=5 for the unvaccinated group). For 4 days post-infection, P=0.0061, P=0.0061, and P=0.0264 for the comparisons made between the unvaccinated and groups 1&2&3, respectively. Statistical significance compared with the control group and each of the vaccinated groups was reported using Kruskal-Wallis test followed by Dunn's multiple comparisons test (**b–d**). ns: P>0.05, *: P<=0.05, **: P<=0.01, ***: P<=0.001, ****: P<=0.0001. The experiment has not been replicated (**a–d**).

Table 4.1. List of selected sarbecovirus sequences used for conservation analysis.

Virus name	Accession Code
SARS-CoV-2	MN908947
RshSTT182	EPI_ISL_852604
GD-Pangolin	MT121216.1
RaTG13	MN996532
GX-Pangolin	EPI_ISL_410542
SARS-CoV-1 GD01	AY278489
SARS-CoV-1 Urbani	AY278741
SARS-CoV-1 BJ01	AY278488.2
SARS-CoV-1 SZ1	AY304489
WIV1	KF367457
RsSHC014	KC881005
HuB2013	KJ473814
Rs4081	KY417143
HKU3-1	DQ022305
RacCS203	MW251308
Rf4092	KY417145
Khosta-1	MZ190137
PRD-0038	QTJ30153.1
BtKY72	KY352407
RhGB01	MW719567
Khosta-2	MZ190138
RsYN04	EPI_ISL_1699444

Table 4.2. Mutations tested in the SARS-CoV-2 S$_2$ prefusion designed constructs.

Design	Residue range	HexaPro	VFLIP inter-protomer disulfide bonds	Intra-protomer disulfide bonds
C-44	686-1208	A892P, A899P, A942P, V987P	Y707C-T883C	F970C-G999C
Design	Residue range	Additional mutations to theC-44 background		
E-31	686-1208	T961F		
E-32	686-1208	D994E		
E-33	686-1208	Q1005R		
E-60	686-1208	F888P, A893P, N907E, T961F, D994Q, T998Q, Q1010M, Q1011M, I1018Y, N1023M		
E-69	686-1208	N907E, T961F, D994Q, Q1011M, I1018Y		
F-53	701-1208	N907E, T961F, D994Q, Q1011M, I1018Y		
SARS1 S$_2$	683-1190	N889E, T943F, D976Q, Q993M, I1000Y		
PRD-0038 S$_2$	684-1191	N890E, V940Q, T944F, D977Q, Q994M, I1001Y		

Table 4.3. CryoEM data collection and refinement statistics.

	E-31	E-60	E-69
Data collection and processing	EMD-43435 PDB 8VQ9	EMD-43436 PDB 8VQA	EMD-43437 PDB 8VQB
Magnification	105,000	105,000	105,000
Voltage (kV)	300	300	300
Electron exposure (e^{-}/Å^2)	63	63	63
Defocus range (µm)	-0.2 - -7.0	-0.2 - -3.0	-0.1 - -3.27
Pixel size (Å)	0.843	0.843	0.843
Symmetry imposed	C3	C3	C3
Final particle images (no.)	671,707	144,044	319,001
Map resolution (Å)	2.7	3.5	3.0
FSC threshold	0.143	0.143	0.143
Map sharpening B factor (Å^2)	-119.4	-143.9	-127.6
Validation			
MolProbity score	0.94	0.96	0.89
Clashscore	0.94	0.78	0.65
Poor rotamers (%)	0.00	0.77	0.71
Ramachandran plot			
Favored (%)	97.12	96.68	96.95
Allowed (%)	2.88	2.61	3.05
Disallowed (%)	0.00	0.71	0.00

CHAPTER 5. Optimizing prefusion-stabilized S_2 vaccines and unraveling their protection mechanism in mice

In the final chapter of this dissertation, I spotlight our various efforts to optimize the previously described sarbecovirus fusion machinery vaccines. Then, I describe how we characterized the protection mechanism of our sarbecovirus fusion machinery vaccines in mice models.

5.1 Chapter Introduction

During the COVID-19 pandemic, mRNA vaccines have demonstrated themselves as a powerful vaccine platform alternative to conventional vaccines. Although the technology appeared more than 3 decades ago, due to its innate nature, being extremely labile and rapidly degrading, made it difficult to use in vaccine development (Martinon et al., 1993; Pardi et al., 2018). Intensive research in the field and key technological innovations that followed have improved mRNA quality over the past few decades improving its stability, safety, and delivery effectiveness, making it ready for vaccine development against SARS-CoV-2 when the COVID-19 pandemic broke out. This led to the development of Spikevax® (Moderna) and Comirnaty® (Pfizer-BioNTech) in an unprecedented record-breaking timeline. Both vaccines successfully induced potent neutralizing antibodies as well as durable immune memory towards SARS-CoV-2 and a number of variants of concern (VOC) (Baden et al., 2021; Goel et al., 2021).

The overall structure of non-replicating mRNA vaccines is composed of antigen-encoding mRNA and mRNA encapsulating lipid nanoparticles (LNPs). The conventional mRNA vaccines contain 5’ cap, 5’ UTR, ORF, 3’ UTR, followed by poly(A) tail (Gote et al., 2023). 5’ cap serves to protect mRNAs from getting cleaved by exonucleases, and is essential in guiding the immune system to discern self- or endogenous mRNA (Daffis et al., 2010). 5’ UTR and 3’ UTR are involved in the overall stability of mRNA and regulating the correct translation of the mRNA (Gote et al., 2023). ORF is the region where target antigen sequences are encoded, which may carry mutations to optimize the immunogenicity of the antigen. For instance, both aforementioned mRNA vaccines for SARS-CoV-2 carry two proline mutations (2P) in the spike glycoprotein to stabilize the spike in its prefusion conformation (Jackson et al., 2020; Vogel et al., 2021). Poly(A) tail determines the lifespan of the mRNA and affects the degradation of the mRNA (Gote et al., 2023). To achieve a longer half-life, often about 100 nt poly(A) tail is added to the mRNA vaccine (Godiska et al., 2010). Nucleotides in mRNA vaccines are also modified, for example, utilization of pseudouridines, to reduce undesirable immune responses (Anderson et al., 2010) exemplified by the use of N1-methylpseudouridine modification by Spikevax® and Comirnaty® (Jackson et al., 2020; Vogel et al., 2021). Lastly, LNPs and their compositions, typically composed of ionizable cationic lipid, cholesterol, PEGylated lipid, and helper phospholipid, are optimized to achieve effective delivery of mRNA and protection of mRNA from internal degradation (Chaudhary et al., 2021).

When administered, mRNA vaccines are taken up by immune or non-immune cells in tissues via endocytosis, where they are translated into protein by the host ribosome (Lindsay et al., 2019). Translated proteins can stimulate the immune system in various ways. Proteins that get secreted out of the cell can be endocytosed by immune cells, broken down to peptides, and presented by MHC class II, resulting in CD4+ helper T cell activation (Cagigi & Loré, 2021; Pardi et al., 2018). They can also be recognized by B cells, resulting in B cell maturation (Kim et al., 2021). Proteins that are carried to the membrane surface of the cell can interact with B cell receptors (BCRs) in B cells as well (Carrasco & Batista, 2006; Gordon et al., 2014; Irvine et al., 2020). Tissue-resident antigen-presenting cells (APCs) near the injection site that have taken up the mRNA will also start producing antigens and present peptides through the MHC class 1 pathway, followed by CD8+ cytotoxic T cell activation (Kim et al., 2021). Some mRNAs that make their way to the lymph node and get taken up by APCs there will initiate priming and activation of T cells and B cells (Carrasco & Batista, 2006; Gordon et al., 2014; Irvine et al., 2020).

Viral proteins are often glycosylated, either encoded in the virus or derived from the host, giving its name viral glycoprotein (Giller et al., 1989). Glycans on the viral glycoproteins can mask epitopes as a shield that otherwise would be easily recognized by B-cell receptors (BCRs). Developing vaccine candidates using HIV-1 Env, for instance, has proven to be extremely difficult as HIV-1 Env is densely glycosylated (Schorcht et al., 2020; Sliepen et al., 2019). In the SARS-CoV-2 spike, there are 22 N-linked glycosylation sites characterized by the N-X-S/T (where X is not Proline) N-glycosylation motif, with 9 of them located in the S_2 subunit (Watanabe et al., 2020). Recently, a group of researchers have designed a vaccine candidate where they expressed SARS-CoV-2 spike ectodomain in GnTI$^-$ HEK293S cells to produce high-mannose glycoform spike, followed by treating with endoglycosidase H (Endo H) to trim off glycans to a single N-acetylglucosamine (GlcNac) which they name S_{MG} (H.-Y.

Huang et al., 2022). In the study, they vaccinated BALB/c mice with different forms of glycoform spike proteins and have shown that vaccinating mice with the S_{MG} vaccine elicited improved humoral responses, including more diverse antibody subclasses and more potent neutralizing ability (H.-Y. Huang et al., 2022). The vaccine also conferred better *in vivo* protection in Syrian hamsters challenged with SARS-CoV-2 wild type compared to the fully glycosylated spike vaccine (H.-Y. Huang et al., 2022). These data suggest that reducing the occupancy of huge, flexible glycan shields from an antigen could improve its immunogenicity.

Self-assembling protein nanoparticle scaffolds are another vaccine delivery platform with rapidly increasing uses in next generation vaccine designs (Boyoglu-Barnum et al., 2021; Kanekiyo et al., 2013; López-Sagaseta et al., 2016; Marcandalli et al., 2019; A. C. Walls et al., 2021; A. C. Walls, Fiala, et al., 2020). Through arraying multivalent antigen presentation in a regular manner, self-assembling protein nanoparticles are ideal for eliciting strong B cell receptor (BCR) signaling, resulting in improved antibody responses. They are designed to achieve high stability that does not require a cold chain supply which can serve as an advantage over mRNA vaccine platforms. A computationally designed two-component nanoparticle that readily assembles into an icosahedral nanoparticle (I53-50) upon mixing is an example of a vaccine with antigens displayed on the surface of self-assembling protein nanoparticle scaffolds (Kraft et al., 2022; Ueda et al., 2020). In our recent works with our collaborator, we have shown that displaying SARS-CoV-2 RBD on an I53-50 nanoparticle elicited potent neutralizing antibody responses that were RBD focused, overcoming the limitations of RBD being too small to be used as a vaccine candidate alone (A. C.

Walls, Fiala, et al., 2020). I53-50 can also display multiple different antigens such as sarbecovirus RBDs, either on the same nanoparticle scaffold or as a cocktail of nanoparticles (A. C. Walls et al., 2021). We have shown that this formulation of nanoparticles successfully elicited antibody responses in both mice and non-human primates, and conferred protection in mice against heterotypic SARS-CoV challenge (A. C. Walls et al., 2021). These data indicate that displaying antigens on the surface of nanoparticles is a vaccine delivery platform to consider with many advantages when optimizing a vaccine candidate.

One of the main goals of a vaccine against viruses is to elicit neutralizing antibodies that, upon encountering virions, will successfully neutralize the virus from infecting the host cells or stop the viral egress from infected cells. However, antibodies that do not show potent neutralizing activity should not be overlooked, as they can participate in vaccine-mediated protection against viruses via Fc-mediated effector functions. Fc-mediated effector functions include antibody-dependent cell-mediated cytotoxicity (ADCC), antibody-dependent cellular phagocytosis (ADCP), and complement-dependent cytotoxicity (CDC), all resulting in the clearing of virus-infected cells and virions (van Erp et al., 2019).

5.2 Antibody responses from different conformations of membrane-anchored SARS-CoV-2 S_2 mRNA-LNP vaccine

To evaluate whether delivering our prefusion-stabilized SARS-CoV-2 S_2 vaccine via the mRNA-LNP platform will elicit potent neutralizing antibodies, we designed an mRNA encoding membrane-anchored SARS-CoV-2 S_2 incorporating our prefusion-stabilizing mutations from our SARS-CoV-2 S_2 subunit E-69 vaccine (**Figure 5.1a**). We also designed the F-53 version of the membrane-anchored SARS-CoV-2 S_2 mRNA as well as the previously described C-44 (splayed-open apex SARS-CoV-2 S_2) version of the mRNA, to assess the effect of different conformations of SARS-CoV-2 S_2 on eliciting potent neutralizing antibodies (**Figure 5.1a**). We included prefusion-stabilized SARS-CoV-2 spike mRNA with 2P mutations to benchmark current vaccines. Groups of 10 mice were immunized with 4 doses of SARS-CoV-2 S_2 mRNA-LNPs or SARS-CoV-2 S mRNA-LNP (**Figure 5.1b**). One group was primed with 2 doses of SARS-CoV-2 S mRNA-LNP and boosted with 2 doses of SARS-CoV-2 S_2 mRNA-LNP to recapitulate the pre-existing immunity (**Figure 5.1b**). Sera ELISA showed all groups had comparable binding titer against F-53, indicating that delivering prefusion-stabilized S_2 in membrane anchored format via mRNA-LNP successfully elicited antibodies in mice (**Figures 5.1c, 5.2**). Groups that received prefusion-stabilized S_2 in any conformation showed higher binding titer against F-53 compared to the group that received SARS-CoV-2 S2P, which is in line with our previous data with protein subunit vaccine of each immunogens (**Figures 5.1c, 5.2, and Figure 4.14a**). Then, we ran inhibition ELISA using S_2 targeting monoclonal antibodies to broadly map regions of epitopes targeted by the elicited polyclonal antibodies (**Figure 5.1d**). All groups that were immunized with either S or S_2 elicited antibodies that have epitopes overlapping with 76E1 (fusion-peptide targeting monoclonal antibody) (Sun et al., 2022), S2P6 (stem-helix targeting mAb) (Pinto et al., 2021), and 54043-5 (prefusion apex targeting mAb) (Johnson et al., 2024) indicating that the conformation of prefusion-stabilized S_2 whether it has extended N terminus (E-69), or splayed open apex (C-44), truncated N terminus and closed apex (F-53) does not significantly impact antibody responses within the set of S_2 targeting monoclonal antibodies that we have tested (**Figures 5.1d,e, 5.3**). Neutralization assays were performed using VSV pseudotyped with SARS-CoV-2 D614G spike. Conforming to previous findings, only the SARS-CoV-2 S immunized group and hybrid group elicited potent neutralizing antibodies, whereas all SARS-CoV-2 S_2 only immunized groups showed no sign of neutralizing antibodies (**Figures 5.1f, 5.4**). These data suggest that regardless of delivery method, whether or not the immunogen is delivered as soluble protein subunit or membrane-anchored full-length S or S_2 encoded by mRNA, full length spike that included the S_1 region was still the most effective in eliciting neutralizing antibodies. Also, comparing different conformations of prefusion-stabilized S_2, whether or not the apex is splayed open or closed, didn't have any impact on the elicited antibody's ability to neutralize.

5.3 Antibody responses from deglycosylated prefusion-stabilized SARS-CoV-2 S_2 protein subunit vaccine

To investigate whether glycans had an effect in eliciting more potent neutralizing antibodies in prefusion-stabilized SARS-CoV-2 S_2 protein subunit vaccine, we designed several constructs that lacked N-linked glycosylation sites by replacing asparagine (N) of NxS/T N-linked glycosylation motif with glutamine (Q) (**Figure 5.5a**). We designed constructs that lacked all glycosylation sites in the SARS-CoV-2 S_2 subunit or only in the stem helix region with varying trimerization domains. We kept two N-glycosylation sites, N801 and N1194 intact in these designs since those two sites have been reported to be critical in proper expression and protein folding of the spike (**Figure 5.5a**) (H.-Y. Huang et al., 2022). However, all designed constructs were poorly expressed in Expi293F cells, aligning with previous reports on the possible role of glycans in proper protein folding and subsequent trafficking of the protein (**Figure 5.5b**). As an alternative way to generate prefusion-stabilized SARS-CoV-2 S_2, we decided to first express our leading prefusion-stabilized SARS-CoV-2 S_2 candidate, F-53, then to truncate N-linked glycans by treating the recombinant protein with Peptide-N-Glycosidase F (PNGaseF) (**Figure 5.5c,d**). We confirmed that the deglycosylated F-53 retained its prefusion-stabilized form by ELISA with prefusion spike-recognizing monoclonal antibody 54043-5 IgG (Johnson et al., 2024) and negative stain EM (**Figure 5.5e,f**). However, mass spectrometry showed that the enzyme treatment was not fully complete, possibly due to a thick glycan shield hindering the access of the enzyme under native conditions and treated F-53 still had mixed glycosylation patterns **(Figure 5.5g)**.

To study the immune response of the partially deglycosylated SARS-CoV-2 S_2 subunit vaccine immunogen, we immunized groups of 10 mice with 1 µg doses of SARS-CoV-2 S2P or F-53 or deglycosylated F-53 or 5 µg doses of F-53 or deglycosylated F-53 (**Figure 5.6a**). Sera were collected 2 weeks post boost, and antibody titers and epitope mapping were performed using ELISA (**Figures 5.6b,c, 5.7, 5.8**). As expected, group 1 that received SARS-CoV-2 S2P showed the highest binding titer against SARS-CoV-2 S2P but the lowest titer against prefusion-stabilized SARS-CoV-2 S_2 F-53 (**Figure 5.6b**). However, no significant difference was observed between the F-53 groups and partially deglycosylated F-53 groups (**Figure 5.6b**). All groups elicited antibodies that have epitopes overlapping with fusion-peptide targeting monoclonal antibody 76E1 (Sun et al., 2022), stem-helix targeting mAb S2P6 (Pinto et al., 2021), and prefusion apex targeting mAb 54043-5 (Johnson et al., 2024) (**Figure 5.6c**). Neutralization assays were performed using VSV pseudotyped with SARS-CoV-2 D614G spike (**Figure 5.6d**). SARS-CoV-2 S2P vaccinated group 1 showed the most potent neutralizing ability as anticipated (**Figures 5.6d, 5.9**). Groups that received F-53, especially higher doses, showed signs of neutralizing ability at the most concentrated sera dilution tested, concurring with our previous work with E-69 as an immunogen (**Figure 5.6d, 5.9**). However, two groups that received deglycosylated F-53 did not show any signs of neutralizing activity (**Figure 5.6d, 5.9**). These data suggest that removing glycan shields, at least partially, in prefusion-stabilized SARS-CoV-2 S_2 F-53 has no significant impact on eliciting more potent neutralizing antibodies.

5.4 Antibody responses from protein nanoparticle vaccine displaying prefusion-stabilized sarbecovirus S_2

Following these observations, we set out to evaluate whether delivering sarbecovirus S_2 subunits displayed on the surface of self-assembling nanoparticles would elicit more potent neutralizing antibodies. We chose I53-50 as our nanoparticle platform, which, from our previous works, have shown to elicit potent neutralizing antibodies when SARS-CoV-2 RBD was displayed on its surface (A. C. Walls, Fiala, et al., 2020). We designed our prefusion-stabilized SARS-CoV-2 S_2 F-53, SARS-CoV-1 S_2, or PRD-0038 S_2 fused to I53-50A, respectively, using 16 GS linkers to allow a single prefusion-stabilized S_2 trimer to be displayed on a single I53-50A trimer complex (**Figure 5.10a**). All three sarbecovirus prefusion-stabilized S_2 I53-50A components were successfully expressed and then mixed with 1.1:1 molar ratio of I53-50B components purified from *E.coli* to initiate nanoparticle assembly (**Figure 5.10a,b**). We also generated a mosaic nanoparticle in which a single nanoparticle displays all three sarbecovirus prefusion-stabilized S_2 and a cocktail of nanoparticles, which is a mixture of all three sarbecovirus prefusion-stabilized S_2 nanoparticles assembled before mixing (**Figure 5.10a**). Excess components were removed by size exclusion chromatography (**Figure 5.10b**). Negative stain images showed that all three sarbecovirus S_2 I53-50 nanoparticles successfully formed, displaying prefusion-stabilized S_2 subunits on their surfaces, and remained intact post freeze-thaw cycle (**Figure 5.10c**). Assembled S_2 nanoparticles retained their antigenicity, as described in our previous work (Lee et al., 2024), and survived the post freeze-thaw cycle (**Figure 5.10d**). Dynamic light scattering (DLS) confirmed the monodispersity of assembled S_2 nanoparticles post freeze-thaw cycle (**Figure 5.10e**).

To examine antibody responses from sarbecovirus prefusion stabilized S_2 and S_2 nanoparticles, we immunized groups of 8 mice with two doses of 1 μg of SARS-CoV-2 S2P, 5 μg of sarbecovirus prefusion stabilized S_2, or a 5 μg antigen dose of sarbecovirus prefusion stabilized S_2 nanoparticles (**Figure 5.11a**). All groups, including S_2 nanoparticle groups, elicited comparable binding titers towards SARS-CoV-2 S_2 F-53, SARS-CoV-1 S_2, and PRD-0038 S_2 (**Figures 5.11b, 5.12, 5.13, 5.14**). Inhibition ELISA showed that all groups elicited antibodies with epitopes that overlap with well-characterized S_2 targeting monoclonal antibodies (**Figures 5.11c, 5.15, 5.16, 5.17**). Both the mosaic nanoparticle group and the cocktail nanoparticle group showed binding to breadth in epitopes compared to the groups that received S2P or a single type of S_2 (**Figures 5.11c, 5.15, 5.16, 5.17**). These data show that our optimized version of

SARS-CoV-2 prefusion-stabilized S_2 F-53 and two other sarbecovirus prefusion-stabilized S_2 (SARS-CoV-1 and PRD-0038) described in our previous work (Lee et al., 2024), along with prefusion-stabilized S_2 displaying nanoparticles, successfully elicited antibody responses in mice.

As expected, the SARS-CoV-2 S2P vaccinated group was able to elicit potent neutralizing activity after two doses of immunization against the pseudovirus neutralization assay with SARS-CoV-2 D614G but not against SARS-CoV-1 or PRD-0038 (**Figures 5.11d, 5.18, 5.19, 5.20**). Neither the S_2-vaccinated nor the S_2 nanoparticle-vaccinated group elicited detectable neutralizing antibodies against SARS-CoV-2 D614G, SARS-CoV-1, and PRD-0038 pseudoviruses, with the exception of the group that received SARS-CoV-2 S_2 F-53, in which a few mice started to show signs of neutralization at the highest serum concentrations tested (**Figures 5.18, 5.19, 5.20**). These data indicate that multivalent display of prefusion-stabilized S_2 does not result in potent neutralizing antibody responses.

5.5 Protection mechanism of prefusion-stabilized sarbecovirus S_2 subunit vaccine in BALB/c mice

Our recent works on exploring different vaccine platforms and optimizing the antigens for sarbecovirus S_2 vaccine candidate, as described in the previous sections, showed that all three approaches of delivering vaccine as mRNA-LNP encoding membrane-anchored SARS-CoV-2 S_2, partial-deglycosylation of protein subunit SARS-CoV-2 S_2, and displaying prefusion-stabilized sarbecovirus S_2 on protein nanoparticle did not significantly elicit potent neutralizing antibodies. However, in our previous work, we have shown that prefusion-stabilized SARS-CoV-2 S_2 subunit vaccine protected mice against challenge with immune-evasive XBB.1.5 variant despite little to no *in vitro* pseudovirus neutralizing activity (Lee et al., 2024). We hypothesized that the mechanism of protection conferred from antibodies targeting the highly conserved S_2 region might not be heavily dependent on neutralizing antibodies, but more on host immune responses via Fc-mediated effector functions. To test our hypothesis, we first vaccinated groups of 8 BALB/c mice each with two doses of 1 µg SARS-CoV-2 S2P, 1 µg or 5 µg of SARS-CoV-2 S_2 F-53, or prefusion-stabilized SARS-CoV-1 S_2 described in the previous section, respectively, along with one group of unvaccinated mice as a control group (**Figure 5.21a**). Sera were collected 3 weeks post-boost for further analysis. First, we ran ELISA with the sera samples against multiple different sarbecovirus spike constructs (**Figure 5.22**). All vaccinated groups elicited antibodies with comparable binding titers targeting SARS-CoV-2 S6P (**Figure 5.22a,b**). Groups that received S_2 vaccines elicited comparable binding titers to SARS-CoV-2 S_2, SARS-CoV-1 S6P, and SARS-CoV-1 S_2, with the group that received SARS-CoV-2 S2P showing relatively weaker binding titers compared to the S_2-receiving groups (**Figure 5.22a,b**). This data again indicates that vaccinating with highly conserved regions elicits antibodies that are less susceptible to antigenic changes. Binding to EFIC was significantly weak in all vaccinated groups (**Figure 5.22a,b**). Polyclonal antibodies that recognize SARS-CoV-1 spike or SARS-CoV-1 spike S_2 subunit exhibited binding to mouse FcɣRIV which corresponds to human FcɣRIII in terms of functionality, indicating possible contribution of antibody-dependent cellular cytotoxicity (ADCC) involved in protection in mice (**Figure 5.22c,d**). Consistent with previous works with VSV pseudovirus neutralization, the group that received SARS-CoV-2 S2P showed potent neutralizing ability against authentic SARS-CoV-2 D614G virus, whereas groups that received S_2 subunit vaccines did not show strong neutralizing activity against both SARS_CoV-2 D614G and SARS-CoV-1 virus in real-virus neutralization assay (**Figure 5.21b**). Concurrently, the trend stayed the same when we performed a pseudovirus neutralization assay with pooled sera from each group, with signs of neutralization starting to be detectable at the highest serum dilution tested in groups that received SARS-CoV-2 S2P and SARS-CoV-1 S_2 against SARS-CoV-1 S pseudotyped VSV neutralization assay (**Figure 5.23**).

Collected sera were pooled for each immunogen group, then passively transferred to groups of 5 wild type BALB/c mice and groups of 6 FcɣR KO mice (**Figure 5.21a**). Mice were challenged with mouse-adapted 10^4 PFU of SARS-CoV MA15 virus 12 hours post passive transfer. We chose SARS-CoV-1 for our challenge virus for 1) its being further deviant and more immune evasive from SARS-CoV-2 Wu/1 and 2) to test our SARS-CoV-1 S_2 immunogen candidate that has been prefusion-stabilized through our broadly generalizable prefusion stabilizing strategy. Weight loss was monitored for all animals until 4 days post-infection. WT mice that received sera from 5 μg of either SARS-CoV-2 S_2 or SARS-CoV-1 S_2 subunit vaccinated mice showed the biggest reduction in weight loss compared to WT mice that received sera from unvaccinated mice, followed by 1 μg of SARS-CoV-2 S_2, then SARS-CoV-2 S2P vaccinated mice sera groups (**Figure 5.21c**). However, no such protection was observed in FcɣR KO mice groups (**Figure 5.21d**). WT mice that received sera from 5 μg of either SARS-CoV-2 S_2 or SARS-CoV-1 S_2 subunit showed the lowest lung congestion score, followed by 1 µg of SARS-CoV-2 S_2, SARS-CoV-2 S2P, and unvaccinated mice, in line with the body weight loss trend (**Figure 5.21e**). This trend was significantly not apparent in FcɣR KO mice (**Figure 5.21f**). Groups that received vaccinated mice sera had overall lower infectious virus titer in lung compared to unvaccinated mice sera group in WT mice whereas no such strong relationship was observed in FcɣR KO mice (**Figure 5.21g,h**). These data showed that first, our prefusion-stabilized SARS-CoV-2 S_2 subunit vaccine conferred protection in mice against SARS-CoV-1, which is even more distantly related to SARS-CoV-2 compared to SARS-CoV-2 XBB.1.5 from our previous study. Second, our prefusion-stabilized SARS-CoV-1 S_2 subunit confers protection against vaccine-matched SARS-CoV-1 virus, highlighting the broadly applicable prefusion stabilization strategy and its efficacy as a vaccine candidate. Lastly, our prefusion-stabilized S_2 subunit vaccine protects mice against SARS-CoV-1 challenge mainly via Fc-mediated effector functions despite low to non-detectable levels of neutralizing antibodies.

5.6 Chapter Discussion

Select fusion machinery targeting monoclonal antibodies that have been discovered exhibit potent virus-neutralizing activity with their IC_{50} values ranging approximately from tens of ng/mL to tens of µg/mL against SARS-CoV-2 (Chou et al., 2005; C.-J. Li & Chang, 2023; Lip et al., 2006; Sui et al., 2004; W.-L. Wu et al., 2022). However, they are generally less potent than RBD targeting neutralizing antibodies, which effectively block viral protein engagement to the host cell receptor (Chou et al., 2005; C.-J. Li & Chang, 2023; Lip et al., 2006; Sui et al., 2004; W.-L. Wu et al., 2022). In our efforts to optimize our prefusion-stabilized sarbecovirus S_2 vaccine to elicit potent neutralizing antibodies, we explored different platforms of vaccine delivery and further antigen engineering.

Our prefusion-stabilized fusion machinery vaccine delivered as mRNA encapsulated in LNPs elicited strong antibody responses to S_2 subunit regardless of open or closed conformation of the apex. Despite the efficacy of mRNA vaccines, they need a cold chain supply system, which is a factor that vaccine developers should take into consideration to optimize other types of platform for logistical reasons. For this reason, combined with the efficacy in multivalent antigen presentation and effective modularity, we tried displaying our prefusion-stabilized S_2 displayed on a self-assembling protein nanoparticle. All of our prefusion-stabilized sarbecovirus S_2 nanoparticle vaccines successfully elicited antibody responses. However, both S_2 delivered by mRNA or protein nanoparticles did not elicit potent neutralizing antibodies.

Our prefusion-stabilized SARS-CoV-2 S_2 protein subunit vaccine that partially lacked N-linked glycans was not capable of eliciting potent neutralizing antibodies and did not outperform the fully glycosylated version in this aspect. Although, with the caveat of incomplete deglycosylation, this is concurrent with another work that reported delivering glycan lacking in soluble spike protein did not elicit potent neutralizing antibodies (Ng et al., 2022). Another study reported delivering S_2 that lacked glycosites in the S_2 or stem region as mRNA elicited detectable neutralizing antibodies (Cheng et al., 2023). Regardless, post-production enzymatic treatment may yield an inconsistent immunogen profile, which is undesirable for a vaccine candidate as in our case of treating with PNGaseF. Further optimization on construct design would be a more viable path forward. Furthermore, whether or not removing glycans would be beneficial for revealing cryptic epitopes requires further study, as those epitopes being easily accessible could also result in hindering BCR maturation and reducing antibody efficacy against the native virion.

Moreover, interestingly, neither SARS-CoV-2 S2P nor S_2 vaccines elicited strong binding titers against EFIC. These data, combined with our data from the mRNA-LNP vaccine study with different conformations of prefusion-stabilized S_2, whether the apex being open or closed, raise questions about sarbecovirus fusion machinery fusion intermediates. These data suggest that alternative forms of fusion machinery during the fusion process might be able to present epitopes that are either too transient or not accessible in prefusion-stabilized form highlighting the need for better understanding of the sarbecovirus fusion process and vaccine optimization.

Nonetheless, our prefusion-stabilized S_2 vaccine conferred *in vivo* protection in mice against SARS-CoV-1 challenge, again highlighting, along with the previous XBB.1.5 challenge data, the efficacy of the vaccine targeting the highly conserved region. Immune responses and protection are often the result of multiple, synergetic mechanisms. We have demonstrated that antibodies targeting the fusion machinery-even those with little to no neutralizing activity- still can provide significant protection against the virus by utilizing Fc-mediated effector functions.

5.7 Methods

Cell lines

Cell lines used in this study were obtained from HEK293T (ATCC, CRL-11268), Expi293F (Thermo Fisher Scientific, A145277) and VeroE6-TMPRSS2. Cells were cultured in 10% FBS, 1% penicillin-streptomycin, 8 µg/mL Puromycin (applicable for Vero cells, only) DMEM at 37°C, 5% CO_2. None of the cell lines were authenticated or tested for mycoplasma contamination.

Production of recombinant S_2 antigen proteins

Prefusion-stabilized S_2 antigens were recombinantly expressed as described previously (Lee et al., 2024). In brief, each S_2 construct was produced in Expi293F cells (ThermoFisher Scientific) and cultured at 37°C in a humidified 8% CO_2 incubator with constant rotation at 130 RPM using Expi293 Expression Medium (ThermoFisher Scientific). DNA transfections were conducted using the ExpiFectamine 293 Transfection Kit (ThermoFisher Scientific) protocols and materials and cultivated for five days before harvest. Cell culture supernatants were clarified by centrifugation and proteins were harvested using HisTrap™ High Performance Ni Sepharose columns (Cytiva). Proteins were washed using 10-15 CVs of buffer containing 25mM Tris, 150mM NaCl, 20mM Imidazole pH 8.0 followed by elution with 10-15 CVs of buffer containing 25mM Tris, 150mM NaCl, 300mM Imidazole pH8.0. Eluates were buffer exchanged and concentrated into 20mM Tris, 150mM NaCl, pH 8.0 using Amicon Ultra-15 Centrifugal Filter Unit (10 kDa) (Millipore). Gel filtration was performed to remove unfolded or aggregated protein thus samples were each run through a Superose-6 Increase 10/300 GL column (Cytiva)) equilibrated in 20mM Tris, 150mM NaCl, pH8.0. Main peaks were collected and protein was snap-frozen and stored at

-80°C with some set aside for stability tests. Purified proteins for immunogenicity study were tested for endotoxin levels using Limulus Amebocyte Lysate (LAL) cartridges (Charles River PTS201F).

Production of deglycosylated S_2 and mass spectrometry

To deglycosylate native F-53, we treated 20 µg of the F-53 protein with 2µL of GlycoBuffer 2 (New England Biolab), with the final volume of 20 µL. Then, 2 µL of PNGaseF (New England Biolab) was mixed into the mixture. The mixture was incubated at 37°C for 22 hours followed by size exclusion chromatography to purify the treated sample. Purified protein samples were treated overnight with Trypsin or GluC with 1x lysis buffer, followed by desalting with StrataX. Mass spectrometry was performed using the treated samples with HCD-pd-EThcD (Higher-energy Collisional Dissociation-product dependent-Electron Transfer/Higher-energy Collision Dissociation) method. Intensity was summed across glycan composition and the plot was generated by considering all unique glycopeptides taking the highest intensity if glycopeptide sampled was bigger than 1.

Production of S_2 displaying self-assembled protein nanoparticles

Purified S_2-I53-50A proteins were mixed with I53-50B components at a molar ratio of 1.1:1 for 30 min at room temperature, rotating. After incubation, the mixture was purified with size exclusion chromatography and stored in buffer condition of 50 mM Tris 50 mM Glutamate, 150 mM NaCl, 4.5% Glycerol pH 7.4. Dynamic light scattering (DLS) (Unchained Labs) was performed with samples diluted to 1 mg/mL in the same buffer.

Production of biotinylated S_2 targeting monoclonal antibodies

S_2 targeting monoclonal antibodies were biotinylated using EZ-Link Sulfo-NHS-SS-Biotin (ThermoScientific). IgGs and the reconstituted EZ-Link Sulfo-NHS-SS-Biotin were mixed and incubated on ice for 2h. Extra reagents were removed by running size exclusion chromatography.

Negative stain electron microscopy preparation and data collection

Carbon copper formvar grids (Ted Pella 01754-F) were glow discharged using a Gloqube Plus (Quorum) at 20mA for 30 s promptly followed by the addition of 3 μL of a prefusion-stabilized S_2 displaying I53-50 protein nanoparticle and deglycosylated F-53 diluted to a concentration of 0.01mg/mL and 0.03mg/mL, respectively. After 1 min the protein was aspirated using filter paper and 3 μL of 2% uranyl formate was applied and quickly removed for washing. Another 3 μL of uranyl formate was added to the grid and left to stain for 30 s before drying with filter paper and left to further air dry before imaging. Automated data collection was carried out using Leginon at a nominal magnification of 67,000 with a pixel size of 1.6 Å. Each micrograph was acquired for 500-900ms. Negative stain data was processed using CryoSPARC. Automatic particle picking and extraction were performed using CryoSPARC for deglycosylated F-53 dataset. Particle images were extracted for subsequent 2D classifications.

Monoclonal antibody ELISAs

Monoclonal antibody ELISAs were performed as previously described (Lee et al., 2024). In brief, 30 µl of the proteins at 3 µg/mL were plated onto 384-well Nunc Maxisorp plate (ThermoFisher, 464718) in 1x TBS and incubated 1 h at 37°C followed by slap drying and blocking with 80 µL of Casein for 1 h at 37°C. After incubation, plates were slapdried and 1:4 serial dilutions of the corresponding mAbs starting from 0.1mg/ml were made in 30 µl TBST, added to the plate and incubated at 37°C for 1 h. Plates were washed 4x in TBST and 30 µl of 1:5000 Goat anti-Human IgG Fc Secondary Antibody, HRP (Thermo Fisher, A18817) were added to each well and incubated at 37°C. After 1 h, plates were washed 4x in TBST and 30 µl of TMB (SeraCare) was added to every well for 2 min at room temperature. Reactions were quenched with the addition of 30 µl of 1 N HCl. Plates were immediately read at 450 nm on a BioTek Neo2 plate reader and data was plotted and fit in Prism 9 (GraphPad) using nonlinear regression sigmoidal, 4PL, X is the concentration to determine EC_{50} values from curve fits.

Immunogenicity

Female BALB/c mice were purchased from Envigo (order code 047) at 7weeks of age and were maintained in a specific pathogen-free facility within the Department of Comparative Medicine at the University of Washington, Seattle, accredited by the Association for Assessment and Accreditation of Laboratory Animal Care (AAALAC). Animal experiments were conducted in accordance with the University of Washington's Institutional Animal Care and Use Committee. Vaccinated mice were bled via the submental route and blood was collected in serum separator tubes (BD # 365967) and rested for 30 min at room temperature for coagulation. Serum tubes were then centrifuged for 10 min at 2000 x g and serum was collected and stored at -80°C until use.

For mRNA-LNP immunogenicity study, 10 mice per group were injected intramuscularly with respective immunogens at weeks 0, 4, 8, and 12. mRNAs were synthesized in TriLink and reconstituted into lipid nanoparticles in Acuitas. mRNA-LNP immunogens were diluted in DBPS (Gibco) prior to the injection to respective dose (E-69 10 µg, E-69 5 µg, F-53 5 µg, C-44 5 µg, SARS-CoV-2 S2P 1 µg). One group was primed twice with 1 µg of SARS-CoV-2 S2P followed by two boost doses of 10 µg of E-69. Sera was collected at weeks 2, 6, 10, 14, and 19.

For deglycosylated F-53 immunogenicity study, 10 mice per group were injected subcutaneously with respective immunogens at weeks 0, 4, and 10. Immunogens were diluted in PBS (Gibco) prior to the injection to respective dose concentrations (SARS-CoV-2 S2P 1 µg, SARS-CoV-2 S_2 F-53 1 µg or 5 µg, and deglycosylated SARS-CoV-2 S_2 F-53 1 µg or 5 µg). Immunogens were mixed with 1:1 volume ratio of AddaVax before the injection. Sera was collected at weeks 2, 6, 12, and 14.

For S_2 displaying protein nanoparticle immunogenicity study, 8 mice per group were injected subcutaneously with respective immunogens at weeks 0 and 3. Immunogens were diluted in the same buffers the samples were prepared in, respectively, prior to the injection to respective dose concentrations (SARS-CoV-2 S2P 1 µg and 5 µg antigen dose of sarbecovirus S_2s and sarbecovirus S_2 I53-50s). Immunogens were mixed with 1:1 volume ratio of AddaVax before the injection. Sera was collected at weeks 2, 5, and 13.

Serological ELISAs

For serological ELISAs, 30 μL of assorted proteins (SARS-CoV-2 S6P, SARS-CoV-2 S2P, SARS-CoV-2 S_2 F-53, SARS-CoV-2 EFIC H-30, SARS-CoV-1 S6P, SARS-CoV-1 S_2, PRD-0038 S_2) at 3 μg/mL were placed into 384-well Nunc Maxisorp plates (ThermoFisher, 464718) in 1x PBS and incubated overnight at 4°C. The next day, plates were slap dried and blocked with 80 μL of Casein for 1 h at 37°C. Afterward, plates were once again slap-dried and a 1:4 serial dilution of our immunized mouse sera was performed starting from 1:20 dilution in 30 μL of TBST and incubated at 37°C for 1 h. Plates were then washed 4x in TBST and 30 μL of 1:5000 Goat antimouse IgG (H + L) Secondary Antibody HRP (ThermoFisher 62-6520) were added to each well and incubated at 37°C for 1 h. Plates were then washed 4x in TBST and 30 μL of TMB (SeraCare) was added to each well and allowed to sit for 2min at room temperature. TMB reactions were quenched with 30 μL of 1 N HCl and immediately read at 450 nm on a BioTek Neo2 plate reader and data plotted and fit in Prism 10 (Graphpad) using nonlinear regression sigmoidal, 4PL, X is the concentration to determine ED_{50} values from curve fits.

Serological inhibition ELISAs

For inhibition ELISA assays, 30 μL of F-53 at 0.5 μg/mL was coated in 384-well Nunc Maxisorp plates (ThermoFisher, 464718) in 1x PBS and incubated overnight at 4°C. The next day, plates were slap dried and blocked with 80 μL of Casein for 2 h at 37°C. Afterward, plates were once again slap-dried and a 1:4 serial dilution of our immunized mouse sera was performed starting from 1:5 dilution in 30 µL of TBST and incubated at 37°C for 1 h. Plates were incubated at 37°C for 1h followed by slap-dry and 4x wash in TBST. 30 µL of S_2 targeting monoclonal antibodies diluted to previously determined EC_{50} in TBST was added to the plate and the mixture was incubated at 37°C for 1h. After 1h, the plate was slap-dried and washed 4x in TBST. Plates were once again slap-dried and washed followed by addition of 30 µL of 1:2,000 diluted UltraStreptavidin-HRP (ThermoFisher) was added. The plates were incubated 37°C for 1 h followed by slap-drying and washing 4x in TBST. Plates were then washed 4x in TBST and 30 µL of TMB (SeraCare) was added to each well and allowed to sit for 2min at room temperature. TMB reactions were quenched with 30 µL of 1 N HCl and immediately read at 450 nm on a BioTek Neo2 plate reader and data plotted and fit in Prism 10 (Graphpad) using nonlinear regression log(inhibitor) vs normalized response – variable slopes. Signals from the wells that did not receive mAbs were defined as 100% blocking and signals from the wells that received mAbs were defined as 0% blocking. The area under the curve was calculated using Prism 10 (Graphpad).

Serological ELISAs with mouse FcɣRIV

For mouse FcɣRIV binding ELISA assays, 30 µL of SARS-CoV-1 S6P and SARS-CoV-1 S_2 at 3 µg/mL were coated into 384-well Nunc Maxisorp plates (ThermoFisher, 464718) in 1x PBS and incubated overnight at 4°C. The next day, plates were slap dried and blocked with 80 µL of Casein for 1 h at 37°C. Afterward, plates were once again slap-dried and a 1:4 serial dilution of our immunized mouse sera was performed starting from 1:20 dilution in 30 µL of TBST and incubated at 37°C for 1 h.

Plates were then washed 4x in TBST and 30 µL of biotinylated mouse FcɣRIV (SinoBiological) were added and incubated at 37°C for 1 h. Plates were once again slap-dried and washed followed by addition of 30 µL of 1:2,000 diluted UltraStreptavidin-HRP (ThermoFisher) was added. The plates were incubated 37°C for 1 h followed by slap-drying and washing 4x in TBST. Plates were then washed 4x in TBST and 30 µL of TMB (SeraCare) was added to each well and allowed to sit for 2min at room temperature. TMB reactions were quenched with 30 µL of 1 N HCl and immediately read at 450 nm on a BioTek Neo2 plate reader and data plotted and fit in Prism 10 (Graphpad) using nonlinear regression sigmoidal, 4PL, X is the concentration.

Production of VSV pseudoviruses

SARS-CoV-2 D614G S, SARS-CoV-1 S, and PRD-0038 S VSV pseudoviruses were produced using HEK293T cells seeded on BioCoat Cell Culture Dish: poly-D-Lysine 100mm (Corning). Cells were transfected with respective S constructs using Lipofectamine 2000 (Life Technologies) in Opti-MEMtransfection medium. After 5 h of incubation at 37°C with 5% CO_2, cells were supplemented with DMEM containing 10% of FBS. On the next day, cells were infected with VSV (G*ΔG-luciferase) for 2 h, followed by five time wash with DMEM medium before the addition of anti-VSV G antibody (I1-mouse hybridoma supernatant diluted 1:40, ATCC CRL-2700) and medium. After 18-24h of incubation at 37°C with 5% CO_2, pseudoviruses were collected and cell debris was removed by centrifugation at 3000 x g for 10min. Pseudoviruses were further filtered using a 0.45 µm syringe filter and concentrated 10x prior to storage at -80°C.

Neutralization assays

For SARS-CoV-2 D614G S VSV and SARS-CoV-1 S VSV neutralization, VeroE6-TMPRSS2 cells in DMEM supplemented with 10% FBS, 1% PenStrep, and 8 µg/mL Puromycin were seeded at 36,000 cells/well into 96-well plates [3610] (Corning) and incubated overnight at 37°C. For PRD-0038 S VSV neutralization, HEK293T cells transfected 1 day prior with *R. alcyone* ACE2 in DMEM supplemented with 10% FBS, 1% PenStrep were seeded at 40,000 cells/well into 96-well plates. The following day, a half-area 96-well plate (Greiner) was prepared with 3-fold serial sera dilutions (starting dilutions determined for each serum and pseudovirus, 22 µL per well). An equal volume of DMEM with diluted pseudoviruses was added to each well. All pseudoviruses were diluted between 1:10-1:50 to reach a target entry of ~10^6 RLU. The mixture was incubated at room temperature for 60 min. Media was removed from the cells prior to the transfer of sera-pseudovirus mixture. 40 µL from each well of the half-area 96-well plate containing sera and pseudovirus were transferred to the 96-well plate seeded with cells and incubated at 37°C for 1 h. After 1 h, an additional 40 µL of DMEM supplemented with 20% FBS and 2% PenStrep was added to the cells. After 18-20 h, 40 µL of One-Glo-EX substrate (Promega) was added to each well and incubated on a plate shaker in the dark for 5 min before reading the relative luciferase units using a BioTek Neo2 plate reader. Relative luciferase units (RLUs) were plotted and normalized in Prism (GraphPad): 100% neutralization being cells in the absence of pseudovirus and 0% neutralization being pseudovirus entry into cells without sera. Prism (GraphPad) nonlinear regression with “log[inhibitor] versus normalized response with a variable slope” was used to fit the curve. Percent neutralization was calculated by taking the interpolated percentage of entry value at a fixed dilution factor of 1/33 (v/v ratio dilution of initial sera, log(dilution factor) of 1.519) using the fit curve. 100% and 0% neutralization were defined as 0% entry and 100% entry, respectively.

Mouse challenges study

For challenge study, 8 female BALB/c mice per groups were immunized with 1 µg of SARS-CoV-2 S2P, 5 µg of SARS-CoV-2 S_2 F-53, 1 µg of SARS-CoV-2 S_2 F-53, and 5 µg of SARS-CoV-1 S_2, respectively. Immunogens were mixed with 1:1 volume ratio of AddaVax and administered intramuscularly (protocol 21-287). One group was administered with PBS and AddaVax to serve as a control group. Mice were primed followed by a boost with 1 month time apart. Bleeds were drawn 3 weeks post injection and the terminal sera were pooled for each immunized group for further analysis and passive transfer.

For FcɣR KO mice challenge study, 9-14 weeks old female Fcer1g (Taconic, 584-F) mice were treated with 70 µL of pooled serum from each group by intraperitoneal (IP) injection. Six mice per treatment group were infected 12 hours post treatment with 1x10^4 PFU of SARS-CoV MA15 intranasally. For comparison, 5 mice of 9-10 weeks old female BALB/c (Envigo, 047) mice per treated group were infected as aforementioned. Infected mice were monitored for daily body weight. On day 4 post-infection mice were necropsied, the degree of lung congestion was scored, and lung (caudal lobe) tissues were harvested to determine viral loads by plaque assay.

5.8 Figures & Tables

Figure 5.1. Membrane-anchored SARS-CoV-2 S_2 mRNA-LNP vaccines and antibody responses.

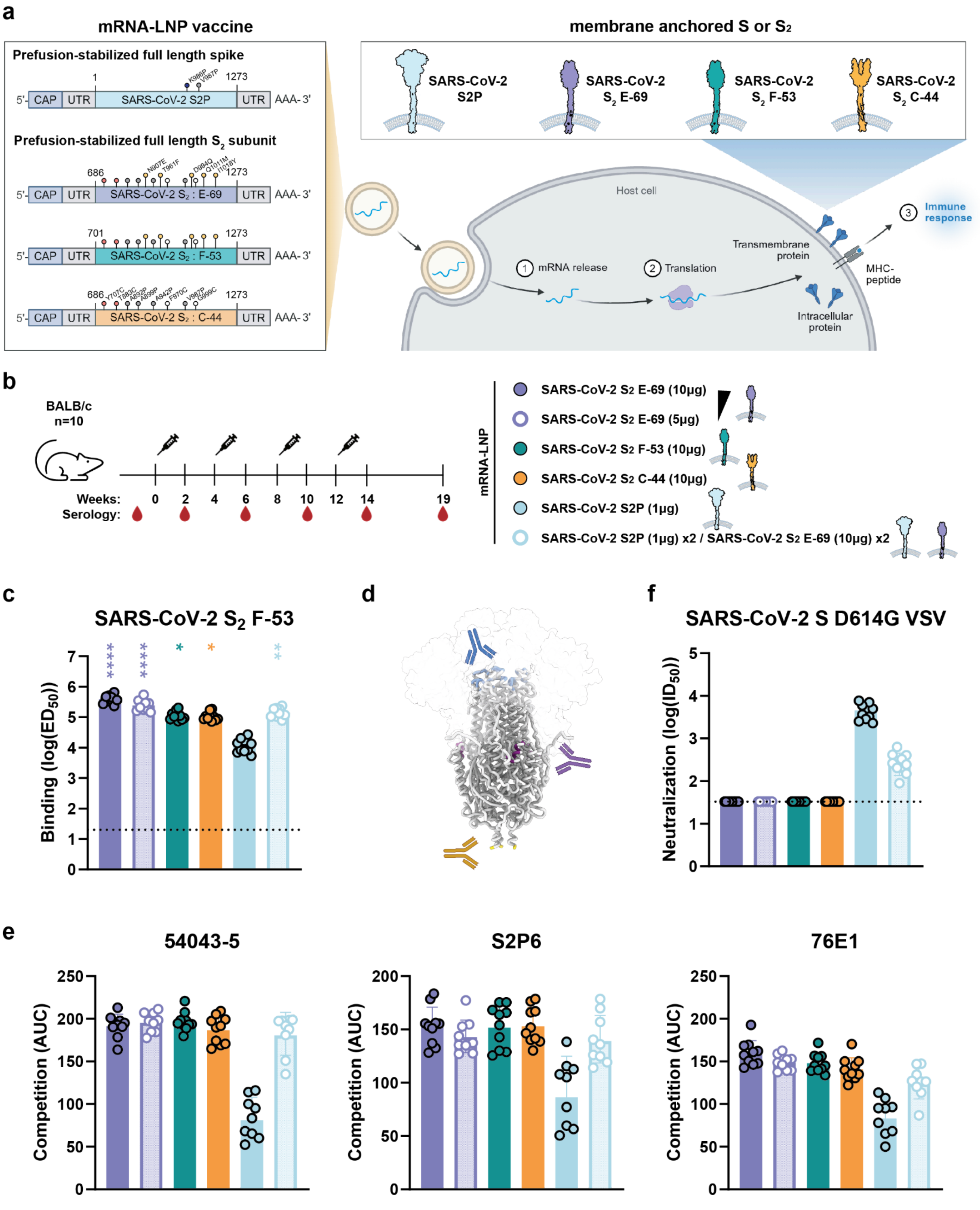

(**a**) Prefusion-stabilized SARS-CoV-2 S or S_2 mRNA-LNP vaccine design and mechanism. Predicted full-length S or S_2 model generated using AlphaFold3 (Abramson et al., 2024), PDB 6VXX (A. C. Walls, Park, et al., 2020), PDB 8VQB (Lee et al., 2024), PDB 8DYA (Bowen, Park, et al., 2022). Figure generated partially with BioRender.com. Biomolecules are not to scale and have been simplified for clearance. (**b**) mRNA-LNP vaccination schedule and study design. (**c**) Analysis of antibody binding titers against prefusion-stabilized SARS-CoV-2 S_2 F-53 using sera from terminal bleeds. Each dot represents the mean of two biological replicates. Geometric mean and geometric SD shown in bar and line, respectively. Comparisons between the S_2 or hybrid group and S2P group were made using two-way ANOVA followed by Dunnett's multiple comparison test. ns: P>0.05, *: P<=0.05, **: P<=0.01, ***: P<=0.001, ****: P<=0.0001. (**d**) S_2 targeting monoclonal antibody epitopes mapped on SARS-CoV-2 S_2 model (generated using PDB 6VXX (A. C. Walls, Park, et al., 2020)). The S_1 subunit is shown as a transparent surface, and IgG epitopes are shown in blue for 54043-5, purple for 76E1, and gold for S2P6. Figure generated partially with BioRender.com. (**e**) Mapping epitopes of polyclonal antibodies from the terminal bleed sera using inhibition ELISA against SARS-CoV-2 S_2 F-53 and S_2 targeting monoclonal antibodies. Inhibiting antibody titer expressed as area under the curve. Each dot represents the mean of two biological replicates. Geometric mean and geometric SD shown in bar and line, respectively. (**f**) Analysis of neutralizing antibody titers against SARS-CoV-2 S D614G pseudotyped VSV using sera from the bleeds 2 weeks post 4th immunization. One representative biologicate replicate shown with geometric mean and geometric SD shown in bar and line, respectively.

Figure 5.2. Analysis of vaccine-elicited serum binding titers against SARS-CoV-2 S_2 F-53.

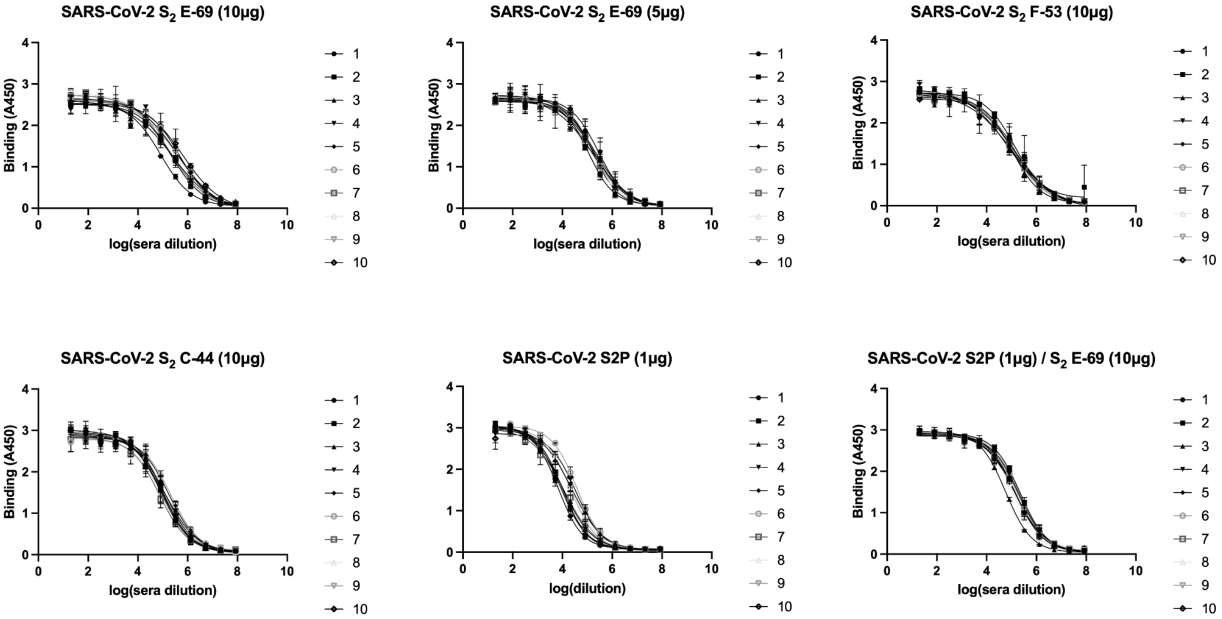

Dose-response curves of serum antibody binding to F-53. Each data point represents the mean of two technical replicates and SD are shown with lines. One representative out of two biological replicates is shown.

Figure 5.3. Analysis of vaccine-elicited polyclonal antibody epitopes on SARS-CoV-2 S_2 F-53

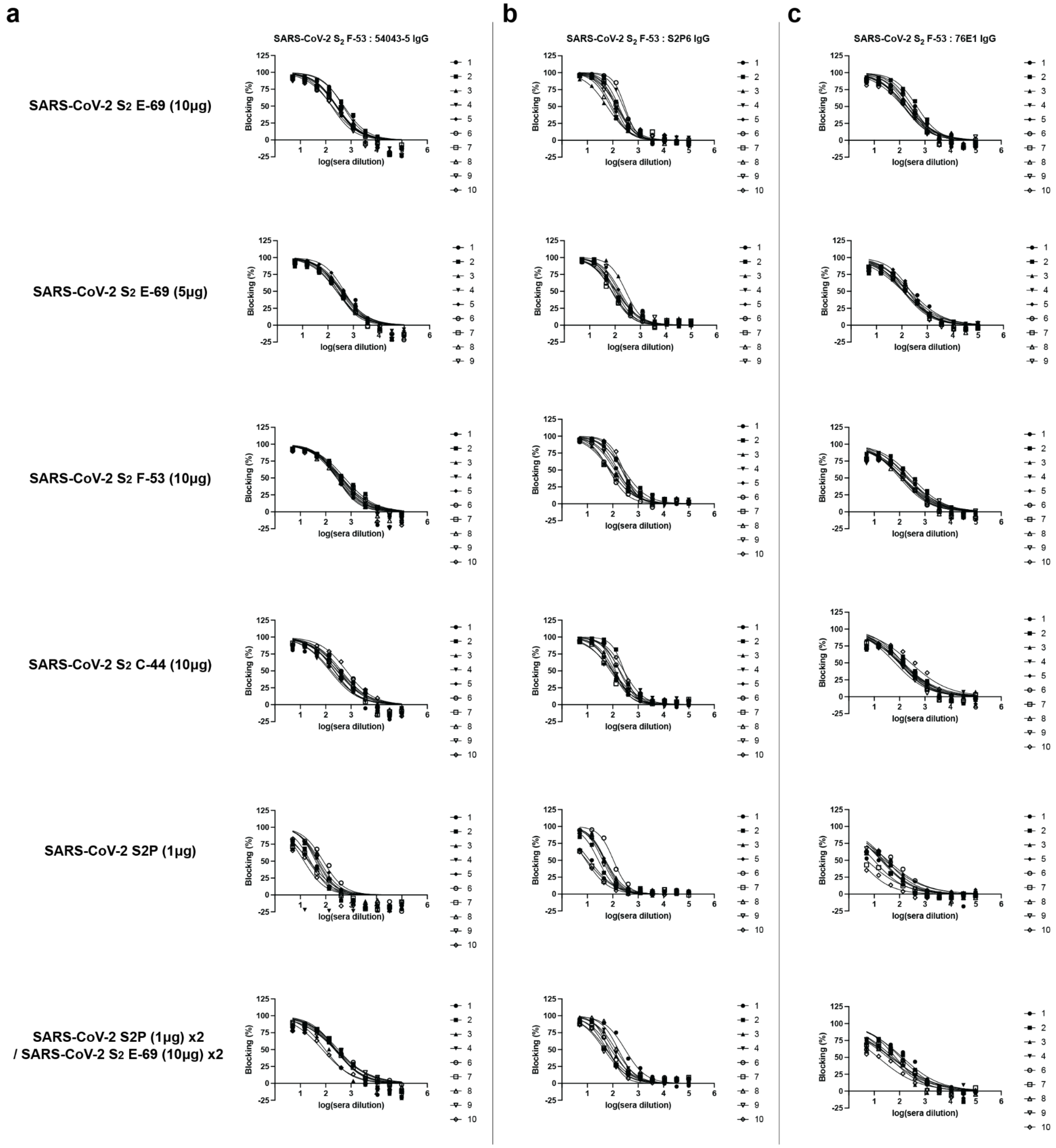

(**a-c**) Dose-response curves of serum antibody inhibition of S_2 targeting monoclonal antibodies 54043-5 (**a**), S2P6 (**b**), and 76E1 (**c**) binding to immobilized SARS-CoV-2 S_2 F-53. One representative out of two biological replicates is shown.

Figure 5.4. Analysis of vaccine-elicited serum neutralizing antibody titers.

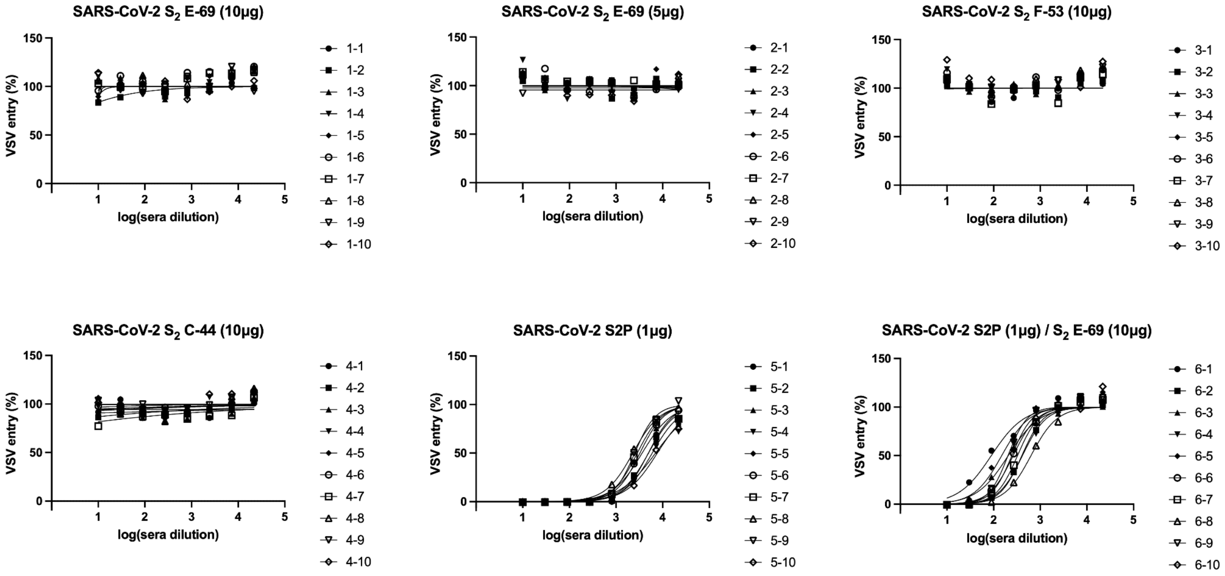

Dose-response curves of serum neutralizing antibody titers against the SARS-CoV-2 D614G S pseudotyped VSV using sera obtained 2 weeks after the 4th immunization. One biological replicate is shown.

Figure 5.5. Design of SARS-CoV-2 S_2 subunit lacking N-linked glycans.

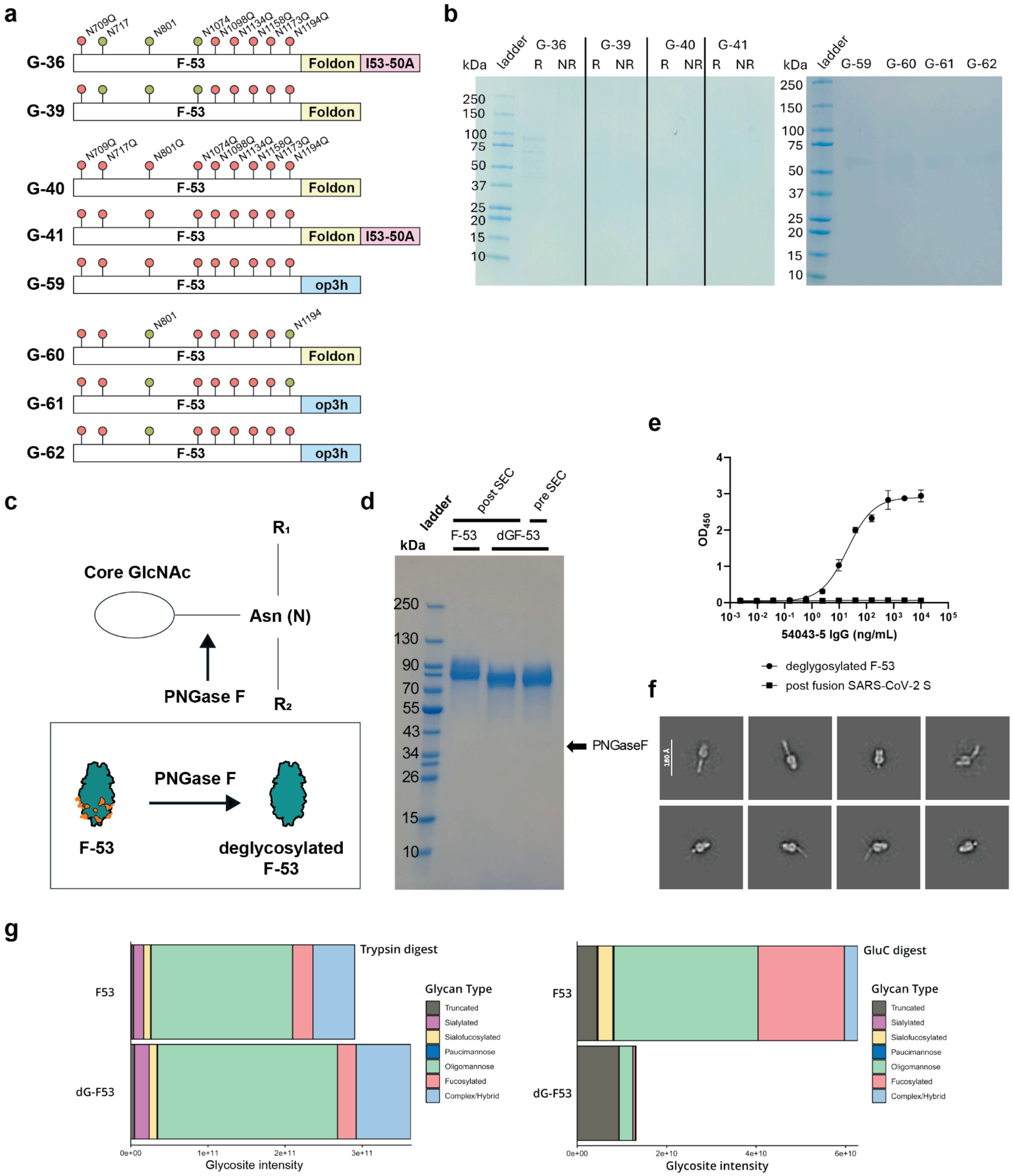

(**a**) Design schematics of deglycosylation of SARS-CoV-2 S_2 subunit by N-linked glycan site mutation. A circle filled with red represents asparagine modified to glutamine and with green represents asparagine kept intact. (**b**) SDS-PAGE image of designed constructs after purification. R stands for with reducing agent and NR stands for with no reducing agent. (**c-d**) Design schematics of deglycosylation of SARS-CoV-2 S_2 F-53 using PNGaseF (**c**) and PNGaseF treatment of the designed construct pre and post size exclusion chromatography (SEC) (**d**). (**e-f**) Deglycosylated F-53 and its retained antigenicity (**e**) and quaternary conformation confirmed by 2D class averages of negative stain EM (**f**). The scale bar represents 180 Å. (**g**) Mass spectrometry analysis of glycosite intensities of F-53 and PNGaseF treated F-53 (dGF-53).

Figure 5.6. Deglycosylation of prefusion-stabilized SARS-CoV-2 S_2 F-53 protein subunit vaccine and antibody responses.

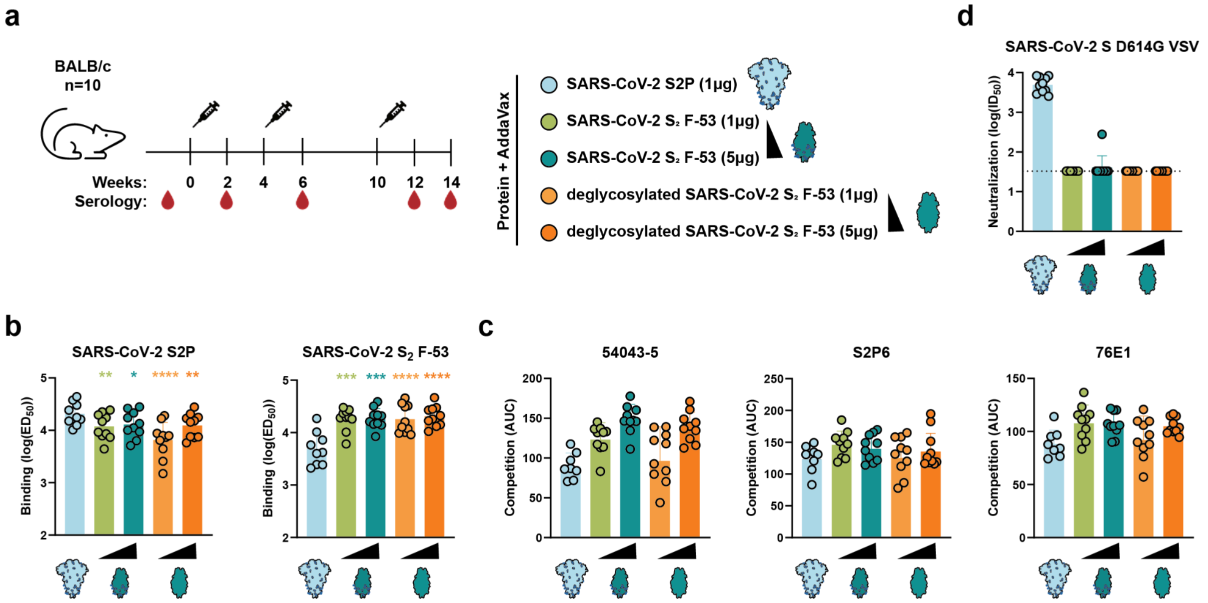

(**a**) Vaccination schedule and study design. (**b**) Analysis of antibody binding titers against SARS-CoV-2 S2P and prefusion-stabilized SARS-CoV-2 S_2 F-53 using sera from terminal bleeds. Each dot represents the mean of two biological replicates. Geometric mean and geometric SD shown in bar and line, respectively. Comparisons between the S_2 groups or glycan-lacking S_2 groups and S2P groups were made using two-way ANOVA followed by Dunnett's multiple comparison test. ns: $P>0.05$, *: $P<=0.05$, **: $P<=0.01$, ***: $P<=0.001$, ****: $P<=0.0001$. (**c**) Mapping epitopes of polyclonal antibodies from the terminal bleed sera using inhibition ELISA against SARS-CoV-2 S_2 F-53 and S_2 targeting monoclonal antibodies. Inhibiting antibody titer expressed as area under the curve. Each dot represents the mean of two biological replicates. Geometric mean and geometric SD shown in bar and line, respectively. (**d**) Analysis of neutralizing antibody titers against SARS-CoV-2 S D614G pseudotyped VSV using sera from the bleeds 2 weeks post 3rd immunization. Each dot represents the mean of two biological replicates with geometric mean and geometric SD shown in bar and line, respectively.

Figure 5.7. Analysis of vaccine-elicited serum binding titers against SARS-CoV-2 S2P and S_2 F-53.

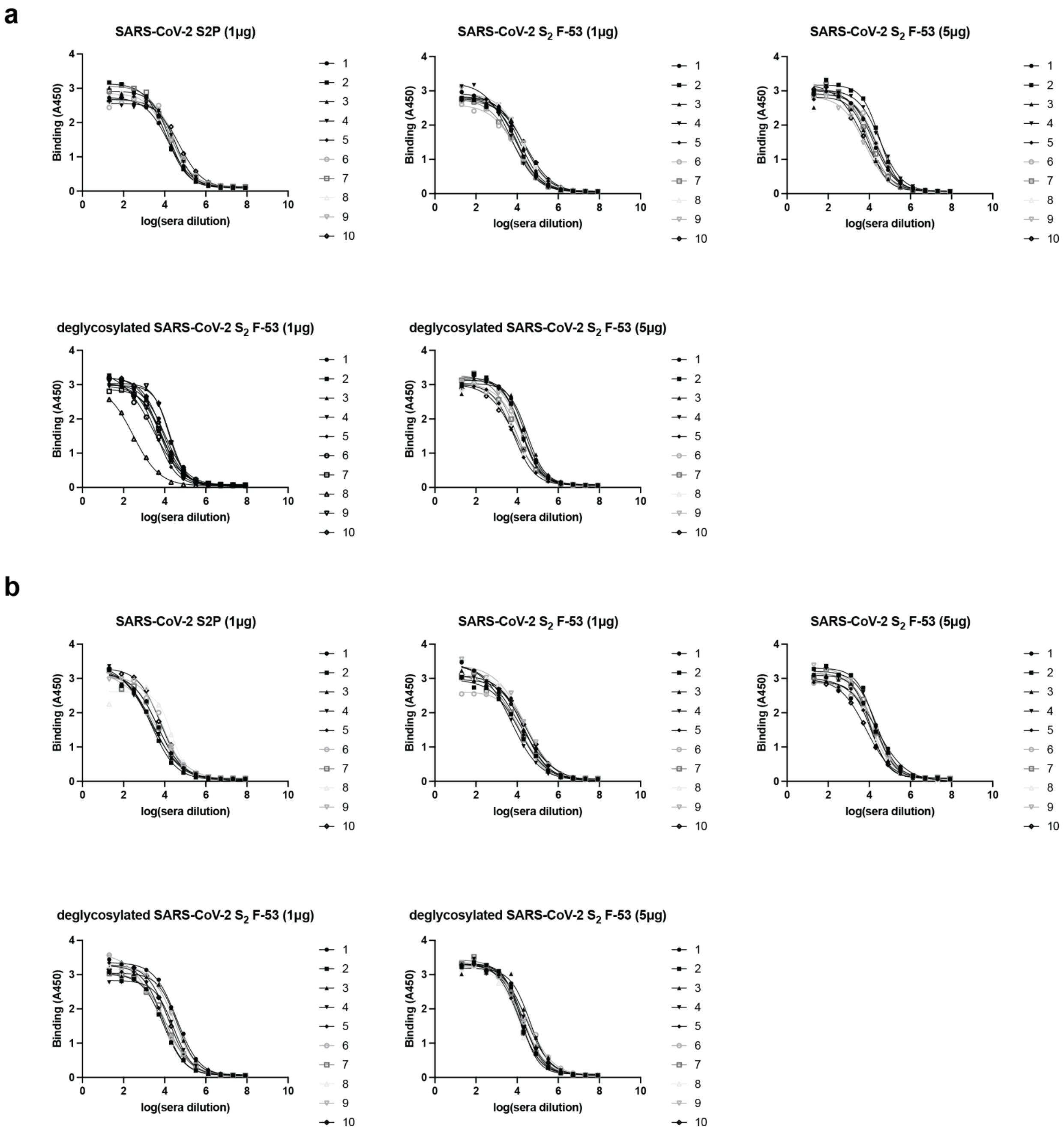

(**a-b**) Dose-response curves of terminal bleed serum antibody binding to SARS-CoV-2 S2P (**a**) and S_2 F-53 (**b**). Each data point represents the mean of two technical replicates and SD are shown with lines. One representative out of two biological replicates is shown.

Figure 5.8. Analysis of vaccine-elicited polyclonal antibody epitopes on SARS-CoV-2 S_2 F-53.

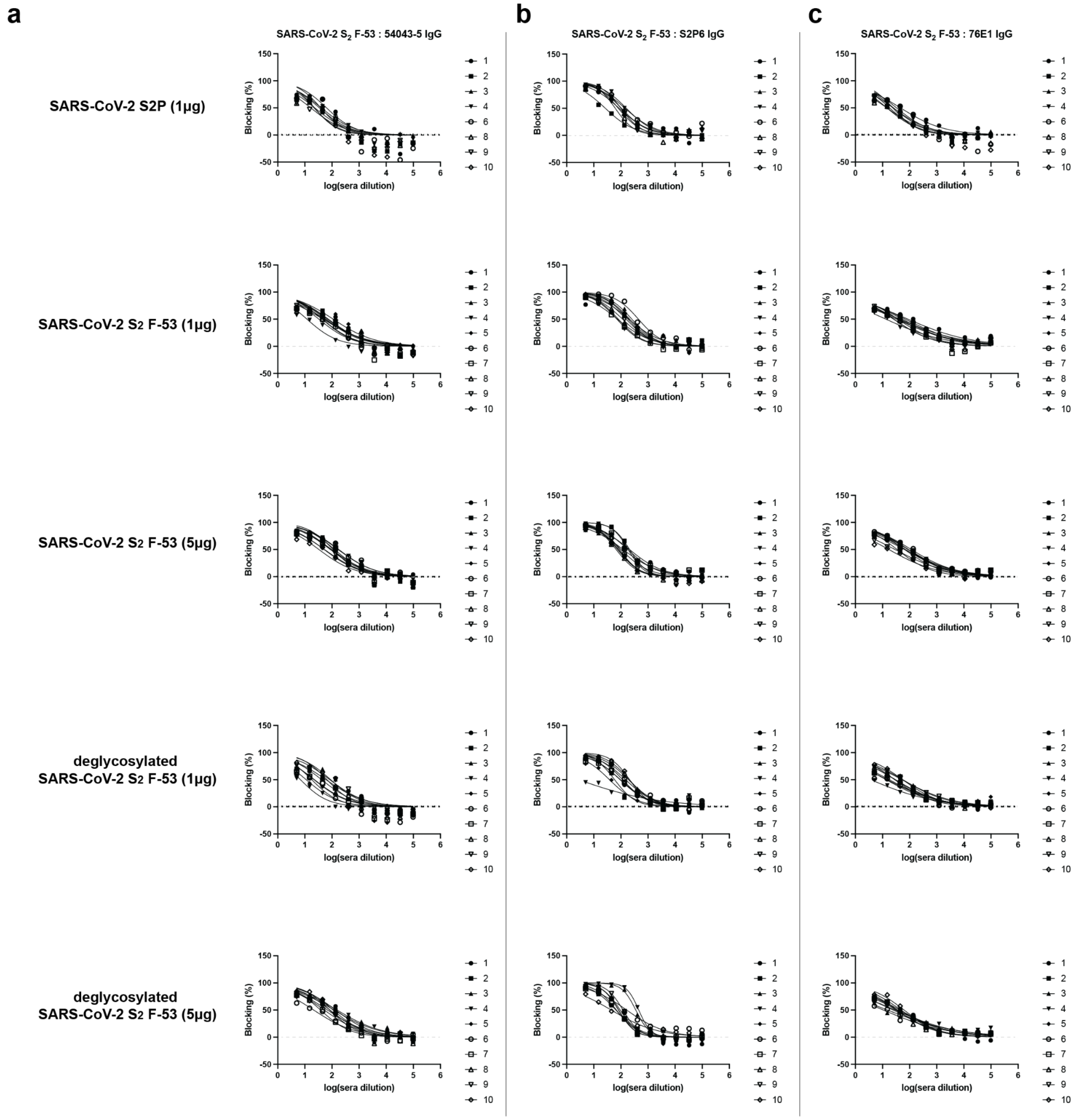

(**a-c**) Dose-response curves of terminal bleed serum antibody inhibition of S_2 targeting monoclonal antibodies 54043-5 (**a**), S2P6 (**b**), and 76E1 (**c**) binding to immobilized SARS-CoV-2 S_2 F-53. One representative out of two biological replicates is shown.

Figure 5.9. Analysis of vaccine-elicited serum neutralizing antibody titers.

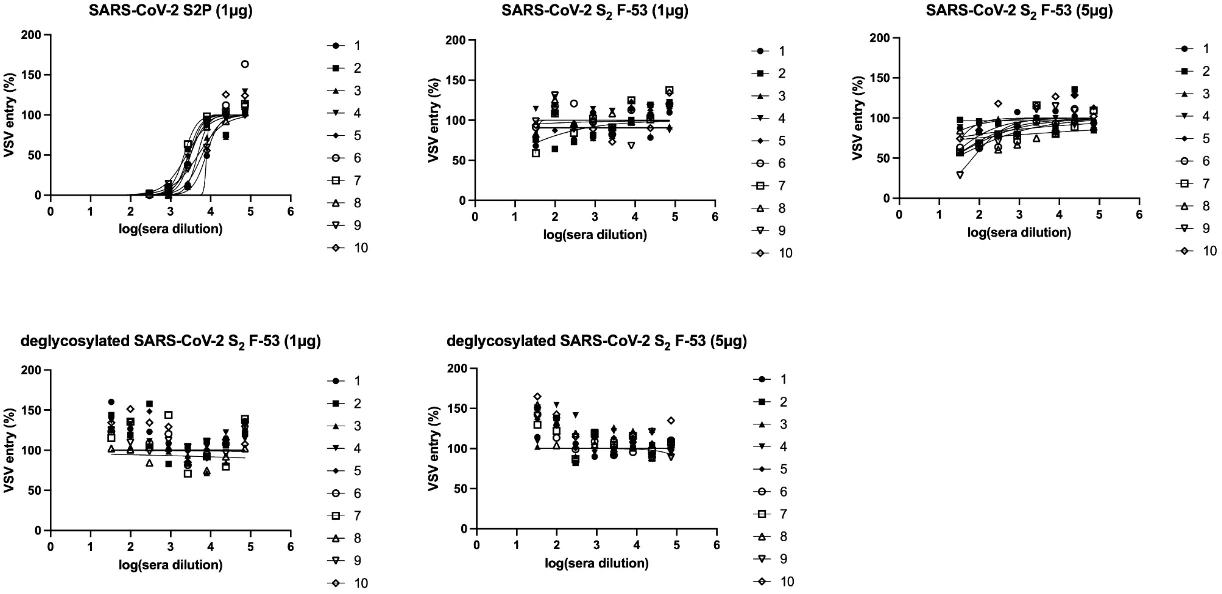

Dose-response curves of serum neutralizing antibody titers against the SARS-CoV-2 D614G S pseudotyped VSV using sera obtained 2 weeks after the 3rd immunization. One representative biological replicate is shown.

Figure 5.10. Protein nanoparticle vaccine candidates displaying prefusion-stabilized sarbecovirus fusionmachineries (S_2 subunit) on their surfaces.

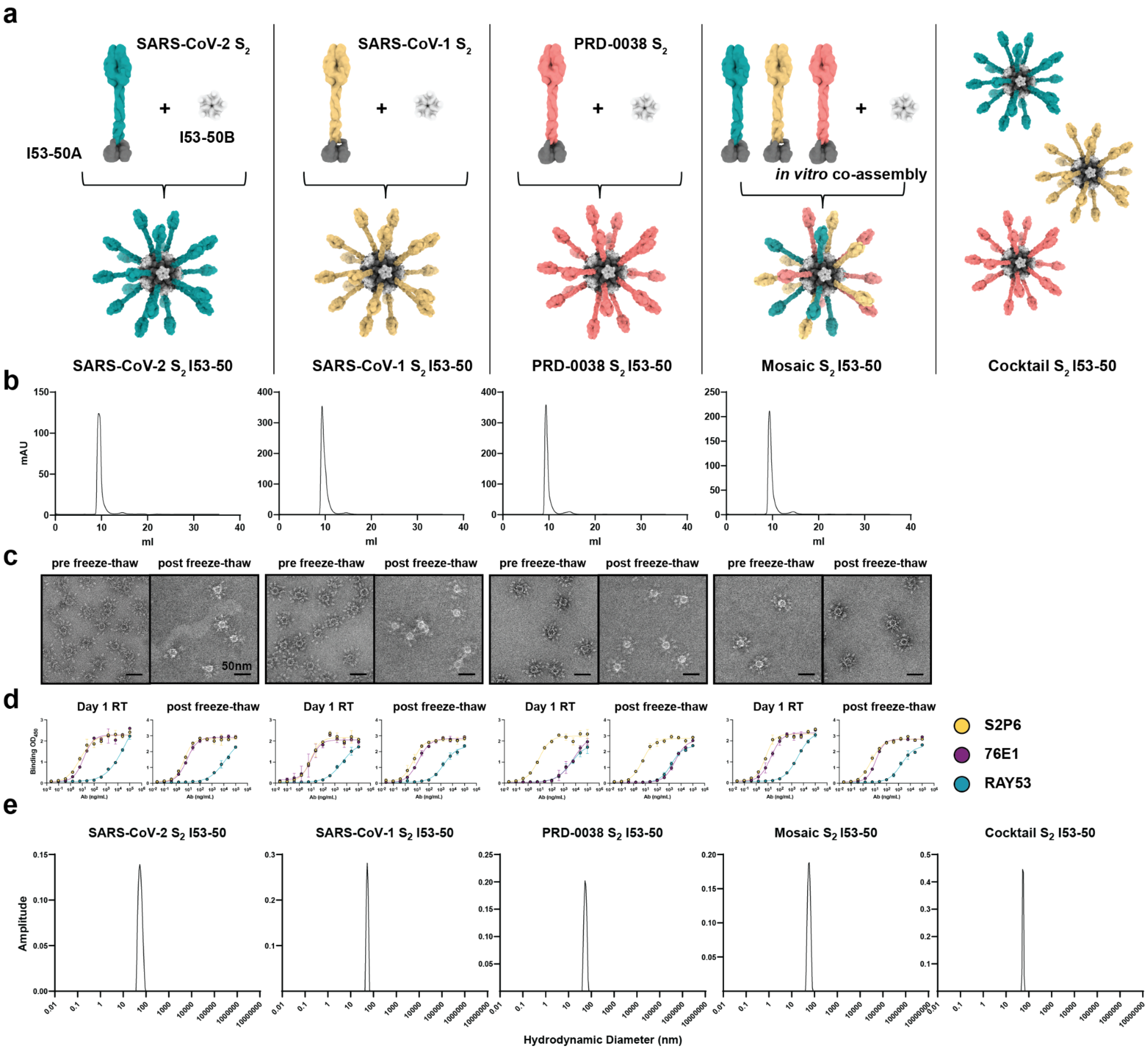

(**a**) Design schematic of sarbecovirus prefusion-stabilized S_2 displaying protein nanoparticles. Models were generated using AlphFold3 (Abramson et al., 2024), PDB 6VXX (A. C. Walls, Park, et al., 2020), PDB 5X5B (Yuan et al., 2017), and PDB 8U29 (Lee et al., 2023). (**b**) Size exclusion chromatography chromatogram of assembled nanoparticles. (**c**) Representative negative stain EM images of assembled nanoparticles pre and post freeze-thaw cycle. The scale bar represents 50nm. (**d**) Retained antigenicity confirmed by ELISA with S_2 targeting monoclonal antibodies at day 1 stored at room temperature (RT) and post freeze-thaw. (**e**) Dynamic light scattering (DLS) analysis of nanoparticles post freeze-thaw.

Figure 5.11. Prefusion-stabilized sarbecovirus S_2 displaying protein nanoparticle vaccines and antibody responses.

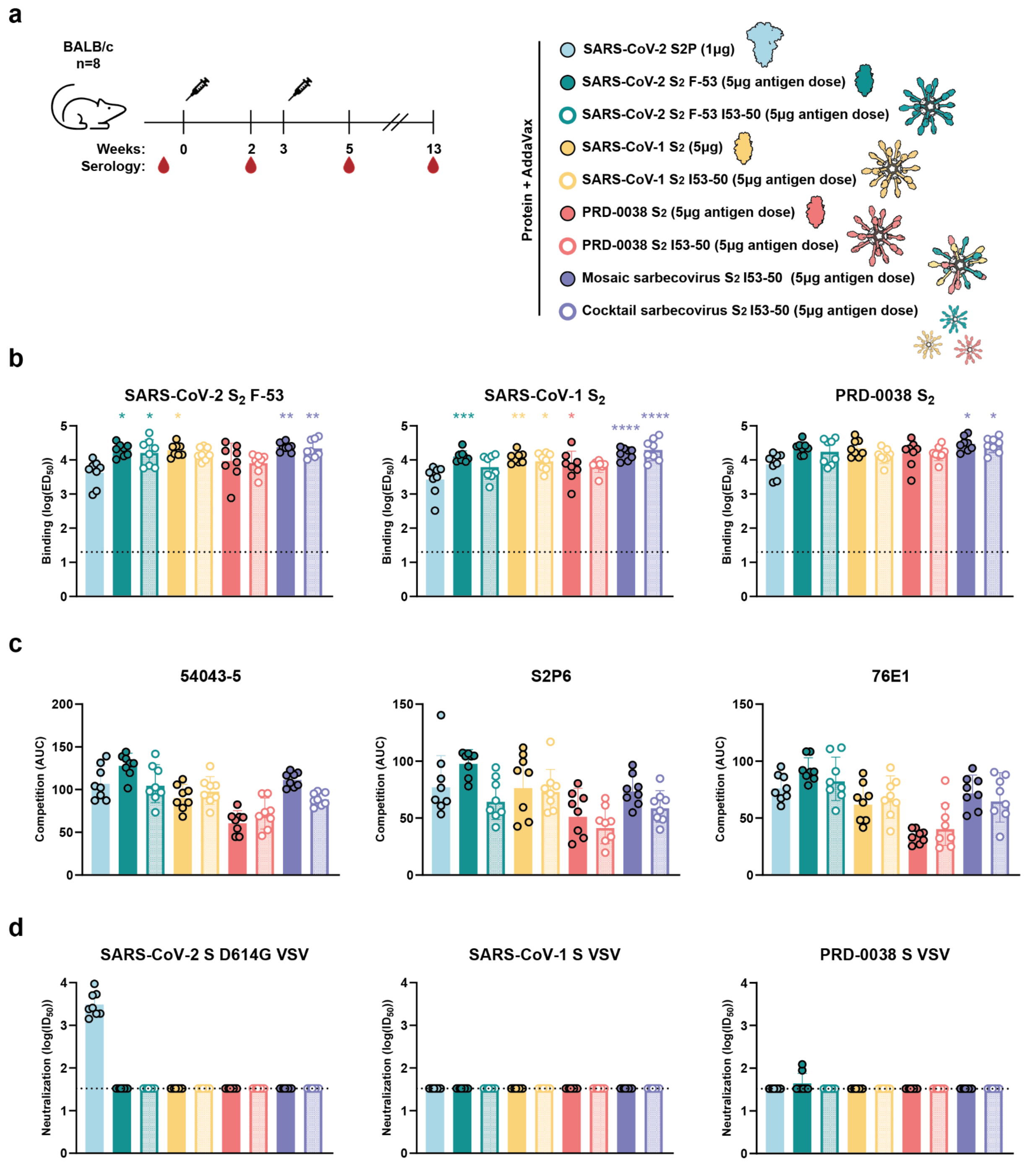

(**a**) Vaccination schedule and study design. (**b**) Analysis of antibody binding titers against prefusion-stabilized SARS-CoV-2 S_2 F-53, SARS-CoV-1 S_2, and PRD-0038 S_2 using sera from terminal bleeds. Each dot represents the mean of two biological replicates. Geometric mean and geometric SD shown in bar and line, respectively.

Comparisons between the SARS-CoV-2 S2P received group and the rest of the groups were made using two-way ANOVA followed by Dunnett's multiple comparison test. ns: P>0.05, *: P<=0.05, **: P<=0.01, ***: P<=0.001, ****: P<=0.0001. (**c**) Mapping epitopes of polyclonal antibodies from the terminal bleed sera using inhibition ELISA against SARS-CoV-2 S_2 F-53 and S_2 targeting monoclonal antibodies. Inhibiting antibody titer expressed as area under the curve. Each dot represents the mean of two biological replicates. Geometric mean and geometric SD shown in bar and line, respectively. (**d**) Analysis of neutralizing antibody titers against SARS-CoV-2 S D614G, SARS-CoV-1 S, and PRD-0038 S pseudotyped VSV using sera from the bleeds 2 weeks post 2nd immunization. One representative biologicate replicate shown with geometric mean and geometric SD shown in bar and line, respectively.

Figure 5.12. Analysis of vaccine-elicited serum binding titers against SARS-CoV-2 S_2 F-53.

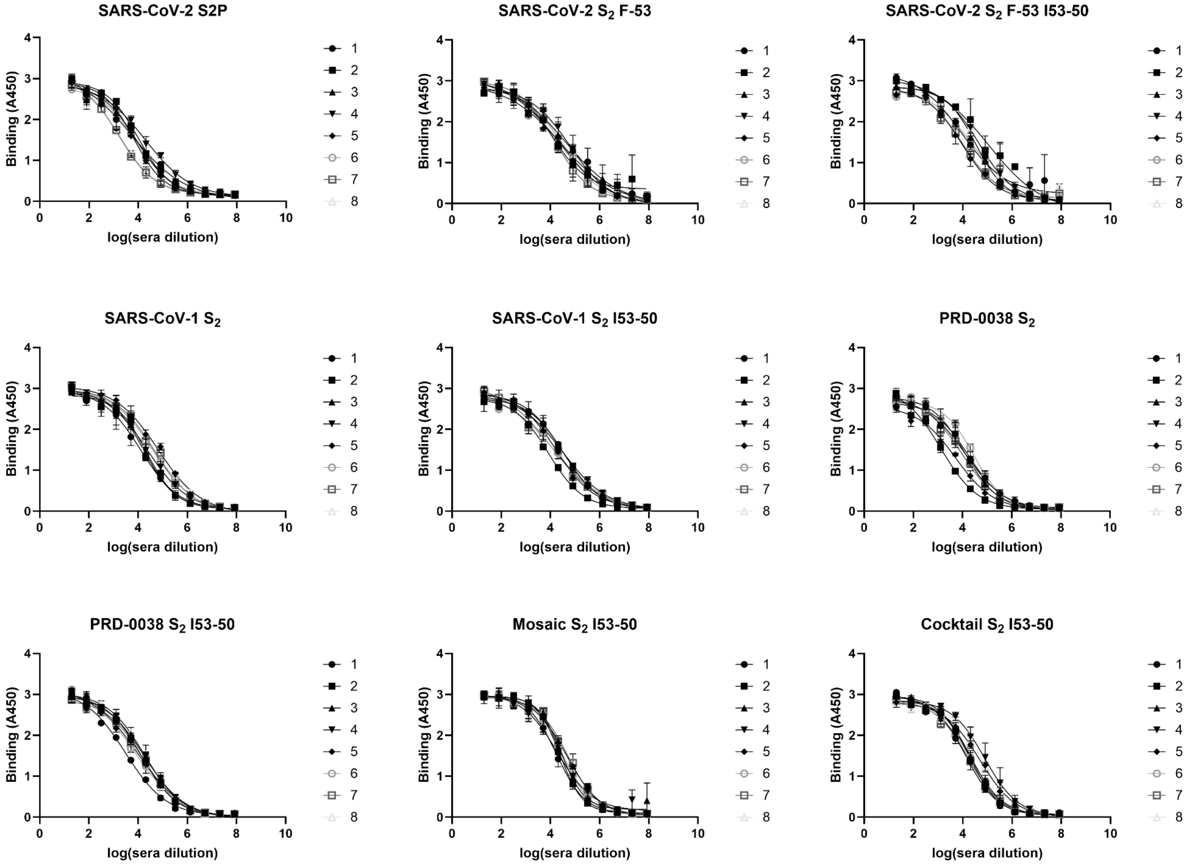

Dose-response curves of terminal bleed serum antibody binding to SARS-CoV-2 S_2 F-53. Each data point represents the mean of two technical replicates and SD are shown with lines. One representative out of two biological replicates is shown.

Figure 5.13. Analysis of vaccine-elicited serum binding titers against SARS-CoV-1 S_2.

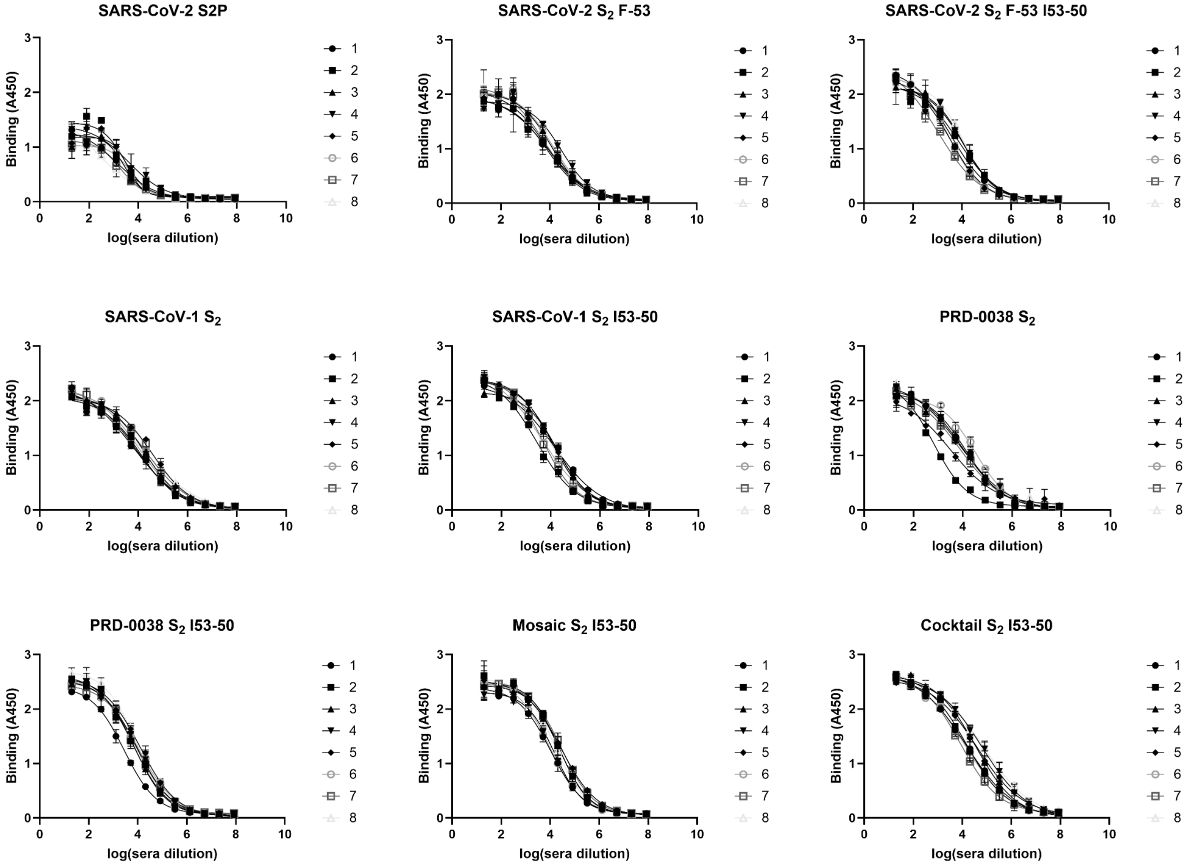

Dose-response curves of terminal bleed serum antibody binding to SARS-CoV-1 S_2. Each data point represents the mean of two technical replicates and SD are shown with lines. One representative out of two biological replicates is shown.

Figure 5.14. Analysis of vaccine-elicited serum binding titers against PRD-0038 S_2.

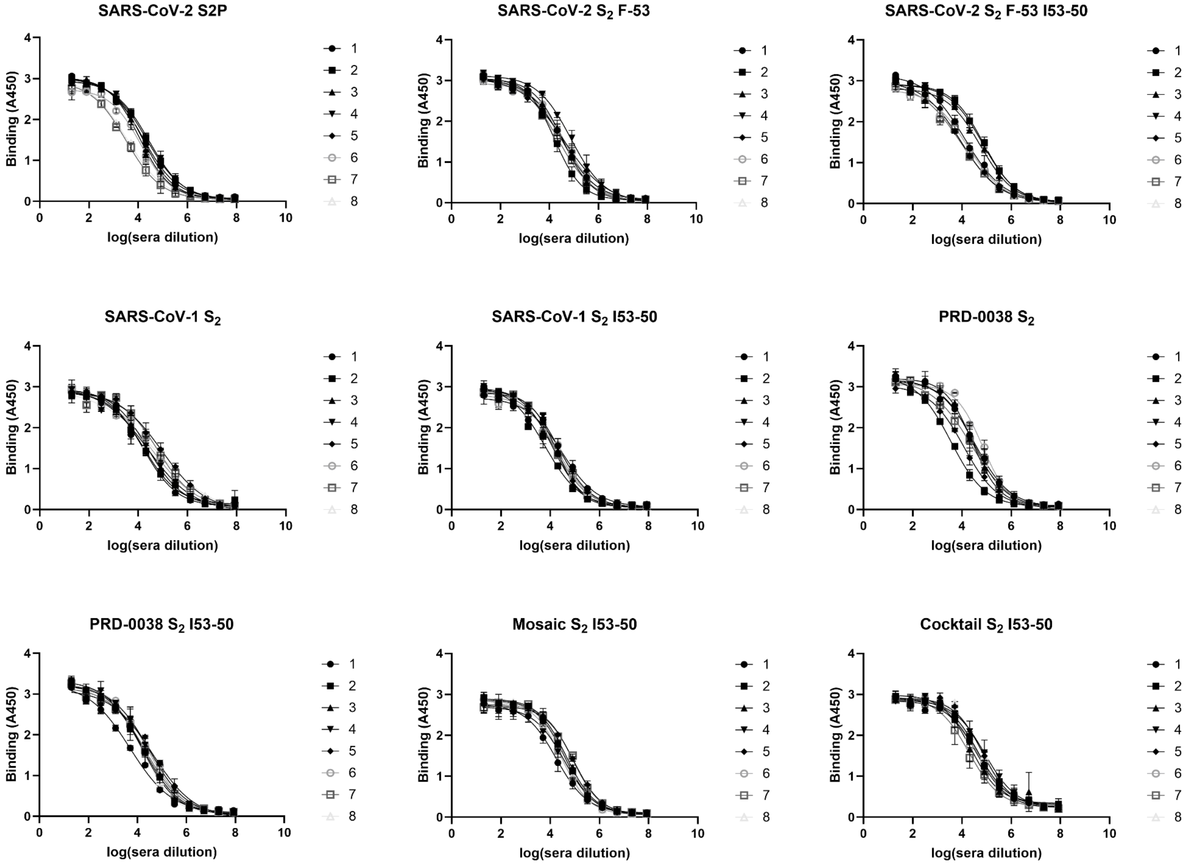

Dose-response curves of terminal bleed serum antibody binding to PRD-0038 S_2. Each data point represents the mean of two technical replicates and SD are shown with lines. One representative out of two biological replicates is shown.

Figure 5.15. Analysis of vaccine-elicited polyclonal antibody epitopes on SARS-CoV-2 S_2 F-53 using monoclonal antibody 54043-5.

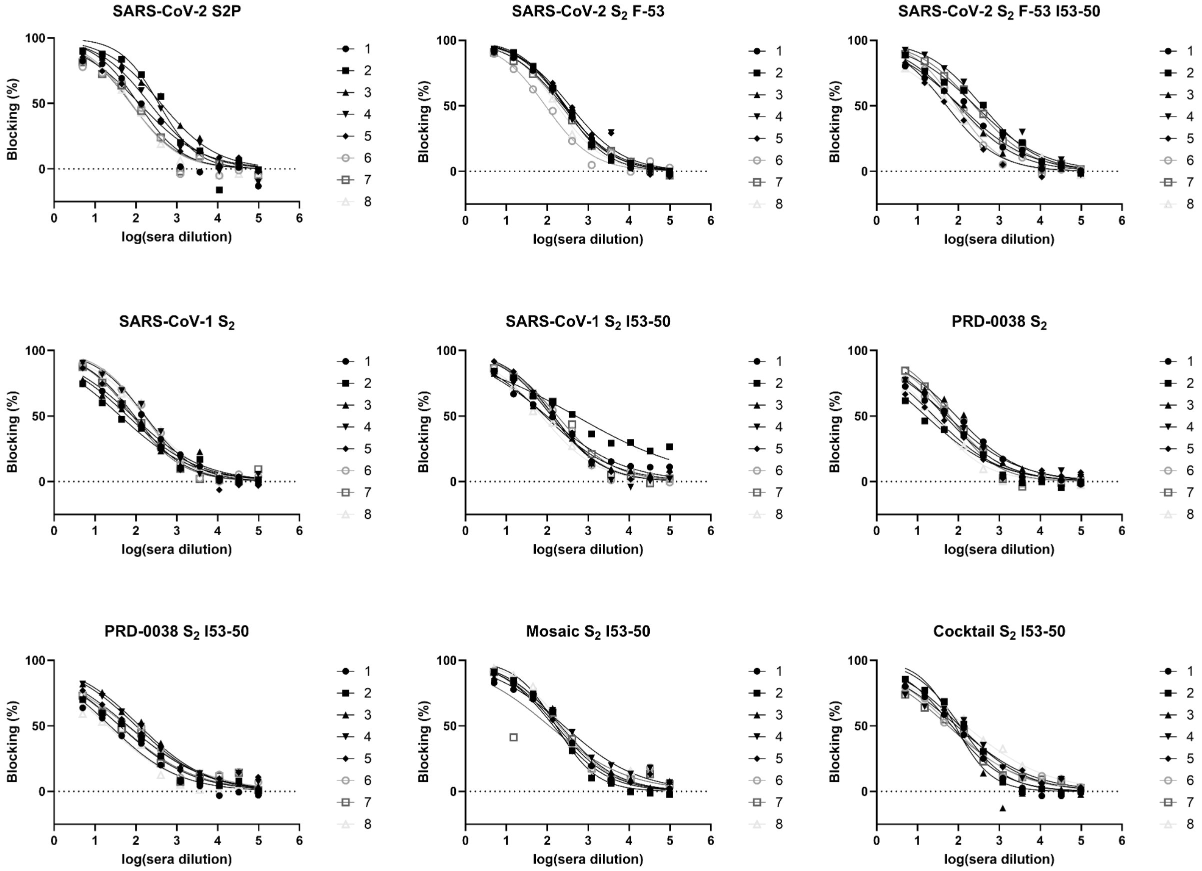

Dose-response curves of terminal bleed serum antibody inhibition of S_2 targeting monoclonal antibodies 54043-5 binding to immobilized SARS-CoV-2 S_2 F-53. One representative out of two biological replicates is shown.

Figure 5.16. Analysis of vaccine-elicited polyclonal antibody epitopes on SARS-CoV-2 S$_2$ F-53 using monoclonal antibody S2P6.

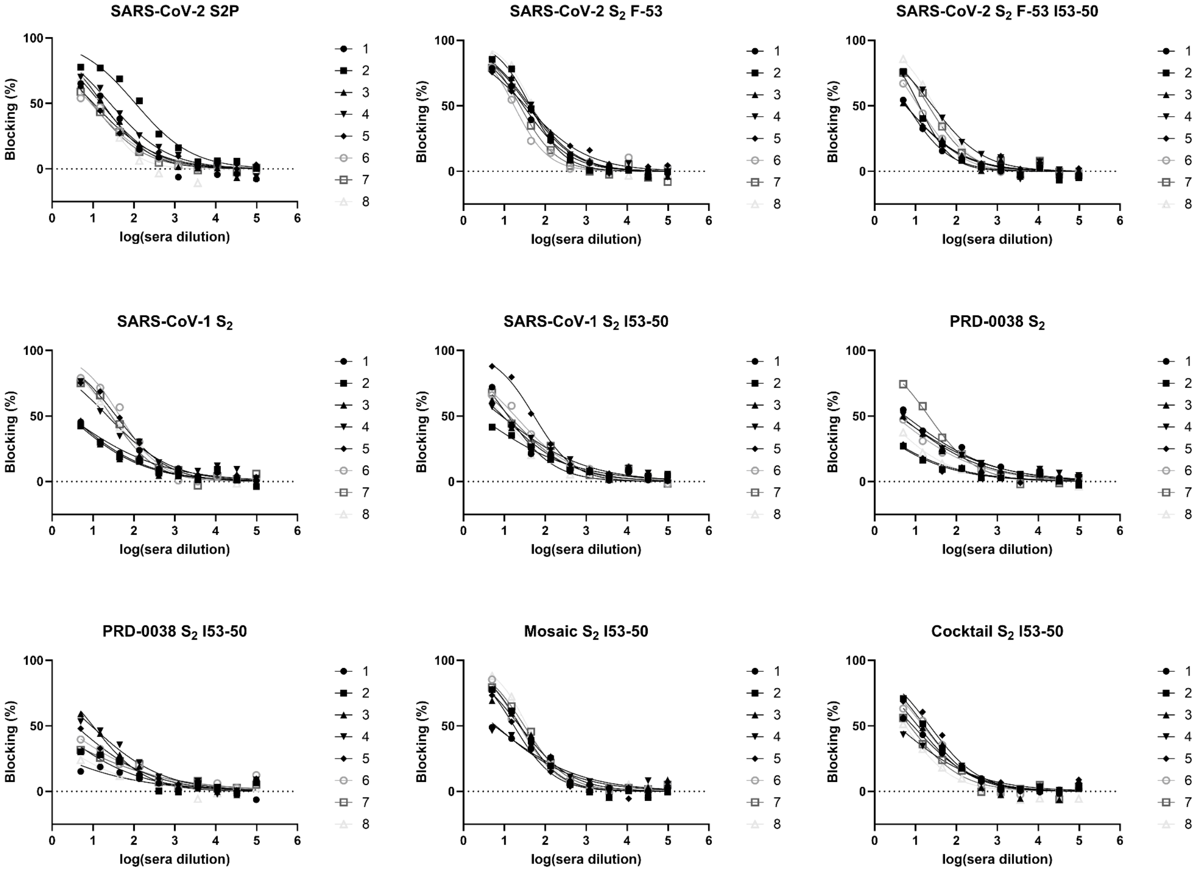

Dose-response curves of terminal bleed serum antibody inhibition of S$_2$ targeting monoclonal antibodies S2P6 binding to immobilized SARS-CoV-2 S$_2$ F-53. One representative out of two biological replicates is shown.

Figure 5.17. Analysis of vaccine-elicited polyclonal antibody epitopes on SARS-CoV-2 S$_2$ F-53 using monoclonal antibody 76E1.

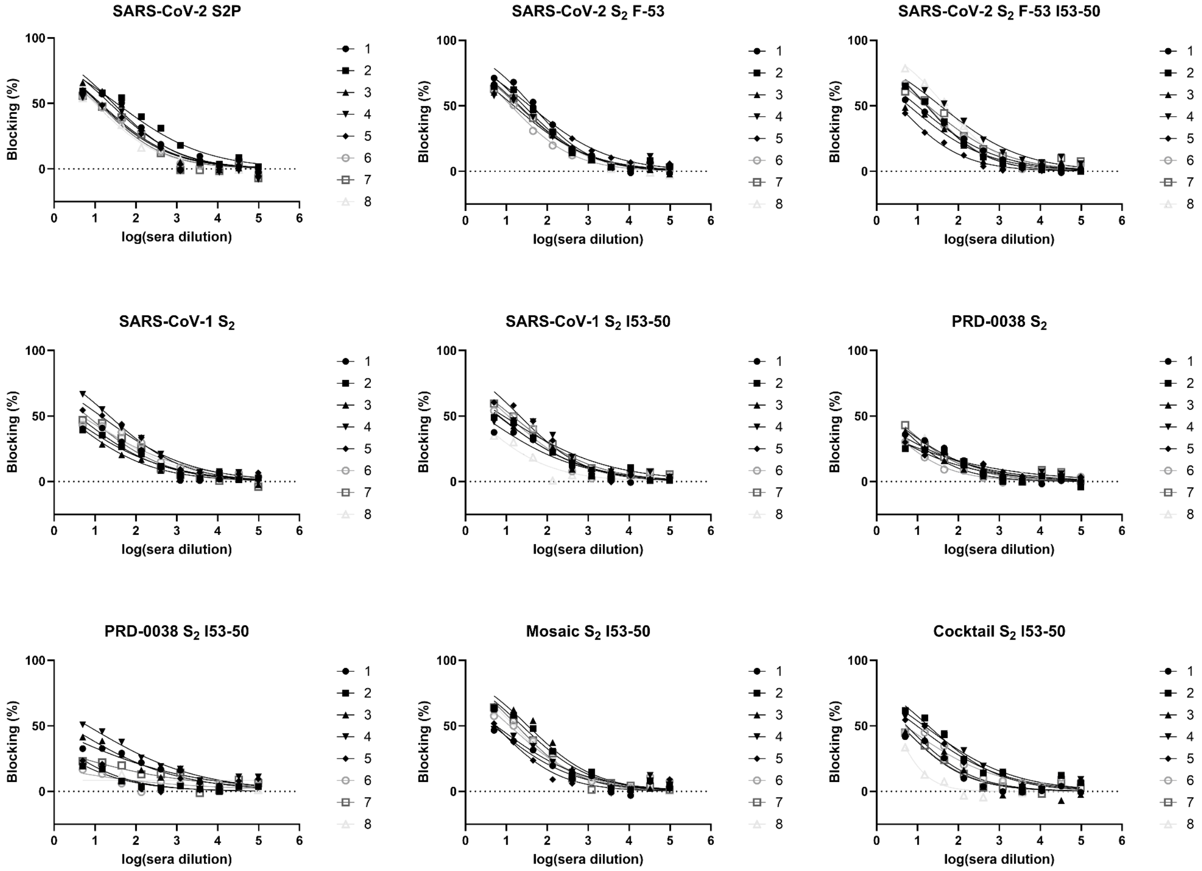

Dose-response curves of terminal bleed serum antibody inhibition of S$_2$ targeting monoclonal antibodies 76E1 binding to immobilized SARS-CoV-2 S$_2$ F-53. One representative out of two biological replicates is shown.

Figure 5.18. Analysis of vaccine-elicited serum neutralizing antibody titers against SARS-CoV-2 S D614G VSV.

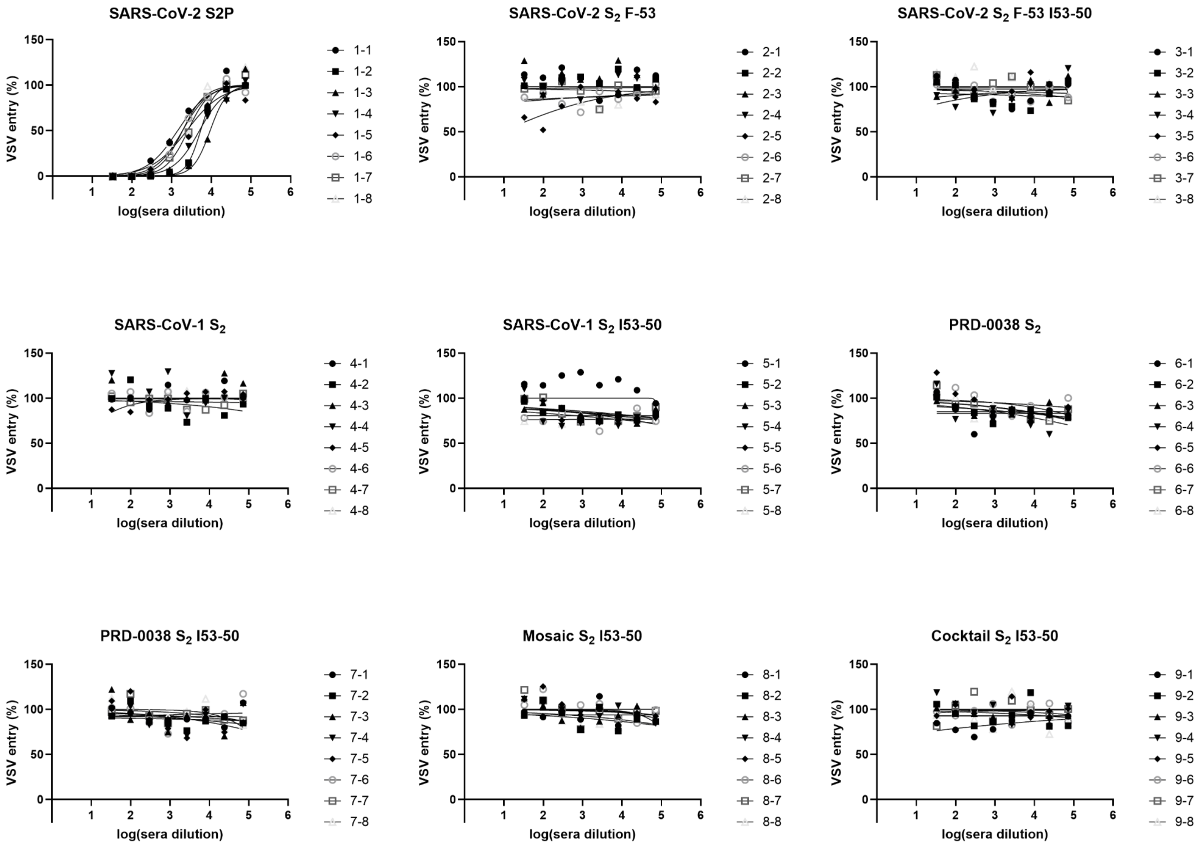

Dose-response curves of serum neutralizing antibody titers against the SARS-CoV-2 S D614G pseudotyped VSV using sera from the bleeds 2 weeks post 2nd immunization. One representative biological replicate is shown.

Figure 5.19. Analysis of vaccine-elicited serum neutralizing antibody titers against SARS-CoV-1 S VSV.

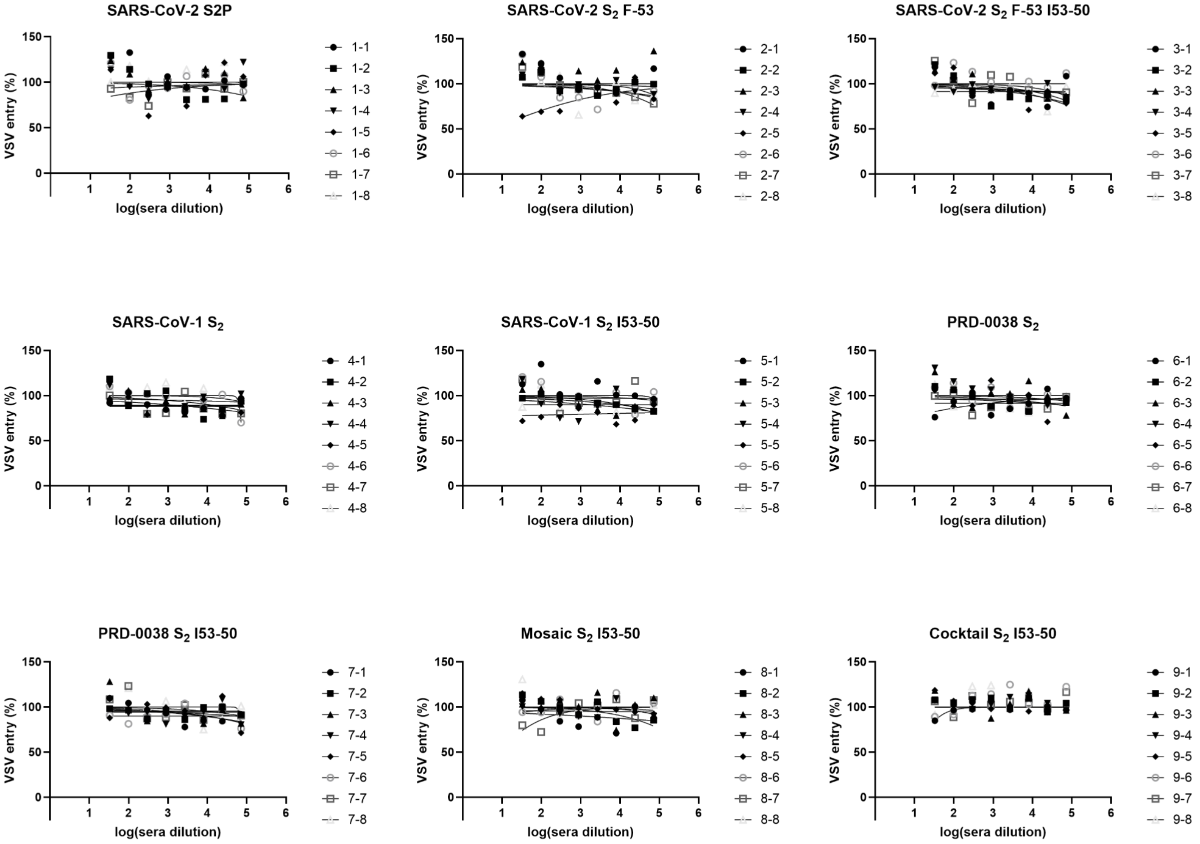

Dose-response curves of serum neutralizing antibody titers against the SARS-CoV-1 S pseudotyped VSV using sera from the bleeds 2 weeks post 2nd immunization. One representative biological replicate is shown.

Figure 5.20. Analysis of vaccine-elicited serum neutralizing antibody titers against PRD-0038 S VSV.

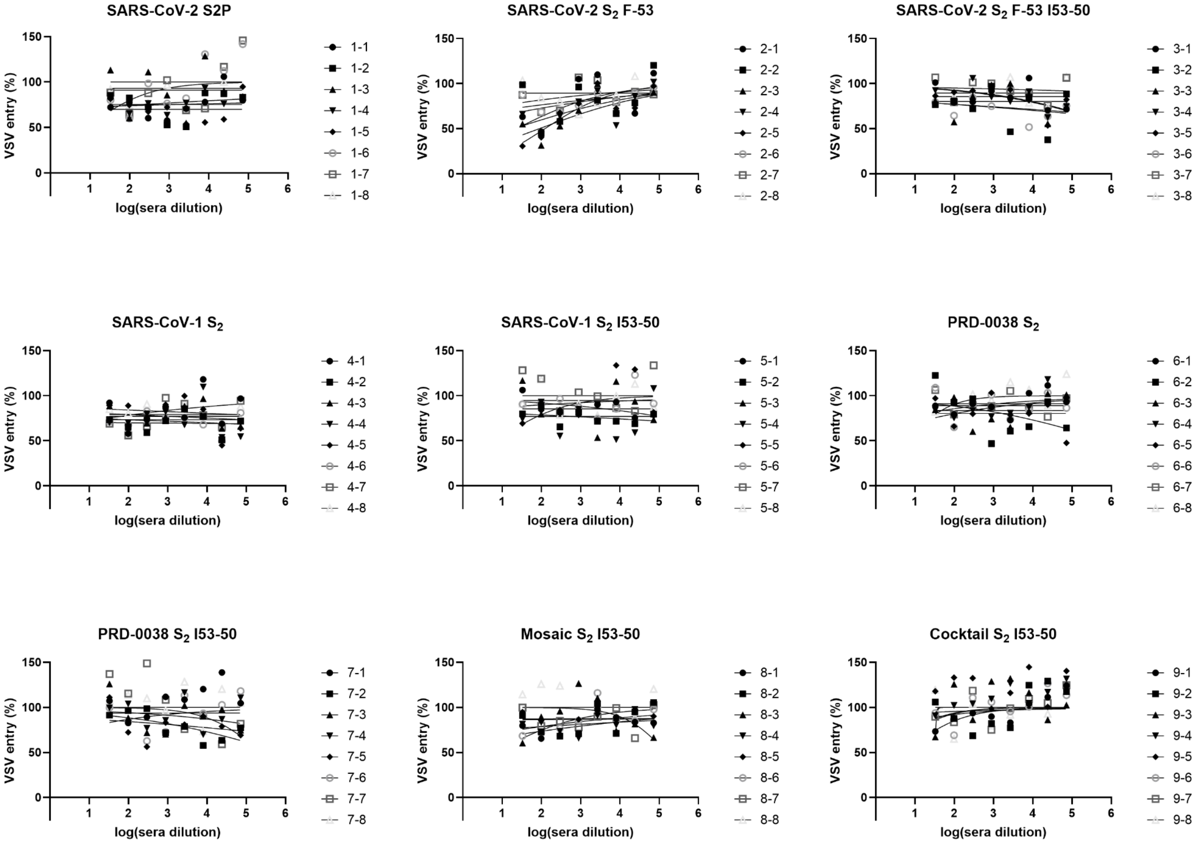

Dose-response curves of serum neutralizing antibody titers against the PRD-0038 S pseudotyped VSV using sera from the bleeds 2 weeks post 2nd immunization. One representative biological replicate is shown.

Figure 5.21. Prefusion-stabilized SARS-CoV-2 S_2 and SARS-CoV-1 protein subunit vaccine protect mice against SARS-CoV-1-induced disease via Fc-mediated effector functions.

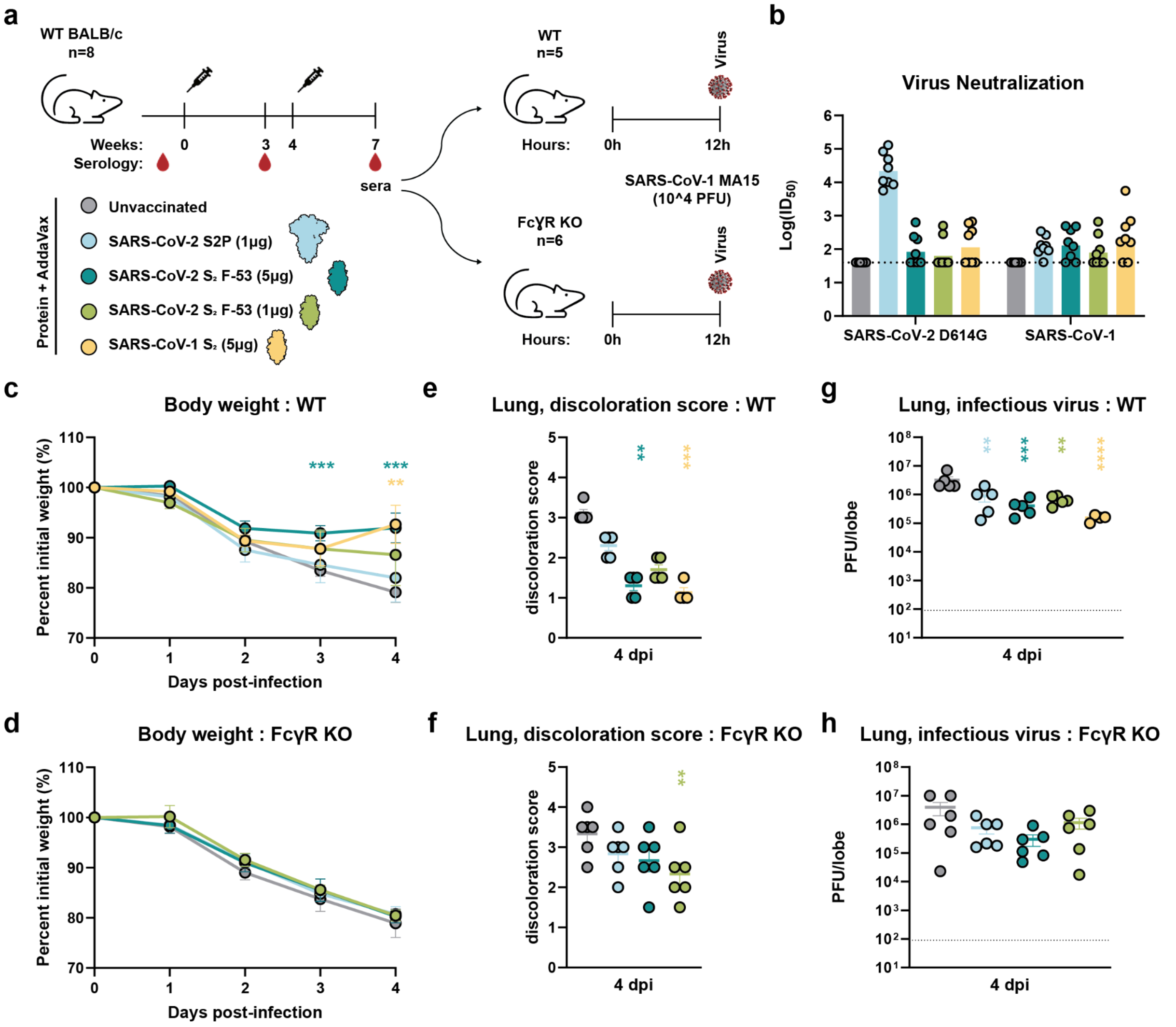

(**a**) Vaccination schedule and study design. (**b**) Authentic virus neutralization with pooled sera from each vaccinated group against SARS-CoV-2 S D614G and SARS-CoV-1. Geometric mean shown as bars. (**c-d**) Weight loss followed 4 days post viral challenge with SARS-CoV-1 MA15 in wild-type (WT) mice (**c**) and FcɣR knockout (KO) mice (**d**). Each dot represents mean and SD shown as lines. Comparison of percent weight loss with the control unvaccinated group and each of the vaccinated groups was done using two-way analysis of variance (ANOVA) followed by Dunnett's multiple comparison test. ns: P>0.05, *: P<=0.05, **: P<=0.01, ***: P<=0.001, ****:P<=0.0001. (**e-f**) Lung discoloration score 4 days post viral challenge with SARS-CoV-1 MA15 in WT mice (**e**) and KO mice (**f**). Mean and SEM shown as horizontal bars and lines, respectively. Comparison between the control unvaccinated group and each of the vaccinated groups was done using Kruskal-Wallis test followed by Dunn's multiple comparisons test. ns: P>0.05, *: P<=0.05, **: P<=0.01, ***: P<=0.001, ****:P<=0.0001. (**g-h**) Quantification of replicating viral titers in the lungs of challenged animals at 4 days post infection in WT mice (**g**) and KO mice (**h**). Mean and SEM shown as horizontal bars and lines, respectively. Comparison between the control unvaccinated group and each of the vaccinated groups was done using one-way ANOVA test followed by Dunnett's multiple comparisons test. ns: P>0.05, *: P<=0.05, **: P<=0.01, ***: P<=0.001, ****:P<=0.0001. The experiment has not been replicated (**b–h**).

Figure 5.22. Analysis of vaccine-elicited serum binding titers against different sarbecovirus spikes and mouse FcɣRIV (mFcɣRIV).

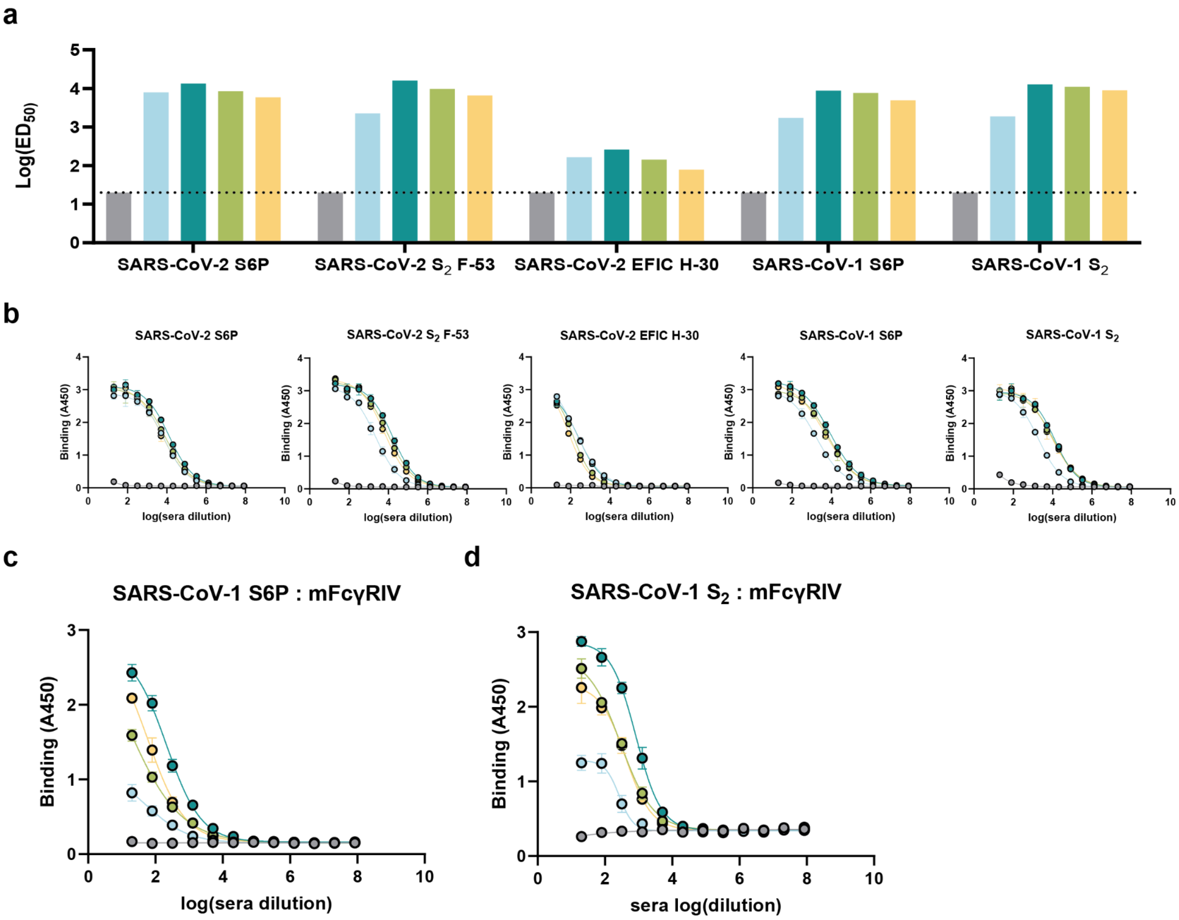

(**a**) Analysis of antibody binding titers against SARS-CoV-2 S6P, SARS-CoV-2 S_2 F-53, in house designed SARS-CoV-2 EFIC H-30, SARS-CoV-1 S6P, and SARS-CoV-1 S_2 analyzed by ELISAs using pooled sera from unvaccinated/vaccinated mice. One representative biological replicate is shown. (**b**) Dose-response curves of pooled sera antibody binding to each of sarbecovirus spikes mentioned in (**a**). Each data point represents the mean of three technical replicates and SDs are shown with lines. One representative is shown. (**c-d**) Analysis of antibody binding titers towards mouse FcɣRIV with SARS-CoV-1 S6P (**c**) or SARS-CoV-1 S_2 (**d**) immobilized.

Figure 5.23. Analysis of vaccine-elicited serum neutralizing antibody titers against SARS-CoV-2 S D614G and SARS-CoV-1 VSV.

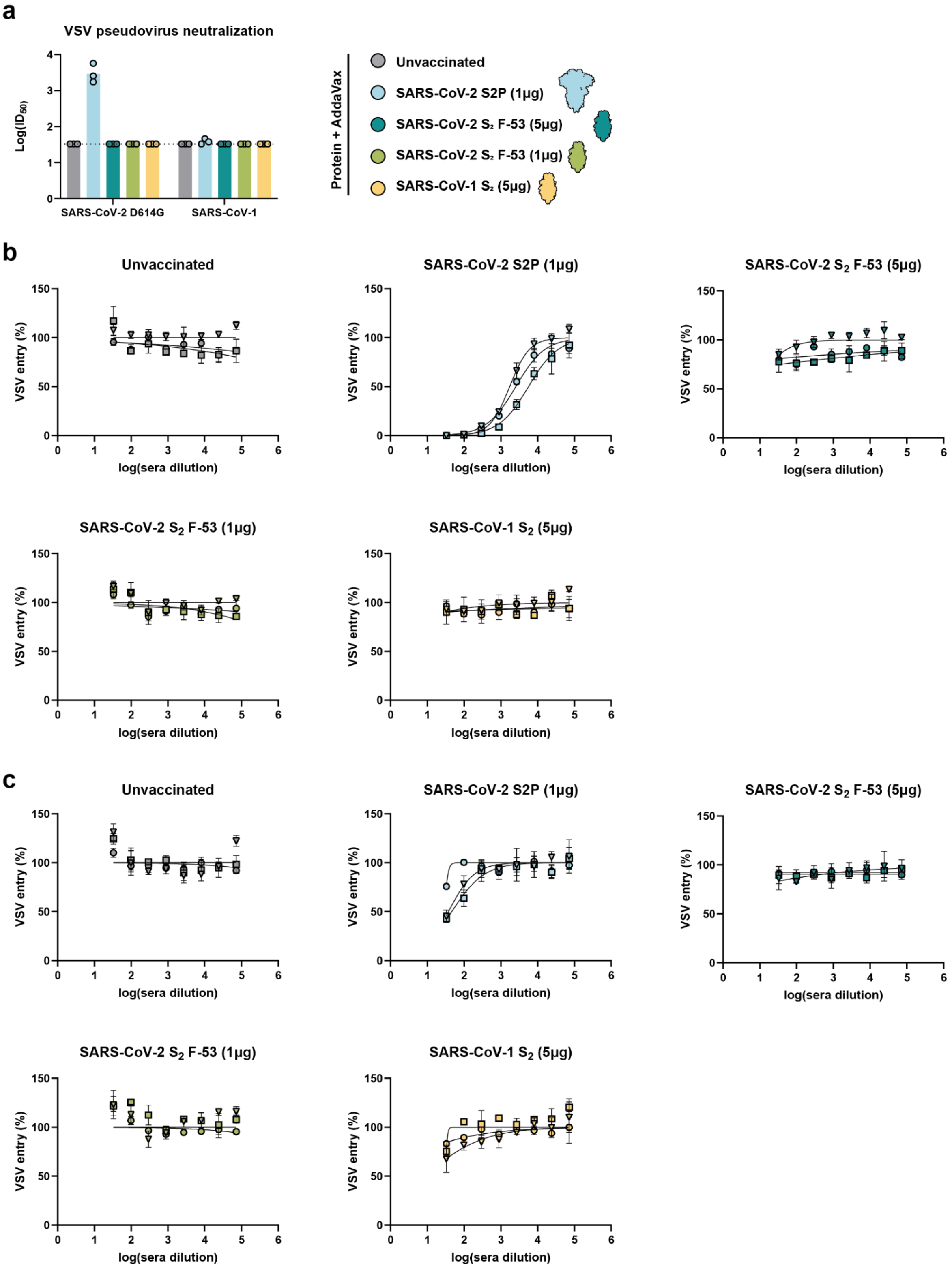

a

VSV pseudovirus neutralization

b

Unvaccinated

SARS-CoV-2 S2P (1μg)

SARS-CoV-2 S_2 F-53 (5μg)

SARS-CoV-2 S_2 F-53 (1μg)

SARS-CoV-1 S_2 (5μg)

c

Unvaccinated

SARS-CoV-2 S2P (1μg)

SARS-CoV-2 S_2 F-53 (5μg)

SARS-CoV-2 S_2 F-53 (1μg)

SARS-CoV-1 S_2 (5μg)

(**a**) Analysis of neutralizing antibody titers of pooled sera from vaccinated mice against SARS-CoV-2 S D614G and SARS-CoV-1 pseudotyped VSV. Each dot one biological replicates. Geometric means are shown as bars. Each biological replicate was performed with three technical replicates. (**b-c**) Dose-response curves of serum neutralizing antibody titers against the SARS-CoV-2 S D614G (**b**) and SARS-CoV-1 S (**c**) pseudotyped VSV using pooled sera. All three biological replicates are shown. Each data point represents the mean values from three technical replicates in each biological replicate.

CHAPTER 6. CONCLUDING REMARKS

From the findings discussed in this dissertation, we have learned that there are tools that we can develop to broadly counteract sarbecoviruses. *De novo* designed miniprotein inhibitors have physical properties that make them highly stable, adequate for alternative administration methods, and manufacturing efficient (Chapter 2). TRI2-2 showed robust reactivity and protection across a vast majority of SARS-CoV-2 variants, where many monoclonal antibodies failed to do so (Chapter 2). With recent technological advances, miniproteins can be rapidly designed and produced, making them a robust countermeasure tool against quickly evolving sarbecoviruses.

We demonstrated that zoonotic sarbecoviruses have the potential to utilize humans as its reservoir or host by showing a clade 3 sarbecovirus PRD-0038 gaining hACE-utilizing ability after only one amino acid mutation (Chapter 3). Vaccination with SARS-CoV-2 spike did not elicit potent neutralizing antibodies against PRD-0038, highlighting the necessity to develop countermeasures that have a broader range of efficacy for better pandemic preparedness should it arise from different clades of sarbecoviruses (Chapter 3).

This has led us to explore vaccine candidates that are broadly applicable against sarbecoviruses, focusing on the fusion machinery of the spike glycoprotein. We have developed a broadly generalizable method for stabilizing sarbecovirus fusion machinery in prefusion form (Chapter 4). Our data confirmed that the prefusion-stabilized sarbecovirus fusion machinery vaccines successfully elicited immune responses in mice (Chapters 4 and 5). However, we did not detect potent neutralizing abilities from these vaccines even when we tried optimizing delivery platforms (mRNA-LNP or protein nanoparticles) or partially removing glycan shields (Chapters 4 and 5). Also, conformational differences in fusion machinery, apex closed or open, did not result in significant differences in antibody epitopes or neutralizing abilities (Chapter 5). Regardless, our data illustrate that developing vaccines against highly conserved regions, such as fusion machinery, can be an effective way for pan-sarbecovirus countermeasures and achieving breadth, even at the expense of potency, a critical goal to meet for future pandemics. This was demonstrated by *in vivo* protection from disease in mice that were challenged with immune-evasive SARS-CoV-2 XBB.1.5 and SARS-CoV-1 after vaccinating with our prefusion-stabilized fusion machinery vaccine, validating the proof of principle (Chapter 4 and Chapter 5).

This dissertation is a compilation of efforts to understand mechanisms of broad-spectrum countermeasures against sarbecoviruses. It provides a foundational work for developing sarbecovirus countermeasures such as miniprotein and next generation sarbecovirus fusion machinery vaccines, offering guidance on what factors to consider when designing therapeutics and vaccine candidates.

Many questions still remain to be explored. We have shown that prefusion S_2 vaccines are highly immunogenic. However, the majority of elicited antibodies have little to no neutralizing activity. Compared with other class 1 fusion proteins such as RSV F, sarbecovirus fusion protein targeting antibodies are relatively less potent in neutralizing efficacy, and we only start seeing detectable neutralizing activity after a minimum of three immunizations of high doses. Is this something intrinsic in the structure of the spike machinery of coronaviruses? Does that also suggest that we should target a different phase of fusion intermediate state to enhance antibody neutralizing titers, such as EFIC? Also, we are limited by the data generated in mice in our study. How would our fusion machinery vaccine work in humans who have been mostly primed with the full spike by either prior infection or vaccination? What are the correlations between protection in humans and Fc-mediated effector functions? These are some questions that will require further research to grasp better understanding of protection against sarbecoviruses.

Apart from the aforementioned projects that I have led, I have also participated in various other projects in the lab that have delved deeper into characterizing coronaviruses. Some of these works include characterizing diverse ACE2 receptor utilization of merbecoviruses and exploring coronavirus entry mechanisms. All the projects have taught me not only valuable experimental techniques but also how to ask questions, set hypotheses, and design experiments as an independent researcher. I hope to carry on working on developing countermeasures against infectious diseases and contribute to global public health throughout my career.

REFERENCES

Abramson, J., Adler, J., Dunger, J., Evans, R., Green, T., Pritzel, A., Ronneberger, O., Willmore, L., Ballard, A. J., Bambrick, J., Bodenstein, S. W., Evans, D. A., Hung, C.-C., O’Neill, M., Reiman, D., Tunyasuvunakool, K., Wu, Z., Žemgulytė, A., Arvaniti, E., … Jumper, J. M. (2024). Accurate structure prediction of biomolecular interactions with AlphaFold 3. *Nature*, *630*(8016), 493–500. https://doi.org/10.1038/s41586-024-07487-w

Adams, L. E., Leist, S. R., Dinnon, K. H., 3rd, West, A., Gully, K. L., Anderson, E. J., Loome, J. F., Madden, E. A., Powers, J. M., Schäfer, A., Sarkar, S., Castillo, I. N., Maron, J. S., McNamara, R. P., Bertera, H. L., Zweigert, M. R., Higgins, J. S., Hampton, B. K., Premkumar, L., … Baric, R. S. (2023). Fc-mediated pan-sarbecovirus protection after alphavirus vector vaccination. *Cell Reports*, *42*(4), 112326. https://doi.org/10.1016/j.celrep.2023.112326

Addetia, A., Piccoli, L., Case, J. B., Park, Y.-J., Beltramello, M., Guarino, B., Dang, H., de Melo, G. D., Pinto, D., Sprouse, K., Scheaffer, S. M., Bassi, J., Silacci-Fregni, C., Muoio, F., Dini, M., Vincenzetti, L., Acosta, R., Johnson, D., Subramanian, S., … Veesler, D. (2023a). Neutralization, effector function and immune imprinting of Omicron variants. *Nature*, *621*(7979), 592–601. https://doi.org/10.1038/s41586-023-06487-6

Addetia, A., Piccoli, L., Case, J. B., Park, Y.-J., Beltramello, M., Guarino, B., Dang, H., Pinto, D., Scheaffer, S., Sprouse, K., Bassi, J., Silacci-Fregni, C., Muoio, F., Dini, M., Vincenzetti, L., Acosta, R., Johnson, D., Subramanian, S., Saliba, C., … Veesler, D. (2023b). Therapeutic and vaccine-induced cross-reactive antibodies with effector function against emerging Omicron variants. In *bioRxivorg*. https://doi.org/10.1101/2023.01.17.523798

Agirre, J., Iglesias-Fernández, J., Rovira, C., Davies, G. J., Wilson, K. S., & Cowtan, K. D. (2015). Privateer: software for the conformational validation of carbohydrate structures. *Nature Structural & Molecular Biology*, *22*(11), 833–834. https://doi.org/10.1038/nsmb.3115

Alkhovsky, S., Lenshin, S., Romashin, A., Vishnevskaya, T., Vyshemirsky, O., Bulycheva, Y., Lvov, D., & Gitelman, A. (2022). SARS-like Coronaviruses in Horseshoe Bats (Rhinolophus spp.) in Russia, 2020. *Viruses*, *14*(1), 113. https://doi.org/10.3390/v14010113

Anderson, B. R., Muramatsu, H., Nallagatla, S. R., Bevilacqua, P. C., Sansing, L. H., Weissman, D., & Karikó, K. (2010). Incorporation of pseudouridine into mRNA enhances translation by diminishing PKR activation. *Nucleic Acids Research*, *38*(17), 5884–5892. https://doi.org/10.1093/nar/gkq347

Argenziano, M. G., Bruce, S. L., Slater, C. L., Tiao, J. R., Baldwin, M. R., Barr, R. G., Chang, B. P., Chau, K. H., Choi, J. J., Gavin, N., Goyal, P., Mills, A. M., Patel, A. A., Romney, M.-L. S., Safford, M. M., Schluger, N. W., Sengupta, S., Sobieszczyk, M. E., Zucker, J. E., … Chen, R. (2020). Characterization and clinical course of 1000 patients with coronavirus disease 2019 in New York: retrospective case series. *BMJ (Clinical Research Ed.)*, *369*, m1996. https://doi.org/10.1136/bmj.m1996

Arunachalam, P. S., Walls, A. C., Golden, N., Atyeo, C., Fischinger, S., Li, C., Aye, P., Navarro, M. J., Lai, L., Edara, V. V., Röltgen, K., Rogers, K., Shirreff, L., Ferrell, D. E., Wrenn, S., Pettie, D., Kraft, J. C., Miranda, M. C., Kepl, E., … Pulendran, B. (2021). Adjuvanting a subunit COVID-19 vaccine to induce protective immunity. *Nature*, *594*(7862), 253–258. https://doi.org/10.1038/s41586-021-03530-2

Asarnow, D., Palovcak, E., & Cheng, Y. (2019). *asarnow/pyem: UCSF pyem v0.5* (Version v0.5). Zenodo. https://doi.org/10.5281/ZENODO.3576630

Baden, L. R., El Sahly, H. M., Essink, B., Kotloff, K., Frey, S., Novak, R., Diemert, D., Spector, S. A., Rouphael, N., Creech, C. B., McGettigan, J., Khetan, S., Segall, N., Solis, J., Brosz, A., Fierro, C., Schwartz, H., Neuzil, K., Corey, L., … COVE Study Group. (2021). Efficacy and safety of the mRNA-1273 SARS-CoV-2 vaccine. *The New England Journal of Medicine*, *384*(5), 403–416. https://doi.org/10.1056/NEJMoa2035389

Belouzard, S., Chu, V. C., & Whittaker, G. R. (2009). Activation of the SARS coronavirus spike protein via sequential proteolytic cleavage at two distinct sites. *Proceedings of the National Academy of Sciences of the United States of America*, *106*(14), 5871–5876. https://doi.org/10.1073/pnas.0809524106

Bepler, T., Morin, A., Rapp, M., Brasch, J., Shapiro, L., Noble, A. J., & Berger, B. (2019). Positive-unlabeled convolutional neural networks for particle picking in cryo-electron micrographs. *Nature Methods*, *16*(11), 1153–1160. https://doi.org/10.1038/s41592-019-0575-8

Boni, M. F., Lemey, P., Jiang, X., Lam, T. T.-Y., Perry, B. W., Castoe, T. A., Rambaut, A., & Robertson, D. L. (2020). Evolutionary origins of the SARS-CoV-2 sarbecovirus lineage responsible for the COVID-19 pandemic. *Nature Microbiology*, *5*(11), 1408–1417. https://doi.org/10.1038/s41564-020-0771-4

Bosch, B. J., van der Zee, R., de Haan, C. A. M., & Rottier, P. J. M. (2003). The coronavirus spike protein is a class I virus fusion protein: structural and functional characterization of the fusion core complex. *Journal of Virology*, *77*(16), 8801–8811. https://doi.org/10.1128/jvi.77.16.8801-8811.2003

Bos, R., Rutten, L., van der Lubbe, J. E. M., Bakkers, M. J. G., Hardenberg, G., Wegmann, F., Zuijdgeest, D., de Wilde, A. H., Koornneef, A., Verwilligen, A., van Manen, D., Kwaks, T., Vogels, R., Dalebout, T. J., Myeni, S. K., Kikkert, M., Snijder, E. J., Li, Z., Barouch, D. H., … Schuitemaker, H. (2020). Ad26 vector-based COVID-19 vaccine encoding a prefusion-stabilized SARS-CoV-2 Spike immunogen induces potent humoral and cellular immune responses. *NPJ Vaccines*, *5*, 91. https://doi.org/10.1038/s41541-020-00243-x

Bowen, J. E., Addetia, A., Dang, H. V., Stewart, C., Brown, J. T., Sharkey, W. K., Sprouse, K. R., Walls, A. C., Mazzitelli, I. G., Logue, J. K., Franko, N. M., Czudnochowski, N., Powell, A. E., Dellota, E., Jr, Ahmed, K., Ansari, A. S., Cameroni, E., Gori, A., Bandera, A., … Veesler, D. (2022). Omicron spike function and neutralizing activity elicited by a comprehensive panel of vaccines. *Science*, eabq0203. https://doi.org/10.1126/science.abq0203

Bowen, J. E., Park, Y.-J., Stewart, C., Brown, J. T., Sharkey, W. K., Walls, A. C., Joshi, A., Sprouse, K. R., McCallum, M., Alejandra Tortorici, M., Franko, N. M., Logue, J. K., Mazzitelli, I. G., Nguyen, A. W., Silva, R. P., Huang, Y., Low, J. S., Jerak, J., Tiles, S. W., … Veesler, D. (2022). SARS-CoV-2 spike conformation determines plasma neutralizing activity elicited by a wide panel of human vaccines. In *Science Immunology*. https://doi.org/10.1126/sciimmunol.adf1421

Boyoglu-Barnum, S., Ellis, D., Gillespie, R. A., Hutchinson, G. B., Park, Y.-J., Moin, S. M., Acton, O. J., Ravichandran, R., Murphy, M., Pettie, D., Matheson, N., Carter, L., Creanga, A., Watson, M. J., Kephart, S., Ataca, S., Vaile, J. R., Ueda, G., Crank, M. C., … Kanekiyo, M. (2021). Quadrivalent influenza nanoparticle vaccines induce broad protection. *Nature*, *592*(7855), 623–628. https://doi.org/10.1038/s41586-021-03365-x

Bussani, R., Schneider, E., Zentilin, L., Collesi, C., Ali, H., Braga, L., Volpe, M. C., Colliva, A., Zanconati, F., Berlot, G., Silvestri, F., Zacchigna, S., & Giacca, M. (2020). Persistence of viral RNA, pneumocyte syncytia and thrombosis are hallmarks of advanced COVID-19 pathology. *EBioMedicine*, *61*(103104), 103104. https://doi.org/10.1016/j.ebiom.2020.103104

Cagigi, A., & Loré, K. (2021). Immune responses induced by mRNA vaccination in mice, monkeys and humans. *Vaccines*, *9*(1), 61. https://doi.org/10.3390/vaccines9010061

Cameroni, E., Bowen, J. E., Rosen, L. E., Saliba, C., Zepeda, S. K., Culap, K., Pinto, D., VanBlargan, L. A., De Marco, A., di Iulio, J., Zatta, F., Kaiser, H., Noack, J., Farhat, N., Czudnochowski, N., Havenar-Daughton, C., Sprouse, K. R., Dillen, J. R., Powell, A. E., … Corti, D. (2022). Broadly neutralizing antibodies overcome SARS-CoV-2 Omicron antigenic shift. *Nature*, *602*(7898), 664–670. https://doi.org/10.1038/s41586-021-04386-2

Cao, L., Coventry, B., Goreshnik, I., Huang, B., Sheffler, W., Park, J. S., Jude, K. M., Marković, I., Kadam, R. U., Verschueren, K. H. G., Verstraete, K., Walsh, S. T. R., Bennett, N., Phal, A., Yang, A., Kozodoy, L., DeWitt, M., Picton, L., Miller, L., … Baker, D. (2022). Design of protein-binding proteins from the target structure alone. *Nature*, *605*(7910), 551–560. https://doi.org/10.1038/s41586-022-04654-9

Cao, L., Goreshnik, I., Coventry, B., Case, J. B., Miller, L., Kozodoy, L., Chen, R. E., Carter, L., Walls, A. C., Park, Y.-J., Strauch, E.-M., Stewart, L., Diamond, M. S., Veesler, D., & Baker, D. (2020). De novo design of picomolar SARS-CoV-2 miniprotein inhibitors. *Science*, *370*(6515), 426–431.

https://doi.org/10.1126/science.abd9909

Cao, Y., Jian, F., Wang, J., Yu, Y., Song, W., Yisimayi, A., Wang, J., An, R., Chen, X., Zhang, N., Wang, Y., Wang, P., Zhao, L., Sun, H., Yu, L., Yang, S., Niu, X., Xiao, T., Gu, Q., … Xie, X. S. (2023). Imprinted SARS-CoV-2 humoral immunity induces convergent Omicron RBD evolution. *Nature*, *614*(7948), 521–529. https://doi.org/10.1038/s41586-022-05644-7

Cao, Y., Jian, F., Zhang, Z., Yisimayi, A., Hao, X., Bao, L., Yuan, F., Yu, Y., Du, S., Wang, J., Xiao, T., Song, W., Zhang, Y., Liu, P., An, R., Wang, P., Wang, Y., Yang, S., Niu, X., … Xie, X. S. (2022). Rational identification of potent and broad sarbecovirus-neutralizing antibody cocktails from SARS convalescents. *Cell Reports*, *41*(12), 111845. https://doi.org/10.1016/j.celrep.2022.111845

Cao, Y., Wang, J., Jian, F., Xiao, T., Song, W., Yisimayi, A., Huang, W., Li, Q., Wang, P., An, R., Wang, J., Wang, Y., Niu, X., Yang, S., Liang, H., Sun, H., Li, T., Yu, Y., Cui, Q., … Xie, X. S. (2022). Omicron escapes the majority of existing SARS-CoV-2 neutralizing antibodies. *Nature*, *602*(7898), 657–663. https://doi.org/10.1038/s41586-021-04385-3

Cao, Y., Yisimayi, A., Jian, F., Song, W., Xiao, T., Wang, L., Du, S., Wang, J., Li, Q., Chen, X., Yu, Y., Wang, P., Zhang, Z., Liu, P., An, R., Hao, X., Wang, Y., Wang, J., Feng, R., … Xie, X. S. (2022). BA.2.12.1, BA.4 and BA.5 escape antibodies elicited by Omicron infection. *Nature*, *608*(7923), 593–602. https://doi.org/10.1038/s41586-022-04980-y

Carrasco, Y. R., & Batista, F. D. (2006). B cell recognition of membrane-bound antigen: an exquisite way of sensing ligands. *Current Opinion in Immunology*, *18*(3), 286–291. https://doi.org/10.1016/j.coi.2006.03.013

Case, J. B., Bailey, A. L., Kim, A. S., Chen, R. E., & Diamond, M. S. (2020). Growth, detection, quantification, and inactivation of SARS-CoV-2. *Virology*, *548*, 39–48. https://doi.org/10.1016/j.virol.2020.05.015

CDC SARS response timeline. (2023, September 12). https://archive.cdc.gov/www_cdc_gov/about/history/sars/timeline.htm

Chalkias, S., Harper, C., Vrbicky, K., Walsh, S. R., Essink, B., Brosz, A., McGhee, N., Tomassini, J. E., Chen, X., Chang, Y., Sutherland, A., Montefiori, D. C., Girard, B., Edwards, D. K., Feng, J., Zhou, H., Baden, L. R., Miller, J. M., & Das, R. (2022). A bivalent omicron-containing booster vaccine against covid-19. *The New England Journal of Medicine*, *387*(14), 1279–1291. https://doi.org/10.1056/NEJMoa2208343

Chalkias, S., McGhee, N., Whatley, J. L., Essink, B., Brosz, A., Tomassini, J. E., Girard, B., Wu, K., Edwards, D. K., Nasir, A., Lee, D., Avena, L. E., Feng, J., Deng, W., Montefiori, D. C., Baden, L. R., Miller, J. M., & Das, R. (2023). Safety and Immunogenicity of XBB.1.5-Containing mRNA Vaccines. In *bioRxiv*. https://doi.org/10.1101/2023.08.22.23293434

Chaudhary, N., Weissman, D., & Whitehead, K. A. (2021). mRNA vaccines for infectious diseases: principles, delivery and clinical translation. *Nature Reviews. Drug Discovery*, *20*(11), 817–838. https://doi.org/10.1038/s41573-021-00283-5

Cheng, C.-W., Wu, C.-Y., Wang, S.-W., Chen, J.-Y., Kung, C.-C., Liao, K.-S., & Wong, C.-H. (2023). Low-sugar universal mRNA vaccine against coronavirus variants with deletion of glycosites in the S2 or stem of SARS-CoV-2 spike messenger RNA (mRNA). *Proceedings of the National Academy of Sciences of the United States of America*, *120*(49), e2314392120. https://doi.org/10.1073/pnas.2314392120

Chen, R. E., Zhang, X., Case, J. B., Winkler, E. S., Liu, Y., VanBlargan, L. A., Liu, J., Errico, J. M., Xie, X., Suryadevara, N., Gilchuk, P., Zost, S. J., Tahan, S., Droit, L., Turner, J. S., Kim, W., Schmitz, A. J., Thapa, M., Wang, D., … Diamond, M. S. (2021). Resistance of SARS-CoV-2 variants to neutralization by monoclonal and serum-derived polyclonal antibodies. *Nature Medicine*, *27*(4), 717–726. https://doi.org/10.1038/s41591-021-01294-w

Chen, S., McMullan, G., Faruqi, A. R., Murshudov, G. N., Short, J. M., Scheres, S. H. W., & Henderson, R. (2013). High-resolution noise substitution to measure overfitting and validate resolution in 3D structure determination by single particle electron cryomicroscopy. *Ultramicroscopy*, *135*, 24–35. https://doi.org/10.1016/j.ultramic.2013.06.004

Chen, V. B., Arendall, W. B., 3rd, Headd, J. J., Keedy, D. A., Immormino, R. M., Kapral, G. J., Murray, L. W., Richardson, J. S., & Richardson, D. C. (2010). MolProbity: all-atom structure validation for macromolecular crystallography. *Acta Crystallographica. Section D, Biological Crystallography*, *66*(Pt 1), 12–21. https://doi.org/10.1107/S0907444909042073

Chevalier, A., Silva, D.-A., Rocklin, G. J., Hicks, D. R., Vergara, R., Murapa, P., Bernard, S. M., Zhang, L., Lam, K.-H., Yao, G., Bahl, C. D., Miyashita, S.-I., Goreshnik, I., Fuller, J. T., Koday, M. T., Jenkins, C. M., Colvin, T., Carter, L., Bohn, A., … Baker, D. (2017). Massively parallel de novo protein design for targeted therapeutics. *Nature*, *550*(7674), 74–79. https://doi.org/10.1038/nature23912

Chi, W.-Y., Li, Y.-D., Huang, H.-C., Chan, T. E. H., Chow, S.-Y., Su, J.-H., Ferrall, L., Hung, C.-F., & Wu, T.-C. (2022). COVID-19 vaccine update: vaccine effectiveness, SARS-CoV-2 variants, boosters, adverse effects, and immune correlates of protection. *Journal of Biomedical Science*, *29*(1), 82. https://doi.org/10.1186/s12929-022-00853-8

Chou, T.-H. W., Wang, S., Sakhatskyy, P. V., Mboudjeka, I., Lawrence, J. M., Huang, S., Coley, S., Yang, B., Li, J., Zhu, Q., & Lu, S. (2005). Epitope mapping and biological function analysis of antibodies produced by immunization of mice with an inactivated Chinese isolate of severe acute respiratory syndrome-associated coronavirus (SARS-CoV). *Virology*, *334*(1), 134–143. https://doi.org/10.1016/j.virol.2005.01.035

Chu, K. H., Tsang, W. K., Tang, C. S., Lam, M. F., Lai, F. M., To, K. F., Fung, K. S., Tang,

H. L., Yan, W. W., Chan, H. W. H., Lai, T. S. T., Tong, K. L., & Lai, K. N. (2005). Acute renal impairment in coronavirus-associated severe acute respiratory syndrome. *Kidney International*, *67*(2), 698–705. https://doi.org/10.1111/j.1523-1755.2005.67130.x

Cohen, A. A., Gnanapragasam, P. N. P., Lee, Y. E., Hoffman, P. R., Ou, S., Kakutani, L. M., Keeffe, J. R., Wu, H.-J., Howarth, M., West, A. P., Barnes, C. O., Nussenzweig, M. C., & Bjorkman, P. J. (2021). Mosaic nanoparticles elicit cross-reactive immune responses to zoonotic coronaviruses in mice. *Science (New York, N.Y.)*, *371*(6530), 735–741. https://doi.org/10.1126/science.abf6840

Cohen, A. A., van Doremalen, N., Greaney, A. J., Andersen, H., Sharma, A., Starr, T. N., Keeffe, J. R., Fan, C., Schulz, J. E., Gnanapragasam, P. N. P., Kakutani, L. M., West, A. P., Saturday, G., Lee, Y. E., Gao, H., Jette, C. A., Lewis, M. G., Tan, T. K., Townsend, A. R., … Bjorkman, P. J. (2022). Mosaic RBD nanoparticles protect against challenge by diverse sarbecoviruses in animal models. *Science*, *377*(6606), eabq0839. https://doi.org/10.1126/science.abq0839

Connors, J. M., & Levy, J. H. (2020). COVID-19 and its implications for thrombosis and anticoagulation. *Blood*, *135*(23), 2033–2040. https://doi.org/10.1182/blood.2020006000

Corbett, K. S., Edwards, D. K., Leist, S. R., Abiona, O. M., Boyoglu-Barnum, S., Gillespie, R. A., Himansu, S., Schäfer, A., Ziwawo, C. T., DiPiazza, A. T., Dinnon, K. H., Elbashir, S. M., Shaw, C. A., Woods, A., Fritch, E. J., Martinez, D. R., Bock, K. W., Minai, M., Nagata, B. M., … Graham, B. S. (2020). SARS-CoV-2 mRNA vaccine design enabled by prototype pathogen preparedness. *Nature*, *586*(7830), 567–571. https://doi.org/10.1038/s41586-020-2622-0

Corti, D., Purcell, L. A., Snell, G., & Veesler, D. (2021). Tackling COVID-19 with neutralizing monoclonal antibodies. *Cell*, *184*(12), 3086–3108. https://doi.org/10.1016/j.cell.2021.05.005

Corti, D., Voss, J., Gamblin, S. J., Codoni, G., Macagno, A., Jarrossay, D., Vachieri, S. G., Pinna, D., Minola, A., Vanzetta, F., Silacci, C., Fernandez-Rodriguez, B. M., Agatic, G., Bianchi, S., Giacchetto-Sasselli, I., Calder, L., Sallusto, F., Collins, P., Haire, L. F., … Lanzavecchia, A. (2011). A neutralizing antibody selected from plasma cells that binds to group 1 and group 2 influenza A hemagglutinins. *Science (New York, N.Y.)*, *333*(6044), 850–856. https://doi.org/10.1126/science.1205669

COVID-19 cases. (n.d.). Datadot. Retrieved January 13, 2026, from https://data.who.int/dashboards/covid19/cases?n=o

Crawford, K. H. D., & Bloom, J. D. (2019). alignparse: A Python package for parsing complex features from high-throughput long-read sequencing. *Journal of Open Source Software*, *4*(44), 1915. https://doi.org/10.21105/joss.01915

Crawford, K. H. D., Eguia, R., Dingens, A. S., Loes, A. N., Malone, K. D., Wolf, C. R., Chu, H. Y., Tortorici, M. A., Veesler, D., Murphy, M., Pettie, D., King, N. P., Balazs,

A. B., & Bloom, J. D. (2020). Protocol and reagents for pseudotyping Lentiviral particles with SARS-CoV-2 Spike protein for neutralization assays. *Viruses*, *12*(5). https://doi.org/10.3390/v12050513

Crook, J. M., Murphy, I., Carter, D. P., Pullan, S. T., Carroll, M., Vipond, R., Cunningham, A. A., & Bell, D. (2021). Metagenomic identification of a new sarbecovirus from horseshoe bats in Europe. *Scientific Reports*, *11*(1), 14723. https://doi.org/10.1038/s41598-021-94011-z

Dacon, C., Tucker, C., Peng, L., Lee, C.-C. D., Lin, T.-H., Yuan, M., Cong, Y., Wang, L., Purser, L., Williams, J. K., Pyo, C.-W., Kosik, I., Hu, Z., Zhao, M., Mohan, D., Cooper, A. J. R., Peterson, M., Skinner, J., Dixit, S., … Tan, J. (2022). Broadly neutralizing antibodies target the coronavirus fusion peptide. *Science*, *377*(6607), 728–735. https://doi.org/10.1126/science.abq3773

Daffis, S., Szretter, K. J., Schriewer, J., Li, J., Youn, S., Errett, J., Lin, T.-Y., Schneller, S., Zust, R., Dong, H., Thiel, V., Sen, G. C., Fensterl, V., Klimstra, W. B., Pierson, T. C., Buller, R. M., Gale, M., Jr, Shi, P.-Y., & Diamond, M. S. (2010). 2’-O methylation of the viral mRNA cap evades host restriction by IFIT family members. *Nature*, *468*(7322), 452–456. https://doi.org/10.1038/nature09489

Dauparas, J., Anishchenko, I., Bennett, N., Bai, H., Ragotte, R. J., Milles, L. F., Wicky, B. I. M., Courbet, A., de Haas, R. J., Bethel, N., Leung, P. J. Y., Huddy, T. F., Pellock, S., Tischer, D., Chan, F., Koepnick, B., Nguyen, H., Kang, A., Sankaran, B., … Baker, D. (2022). Robust deep learning-based protein sequence design using ProteinMPNN. *Science (New York, N.Y.)*, *378*(6615), 49–56. https://doi.org/10.1126/science.add2187

de Vries, R. D., Schmitz, K. S., Bovier, F. T., Predella, C., Khao, J., Noack, D., Haagmans, B. L., Herfst, S., Stearns, K. N., Drew-Bear, J., Biswas, S., Rockx, B., McGill, G., Dorrello, N. V., Gellman, S. H., Alabi, C. A., de Swart, R. L., Moscona, A., & Porotto, M. (2021). Intranasal fusion inhibitory lipopeptide prevents direct-contact SARS-CoV-2 transmission in ferrets. *Science (New York, N.Y.)*, *371*(6536), 1379–1382. https://doi.org/10.1126/science.abf4896

Drexler, J. F., Gloza-Rausch, F., Glende, J., Corman, V. M., Muth, D., Goettsche, M., Seebens, A., Niedrig, M., Pfefferle, S., Yordanov, S., Zhelyazkov, L., Hermanns, U., Vallo, P., Lukashev, A., Müller, M. A., Deng, H., Herrler, G., & Drosten, C. (2010). Genomic characterization of severe acute respiratory syndrome-related coronavirus in European bats and classification of coronaviruses based on partial RNA-dependent RNA polymerase gene sequences. *Journal of Virology*, *84*(21), 11336–11349. https://doi.org/10.1128/JVI.00650-10

Drosten, C., Günther, S., Preiser, W., van der Werf, S., Brodt, H.-R., Becker, S., Rabenau, H., Panning, M., Kolesnikova, L., Fouchier, R. A. M., Berger, A., Burguière, A.-M., Cinatl, J., Eickmann, M., Escriou, N., Grywna, K., Kramme, S., Manuguerra, J.-C., Müller, S., … Doerr, H. W. (2003). Identification of a novel coronavirus in patients with severe acute respiratory syndrome. *The New England Journal of Medicine*, *348*(20), 1967–1976. https://doi.org/10.1056/NEJMoa030747

Efficacy Safety COVID-19 Inactivated Vaccine Healthcare Professionals Brazil: PROFISCOV Study. (n.d.).

Ekiert, D. C., Bhabha, G., Elsliger, M.-A., Friesen, R. H. E., Jongeneelen, M., Throsby, M., Goudsmit, J., & Wilson, I. A. (2009). Antibody recognition of a highly conserved influenza virus epitope. *Science (New York, N.Y.)*, *324*(5924), 246–251. https://doi.org/10.1126/science.1171491

Ekiert, D. C., Friesen, R. H. E., Bhabha, G., Kwaks, T., Jongeneelen, M., Yu, W., Ophorst, C., Cox, F., Korse, H. J. W. M., Brandenburg, B., Vogels, R., Brakenhoff, J. P. J., Kompier, R., Koldijk, M. H., Cornelissen, L. A. H. M., Poon, L. L. M., Peiris, M., Koudstaal, W., Wilson, I. A., & Goudsmit, J. (2011). A highly conserved neutralizing epitope on group 2 influenza A viruses. *Science (New York, N.Y.)*, *333*(6044), 843–850. https://doi.org/10.1126/science.1204839

Emsley, P., Lohkamp, B., Scott, W. G., & Cowtan, K. (2010). Features and development of coot. *Acta Crystallographica. Section D, Biological Crystallography*, *66*(Pt 4), 486–501. https://doi.org/10.1107/S0907444910007493

Evans, T. S., Tan, C. W., Aung, O., Phyu, S., Lin, H., Coffey, L. L., Toe, A. T., Aung, P., Aung, T. H., Aung, N. T., Weiss, C. M., Thant, K. Z., Htun, Z. T., Murray, S., Wang, L., Johnson, C. K., & Thu, H. M. (2023). Exposure to diverse sarbecoviruses indicates frequent zoonotic spillover in human communities interacting with wildlife. *International Journal of Infectious Diseases: IJID: Official Publication of the International Society for Infectious Diseases*, *131*, 57–64. https://doi.org/10.1016/j.ijid.2023.02.015

Fleishman, S. J., Whitehead, T. A., Ekiert, D. C., Dreyfus, C., Corn, J. E., Strauch, E.-M., Wilson, I. A., & Baker, D. (2011). Computational design of proteins targeting the conserved stem region of influenza hemagglutinin. *Science (New York, N.Y.)*, *332*(6031), 816–821. https://doi.org/10.1126/science.1202617

Folegatti, P. M., Ewer, K. J., Aley, P. K., Angus, B., Becker, S., Belij-Rammerstorfer, S., Bellamy, D., Bibi, S., Bittaye, M., Clutterbuck, E. A., Dold, C., Faust, S. N., Finn, A., Flaxman, A. L., Hallis, B., Heath, P., Jenkin, D., Lazarus, R., Makinson, R., … Oxford COVID Vaccine Trial Group. (2020). Safety and immunogenicity of the ChAdOx1 nCoV-19 vaccine against SARS-CoV-2: a preliminary report of a phase 1/2, single-blind, randomised controlled trial. *Lancet*, *396*(10249), 467–478. https://doi.org/10.1016/S0140-6736(20)31604-4

Freitas, A. R. R., Beckedorff, O. A., Cavalcanti, L. P. de G., Siqueira, A. M., Castro, D. B. de, Costa, C. F. da, Lemos, D. R. Q., & Barros, E. N. C. (2021). The emergence of novel SARS-CoV-2 variant P.1 in Amazonas (Brazil) was temporally associated with a change in the age and sex profile of COVID-19 mortality: A population based ecological study. *Lancet Regional Health. Americas*, *1*(100021), 100021.

https://doi.org/10.1016/j.lana.2021.100021

Frenz, B., Rämisch, S., Borst, A. J., Walls, A. C., Adolf-Bryfogle, J., Schief, W. R., Veesler, D., & DiMaio, F. (2019). Automatically fixing errors in glycoprotein structures with Rosetta. *Structure (London, England: 1993)*, *27*(1), 134–139.e3. https://doi.org/10.1016/j.str.2018.09.006

Fujino, T., Nomoto, H., Kutsuna, S., Ujiie, M., Suzuki, T., Sato, R., Fujimoto, T., Kuroda, M., Wakita, T., & Ohmagari, N. (2021). Novel SARS-CoV-2 variant in travelers from Brazil to Japan. *Emerging Infectious Diseases*, *27*(4). https://doi.org/10.3201/eid2704.210138

Ge, X.-Y., Li, J.-L., Yang, X.-L., Chmura, A. A., Zhu, G., Epstein, J. H., Mazet, J. K., Hu, B., Zhang, W., Peng, C., Zhang, Y.-J., Luo, C.-M., Tan, B., Wang, N., Zhu, Y., Crameri, G., Zhang, S.-Y., Wang, L.-F., Daszak, P., & Shi, Z.-L. (2013). Isolation and characterization of a bat SARS-like coronavirus that uses the ACE2 receptor. *Nature*, *503*(7477), 535–538. https://doi.org/10.1038/nature12711

Giamarellos-Bourboulis, E. J., Netea, M. G., Rovina, N., Akinosoglou, K., Antoniadou, A., Antonakos, N., Damoraki, G., Gkavogianni, T., Adami, M.-E., Katsaounou, P., Ntaganou, M., Kyriakopoulou, M., Dimopoulos, G., Koutsodimitropoulos, I., Velissaris, D., Koufargyris, P., Karageorgos, A., Katrini, K., Lekakis, V., … Koutsoukou, A. (2020). Complex immune dysregulation in COVID-19 patients with severe respiratory failure. *Cell Host & Microbe*, *27*(6), 992–1000.e3. https://doi.org/10.1016/j.chom.2020.04.009

Giller, R. H., Winistorfer, S., & Grose, C. (1989). Cellular and humoral immunity to varicella zoster virus glycoproteins in immune and susceptible human subjects. *The Journal of Infectious Diseases*, *160*(6), 919–928. https://doi.org/10.1093/infdis/160.6.919

Goddard, T. D., Huang, C. C., Meng, E. C., Pettersen, E. F., Couch, G. S., Morris, J. H., & Ferrin, T. E. (2018). UCSF ChimeraX: Meeting modern challenges in visualization and analysis. *Protein Science*, *27*(1), 14–25. https://doi.org/10.1002/pro.3235

Godiska, R., Mead, D., Dhodda, V., Wu, C., Hochstein, R., Karsi, A., Usdin, K., Entezam, A., & Ravin, N. (2010). Linear plasmid vector for cloning of repetitive or unstable sequences in Escherichia coli. *Nucleic Acids Research*, *38*(6), e88. https://doi.org/10.1093/nar/gkp1181

Goel, R. R., Painter, M. M., Apostolidis, S. A., Mathew, D., Meng, W., Rosenfeld, A. M., Lundgreen, K. A., Reynaldi, A., Khoury, D. S., Pattekar, A., Gouma, S., Kuri-Cervantes, L., Hicks, P., Dysinger, S., Hicks, A., Sharma, H., Herring, S., Korte, S., Baxter, A. E., … Wherry, E. J. (2021). mRNA vaccines induce durable immune memory to SARS-CoV-2 and variants of concern. *Science (New York, N.Y.)*, *374*(6572), abm0829. https://doi.org/10.1126/science.abm0829

Gordon, S., Plüddemann, A., & Mukhopadhyay, S. (2014). Sinusoidal immunity: macrophages at the lymphohematopoietic interface. *Cold Spring Harbor*

Perspectives in Biology, *7*(4), a016378. https://doi.org/10.1101/cshperspect.a016378

Gote, V., Bolla, P. K., Kommineni, N., Butreddy, A., Nukala, P. K., Palakurthi, S. S., & Khan, W. (2023). A comprehensive review of mRNA vaccines. *International Journal of Molecular Sciences*, *24*(3), 2700. https://doi.org/10.3390/ijms24032700

Greaney, A. J., Loes, A. N., Gentles, L. E., Crawford, K. H. D., Starr, T. N., Malone, K. D., Chu, H. Y., & Bloom, J. D. (2021). Antibodies elicited by mRNA-1273 vaccination bind more broadly to the receptor binding domain than do those from SARS-CoV-2 infection. *Science Translational Medicine*, *13*(600), eabi9915. https://doi.org/10.1126/scitranslmed.abi9915

Greaney, A. J., Starr, T. N., Eguia, R. T., Loes, A. N., Khan, K., Karim, F., Cele, S., Bowen, J. E., Logue, J. K., Corti, D., Veesler, D., Chu, H. Y., Sigal, A., & Bloom, J. D. (2022). A SARS-CoV-2 variant elicits an antibody response with a shifted immunodominance hierarchy. *PLoS Pathogens*, *18*(2), e1010248. https://doi.org/10.1371/journal.ppat.1010248

Guo, H., Hu, B.-J., Yang, X.-L., Zeng, L.-P., Li, B., Ouyang, S., & Shi, Z.-L. (2020). Evolutionary arms race between virus and host drives genetic diversity in bat severe acute respiratory syndrome-related Coronavirus spike genes. *Journal of Virology*, *94*(20). https://doi.org/10.1128/JVI.00902-20

Halfmann, P. J., Frey, S. J., Loeffler, K., Kuroda, M., Maemura, T., Armbrust, T., Yang, J. E., Hou, Y. J., Baric, R., Wright, E. R., Kawaoka, Y., & Kane, R. S. (2022). Multivalent S2-based vaccines provide broad protection against SARS-CoV-2 variants of concern and pangolin coronaviruses. *EBioMedicine*, *86*(104341), 104341. https://doi.org/10.1016/j.ebiom.2022.104341

Harbison, A. M., Fogarty, C. A., Phung, T. K., Satheesan, A., Schulz, B. L., & Fadda, E. (2022). Fine-tuning the spike: role of the nature and topology of the glycan shield in the structure and dynamics of the SARS-CoV-2 S. *Chemical Science* , *13*(2), 386–395. https://doi.org/10.1039/D1SC04832E

Harrison, S. C. (2008). Viral membrane fusion. *Nature Structural & Molecular Biology*, *15*(7), 690–698. https://doi.org/10.1038/nsmb.1456

Hassan, A. O., Feldmann, F., Zhao, H., Curiel, D. T., Okumura, A., Tang-Huau, T.-L., Case, J. B., Meade-White, K., Callison, J., Chen, R. E., Lovaglio, J., Hanley, P. W., Scott, D. P., Fremont, D. H., Feldmann, H., & Diamond, M. S. (2021). A single intranasal dose of chimpanzee adenovirus-vectored vaccine protects against SARS-CoV-2 infection in rhesus macaques. *Cell Reports. Medicine*, *2*(4), 100230. https://doi.org/10.1016/j.xcrm.2021.100230

Heald-Sargent, T., & Gallagher, T. (2012). Ready, set, fuse! The coronavirus spike protein and acquisition of fusion competence. *Viruses*, *4*(4), 557–580. https://doi.org/10.3390/v4040557

Hoffmann, M., Kleine-Weber, H., & Pöhlmann, S. (2020). A multibasic cleavage site in the spike protein of SARS-CoV-2 is essential for infection of human lung cells. *Molecular Cell*, *78*(4), 779–784.e5. https://doi.org/10.1016/j.molcel.2020.04.022

Hoffmann, M., Kleine-Weber, H., Schroeder, S., Krüger, N., Herrler, T., Erichsen, S., Schiergens, T. S., Herrler, G., Wu, N.-H., Nitsche, A., Müller, M. A., Drosten, C., & Pöhlmann, S. (2020). SARS-CoV-2 cell entry depends on ACE2 and TMPRSS2 and is blocked by a clinically proven protease inhibitor. *Cell*, *181*(2), 271–280.e8. https://doi.org/10.1016/j.cell.2020.02.052

Houser, K. V., Gaudinski, M. R., Happe, M., Narpala, S., Verardi, R., Sarfo, E. K., Corrigan, A. R., Wu, R., Rothwell, R. S., Novik, L., Hendel, C. S., Gordon, I. J., Berkowitz, N. M., Cartagena, C. T., Widge, A. T., Coates, E. E., Strom, L., Hickman, S., Conan-Cibotti, M., … VRC 018 Study Team. (2022). Safety and immunogenicity of an HIV-1 prefusion-stabilized envelope trimer (Trimer 4571) vaccine in healthy adults: A first-in-human open-label, randomized, dose-escalation, phase 1 clinical trial. *EClinicalMedicine*, *48*(101477), 101477. https://doi.org/10.1016/j.eclinm.2022.101477

Hsieh, C.-L., Goldsmith, J. A., Schaub, J. M., DiVenere, A. M., Kuo, H.-C., Javanmardi, K., Le, K. C., Wrapp, D., Lee, A. G., Liu, Y., Chou, C.-W., Byrne, P. O., Hjorth, C. K., Johnson, N. V., Ludes-Meyers, J., Nguyen, A. W., Park, J., Wang, N., Amengor, D., … McLellan, J. S. (2020). Structure-based design of prefusion-stabilized SARS-CoV-2 spikes. *Science (New York, N.Y.)*, *369*(6510), 1501–1505. https://doi.org/10.1126/science.abd0826

Hsieh, C.-L., Werner, A. P., Leist, S. R., Stevens, L. J., Falconer, E., Goldsmith, J. A., Chou, C.-W., Abiona, O. M., West, A., Westendorf, K., Muthuraman, K., Fritch, E. J., Dinnon, K. H., 3rd, Schäfer, A., Denison, M. R., Chappell, J. D., Baric, R. S., Graham, B. S., Corbett, K. S., & McLellan, J. S. (2021). Stabilized coronavirus spike stem elicits a broadly protective antibody. *Cell Reports*, *37*(5), 109929. https://doi.org/10.1016/j.celrep.2021.109929

Huang, C., Wang, Y., Li, X., Ren, L., Zhao, J., Hu, Y., Zhang, L., Fan, G., Xu, J., Gu, X., Cheng, Z., Yu, T., Xia, J., Wei, Y., Wu, W., Xie, X., Yin, W., Li, H., Liu, M., … Cao, B. (2020). Clinical features of patients infected with 2019 novel coronavirus in Wuhan, China. *Lancet*, *395*(10223), 497–506. https://doi.org/10.1016/S0140-6736(20)30183-5

Huang, H.-Y., Liao, H.-Y., Chen, X., Wang, S.-W., Cheng, C.-W., Shahed-Al-Mahmud, M., Liu, Y.-M., Mohapatra, A., Chen, T.-H., Lo, J. M., Wu, Y.-M., Ma, H.-H., Chang, Y.-H., Tsai, H.-Y., Chou, Y.-C., Hsueh, Y.-P., Tsai, C.-Y., Huang, P.-Y., Chang, S.-Y., … Wong, C.-H. (2022). Vaccination with SARS-CoV-2 spike protein lacking glycan shields elicits enhanced protective responses in animal models. *Science Translational Medicine*, *14*(639), eabm0899. https://doi.org/10.1126/scitranslmed.abm0899

Hu, B., Zeng, L.-P., Yang, X.-L., Ge, X.-Y., Zhang, W., Li, B., Xie, J.-Z., Shen, X.-R., Zhang, Y.-Z., Wang, N., Luo, D.-S., Zheng, X.-S., Wang, M.-N., Daszak, P., Wang, L.-F., Cui, J., & Shi, Z.-L. (2017). Discovery of a rich gene pool of bat SARS-related coronaviruses provides new insights into the origin of SARS coronavirus. *PLoS Pathogens*, *13*(11), e1006698. https://doi.org/10.1371/journal.ppat.1006698

Hunt, A. C., Case, J. B., Park, Y.-J., Cao, L., Wu, K., Walls, A. C., Liu, Z., Bowen, J. E., Yeh, H.-W., Saini, S., Helms, L., Zhao, Y. T., Hsiang, T.-Y., Starr, T. N., Goreshnik, I., Kozodoy, L., Carter, L., Ravichandran, R., Green, L. B., … Baker, D. (2022). Multivalent designed proteins neutralize SARS-CoV-2 variants of concern and confer protection against infection in mice. *Science Translational Medicine*, *14*(646), eabn1252. https://doi.org/10.1126/scitranslmed.abn1252

Impagliazzo, A., Milder, F., Kuipers, H., Wagner, M. V., Zhu, X., Hoffman, R. M. B., van Meersbergen, R., Huizingh, J., Wanningen, P., Verspuij, J., de Man, M., Ding, Z., Apetri, A., Kükrer, B., Sneekes-Vriese, E., Tomkiewicz, D., Laursen, N. S., Lee, P. S., Zakrzewska, A., … Radošević, K. (2015). A stable trimeric influenza hemagglutinin stem as a broadly protective immunogen. *Science (New York, N.Y.)*, *349*(6254), 1301–1306. https://doi.org/10.1126/science.aac7263

Irvine, D. J., Aung, A., & Silva, M. (2020). Controlling timing and location in vaccines. *Advanced Drug Delivery Reviews*, *158*, 91–115. https://doi.org/10.1016/j.addr.2020.06.019

Jackson, L. A., Anderson, E. J., Rouphael, N. G., Roberts, P. C., Makhene, M., Coler, R. N., McCullough, M. P., Chappell, J. D., Denison, M. R., Stevens, L. J., Pruijssers, A. J., McDermott, A., Flach, B., Doria-Rose, N. A., Corbett, K. S., Morabito, K. M., O'Dell, S., Schmidt, S. D., Swanson, P. A., 2nd, … mRNA-1273 Study Group. (2020). An mRNA vaccine against SARS-CoV-2 - preliminary report. *The New England Journal of Medicine*, *383*(20), 1920–1931. https://doi.org/10.1056/NEJMoa2022483

Jamali, K., Käll, L., Zhang, R., Brown, A., Kimanius, D., & Scheres, S. H. W. (2024). Automated model building and protein identification in cryo-EM maps. *Nature*, *628*(8007), 450–457. https://doi.org/10.1038/s41586-024-07215-4

Janeway, C. A., Jr, Travers, P., Walport, M., & Shlomchik, M. J. (2001). *Antigen recognition by B-cell and T-cell receptors*. Garland Science. https://www.ncbi.nlm.nih.gov/books/NBK10770/

Jette, C. A., Cohen, A. A., Gnanapragasam, P. N. P., Muecksch, F., Lee, Y. E., Huey-Tubman, K. E., Schmidt, F., Hatziioannou, T., Bieniasz, P. D., Nussenzweig, M. C., West, A. P., Jr, Keeffe, J. R., Bjorkman, P. J., & Barnes, C. O. (2021). Broad cross-reactivity across sarbecoviruses exhibited by a subset of COVID-19 donor-derived neutralizing antibodies. *Cell Reports*, *36*(13), 109760. https://doi.org/10.1016/j.celrep.2021.109760

Johnson, N. V., Wall, S. C., Kramer, K. J., Holt, C. M., Periasamy, S., Richardson, S. I., Manamela, N. P., Suryadevara, N., Andreano, E., Paciello, I., Pierleoni, G., Piccini, G., Huang, Y., Ge, P., Allen, J. D., Uno, N., Shiakolas, A. R., Pilewski, K. A., Nargi, R. S., … Georgiev, I. S. (2024). Discovery and characterization of a pan-betacoronavirus S2-binding antibody. *Structure (London, England: 1993)*, *32*(11), 1893–1909.e11. https://doi.org/10.1016/j.str.2024.08.022

Jumper, J., Evans, R., Pritzel, A., Green, T., Figurnov, M., Ronneberger, O., Tunyasuvunakool, K., Bates, R., Žídek, A., Potapenko, A., Bridgland, A., Meyer, C., Kohl, S. A. A., Ballard, A. J., Cowie, A., Romera-Paredes, B., Nikolov, S., Jain, R., Adler, J., … Hassabis, D. (2021). Highly accurate protein structure prediction with AlphaFold. *Nature*, *596*(7873), 583–589. https://doi.org/10.1038/s41586-021-03819-2

Kaname, Y., Tani, H., Kataoka, C., Shiokawa, M., Taguwa, S., Abe, T., Moriishi, K., Kinoshita, T., & Matsuura, Y. (2010). Acquisition of complement resistance through incorporation of CD55/decay-accelerating factor into viral particles bearing baculovirus GP64. *Journal of Virology*, *84*(7), 3210–3219. https://doi.org/10.1128/JVI.02519-09

Kanekiyo, M., Wei, C.-J., Yassine, H. M., McTamney, P. M., Boyington, J. C., Whittle, J. R. R., Rao, S. S., Kong, W.-P., Wang, L., & Nabel, G. J. (2013). Self-assembling influenza nanoparticle vaccines elicit broadly neutralizing H1N1 antibodies. *Nature*, *499*(7456), 102–106. https://doi.org/10.1038/nature12202

Keech, C., Albert, G., Cho, I., Robertson, A., Reed, P., Neal, S., Plested, J. S., Zhu, M., Cloney-Clark, S., Zhou, H., Smith, G., Patel, N., Frieman, M. B., Haupt, R. E., Logue, J., McGrath, M., Weston, S., Piedra, P. A., Desai, C., … Glenn, G. M. (2020). Phase 1-2 trial of a SARS-CoV-2 recombinant spike protein nanoparticle vaccine. *The New England Journal of Medicine*, *383*(24), 2320–2332. https://doi.org/10.1056/NEJMoa2026920

Kim, J., Eygeris, Y., Gupta, M., & Sahay, G. (2021). Self-assembled mRNA vaccines. *Advanced Drug Delivery Reviews*, *170*, 83–112. https://doi.org/10.1016/j.addr.2020.12.014

Kirchdoerfer, R. N., Cottrell, C. A., Wang, N., Pallesen, J., Yassine, H. M., Turner, H. L., Corbett, K. S., Graham, B. S., McLellan, J. S., & Ward, A. B. (2016). Pre-fusion structure of a human coronavirus spike protein. *Nature*, *531*(7592), 118–121. https://doi.org/10.1038/nature17200

Kirchdoerfer, R. N., Wang, N., Pallesen, J., Wrapp, D., Turner, H. L., Cottrell, C. A., Corbett, K. S., Graham, B. S., McLellan, J. S., & Ward, A. B. (2018). Stabilized coronavirus spikes are resistant to conformational changes induced by receptor recognition or proteolysis. *Scientific Reports*, *8*(1), 15701. https://doi.org/10.1038/s41598-018-34171-7

Kodaka, M., Yang, Z., Nakagawa, K., Maruyama, J., Xu, X., Sarkar, A., Ichimura, A., Nasu, Y., Ozawa, T., Iwasa, H., Ishigami-Yuasa, M., Ito, S., Kagechika, H., & Hata, Y. (2015). A new cell-based assay to evaluate myogenesis in mouse myoblast

C2C12 cells. *Experimental Cell Research*, *336*(2), 171–181. https://doi.org/10.1016/j.yexcr.2015.06.015

Koday, M. T., Nelson, J., Chevalier, A., Koday, M., Kalinoski, H., Stewart, L., Carter, L., Nieusma, T., Lee, P. S., Ward, A. B., Wilson, I. A., Dagley, A., Smee, D. F., Baker, D., & Fuller, D. H. (2016). A computationally designed hemagglutinin stem-binding protein provides in vivo protection from influenza independent of a host immune response. *PLoS Pathogens*, *12*(2), e1005409. https://doi.org/10.1371/journal.ppat.1005409

Kraft, J. C., Pham, M. N., Shehata, L., Brinkkemper, M., Boyoglu-Barnum, S., Sprouse, K. R., Walls, A. C., Cheng, S., Murphy, M., Pettie, D., Ahlrichs, M., Sydeman, C., Johnson, M., Blackstone, A., Ellis, D., Ravichandran, R., Fiala, B., Wrenn, S., Miranda, M., … King, N. P. (2022). Antigen- and scaffold-specific antibody responses to protein nanoparticle immunogens. *Cell Reports. Medicine*, *3*(10), 100780. https://doi.org/10.1016/j.xcrm.2022.100780

Krammer, F., Pica, N., Hai, R., Margine, I., & Palese, P. (2013). Chimeric hemagglutinin influenza virus vaccine constructs elicit broadly protective stalk-specific antibodies. *Journal of Virology*, *87*(12), 6542–6550. https://doi.org/10.1128/JVI.00641-13

Krissinel, E., & Henrick, K. (2007). Inference of macromolecular assemblies from crystalline state. *Journal of Molecular Biology*, *372*(3), 774–797. https://doi.org/10.1016/j.jmb.2007.05.022

Ksiazek, T. G., Erdman, D., Goldsmith, C. S., Zaki, S. R., Peret, T., Emery, S., Tong, S., Urbani, C., Comer, J. A., Lim, W., Rollin, P. E., Dowell, S. F., Ling, A.-E., Humphrey, C. D., Shieh, W.-J., Guarner, J., Paddock, C. D., Rota, P., Fields, B., … SARS Working Group. (2003). A novel coronavirus associated with severe acute respiratory syndrome. *The New England Journal of Medicine*, *348*(20), 1953–1966. https://doi.org/10.1056/NEJMoa030781

Lam, T. T.-Y., Jia, N., Zhang, Y.-W., Shum, M. H.-H., Jiang, J.-F., Zhu, H.-C., Tong, Y.-G., Shi, Y.-X., Ni, X.-B., Liao, Y.-S., Li, W.-J., Jiang, B.-G., Wei, W., Yuan, T.-T., Zheng, K., Cui, X.-M., Li, J., Pei, G.-Q., Qiang, X., … Cao, W.-C. (2020). Identifying SARS-CoV-2-related coronaviruses in Malayan pangolins. *Nature*, *583*(7815), 282–285. https://doi.org/10.1038/s41586-020-2169-0

Langel, S. N., Johnson, S., Martinez, C. I., Tedjakusuma, S. N., Peinovich, N., Dora, E. G., Kuehl, P. J., Irshad, H., Barrett, E. G., Werts, A. D., & Tucker, S. N. (2022). Adenovirus type 5 SARS-CoV-2 vaccines delivered orally or intranasally reduced disease severity and transmission in a hamster model. *Science Translational Medicine*, *14*(658), eabn6868. https://doi.org/10.1126/scitranslmed.abn6868

Lan, J., Ge, J., Yu, J., Shan, S., Zhou, H., Fan, S., Zhang, Q., Shi, X., Wang, Q., Zhang, L., & Wang, X. (2020). Structure of the SARS-CoV-2 spike receptor-binding domain bound to the ACE2 receptor. *Nature*, *581*(7807), 215–220. https://doi.org/10.1038/s41586-020-2180-5

Lee, J., Stewart, C., Schäfer, A., Leaf, E. M., Park, Y.-J., Asarnow, D., Powers, J. M., Treichel, C., Sprouse, K. R., Corti, D., Baric, R., King, N. P., & Veesler, D. (2024). A broadly generalizable stabilization strategy for sarbecovirus fusion machinery vaccines. *Nature Communications*, *15*(1), 5496. https://doi.org/10.1038/s41467-024-49656-5

Lee, J., Zepeda, S. K., Park, Y.-J., Taylor, A. L., Quispe, J., Stewart, C., Leaf, E. M., Treichel, C., Corti, D., King, N. P., Starr, T. N., & Veesler, D. (2023). Broad receptor tropism and immunogenicity of a clade 3 sarbecovirus. *Cell Host & Microbe*, *31*(12), 1961–1973.e11. https://doi.org/10.1016/j.chom.2023.10.018

Leist, S. R., Dinnon, K. H., 3rd, Schäfer, A., Tse, L. V., Okuda, K., Hou, Y. J., West, A., Edwards, C. E., Sanders, W., Fritch, E. J., Gully, K. L., Scobey, T., Brown, A. J., Sheahan, T. P., Moorman, N. J., Boucher, R. C., Gralinski, L. E., Montgomery, S. A., & Baric, R. S. (2020). A mouse-adapted SARS-CoV-2 induces acute lung injury and mortality in standard laboratory mice. *Cell*, *183*(4), 1070–1085.e12. https://doi.org/10.1016/j.cell.2020.09.050

Letko, M., Marzi, A., & Munster, V. (2020). Functional assessment of cell entry and receptor usage for SARS-CoV-2 and other lineage B betacoronaviruses. *Nature Microbiology*, *5*(4), 562–569. https://doi.org/10.1038/s41564-020-0688-y

Levine-Tiefenbrun, M., Yelin, I., Alapi, H., Katz, R., Herzel, E., Kuint, J., Chodick, G., Gazit, S., Patalon, T., & Kishony, R. (2021). Viral loads of Delta-variant SARS-CoV-2 breakthrough infections after vaccination and booster with BNT162b2. *Nature Medicine*, *27*(12), 2108–2110. https://doi.org/10.1038/s41591-021-01575-4

Li, C.-J., & Chang, S.-C. (2023). SARS-CoV-2 spike S2-specific neutralizing antibodies. *Emerging Microbes & Infections*, *12*(2), 2220582. https://doi.org/10.1080/22221751.2023.2220582

Liebschner, D., Afonine, P. V., Baker, M. L., Bunkóczi, G., Chen, V. B., Croll, T. I., Hintze, B., Hung, L. W., Jain, S., McCoy, A. J., Moriarty, N. W., Oeffner, R. D., Poon, B. K., Prisant, M. G., Read, R. J., Richardson, J. S., Richardson, D. C., Sammito, M. D., Sobolev, O. V., … Adams, P. D. (2019). Macromolecular structure determination using X-rays, neutrons and electrons: recent developments in Phenix. *Acta Crystallographica. Section D, Structural Biology*, *75*(Pt 10), 861–877. https://doi.org/10.1107/S2059798319011471

Li, F., Li, W., Farzan, M., & Harrison, S. C. (2005). Structure of SARS coronavirus spike receptor-binding domain complexed with receptor. *Science (New York, N.Y.)*, *309*(5742), 1864–1868. https://doi.org/10.1126/science.1116480

Lindsay, K. E., Bhosle, S. M., Zurla, C., Beyersdorf, J., Rogers, K. A., Vanover, D., Xiao, P., Araínga, M., Shirreff, L. M., Pitard, B., Baumhof, P., Villinger, F., & Santangelo, P. J. (2019). Visualization of early events in mRNA vaccine delivery in non-human primates via PET-CT and near-infrared imaging. *Nature Biomedical Engineering*, *3*(5), 371–380. https://doi.org/10.1038/s41551-019-0378-3

Lin, L., Jiang, X., Zhang, Z., Huang, S., Zhang, Z., Fang, Z., Gu, Z., Gao, L., Shi, H., Mai, L., Liu, Y., Lin, X., Lai, R., Yan, Z., Li, X., & Shan, H. (2020). Gastrointestinal symptoms of 95 cases with SARS-CoV-2 infection. *Gut*, *69*(6), 997–1001. https://doi.org/10.1136/gutjnl-2020-321013

Lip, K.-M., Shen, S., Yang, X., Keng, C.-T., Zhang, A., Oh, H.-L. J., Li, Z.-H., Hwang, L.-A., Chou, C.-F., Fielding, B. C., Tan, T. H. P., Mayrhofer, J., Falkner, F. G., Fu, J., Lim, S. G., Hong, W., & Tan, Y.-J. (2006). Monoclonal antibodies targeting the HR2 domain and the region immediately upstream of the HR2 of the S protein neutralize in vitro infection of severe acute respiratory syndrome coronavirus. *Journal of Virology*, *80*(2), 941–950. https://doi.org/10.1128/JVI.80.2.941-950.2006

Liu, B., Zhao, P., Xu, P., Han, Y., Wang, Y., Chen, L., Wu, Z., & Yang, J. (2023). A comprehensive dataset of animal-associated sarbecoviruses. *Scientific Data*, *10*(1), 681. https://doi.org/10.1038/s41597-023-02558-5

Liu, Y., Liu, J., Johnson, B. A., Xia, H., Ku, Z., Schindewolf, C., Widen, S. G., An, Z., Weaver, S. C., Menachery, V. D., Xie, X., & Shi, P.-Y. (2022). Delta spike P681R mutation enhances SARS-CoV-2 fitness over Alpha variant. *Cell Reports*, *39*(7), 110829. https://doi.org/10.1016/j.celrep.2022.110829

Li, W., Moore, M. J., Vasilieva, N., Sui, J., Wong, S. K., Berne, M. A., Somasundaran, M., Sullivan, J. L., Luzuriaga, K., Greenough, T. C., Choe, H., & Farzan, M. (2003). Angiotensin-converting enzyme 2 is a functional receptor for the SARS coronavirus. *Nature*, *426*(6965), 450–454. https://doi.org/10.1038/nature02145

López-Sagaseta, J., Malito, E., Rappuoli, R., & Bottomley, M. J. (2016). Self-assembling protein nanoparticles in the design of vaccines. *Computational and Structural Biotechnology Journal*, *14*, 58–68. https://doi.org/10.1016/j.csbj.2015.11.001

Low, J. S., Jerak, J., Tortorici, M. A., McCallum, M., Pinto, D., Cassotta, A., Foglierini, M., Mele, F., Abdelnabi, R., Weynand, B., Noack, J., Montiel-Ruiz, M., Bianchi, S., Benigni, F., Sprugasci, N., Joshi, A., Bowen, J. E., Stewart, C., Rexhepaj, M., … Sallusto, F. (2022). ACE2-binding exposes the SARS-CoV-2 fusion peptide to broadly neutralizing coronavirus antibodies. *Science*, *377*(6607), 735–742. https://doi.org/10.1126/science.abq2679

Mackin, S. R., Desai, P., Whitener, B. M., Karl, C. E., Liu, M., Baric, R. S., Edwards, D. K., Chicz, T. M., McNamara, R. P., Alter, G., & Diamond, M. S. (2023). Fc-γR-dependent antibody effector functions are required for vaccine-mediated protection against antigen-shifted variants of SARS-CoV-2. *Nature Microbiology*, *8*(4), 569–580. https://doi.org/10.1038/s41564-023-01359-1

Maeda, D. L. N. F., Tian, D., Yu, H., Dar, N., Rajasekaran, V., Meng, S., Mahsoub, H. M., Sooryanarain, H., Wang, B., Heffron, C. L., Hassebroek, A., LeRoith, T., Meng, X.-J., & Zeichner, S. L. (2021). Killed whole-genome reduced-bacteria surface-expressed coronavirus fusion peptide vaccines protect against disease in a porcine model. *Proceedings of the National Academy of Sciences of the United States of America*, *118*(18). https://doi.org/10.1073/pnas.2025622118

Magro, M., Mas, V., Chappell, K., Vázquez, M., Cano, O., Luque, D., Terrón, M. C., Melero, J. A., & Palomo, C. (2012). Neutralizing antibodies against the preactive form of respiratory syncytial virus fusion protein offer unique possibilities for clinical intervention. *Proceedings of the National Academy of Sciences of the United States of America*, *109*(8), 3089–3094. https://doi.org/10.1073/pnas.1115941109

Mao, L., Jin, H., Wang, M., Hu, Y., Chen, S., He, Q., Chang, J., Hong, C., Zhou, Y., Wang, D., Miao, X., Li, Y., & Hu, B. (2020). Neurologic manifestations of hospitalized patients with Coronavirus disease 2019 in Wuhan, China. *JAMA Neurology*, *77*(6), 683–690. https://doi.org/10.1001/jamaneurol.2020.1127

Mao, T., Israelow, B., Peña-Hernández, M. A., Suberi, A., Zhou, L., Luyten, S., Reschke, M., Dong, H., Homer, R. J., Saltzman, W. M., & Iwasaki, A. (2022). Unadjuvanted intranasal spike vaccine elicits protective mucosal immunity against sarbecoviruses. *Science (New York, N.Y.)*, *378*(6622), eabo2523. https://doi.org/10.1126/science.abo2523

Marcandalli, J., Fiala, B., Ols, S., Perotti, M., de van der Schueren, W., Snijder, J., Hodge, E., Benhaim, M., Ravichandran, R., Carter, L., Sheffler, W., Brunner, L., Lawrenz, M., Dubois, P., Lanzavecchia, A., Sallusto, F., Lee, K. K., Veesler, D., Correnti, C. E., … King, N. P. (2019). Induction of potent neutralizing antibody responses by a designed protein nanoparticle vaccine for respiratory syncytial virus. *Cell*, *176*(6), 1420–1431.e17. https://doi.org/10.1016/j.cell.2019.01.046

Martinez, D. R., Schäfer, A., Gobeil, S., Li, D., De la Cruz, G., Parks, R., Lu, X., Barr, M., Stalls, V., Janowska, K., Beaudoin, E., Manne, K., Mansouri, K., Edwards, R. J., Cronin, K., Yount, B., Anasti, K., Montgomery, S. A., Tang, J., … Baric, R. S. (2022). A broadly cross-reactive antibody neutralizes and protects against sarbecovirus challenge in mice. *Science Translational Medicine*, *14*(629), eabj7125. https://doi.org/10.1126/scitranslmed.abj7125

Martinez, D. R., Schäfer, A., Leist, S. R., De la Cruz, G., West, A., Atochina-Vasserman, E. N., Lindesmith, L. C., Pardi, N., Parks, R., Barr, M., Li, D., Yount, B., Saunders, K. O., Weissman, D., Haynes, B. F., Montgomery, S. A., & Baric, R. S. (2021). Chimeric spike mRNA vaccines protect against Sarbecovirus challenge in mice. *Science (New York, N.Y.)*, *373*(6558), 991–998. https://doi.org/10.1126/science.abi4506

Martinon, F., Krishnan, S., Lenzen, G., Magné, R., Gomard, E., Guillet, J. G., Lévy, J. P., & Meulien, P. (1993). Induction of virus-specific cytotoxic T lymphocytes in vivo by liposome-entrapped mRNA. *European Journal of Immunology*, *23*(7), 1719–1722. https://doi.org/10.1002/eji.1830230749

Mastronarde, D. N. (2005). Automated electron microscope tomography using robust prediction of specimen movements. *Journal of Structural Biology*, *152*(1), 36–51.

https://doi.org/10.1016/j.jsb.2005.07.007

Ma, X., Zou, F., Yu, F., Li, R., Yuan, Y., Zhang, Y., Zhang, X., Deng, J., Chen, T., Song, Z., Qiao, Y., Zhan, Y., Liu, J., Zhang, J., Zhang, X., Peng, Z., Li, Y., Lin, Y., Liang, L., … Zhang, H. (2020). Nanoparticle vaccines based on the receptor binding domain (RBD) and heptad repeat (HR) of SARS-CoV-2 elicit robust protective immune responses. *Immunity*, *53*(6), 1315–1330.e9. https://doi.org/10.1016/j.immuni.2020.11.015

McCallum, M., Bassi, J., De Marco, A., Chen, A., Walls, A. C., Di Iulio, J., Tortorici, M. A., Navarro, M.-J., Silacci-Fregni, C., Saliba, C., Sprouse, K. R., Agostini, M., Pinto, D., Culap, K., Bianchi, S., Jaconi, S., Cameroni, E., Bowen, J. E., Tilles, S. W., … Veesler, D. (2021). SARS-CoV-2 immune evasion by the B.1.427/B.1.429 variant of concern. *Science*, *373*(6555), 648–654. https://doi.org/10.1126/science.abi7994

McCallum, M., Czudnochowski, N., Rosen, L. E., Zepeda, S. K., Bowen, J. E., Walls, A. C., Hauser, K., Joshi, A., Stewart, C., Dillen, J. R., Powell, A. E., Croll, T. I., Nix, J., Virgin, H. W., Corti, D., Snell, G., & Veesler, D. (2022). Structural basis of SARS-CoV-2 Omicron immune evasion and receptor engagement. *Science (New York, N.Y.)*, *375*(6583), 864–868. https://doi.org/10.1126/science.abn8652

McCallum, M., De Marco, A., Lempp, F. A., Tortorici, M. A., Pinto, D., Walls, A. C., Beltramello, M., Chen, A., Liu, Z., Zatta, F., Zepeda, S., di Iulio, J., Bowen, J. E., Montiel-Ruiz, M., Zhou, J., Rosen, L. E., Bianchi, S., Guarino, B., Fregni, C. S., … Veesler, D. (2021). N-terminal domain antigenic mapping reveals a site of vulnerability for SARS-CoV-2. *Cell*, *184*(9), 2332–2347.e16. https://doi.org/10.1016/j.cell.2021.03.028

McCallum, M., Walls, A. C., Sprouse, K. R., Bowen, J. E., Rosen, L. E., Dang, H. V., De Marco, A., Franko, N., Tilles, S. W., Logue, J., Miranda, M. C., Ahlrichs, M., Carter, L., Snell, G., Pizzuto, M. S., Chu, H. Y., Van Voorhis, W. C., Corti, D., & Veesler, D. (2021). Molecular basis of immune evasion by the Delta and Kappa SARS-CoV-2 variants. *Science (New York, N.Y.)*, *374*(6575), 1621–1626. https://doi.org/10.1126/science.abl8506

McLellan, J. S., Chen, M., Joyce, M. G., Sastry, M., Stewart-Jones, G. B. E., Yang, Y., Zhang, B., Chen, L., Srivatsan, S., Zheng, A., Zhou, T., Graepel, K. W., Kumar, A., Moin, S., Boyington, J. C., Chuang, G.-Y., Soto, C., Baxa, U., Bakker, A. Q., … Kwong, P. D. (2013). Structure-based design of a fusion glycoprotein vaccine for respiratory syncytial virus. *Science (New York, N.Y.)*, *342*(6158), 592–598. https://doi.org/10.1126/science.1243283

McLellan, J. S., Chen, M., Leung, S., Graepel, K. W., Du, X., Yang, Y., Zhou, T., Baxa, U., Yasuda, E., Beaumont, T., Kumar, A., Modjarrad, K., Zheng, Z., Zhao, M., Xia, N., Kwong, P. D., & Graham, B. S. (2013). Structure of RSV fusion glycoprotein trimer bound to a prefusion-specific neutralizing antibody. *Science (New York, N.Y.)*, *340*(6136), 1113–1117. https://doi.org/10.1126/science.1234914

Menachery, V. D., Yount, B. L., Jr, Debbink, K., Agnihothram, S., Gralinski, L. E., Plante, J. A., Graham, R. L., Scobey, T., Ge, X.-Y., Donaldson, E. F., Randell, S. H., Lanzavecchia, A., Marasco, W. A., Shi, Z.-L., & Baric, R. S. (2015). A SARS-like cluster of circulating bat coronaviruses shows potential for human emergence. *Nature Medicine*, *21*(12), 1508–1513. https://doi.org/10.1038/nm.3985

Menachery, V. D., Yount, B. L., Jr, Sims, A. C., Debbink, K., Agnihothram, S. S., Gralinski, L. E., Graham, R. L., Scobey, T., Plante, J. A., Royal, S. R., Swanstrom, J., Sheahan, T. P., Pickles, R. J., Corti, D., Randell, S. H., Lanzavecchia, A., Marasco, W. A., & Baric, R. S. (2016). SARS-like WIV1-CoV poised for human emergence. *Proceedings of the National Academy of Sciences of the United States of America*, *113*(11), 3048–3053. https://doi.org/10.1073/pnas.1517719113

Meng, B., Abdullahi, A., Ferreira, I. A. T. M., Goonawardane, N., Saito, A., Kimura, I., Yamasoba, D., Gerber, P. P., Fatihi, S., Rathore, S., Zepeda, S. K., Papa, G., Kemp, S. A., Ikeda, T., Toyoda, M., Tan, T. S., Kuramochi, J., Mitsunaga, S., Ueno, T., … Gupta, R. K. (2022). Altered TMPRSS2 usage by SARS-CoV-2 Omicron impacts infectivity and fusogenicity. *Nature*, *603*(7902), 706–714. https://doi.org/10.1038/s41586-022-04474-x

Millet, J. K., & Whittaker, G. R. (2015). Host cell proteases: Critical determinants of coronavirus tropism and pathogenesis. *Virus Research*, *202*, 120–134. https://doi.org/10.1016/j.virusres.2014.11.021

Millet, J. K., & Whittaker, G. R. (2016). Murine leukemia virus (MLV)-based Coronavirus spike-pseudotyped particle production and infection. *Bio-Protocol*, *6*(23). https://doi.org/10.21769/BioProtoc.2035

Mirdita, M., Schütze, K., Moriwaki, Y., Heo, L., Ovchinnikov, S., & Steinegger, M. (2022). ColabFold: making protein folding accessible to all. *Nature Methods*, *19*(6), 679–682. https://doi.org/10.1038/s41592-022-01488-1

Miroshnikov, K. A., Marusich, E. I., Cerritelli, M. E., Cheng, N., Hyde, C. C., Steven, A. C., & Mesyanzhinov, V. V. (1998). Engineering trimeric fibrous proteins based on bacteriophage T4 adhesins. *Protein Engineering*, *11*(4), 329–332. https://doi.org/10.1093/protein/11.4.329

Mlcochova, P., Kemp, S. A., Dhar, M. S., Papa, G., Meng, B., Ferreira, I. A. T. M., Datir, R., Collier, D. A., Albecka, A., Singh, S., Pandey, R., Brown, J., Zhou, J., Goonawardane, N., Mishra, S., Whittaker, C., Mellan, T., Marwal, R., Datta, M., … Gupta, R. K. (2021). SARS-CoV-2 B.1.617.2 Delta variant replication and immune evasion. *Nature*, *599*(7883), 114–119. https://doi.org/10.1038/s41586-021-03944-y

Ng, K. W., Faulkner, N., Finsterbusch, K., Wu, M., Harvey, R., Hussain, S., Greco, M., Liu, Y., Kjaer, S., Swanton, C., Gandhi, S., Beale, R., Gamblin, S. J., Cherepanov, P., McCauley, J., Daniels, R., Howell, M., Arase, H., Wack, A., … Kassiotis, G. (2022). SARS-CoV-2 S2-targeted vaccination elicits broadly neutralizing antibodies. *Science Translational Medicine*, *14*(655), eabn3715.

https://doi.org/10.1126/scitranslmed.abn3715

Niu, S., Wang, J., Bai, B., Wu, L., Zheng, A., Chen, Q., Du, P., Han, P., Zhang, Y., Jia, Y., Qiao, C., Qi, J., Tian, W.-X., Wang, H.-W., Wang, Q., & Gao, G. F. (2022). Molecular basis of cross-species ACE2 interactions with SARS-CoV-2-like viruses of pangolin origin. *The EMBO Journal*, *41*(1), e109962. https://doi.org/10.15252/embj.2021109962

Oh, J. E., Song, E., Moriyama, M., Wong, P., Zhang, S., Jiang, R., Strohmeier, S., Kleinstein, S. H., Krammer, F., & Iwasaki, A. (2021). Intranasal priming induces local lung-resident B cell populations that secrete protective mucosal antiviral IgA. *Science Immunology*, *6*(66), eabj5129. https://doi.org/10.1126/sciimmunol.abj5129

Olia, A. S., Cheng, C., Zhou, T., Biju, A., Harris, D. R., Changela, A., Duan, H., Ivleva, V. B., Kong, W.-P., Ou, L., Rawi, R., Tsybovsky, Y., Van Wazer, D. J., Corrigan, A. R., Gonelli, C. A., Lee, M., McKee, K., Narpala, S., O’Dell, S., … Kwong, P. D. (2023). Soluble prefusion-closed HIV-envelope trimers with glycan-covered bases. *iScience*, *26*(8), 107403. https://doi.org/10.1016/j.isci.2023.107403

Olmedillas, E., Mann, C. J., Peng, W., Wang, Y.-T., Avalos, R. D., Bedinger, D., Valentine, K., Shafee, N., Schendel, S. L., Yuan, M., Lang, G., Rouet, R., Christ, D., Jiang, W., Wilson, I. A., Germann, T., Shresta, S., Snijder, J., & Saphire, E. O. (2021). Structure-based design of a highly stable, covalently-linked SARS-CoV-2 spike trimer with improved structural properties and immunogenicity. In *bioRxiv*. bioRxiv. https://doi.org/10.1101/2021.05.06.441046

Ou, X., Liu, Y., Lei, X., Li, P., Mi, D., Ren, L., Guo, L., Guo, R., Chen, T., Hu, J., Xiang, Z., Mu, Z., Chen, X., Chen, J., Hu, K., Jin, Q., Wang, J., & Qian, Z. (2020). Characterization of spike glycoprotein of SARS-CoV-2 on virus entry and its immune cross-reactivity with SARS-CoV. *Nature Communications*, *11*(1), 1620. https://doi.org/10.1038/s41467-020-15562-9

Pacesa, M., Nickel, L., Schellhaas, C., Schmidt, J., Pyatova, E., Kissling, L., Barendse, P., Choudhury, J., Kapoor, S., Alcaraz-Serna, A., Cho, Y., Ghamary, K. H., Vinué, L., Yachnin, B. J., Wollacott, A. M., Buckley, S., Westphal, A. H., Lindhoud, S., Georgeon, S., … Correia, B. E. (2025). One-shot design of functional protein binders with BindCraft. *Nature*, *646*(8084), 483–492. https://doi.org/10.1038/s41586-025-09429-6

Pallesen, J., Wang, N., Corbett, K. S., Wrapp, D., Kirchdoerfer, R. N., Turner, H. L., Cottrell, C. A., Becker, M. M., Wang, L., Shi, W., Kong, W.-P., Andres, E. L., Kettenbach, A. N., Denison, M. R., Chappell, J. D., Graham, B. S., Ward, A. B., & McLellan, J. S. (2017). Immunogenicity and structures of a rationally designed prefusion MERS-CoV spike antigen. *Proceedings of the National Academy of Sciences of the United States of America*, *114*(35), E7348–E7357. https://doi.org/10.1073/pnas.1707304114

Pancera, M., Zhou, T., Druz, A., Georgiev, I. S., Soto, C., Gorman, J., Huang, J., Acharya, P., Chuang, G.-Y., Ofek, G., Stewart-Jones, G. B. E., Stuckey, J., Bailer, R. T., Joyce, M. G., Louder, M. K., Tumba, N., Yang, Y., Zhang, B., Cohen, M. S., … Kwong, P. D. (2014). Structure and immune recognition of trimeric pre-fusion HIV-1 Env. *Nature*, *514*(7523), 455–461. https://doi.org/10.1038/nature13808

Pang, W., Lu, Y., Zhao, Y.-B., Shen, F., Fan, C.-F., Wang, Q., He, W.-Q., He, X.-Y., Li, Z.-K., Chen, T.-T., Yang, C.-X., Li, Y.-Z., Xiao, S.-X., Zhao, Z.-J., Huang, X.-S., Luo, R.-H., Yang, L.-M., Zhang, M., Dong, X.-Q., … Zheng, Y.-T. (2022). A variant-proof SARS-CoV-2 vaccine targeting HR1 domain in S2 subunit of spike protein. *Cell Research*, *32*(12), 1068–1085. https://doi.org/10.1038/s41422-022-00746-3

Pardi, N., Hogan, M. J., Porter, F. W., & Weissman, D. (2018). mRNA vaccines — a new era in vaccinology. *Nature Reviews. Drug Discovery*, *17*(4), 261–279. https://doi.org/10.1038/nrd.2017.243

Park, Y.-J., De Marco, A., Starr, T. N., Liu, Z., Pinto, D., Walls, A. C., Zatta, F., Zepeda, S. K., Bowen, J. E., Sprouse, K. R., Joshi, A., Giurdanella, M., Guarino, B., Noack, J., Abdelnabi, R., Foo, S.-Y. C., Rosen, L. E., Lempp, F. A., Benigni, F., … Veesler, D. (2022). Antibody-mediated broad sarbecovirus neutralization through ACE2 molecular mimicry. *Science (New York, N.Y.)*, *375*(6579), 449–454. https://doi.org/10.1126/science.abm8143

Park, Y.-J., Pinto, D., Walls, A. C., Liu, Z., De Marco, A., Benigni, F., Zatta, F., Silacci-Fregni, C., Bassi, J., Sprouse, K. R., Addetia, A., Bowen, J. E., Stewart, C., Giurdanella, M., Saliba, C., Guarino, B., Schmid, M. A., Franko, N. M., Logue, J. K., … Veesler, D. (2022). Imprinted antibody responses against SARS-CoV-2 Omicron sublineages. *Science (New York, N.Y.)*, *378*(6620), 619–627. https://doi.org/10.1126/science.adc9127

Pennington, H. (2004). DAVID TYRRELL and MICHAEL FIELDER, cold wars: The fight against the common cold. Oxford: Oxford university press, 2002. Pp. Xiv+253. ISBN 0-19-263285-X. £17.99 (hardback). *British Journal for the History of Science*, *37*(3), 362–363. https://doi.org/10.1017/s0007087404386127

Pettersen, E. F., Goddard, T. D., Huang, C. C., Couch, G. S., Greenblatt, D. M., Meng, E. C., & Ferrin, T. E. (2004). UCSF Chimera--a visualization system for exploratory research and analysis. *Journal of Computational Chemistry*, *25*(13), 1605–1612. https://doi.org/10.1002/jcc.20084

Piccoli, L., Park, Y.-J., Tortorici, M. A., Czudnochowski, N., Walls, A. C., Beltramello, M., Silacci-Fregni, C., Pinto, D., Rosen, L. E., Bowen, J. E., Acton, O. J., Jaconi, S., Guarino, B., Minola, A., Zatta, F., Sprugasci, N., Bassi, J., Peter, A., De Marco, A., … Veesler, D. (2020). Mapping neutralizing and immunodominant sites on the SARS-CoV-2 spike receptor-binding domain by structure-guided high-resolution serology. *Cell*, *183*(4), 1024–1042.e21. https://doi.org/10.1016/j.cell.2020.09.037

Pinto, D., Park, Y.-J., Beltramello, M., Walls, A. C., Tortorici, M. A., Bianchi, S., Jaconi, S., Culap, K., Zatta, F., De Marco, A., Peter, A., Guarino, B., Spreafico, R., Cameroni, E., Case, J. B., Chen, R. E., Havenar-Daughton, C., Snell, G., Telenti, A., … Corti, D. (2020). Cross-neutralization of SARS-CoV-2 by a human monoclonal SARS-CoV antibody. *Nature*, *583*(7815), 290–295. https://doi.org/10.1038/s41586-020-2349-y

Pinto, D., Sauer, M. M., Czudnochowski, N., Low, J. S., Tortorici, M. A., Housley, M. P., Noack, J., Walls, A. C., Bowen, J. E., Guarino, B., Rosen, L. E., di Iulio, J., Jerak, J., Kaiser, H., Islam, S., Jaconi, S., Sprugasci, N., Culap, K., Abdelnabi, R., … Veesler, D. (2021). Broad betacoronavirus neutralization by a stem helix–specific human antibody. *Science*, *373*(6559), 1109–1116. https://doi.org/10.1126/science.abj3321

Pollard, A. J., & Bijker, E. M. (2021). A guide to vaccinology: from basic principles to new developments. *Nature Reviews. Immunology*, *21*(2), 83–100. https://doi.org/10.1038/s41577-020-00479-7

Powers, J. M., Leist, S. R., Mallory, M. L., Yount, B. L., Gully, K. L., Zweigart, M. R., Bailey, A. B., Sheahan, T. P., Harkema, J. R., & Baric, R. S. (2024). Divergent pathogenetic outcomes in BALB/c mice following Omicron subvariant infection. *Virus Research*, *341*(199319), 199319. https://doi.org/10.1016/j.virusres.2024.199319

Punjani, A., Rubinstein, J. L., Fleet, D. J., & Brubaker, M. A. (2017). cryoSPARC: algorithms for rapid unsupervised cryo-EM structure determination. *Nature Methods*, *14*(3), 290–296. https://doi.org/10.1038/nmeth.4169

Punjani, A., Zhang, H., & Fleet, D. J. (2020). Non-uniform refinement: adaptive regularization improves single-particle cryo-EM reconstruction. *Nature Methods*, *17*(12), 1214–1221. https://doi.org/10.1038/s41592-020-00990-8

Ragotte, R. J., Tortorici, M. A., Catanzaro, N. J., Addetia, A., Coventry, B., Froggatt, H. M., Lee, J., Stewart, C., Brown, J. T., Goreshnik, I., Sims, J. N., Milles, L. F., Wicky, B. I. M., Glögl, M., Gerben, S., Kang, A., Bera, A. K., Sharkey, W., Schäfer, A., … Veesler, D. (2025). Designed miniproteins potently inhibit and protect against MERS-CoV. *Cell Reports*, *44*(6), 115760. https://doi.org/10.1016/j.celrep.2025.115760

Rich, R. R., Fleisher, T., Shearer, W. T., Schroeder, H. W., Frew, A. J., & Weyand, C. M. (n.d.). *27 - Immune responses viruses*.

Robbiani, D. F., Gaebler, C., Muecksch, F., Lorenzi, J. C. C., Wang, Z., Cho, A., Agudelo, M., Barnes, C. O., Gazumyan, A., Finkin, S., Hägglöf, T., Oliveira, T. Y., Viant, C., Hurley, A., Hoffmann, H.-H., Millard, K. G., Kost, R. G., Cipolla, M., Gordon, K., … Nussenzweig, M. C. (2020). Convergent antibody responses to SARS-CoV-2 in convalescent individuals. *Nature*, *584*(7821), 437–442. https://doi.org/10.1038/s41586-020-2456-9

Robert, X., & Gouet, P. (2014). Deciphering key features in protein structures with the new ENDscript server. *Nucleic Acids Research*, *42*(Web Server issue), W320–W324. https://doi.org/10.1093/nar/gku316

Roelle, S. M., Shukla, N., Pham, A. T., Bruchez, A. M., & Matreyek, K. A. (2022). Expanded ACE2 dependencies of diverse SARS-like coronavirus receptor binding domains. *PLoS Biology*, *20*(7), e3001738. https://doi.org/10.1371/journal.pbio.3001738

Rosen, L. E., Tortorici, M. A., De Marco, A., Pinto, D., Foreman, W. B., Taylor, A. L., Park, Y.-J., Bohan, D., Rietz, T., Errico, J. M., Hauser, K., Dang, H. V., Chartron, J. W., Giurdanella, M., Cusumano, G., Saliba, C., Zatta, F., Sprouse, K. R., Addetia, A., … Starr, T. N. (2024). A potent pan-sarbecovirus neutralizing antibody resilient to epitope diversification. *Cell*, *187*(25), 7196–7213.e26. https://doi.org/10.1016/j.cell.2024.09.026

Rosenthal, P. B., & Henderson, R. (2003). Optimal determination of particle orientation, absolute hand, and contrast loss in single-particle electron cryomicroscopy. *Journal of Molecular Biology*, *333*(4), 721–745. https://doi.org/10.1016/j.jmb.2003.07.013

Russo, C. J., & Passmore, L. A. (2014). Electron microscopy: Ultrastable gold substrates for electron cryomicroscopy. *Science (New York, N.Y.)*, *346*(6215), 1377–1380. https://doi.org/10.1126/science.1259530

Saito, A., Irie, T., Suzuki, R., Maemura, T., Nasser, H., Uriu, K., Kosugi, Y., Shirakawa, K., Sadamasu, K., Kimura, I., Ito, J., Wu, J., Iwatsuki-Horimoto, K., Ito, M., Yamayoshi, S., Loeber, S., Tsuda, M., Wang, L., Ozono, S., … Sato, K. (2022). Enhanced fusogenicity and pathogenicity of SARS-CoV-2 Delta P681R mutation. *Nature*, *602*(7896), 300–306. https://doi.org/10.1038/s41586-021-04266-9

SARS-CoV-2 evolution, post-Omicron. (2023, August 8). Virological. https://virological.org/t/sars-cov-2-evolution-post-omicron/911

Sauer, M. M., Tortorici, M. A., Park, Y.-J., Walls, A. C., Homad, L., Acton, O. J., Bowen, J. E., Wang, C., Xiong, X., de van der Schueren, W., Quispe, J., Hoffstrom, B. G., Bosch, B.-J., McGuire, A. T., & Veesler, D. (2021). Structural basis for broad coronavirus neutralization. *Nature Structural & Molecular Biology*, *28*(6), 478–486. https://doi.org/10.1038/s41594-021-00596-4

Schäfer, A., Muecksch, F., Lorenzi, J. C. C., Leist, S. R., Cipolla, M., Bournazos, S., Schmidt, F., Maison, R. M., Gazumyan, A., Martinez, D. R., Baric, R. S., Robbiani, D. F., Hatziioannou, T., Ravetch, J. V., Bieniasz, P. D., Bowen, R. A., Nussenzweig, M. C., & Sheahan, T. P. (2021). Antibody potency, effector function, and combinations in protection and therapy for SARS-CoV-2 infection in vivo. *The Journal of Experimental Medicine*, *218*(3). https://doi.org/10.1084/jem.20201993

Scheaffer, S. M., Lee, D., Whitener, B., Ying, B., Wu, K., Liang, C.-Y., Jani, H., Martin, P., Amato, N. J., Avena, L. E., Berrueta, D. M., Schmidt, S. D., O'Dell, S., Nasir, A., Chuang, G.-Y., Stewart-Jones, G., Koup, R. A., Doria-Rose, N. A., Carfi, A., … Diamond, M. S. (2023). Bivalent SARS-CoV-2 mRNA vaccines increase breadth of neutralization and protect against the BA.5 Omicron variant in mice. *Nature*

Medicine, *29*(1), 247–257. https://doi.org/10.1038/s41591-022-02092-8

Scheres, S. H. W. (2012a). A Bayesian view on cryo-EM structure determination. *Journal of Molecular Biology*, *415*(2), 406–418. https://doi.org/10.1016/j.jmb.2011.11.010

Scheres, S. H. W. (2012b). RELION: implementation of a Bayesian approach to cryo-EM structure determination. *Journal of Structural Biology*, *180*(3), 519–530. https://doi.org/10.1016/j.jsb.2012.09.006

Schorcht, A., van den Kerkhof, T. L. G. M., Cottrell, C. A., Allen, J. D., Torres, J. L., Behrens, A.-J., Schermer, E. E., Burger, J. A., de Taeye, S. W., Torrents de la Peña, A., Bontjer, I., Gumbs, S., Ozorowski, G., LaBranche, C. C., de Val, N., Yasmeen, A., Klasse, P. J., Montefiori, D. C., Moore, J. P., … Sanders, R. W. (2020). Neutralizing antibody responses induced by HIV-1 envelope glycoprotein SOSIP trimers derived from elite neutralizers. *Journal of Virology*, *94*(24). https://doi.org/10.1128/JVI.01214-20

Seifert, S. N., Bai, S., Fawcett, S., Norton, E. B., Zwezdaryk, K. J., Robinson, J., Gunn, B., & Letko, M. (2022). An ACE2-dependent Sarbecovirus in Russian bats is resistant to SARS-CoV-2 vaccines. *PLoS Pathogens*, *18*(9), e1010828. https://doi.org/10.1371/journal.ppat.1010828

Shi, W., Cai, Y., Zhu, H., Peng, H., Voyer, J., Rits-Volloch, S., Cao, H., Mayer, M. L., Song, K., Xu, C., Lu, J., Zhang, J., & Chen, B. (2023). Cryo-EM structure of SARS-CoV-2 postfusion spike in membrane. *Nature*, *619*(7969), 403–409. https://doi.org/10.1038/s41586-023-06273-4

Silva, R. P., Huang, Y., Nguyen, A. W., Hsieh, C.-L., Olaluwoye, O. S., Kaoud, T. S., Wilen, R. E., Qerqez, A. N., Park, J.-G., Khalil, A. M., Azouz, L. R., Le, K. C., Bohanon, A. L., DiVenere, A. M., Liu, Y., Lee, A. G., Amengor, D. A., Shoemaker, S. R., Costello, S. M., … Maynard, J. A. (2023). Identification of a conserved S2 epitope present on spike proteins from all highly pathogenic coronaviruses. *eLife*, *12*. https://doi.org/10.7554/eLife.83710

Skehel, J. J., Bayley, P. M., Brown, E. B., Martin, S. R., Waterfield, M. D., White, J. M., Wilson, I. A., & Wiley, D. C. (1982). Changes in the conformation of influenza virus hemagglutinin at the pH optimum of virus-mediated membrane fusion. *Proceedings of the National Academy of Sciences of the United States of America*, *79*(4), 968–972. https://doi.org/10.1073/pnas.79.4.968

Skehel, J. J., & Waterfield, M. D. (1975). Studies on the primary structure of the influenza virus hemagglutinin. *Proceedings of the National Academy of Sciences of the United States of America*, *72*(1), 93–97. https://doi.org/10.1073/pnas.72.1.93

Sliepen, K., Han, B. W., Bontjer, I., Mooij, P., Garces, F., Behrens, A.-J., Rantalainen, K., Kumar, S., Sarkar, A., Brouwer, P. J. M., Hua, Y., Tolazzi, M., Schermer, E., Torres, J. L., Ozorowski, G., van der Woude, P., de la Peña, A. T., van Breemen, M. J., Camacho-Sánchez, J. M., … Sanders, R. W. (2019). Structure and immunogenicity of a stabilized HIV-1 envelope trimer based on a group-M consensus sequence. *Nature Communications*, *10*(1), 2355. https://doi.org/10.1038/s41467-019-10262-5

Snijder, J., Borst, A. J., Dosey, A., Walls, A. C., Burrell, A., Reddy, V. S., Kollman, J. M., & Veesler, D. (2017). Vitrification after multiple rounds of sample application and blotting improves particle density on cryo-electron microscopy grids. *Journal of Structural Biology*, *198*(1), 38–42. https://doi.org/10.1016/j.jsb.2017.02.008

Song, J. Y., Choi, W. S., Heo, J. Y., Lee, J. S., Jung, D. S., Kim, S.-W., Park, K.-H., Eom, J. S., Jeong, S. J., Lee, J., Kwon, K. T., Choi, H. J., Sohn, J. W., Kim, Y. K., Noh, J. Y., Kim, W. J., Roman, F., Ceregido, M. A., Solmi, F., … Cheong, H. J. (2022). Safety and immunogenicity of a SARS-CoV-2 recombinant protein nanoparticle vaccine (GBP510) adjuvanted with AS03: A randomised, placebo-controlled, observer-blinded phase 1/2 trial. *EClinicalMedicine*, *51*(101569), 101569. https://doi.org/10.1016/j.eclinm.2022.101569

Song, R., Zeng, G., Yu, J., Meng, X., Chen, X., Li, J., Xie, X., Lian, X., Zhang, Z., Cao, Y., Yin, W., & Jin, R. (2023). Post-exposure prophylaxis with SA58 (anti-SARS-COV-2 monoclonal antibody) nasal spray for the prevention of symptomatic COVID-19 in healthy adult workers: a randomized, single-blind, placebo-controlled clinical study. *Emerging Microbes & Infections*, *12*(1), 2212806. https://doi.org/10.1080/22221751.2023.2212806

Stalls, V., Lindenberger, J., Gobeil, S. M.-C., Henderson, R., Parks, R., Barr, M., Deyton, M., Martin, M., Janowska, K., Huang, X., May, A., Speakman, M., Beaudoin, E., Kraft, B., Lu, X., Edwards, R. J., Eaton, A., Montefiori, D. C., Williams, W. B., … Acharya, P. (2022). Cryo-EM structures of SARS-CoV-2 Omicron BA.2 spike. *Cell Reports*, *39*(13), 111009. https://doi.org/10.1016/j.celrep.2022.111009

Stamatatos, L., Czartoski, J., Wan, Y.-H., Homad, L. J., Rubin, V., Glantz, H., Neradilek, M., Seydoux, E., Jennewein, M. F., MacCamy, A. J., Feng, J., Mize, G., De Rosa, S. C., Finzi, A., Lemos, M. P., Cohen, K. W., Moodie, Z., McElrath, M. J., & McGuire, A. T. (2021). mRNA vaccination boosts cross-variant neutralizing antibodies elicited by SARS-CoV-2 infection. *Science (New York, N.Y.)*, *372*(6549), 1413–1418. https://doi.org/10.1126/science.abg9175

Starr, T. N., Czudnochowski, N., Liu, Z., Zatta, F., Park, Y.-J., Addetia, A., Pinto, D., Beltramello, M., Hernandez, P., Greaney, A. J., Marzi, R., Glass, W. G., Zhang, I., Dingens, A. S., Bowen, J. E., Tortorici, M. A., Walls, A. C., Wojcechowskyj, J. A., De Marco, A., … Snell, G. (2021). SARS-CoV-2 RBD antibodies that maximize breadth and resistance to escape. *Nature*, *597*(7874), 97–102. https://doi.org/10.1038/s41586-021-03807-6

Starr, T. N., Greaney, A. J., Hannon, W. W., Loes, A. N., Hauser, K., Dillen, J. R., Ferri, E., Farrell, A. G., Dadonaite, B., McCallum, M., Matreyek, K. A., Corti, D., Veesler, D., Snell, G., & Bloom, J. D. (2022). Shifting mutational constraints in the SARS-CoV-2 receptor-binding domain during viral evolution. *Science*, *377*(6604), 420–424. https://doi.org/10.1126/science.abo7896

Starr, T. N., Greaney, A. J., Hilton, S. K., Ellis, D., Crawford, K. H. D., Dingens, A. S., Navarro, M. J., Bowen, J. E., Tortorici, M. A., Walls, A. C., King, N. P., Veesler, D., & Bloom, J. D. (2020). Deep mutational scanning of SARS-CoV-2 receptor binding domain reveals constraints on folding and ACE2 binding. *Cell*, *182*(5), 1295–1310.e20. https://doi.org/10.1016/j.cell.2020.08.012

Starr, T. N., Greaney, A. J., Stewart, C. M., Walls, A. C., Hannon, W. W., Veesler, D., & Bloom, J. D. (2022). Deep mutational scans for ACE2 binding, RBD expression, and antibody escape in the SARS-CoV-2 Omicron BA.1 and BA.2 receptor-binding domains. *PLoS Pathogens*, *18*(11), e1010951. https://doi.org/10.1371/journal.ppat.1010951

Starr, T. N., Zepeda, S. K., Walls, A. C., Greaney, A. J., Alkhovsky, S., Veesler, D., & Bloom, J. D. (2022). ACE2 binding is an ancestral and evolvable trait of sarbecoviruses. *Nature*, *603*(7903), 913–918. https://doi.org/10.1038/s41586-022-04464-z

Sui, J., Hwang, W. C., Perez, S., Wei, G., Aird, D., Chen, L.-M., Santelli, E., Stec, B., Cadwell, G., Ali, M., Wan, H., Murakami, A., Yammanuru, A., Han, T., Cox, N. J., Bankston, L. A., Donis, R. O., Liddington, R. C., & Marasco, W. A. (2009). Structural and functional bases for broad-spectrum neutralization of avian and human influenza A viruses. *Nature Structural & Molecular Biology*, *16*(3), 265–273. https://doi.org/10.1038/nsmb.1566

Sui, J., Li, W., Murakami, A., Tamin, A., Matthews, L. J., Wong, S. K., Moore, M. J., Tallarico, A. S. C., Olurinde, M., Choe, H., Anderson, L. J., Bellini, W. J., Farzan, M., & Marasco, W. A. (2004). Potent neutralization of severe acute respiratory syndrome (SARS) coronavirus by a human mAb to S1 protein that blocks receptor association. *Proceedings of the National Academy of Sciences of the United States of America*, *101*(8), 2536–2541. https://doi.org/10.1073/pnas.0307140101

Suloway, C., Pulokas, J., Fellmann, D., Cheng, A., Guerra, F., Quispe, J., Stagg, S., Potter, C. S., & Carragher, B. (2005). Automated molecular microscopy: the new Leginon system. *Journal of Structural Biology*, *151*(1), 41–60. https://doi.org/10.1016/j.jsb.2005.03.010

Sun, X., Yi, C., Zhu, Y., Ding, L., Xia, S., Chen, X., Liu, M., Gu, C., Lu, X., Fu, Y., Chen, S., Zhang, T., Zhang, Y., Yang, Z., Ma, L., Gu, W., Hu, G., Du, S., Yan, R., … Sun, B. (2022). Neutralization mechanism of a human antibody with pan-coronavirus reactivity including SARS-CoV-2. *Nature Microbiology*, *7*(7), 1063–1074. https://doi.org/10.1038/s41564-022-01155-3

Tan, C. W., Chia, W. N., Zhu, F., Young, B. E., Chantasrisawad, N., Hwa, S.-H., Yeoh, A. Y.-Y., Lim, B. L., Yap, W. C., Pada, S. K. M. S., Tan, S. Y., Jantarabenjakul, W., Toh, L. K., Chen, S., Zhang, J., Mah, Y. Y., Chen, V. C.-W., Chen, M. I.-C., Wacharapluesadee, S., … Wang, L.-F. (2022). SARS-CoV-2 Omicron variant emerged under immune selection. *Nature Microbiology*, *7*(11), 1756–1761. https://doi.org/10.1038/s41564-022-01246-1

Tang, J., Zeng, C., Cox, T. M., Li, C., Son, Y. M., Cheon, I. S., Wu, Y., Behl, S., Taylor, J. J., Chakaraborty, R., Johnson, A. J., Shiavo, D. N., Utz, J. P., Reisenauer, J. S., Midthun, D. E., Mullon, J. J., Edell, E. S., Alameh, M. G., Borish, L., … Sun, J. (2022). Respiratory mucosal immunity against SARS-CoV-2 after mRNA vaccination. *Science Immunology*, *7*(76), eadd4853. https://doi.org/10.1126/sciimmunol.add4853

Tan, T. J. C., Mou, Z., Lei, R., Ouyang, W. O., Yuan, M., Song, G., Andrabi, R., Wilson, I. A., Kieffer, C., Dai, X., Matreyek, K. A., & Wu, N. C. (2023). High-throughput identification of prefusion-stabilizing mutations in SARS-CoV-2 spike. *Nature Communications*, *14*(1), 2003. https://doi.org/10.1038/s41467-023-37786-1

Tao, Y., & Tong, S. (2019). Complete genome sequence of a severe acute respiratory syndrome-related Coronavirus from Kenyan bats. *Microbiology Resource Announcements*, *8*(28). https://doi.org/10.1128/MRA.00548-19

Tegally, H., Moir, M., Everatt, J., Giovanetti, M., Scheepers, C., Wilkinson, E., Subramoney, K., Makatini, Z., Moyo, S., Amoako, D. G., Baxter, C., Althaus, C. L., Anyaneji, U. J., Kekana, D., Viana, R., Giandhari, J., Lessells, R. J., Maponga, T., Maruapula, D., … de Oliveira, T. (2022). Emergence of SARS-CoV-2 Omicron lineages BA.4 and BA.5 in South Africa. *Nature Medicine*, *28*(9), 1785–1790. https://doi.org/10.1038/s41591-022-01911-2

Tegally, H., Wilkinson, E., Giovanetti, M., Iranzadeh, A., Fonseca, V., Giandhari, J., Doolabh, D., Pillay, S., San, E. J., Msomi, N., Mlisana, K., von Gottberg, A., Walaza, S., Allam, M., Ismail, A., Mohale, T., Glass, A. J., Engelbrecht, S., Van Zyl, G., … de Oliveira, T. (2021). Detection of a SARS-CoV-2 variant of concern in South Africa. *Nature*, *592*(7854), 438–443. https://doi.org/10.1038/s41586-021-03402-9

Tegunov, D., & Cramer, P. (2019). Real-time cryo-electron microscopy data preprocessing with Warp. *Nature Methods*, *16*(11), 1146–1152. https://doi.org/10.1038/s41592-019-0580-y

Temmam, S., Vongphayloth, K., Baquero, E., Munier, S., Bonomi, M., Regnault, B., Douangboubpha, B., Karami, Y., Chrétien, D., Sanamxay, D., Xayaphet, V., Paphaphanh, P., Lacoste, V., Somlor, S., Lakeomany, K., Phommavanh, N., Pérot, P., Dehan, O., Amara, F., … Eloit, M. (2022). Bat coronaviruses related to SARS-CoV-2 and infectious for human cells. *Nature*, *604*(7905), 330–336. https://doi.org/10.1038/s41586-022-04532-4

Throsby, M., van den Brink, E., Jongeneelen, M., Poon, L. L. M., Alard, P., Cornelissen, L., Bakker, A., Cox, F., van Deventer, E., Guan, Y., Cinatl, J., ter Meulen, J., Lasters, I., Carsetti, R., Peiris, M., de Kruif, J., & Goudsmit, J. (2008). Heterosubtypic neutralizing monoclonal antibodies cross-protective against H5N1 and H1N1 recovered from human IgM+ memory B cells. *PloS One*, *3*(12), e3942. https://doi.org/10.1371/journal.pone.0003942

Tian, J.-H., Patel, N., Haupt, R., Zhou, H., Weston, S., Hammond, H., Logue, J., Portnoff, A. D., Norton, J., Guebre-Xabier, M., Zhou, B., Jacobson, K., Maciejewski, S., Khatoon, R., Wisniewska, M., Moffitt, W., Kluepfel-Stahl, S., Ekechukwu, B., Papin, J., … Smith, G. (2021). SARS-CoV-2 spike glycoprotein vaccine candidate NVX-CoV2373 immunogenicity in baboons and protection in mice. *Nature Communications*, *12*(1), 372. https://doi.org/10.1038/s41467-020-20653-8

Toelzer, C., Gupta, K., Yadav, S. K. N., Borucu, U., Davidson, A. D., Kavanagh Williamson, M., Shoemark, D. K., Garzoni, F., Staufer, O., Milligan, R., Capin, J., Mulholland, A. J., Spatz, J., Fitzgerald, D., Berger, I., & Schaffitzel, C. (2020). Free fatty acid binding pocket in the locked structure of SARS-CoV-2 spike protein. *Science*, *370*(6517), 725–730. https://doi.org/10.1126/science.abd3255

Tong, S., Conrardy, C., Ruone, S., Kuzmin, I. V., Guo, X., Tao, Y., Niezgoda, M., Haynes, L., Agwanda, B., Breiman, R. F., Anderson, L. J., & Rupprecht, C. E. (2009). Detection of novel SARS-like and other coronaviruses in bats from Kenya. *Emerging Infectious Diseases*, *15*(3), 482–485. https://doi.org/10.3201/eid1503.081013

Tortorici, M. A., Beltramello, M., Lempp, F. A., Pinto, D., Dang, H. V., Rosen, L. E., McCallum, M., Bowen, J., Minola, A., Jaconi, S., Zatta, F., De Marco, A., Guarino, B., Bianchi, S., Lauron, E. J., Tucker, H., Zhou, J., Peter, A., Havenar-Daughton, C., … Veesler, D. (2020). Ultrapotent human antibodies protect against SARS-CoV-2 challenge via multiple mechanisms. *Science (New York, N.Y.)*, *370*(6519), 950–957. https://doi.org/10.1126/science.abe3354

Tortorici, M. A., Czudnochowski, N., Starr, T. N., Marzi, R., Walls, A. C., Zatta, F., Bowen, J. E., Jaconi, S., Di Iulio, J., Wang, Z., De Marco, A., Zepeda, S. K., Pinto, D., Liu, Z., Beltramello, M., Bartha, I., Housley, M. P., Lempp, F. A., Rosen, L. E., … Pizzuto, M. S. (2021). Broad sarbecovirus neutralization by a human monoclonal antibody. *Nature*, *597*(7874), 103–108. https://doi.org/10.1038/s41586-021-03817-4

Tortorici, M. A., & Veesler, D. (2019). Structural insights into coronavirus entry. *Advances in Virus Research*, *105*, 93–116. https://doi.org/10.1016/bs.aivir.2019.08.002

Tortorici, M. A., Walls, A. C., Lang, Y., Wang, C., Li, Z., Koerhuis, D., Boons, G.-J., Bosch, B.-J., Rey, F. A., de Groot, R. J., & Veesler, D. (2019). Structural basis for human coronavirus attachment to sialic acid receptors. *Nature Structural & Molecular Biology*, *26*(6), 481–489. https://doi.org/10.1038/s41594-019-0233-y

Ueda, G., Antanasijevic, A., Fallas, J. A., Sheffler, W., Copps, J., Ellis, D., Hutchinson, G. B., Moyer, A., Yasmeen, A., Tsybovsky, Y., Park, Y.-J., Bick, M. J., Sankaran, B., Gillespie, R. A., Brouwer, P. J., Zwart, P. H., Veesler, D., Kanekiyo, M., Graham, B. S., … Baker, D. (2020). Tailored design of protein nanoparticle scaffolds for multivalent presentation of viral glycoprotein antigens. *eLife*, *9*(e57659). https://doi.org/10.7554/eLife.57659

van Erp, E. A., Luytjes, W., Ferwerda, G., & van Kasteren, P. B. (2019). Fc-Mediated Antibody Effector Functions During Respiratory Syncytial Virus Infection and Disease. *Frontiers in Immunology*, *10*, 548. https://doi.org/10.3389/fimmu.2019.00548

Viana, R., Moyo, S., Amoako, D. G., Tegally, H., Scheepers, C., Althaus, C. L., Anyaneji, U. J., Bester, P. A., Boni, M. F., Chand, M., Choga, W. T., Colquhoun, R., Davids, M., Deforche, K., Doolabh, D., du Plessis, L., Engelbrecht, S., Everatt, J., Giandhari, J., … de Oliveira, T. (2022). Rapid epidemic expansion of the SARS-CoV-2 Omicron variant in southern Africa. *Nature*, *603*(7902), 679–686. https://doi.org/10.1038/s41586-022-04411-y

V'kovski, P., Kratzel, A., Steiner, S., Stalder, H., & Thiel, V. (2021). Coronavirus biology and replication: implications for SARS-CoV-2. *Nature Reviews. Microbiology*, *19*(3), 155–170. https://doi.org/10.1038/s41579-020-00468-6

Vogel, A. B., Kanevsky, I., Che, Y., Swanson, K. A., Muik, A., Vormehr, M., Kranz, L. M., Walzer, K. C., Hein, S., Güler, A., Loschko, J., Maddur, M. S., Ota-Setlik, A., Tompkins, K., Cole, J., Lui, B. G., Ziegenhals, T., Plaschke, A., Eisel, D., … Sahin, U. (2021). BNT162b vaccines protect rhesus macaques from SARS-CoV-2. *Nature*, *592*(7853), 283–289. https://doi.org/10.1038/s41586-021-03275-y

Wacharapluesadee, S., Tan, C. W., Maneeorn, P., Duengkae, P., Zhu, F., Joyjinda, Y., Kaewpom, T., Chia, W. N., Ampoot, W., Lim, B. L., Worachotsueptrakun, K., Chen, V. C.-W., Sirichan, N., Ruchisrisarod, C., Rodpan, A., Noradechanon, K., Phaichana, T., Jantarat, N., Thongnumchaima, B., … Wang, L.-F. (2021). Evidence for SARS-CoV-2 related coronaviruses circulating in bats and pangolins in Southeast Asia. *Nature Communications*, *12*(1), 972. https://doi.org/10.1038/s41467-021-21240-1

Walls, A. C., Fiala, B., Schäfer, A., Wrenn, S., Pham, M. N., Murphy, M., Tse, L. V., Shehata, L., O'Connor, M. A., Chen, C., Navarro, M. J., Miranda, M. C., Pettie, D., Ravichandran, R., Kraft, J. C., Ogohara, C., Palser, A., Chalk, S., Lee, E.-C., … King, N. P. (2020). Elicitation of Potent Neutralizing Antibody Responses by Designed Protein Nanoparticle Vaccines for SARS-CoV-2. *Cell*, *183*(5), 1367–1382.e17. https://doi.org/10.1016/j.cell.2020.10.043

Walls, A. C., Miranda, M. C., Schäfer, A., Pham, M. N., Greaney, A., Arunachalam, P. S., Navarro, M.-J., Tortorici, M. A., Rogers, K., O'Connor, M. A., Shirreff, L., Ferrell, D. E., Bowen, J., Brunette, N., Kepl, E., Zepeda, S. K., Starr, T., Hsieh, C.-L., Fiala, B., … Veesler, D. (2021). Elicitation of broadly protective sarbecovirus immunity by receptor-binding domain nanoparticle vaccines. *Cell*, *184*(21), 5432–5447.e16. https://doi.org/10.1016/j.cell.2021.09.015

Walls, A. C., Park, Y.-J., Tortorici, M. A., Wall, A., McGuire, A. T., & Veesler, D. (2020).

Structure, function, and antigenicity of the SARS-CoV-2 spike glycoprotein. *Cell*, *181*(2), 281–292.e6. https://doi.org/10.1016/j.cell.2020.02.058

Walls, A. C., Sprouse, K. R., Bowen, J. E., Joshi, A., Franko, N., Navarro, M. J., Stewart, C., Cameroni, E., McCallum, M., Goecker, E. A., Degli-Angeli, E. J., Logue, J., Greninger, A., Corti, D., Chu, H. Y., & Veesler, D. (2022). SARS-CoV-2 breakthrough infections elicit potent, broad, and durable neutralizing antibody responses. *Cell*, *185*(5), 872–880.e3. https://doi.org/10.1016/j.cell.2022.01.011

Walls, A. C., Tortorici, M. A., Bosch, B.-J., Frenz, B., Rottier, P. J. M., DiMaio, F., Rey, F. A., & Veesler, D. (2016). Cryo-electron microscopy structure of a coronavirus spike glycoprotein trimer. *Nature*, *531*(7592), 114–117. https://doi.org/10.1038/nature16988

Walls, A. C., Tortorici, M. A., Snijder, J., Xiong, X., Bosch, B.-J., Rey, F. A., & Veesler, D. (2017). Tectonic conformational changes of a coronavirus spike glycoprotein promote membrane fusion. *Proceedings of the National Academy of Sciences of the United States of America*, *114*(42), 11157–11162. https://doi.org/10.1073/pnas.1708727114

Walls, A. C., Xiong, X., Park, Y.-J., Tortorici, M. A., Snijder, J., Quispe, J., Cameroni, E., Gopal, R., Dai, M., Lanzavecchia, A., Zambon, M., Rey, F. A., Corti, D., & Veesler, D. (2019). Unexpected receptor functional mimicry elucidates activation of Coronavirus fusion. *Cell*, *176*(5), 1026–1039.e15. https://doi.org/10.1016/j.cell.2018.12.028

Walls, A., Tortorici, M. A., Bosch, B.-J., Frenz, B., Rottier, P. J. M., DiMaio, F., Rey, F. A., & Veesler, D. (2017). Crucial steps in the structure determination of a coronavirus spike glycoprotein using cryo-electron microscopy. *Protein Science*, *26*(1), 113–121. https://doi.org/10.1002/pro.3048

Walsh, E. E., Frenck, R. W., Jr, Falsey, A. R., Kitchin, N., Absalon, J., Gurtman, A., Lockhart, S., Neuzil, K., Mulligan, M. J., Bailey, R., Swanson, K. A., Li, P., Koury, K., Kalina, W., Cooper, D., Fontes-Garfias, C., Shi, P.-Y., Türeci, Ö., Tompkins, K. R., … Gruber, W. C. (2020). Safety and immunogenicity of two RNA-based Covid-19 vaccine candidates. *The New England Journal of Medicine*, *383*(25), 2439–2450. https://doi.org/10.1056/NEJMoa2027906

Wang, C., van Haperen, R., Gutiérrez-Álvarez, J., Li, W., Okba, N. M. A., Albulescu, I., Widjaja, I., van Dieren, B., Fernandez-Delgado, R., Sola, I., Hurdiss, D. L., Daramola, O., Grosveld, F., van Kuppeveld, F. J. M., Haagmans, B. L., Enjuanes, L., Drabek, D., & Bosch, B.-J. (2021). A conserved immunogenic and vulnerable site on the coronavirus spike protein delineated by cross-reactive monoclonal antibodies. *Nature Communications*, *12*(1), 1715. https://doi.org/10.1038/s41467-021-21968-w

Wang, N., Li, S.-Y., Yang, X.-L., Huang, H.-M., Zhang, Y.-J., Guo, H., Luo, C.-M., Miller, M., Zhu, G., Chmura, A. A., Hagan, E., Zhou, J.-H., Zhang, Y.-Z., Wang, L.-F., Daszak, P., & Shi, Z.-L. (2018). Serological evidence of bat SARS-related Coronavirus infection in humans, China. *Virologica Sinica*, *33*(1), 104–107. https://doi.org/10.1007/s12250-018-0012-7

Wang, R. Y.-R., Song, Y., Barad, B. A., Cheng, Y., Fraser, J. S., & DiMaio, F. (2016). Automated structure refinement of macromolecular assemblies from cryo-EM maps using Rosetta. *eLife*, *5*(e17219). https://doi.org/10.7554/elife.17219

Watanabe, Y., Allen, J. D., Wrapp, D., McLellan, J. S., & Crispin, M. (2020). Site-specific glycan analysis of the SARS-CoV-2 spike. *Science (New York, N.Y.)*, *369*(6501), 330–333. https://doi.org/10.1126/science.abb9983

Watson, J. L., Juergens, D., Bennett, N. R., Trippe, B. L., Yim, J., Eisenach, H. E., Ahern, W., Borst, A. J., Ragotte, R. J., Milles, L. F., Wicky, B. I. M., Hanikel, N., Pellock, S. J., Courbet, A., Sheffler, W., Wang, J., Venkatesh, P., Sappington, I., Torres, S. V., … Baker, D. (2023). De novo design of protein structure and function with RFdiffusion. *Nature*, *620*(7976), 1089–1100. https://doi.org/10.1038/s41586-023-06415-8

Wells, H. L., Letko, M., Lasso, G., Ssebide, B., Nziza, J., Byarugaba, D. K., Navarrete-Macias, I., Liang, E., Cranfield, M., Han, B. A., Tingley, M. W., Diuk-Wasser, M., Goldstein, T., Johnson, C. K., Mazet, J. A. K., Chandran, K., Munster, V. J., Gilardi, K., & Anthony, S. J. (2021). The evolutionary history of ACE2 usage within the coronavirus subgenus Sarbecovirus. *Virus Evolution*, *7*(1), veab007. https://doi.org/10.1093/ve/veab007

Wentz, A. E., & Shusta, E. V. (2007). A novel high-throughput screen reveals yeast genes that increase secretion of heterologous proteins. *Applied and Environmental Microbiology*, *73*(4), 1189–1198. https://doi.org/10.1128/AEM.02427-06

Westendorf, K., Žentelis, S., Wang, L., Foster, D., Vaillancourt, P., Wiggin, M., Lovett, E., van der Lee, R., Hendle, J., Pustilnik, A., Sauder, J. M., Kraft, L., Hwang, Y., Siegel, R. W., Chen, J., Heinz, B. A., Higgs, R. E., Kallewaard, N. L., Jepson, K., … Barnhart, B. C. (2022). LY-CoV1404 (bebtelovimab) potently neutralizes SARS-CoV-2 variants. *Cell Reports*, *39*(7), 110812. https://doi.org/10.1016/j.celrep.2022.110812

Willett, B. J., Grove, J., MacLean, O. A., Wilkie, C., De Lorenzo, G., Furnon, W., Cantoni, D., Scott, S., Logan, N., Ashraf, S., Manali, M., Szemiel, A., Cowton, V., Vink, E., Harvey, W. T., Davis, C., Asamaphan, P., Smollett, K., Tong, L., … Thomson, E. C. (2022). SARS-CoV-2 Omicron is an immune escape variant with an altered cell entry pathway. *Nature Microbiology*, *7*(8), 1161–1179. https://doi.org/10.1038/s41564-022-01143-7

Wilson, I. A., Skehel, J. J., & Wiley, D. C. (1981). Structure of the haemagglutinin membrane glycoprotein of influenza virus at 3 Å resolution. *Nature*, *289*(5796), 366–373. https://doi.org/10.1038/289366a0

Winkler, E. S., Bailey, A. L., Kafai, N. M., Nair, S., McCune, B. T., Yu, J., Fox, J. M., Chen, R. E., Earnest, J. T., Keeler, S. P., Ritter, J. H., Kang, L.-I., Dort, S., Robichaud, A., Head, R., Holtzman, M. J., & Diamond, M. S. (2020). SARS-CoV-2 infection of human ACE2-transgenic mice causes severe lung inflammation and impaired function. *Nature Immunology*, *21*(11), 1327–1335. https://doi.org/10.1038/s41590-020-0778-2

Winkler, E. S., Gilchuk, P., Yu, J., Bailey, A. L., Chen, R. E., Chong, Z., Zost, S. J., Jang, H., Huang, Y., Allen, J. D., Case, J. B., Sutton, R. E., Carnahan, R. H., Darling, T. L., Boon, A. C. M., Mack, M., Head, R. D., Ross, T. M., Crowe, J. E., Jr, & Diamond, M. S. (2021). Human neutralizing antibodies against SARS-CoV-2 require intact Fc effector functions for optimal therapeutic protection. *Cell*, *184*(7), 1804–1820.e16. https://doi.org/10.1016/j.cell.2021.02.026

Wrapp, D., Wang, N., Corbett, K. S., Goldsmith, J. A., Hsieh, C.-L., Abiona, O., Graham, B. S., & McLellan, J. S. (2020). Cryo-EM structure of the 2019-nCoV spike in the prefusion conformation. *Science (New York, N.Y.)*, *367*(6483), 1260–1263. https://doi.org/10.1126/science.abb2507

Wrobel, A. G., Benton, D. J., Xu, P., Calder, L. J., Borg, A., Roustan, C., Martin, S. R., Rosenthal, P. B., Skehel, J. J., & Gamblin, S. J. (2021). Structure and binding properties of Pangolin-CoV spike glycoprotein inform the evolution of SARS-CoV-2. *Nature Communications*, *12*(1), 837. https://doi.org/10.1038/s41467-021-21006-9

Wu, W.-L., Chiang, C.-Y., Lai, S.-C., Yu, C.-Y., Huang, Y.-L., Liao, H.-C., Liao, C.-L., Chen, H.-W., & Liu, S.-J. (2022). Monoclonal antibody targeting the conserved region of the SARS-CoV-2 spike protein to overcome viral variants. *JCI Insight*, *7*(8). https://doi.org/10.1172/jci.insight.157597

Wu, Y., & Zhao, S. (2021). Furin cleavage sites naturally occur in coronaviruses. *Stem Cell Research*, *50*(102115), 102115. https://doi.org/10.1016/j.scr.2020.102115

Xing, L., Liu, Z., Wang, X., Liu, Q., Xu, W., Mao, Q., Zhang, X., Hao, A., Xia, S., Liu, Z., Sun, L., Zhang, G., Wang, Q., Chen, Z., Jiang, S., Sun, L., & Lu, L. (2025). Early fusion intermediate of ACE2-using coronavirus spike acting as an antiviral target. *Cell*, *188*(5), 1297–1314.e24. https://doi.org/10.1016/j.cell.2025.01.012

Xiong, Q., Cao, L., Ma, C., Tortorici, M. A., Liu, C., Si, J., Liu, P., Gu, M., Walls, A. C., Wang, C., Shi, L., Tong, F., Huang, M., Li, J., Zhao, C., Shen, C., Chen, Y., Zhao, H., Lan, K., … Yan, H. (2022). Close relatives of MERS-CoV in bats use ACE2 as their functional receptors. *Nature*, *612*(7941), 748–757. https://doi.org/10.1038/s41586-022-05513-3

Yang, X.-L., Hu, B., Wang, B., Wang, M.-N., Zhang, Q., Zhang, W., Wu, L.-J., Ge, X.-Y., Zhang, Y.-Z., Daszak, P., Wang, L.-F., & Shi, Z.-L. (2015). Isolation and characterization of a novel bat Coronavirus closely related to the direct progenitor of severe acute respiratory syndrome Coronavirus. *Journal of Virology*, *90*(6), 3253–3256. https://doi.org/10.1128/JVI.02582-15

Yassine, H. M., Boyington, J. C., McTamney, P. M., Wei, C.-J., Kanekiyo, M., Kong, W.-P., Gallagher, J. R., Wang, L., Zhang, Y., Joyce, M. G., Lingwood, D., Moin, S. M., Andersen, H., Okuno, Y., Rao, S. S., Harris, A. K., Kwong, P. D., Mascola, J. R., Nabel, G. J., & Graham, B. S. (2015). Hemagglutinin-stem nanoparticles generate heterosubtypic influenza protection. *Nature Medicine*, *21*(9), 1065–1070. https://doi.org/10.1038/nm.3927

Ying, B., Darling, T. L., Desai, P., Liang, C.-Y., Dmitriev, I. P., Soudani, N., Bricker, T., Kashentseva, E. A., Harastani, H., Raju, S., Liu, M., Schmidt, A. G., Curiel, D. T., Boon, A. C. M., & Diamond, M. S. (2024). Mucosal vaccine-induced cross-reactive CD8+ T cells protect against SARS-CoV-2 XBB.1.5 respiratory tract infection. *Nature Immunology*, *25*(3), 537–551. https://doi.org/10.1038/s41590-024-01743-x

Yisimayi, A., Song, W., Wang, J., Jian, F., Yu, Y., Chen, X., Xu, Y., Yang, S., Niu, X., Xiao, T., Wang, J., Zhao, L., Sun, H., An, R., Zhang, N., Wang, Y., Wang, P., Yu, L., Lv, Z., … Cao, Y. (2024). Repeated Omicron exposures override ancestral SARS-CoV-2 immune imprinting. *Nature*, *625*(7993), 148–156. https://doi.org/10.1038/s41586-023-06753-7

Yuan, Y., Cao, D., Zhang, Y., Ma, J., Qi, J., Wang, Q., Lu, G., Wu, Y., Yan, J., Shi, Y., Zhang, X., & Gao, G. F. (2017). Cryo-EM structures of MERS-CoV and SARS-CoV spike glycoproteins reveal the dynamic receptor binding domains. *Nature Communications*, *8*(1), 15092. https://doi.org/10.1038/ncomms15092

Zambaldi, V., La, D., Chu, A. E., Patani, H., Danson, A. E., Kwan, T. O. C., Frerix, T., Schneider, R. G., Saxton, D., Thillaisundaram, A., Wu, Z., Moraes, I., Lange, O., Papa, E., Stanton, G., Martin, V., Singh, S., Wong, L. H., Bates, R., … Wang, J. (2024). De novo design of high-affinity protein binders with AlphaProteo. In *arXiv [q-bio.BM]*. arXiv. http://arxiv.org/abs/2409.08022

Zhang, S., Liang, Q., He, X., Zhao, C., Ren, W., Yang, Z., Wang, Z., Ding, Q., Deng, H., Wang, T., Zhang, L., & Wang, X. (2022). Loss of Spike N370 glycosylation as an important evolutionary event for the enhanced infectivity of SARS-CoV-2. *Cell Research*, *32*(3), 315–318. https://doi.org/10.1038/s41422-021-00600-y

Zhou, H., Ji, J., Chen, X., Bi, Y., Li, J., Wang, Q., Hu, T., Song, H., Zhao, R., Chen, Y., Cui, M., Zhang, Y., Hughes, A. C., Holmes, E. C., & Shi, W. (2021). Identification of novel bat coronaviruses sheds light on the evolutionary origins of SARS-CoV-2 and related viruses. *Cell*, *184*(17), 4380–4391.e14. https://doi.org/10.1016/j.cell.2021.06.008

Zhou, P., Song, G., Liu, H., Yuan, M., He, W.-T., Beutler, N., Zhu, X., Tse, L. V., Martinez, D. R., Schäfer, A., Anzanello, F., Yong, P., Peng, L., Dueker, K., Musharrafieh, R., Callaghan, S., Capozzola, T., Limbo, O., Parren, M., … Andrabi, R. (2023). Broadly neutralizing anti-S2 antibodies protect against all three human betacoronaviruses that cause deadly disease. *Immunity*, *0*(0). https://doi.org/10.1016/j.immuni.2023.02.005

Zhou, P., Yang, X.-L., Wang, X.-G., Hu, B., Zhang, L., Zhang, W., Si, H.-R., Zhu, Y., Li, B., Huang, C.-L., Chen, H.-D., Chen, J., Luo, Y., Guo, H., Jiang, R.-D., Liu, M.-Q., Chen, Y., Shen, X.-R., Wang, X., … Shi, Z.-L. (2020). A pneumonia outbreak associated with a new coronavirus of probable bat origin. *Nature*, *579*(7798), 270–273. https://doi.org/10.1038/s41586-020-2012-7

Zhou, P., Yuan, M., Song, G., Beutler, N., Shaabani, N., Huang, D., He, W.-T., Zhu, X., Callaghan, S., Yong, P., Anzanello, F., Peng, L., Ricketts, J., Parren, M., Garcia, E., Rawlings, S. A., Smith, D. M., Nemazee, D., Teijaro, J. R., … Andrabi, R. (2022). A human antibody reveals a conserved site on beta-coronavirus spike proteins and confers protection against SARS-CoV-2 infection. *Science Translational Medicine*, *14*(637), eabi9215. https://doi.org/10.1126/scitranslmed.abi9215

Zhu, N., Zhang, D., Wang, W., Li, X., Yang, B., Song, J., Zhao, X., Huang, B., Shi, W., Lu, R., Niu, P., Zhan, F., Ma, X., Wang, D., Xu, W., Wu, G., Gao, G. F., Tan, W., & China Novel Coronavirus Investigating and Research Team. (2020). A novel Coronavirus from patients with pneumonia in China, 2019. *The New England Journal of Medicine*, *382*(8), 727–733. https://doi.org/10.1056/NEJMoa2001017

Zhu, W., Huang, Y., Gong, J., Dong, L., Yu, X., Chen, H., Li, D., Zhou, L., Yang, J., & Lu, S. (2023). A novel bat coronavirus with a polybasic furin-like cleavage site. *Virologica Sinica*, *38*(3), 344–350. https://doi.org/10.1016/j.virs.2023.04.009

Zivanov, J., Nakane, T., Forsberg, B. O., Kimanius, D., Hagen, W. J., Lindahl, E., & Scheres, S. H. (2018). New tools for automated high-resolution cryo-EM structure determination in RELION-3. *eLife*, *7*(e42166). https://doi.org/10.7554/eLife.42166

Zivanov, J., Nakane, T., & Scheres, S. H. W. (2019). A Bayesian approach to beam-induced motion correction in cryo-EM single-particle analysis. *IUCrJ*, *6*(Pt 1), 5–17. https://doi.org/10.1107/S205225251801463X